On the role of Hall magnetohydrodynamics in magnetic reconnection: Astrophysical Plasmas

A thesis submitted in partial fulfillment of

the requirements for the degree of

Doctor of Philosophy

by

Kamlesh Bora

(Roll No. 17330016)

Under the guidance of

Dr. Ramitendranath Bhattacharyya

Professor

Udaipur Solar Observatory

Physical Research Laboratory, Udaipur, India.

DEPARTMENT OF PHYSICS

INDIAN INSTITUTE OF TECHNOLOGY GANDHINAGAR

2022

to

my parents

&

teachers

Declaration

I declare that this written submission represents my ideas in my own words and where others' ideas or words have been included, I have adequately cited and referenced the original sources. I also declare that I have adhered to all principles of academic honesty and integrity and have not misrepresented or fabricated or falsified any idea/data/fact/source in my submission. I understand that any violation of the above will be cause for disciplinary action by the Institute and can also evoke penal action from the sources which have thus not been properly cited or from whom proper permission has not been taken when needed.

(Signature)

(Name: Kamlesh Bora)

(Roll No: 17330016)

CERTIFICATE

It is certified that the work contained in the thesis titled **"On the role of Hall magnetohydrodynamics in magnetic reconnection: Astrophysical Plasmas"** by **Miss. Kamlesh Bora** (Roll no: 17330016), has been carried out under my supervision and that this work has not been submitted elsewhere for degree.

I have read this dissertation and in my opinion, it is fully adequate in scope and quality as a dissertation for the degree of Doctor of Philosophy.

Dr. Ramitendranath Bhattacharyya
(Thesis Supervisor)
Professor
Udaipur Solar Observatory
Physical Research Laboratory
Badi Road, Udaipur 313001, India

Thesis Approval

The thesis entitled

On the role of Hall magnetohydrodynamics in magnetic reconnection: Astrophysical Plasmas

by

Kamlesh Bora
(Roll No. 17330016)

is approved for the degree of

Doctor of Philosophy

Examiner	Examiner
Supervisor	Chairman

Date: _____

Place: _____

Acknowledgements

The completion of this thesis would not have been possible without the help and support of many people. Here, I would like to express my deep gratitude toward all of them.

Firstly, I am grateful to my Ph.D. supervisor Prof. Ramit Bhattacharyya for giving me the opportunity to work with him. I thank him for his continuous patience, support and valuable guidance throughout my Ph.D. tenure. Working with such a courteous mentor, who allowed me to work without any constraint, has been a great experience for me and turned me into an independent researcher.

I am indebted to my collaborators Prof. Piotr K. Smolarkiewicz, Prof. Qiang Hu, and Dr. Avijeet Prasad for their invaluable contribution and support in my scientific endeavors. I sincerely thank the members of my Doctoral Studies Committee, Dr. Aveek Sarkar, Dr. Brajesh Kumar and Dr. Bhuwan Joshi for evaluating my work on a regular basis. Their valuable comments helped me to improve the scientific outcomes.

I am thankful to USO admin Deputy Head, Prof. Nandita Srivastava for her kind support in the past four years. I extend my gratitude to Prof. Anil Bhardwaj, Director, PRL, Ahmedabad for providing necessary facilities to carry out my research work and organizing different acitivities to make the enviornment engaging. I express my deep gratitude toward IIT Gandhinagar for Ph.D. registration. I am also thankful to Dr. Bhushit Vaishnav, Head Academic Services, for his support with the academic matters. I wish to acknowledge the support of Vikram-100 cluster and thank all the staff members of PRL computer center for providing computational facilities. A special thanks to Mr. Jigar Raval for his timely help over any computational issues. I thank the SDO team for their open data policy. Thanks are due to administration and library staff members at USO and Ahmedabad for their timely and kind cooperation throughout my Ph.D. tenure. A special thanks to Mr. Abhishek, administrative officer at USO for always helping me out with the admin matters with his kind and generous behavior.

This journey of past five years would not have been possible without the joyful company of my dear batch mates, seniors and juniors in PRL. I convey my sincere thanks to all of them for a pleasant stay in USO and PRL, Ahmedabad. I heartily thank my seniors, Dr. Avijeet Prasad, Dr. Sanjay Kumar, Dr. Ranadeep Sarkar, and Dr. Prabir Kumar Mitra for their invaluable support, and help toward learning the subject at initial stage. Without kind affection and company of Dr. Ranadeep Sarkar, Dr. Prabir Kumar Mitra, Binal Patel, and Satyam Agarwal, it would not

have been possible to get through the COVID-19 pandemic. I specially thank my friends, Mr. Himanshu Saxena, Ms. Shanwlee Sow Mondal, Mr. Partha S Jena, Mr. Vipin Kumar, Mrs. Rekha and my senior Surendra Vikram Singh for their kind support during my medical urgencies. I would also like to thank Sana, Pooja, and Anu for their joyful company always.

Thanks are due to (Mr.) Kushagra Upadhyay and Ritesh Patel for supporting me and extending their help to me in my hardest time. I am indebted to Ms. Sapna Bist, who is like sister to me, for her unconditional love and support. I would also like to thank (Ms.) Eesha Dangi and Kriti Deva for always standing by me and for their love. It would be incomplete without accrediting Mr. Mintu Kumar for his continuous help and motivation to me. Completing this thesis timely without the constant help and support of Mr. Satyam Agarwal would not have been possible, I am deeply indebted to him for his valuable and unconditional support.

Lastly, I would like to thank my family, above all, my parents, for their unconditional love, lifelong support, and the freedom they have given me to pursue research. It gives me immense pleasure to dedicate this thesis to them. I must say, that being away from home, I have missed many opportunities to be with my family members. But, they have always been by my side everytime.

(Kamlesh Bora)

Abstract

Magnetic reconnection is a distinctive fundamental process that often causes explosive energy release phenomena in various astrophysical plasmas. Generally, the astrophysical plasmas are characterized by large magnetic Reynolds number ($R_M = Lv/\lambda$, in usual notations) owing to their inherent large length scale and high temperature. Large R_M causes the Alfvèn flux freezing theorem—magnetic flux being frozen to the plasma flow—to be satisfied. Reconnection occurs due to the violation of Alfvén's flux-freezing theorem at small length scales which generate as a consequence of large-scale dynamics. Such small-scales are characterized by large gradients in the magnetic field and may occur as current sheets (regions of high current density) and magnetic nulls (locations where the magnetic field vanishes; $\mathbf{B} = 0$). The multiscale behavior of reconnection makes it challenging to study the physics at small-scales and capture its effect on large-scale dynamics simultaneously. Identification of the reconnection scale depends on the specific physical system under consideration. The outermost atmosphere of our nearest star Sun—the solar corona, serves as a prototype astrophysical plasma. Large-scale solar eruptions observed on the Sun, such as flares and coronal mass ejections (CMEs) are the manifestation of magnetic reconnection. In particular, solar flares are fast and impulsive phenomena since a huge amount of energy ($\approx 10^{32}$ erg) is released suddenly and rapidly within a very short time period ($\approx$ a few minutes to hours). Therefore, the underlying reconnections must be fast and impulsive too. The reconnection length scale in the solar corona (based on the observed impulsive rise time of hard X-ray emission during the solar flares) turns out to be a few tens of meters. At this scale, the order analysis of the induction equation indicates that the order of the Hall effect is much higher than the resistive diffusion. This leads to the Hall MHD description which can account for impulsive behavior as compared to the traditional theoretical models of reconnection.

Against the above backdrop, this thesis focuses on the investigation of the Hall effect in 3D magnetic reconnection through numerical simulations. For this purpose, a Hall MHD solver is developed and benchmarked toward the known properties of Hall-assisted reconnection. For benchmarking, a comparative study using Hall MHD and MHD simulations is carried out. The simulations are initi-

ated with an unidirectional sinusoidal magnetic field (contained in the xz plane of employed Cartesian geometry), having a non-zero Lorentz force which initiates the dynamics. In MHD simulation, the evolution of magnetic field lines is symmetric and confined within the xz planes. Magnetic reconnections within each plane generate magnetic islands which, when stacked together along the y direction, appear as magnetic flux tube made by disjoint magnetic field lines. Contrarily, the Hall MHD simulation exhibits an asymmetric and three-dimensional (3D) evolution, owing to the development of an out-of-reconnection plane (xz plane) magnetic field component (B_y) which is quadrupolar. This is in agreement with the earlier Hall MHD simulations in the literature. Subsequently, the B_y component causes the formation of a magnetic flux rope (MFR) in the computational domain. In their 2D projections, the rope and the flux tube appear as magnetic islands. Subsequent evolution exhibits the breakage of primary islands into secondary islands followed by their coalescence in both the simulations. However, the dynamics are faster during the Hall MHD. An important finding is the formation of twisted 3D magnetic structures which cannot be apprehended from 2D calculations, although their projections agree with the latter. The volume-averaged current density rate shows abrupt changes during the Hall MHD—signifying impulsiveness. Alongside, we have also explored the Whistler wave mode numerically vis-a-vis its analytical model and found the two to be matching reasonably well in Hall MHD simulations. Overall, the results agree with the existing scenario of Hall-assisted reconnection, thus validating the model.

Since the evolution of an MFR is instructive to understand the CMEs and eruptive flares on the Sun, the numerical model is employed to perform Hall MHD and MHD simulations toward the generation and evolution of an MFR. The simulations are initiated with 2.5D and 3D bipolar sheared magnetic fields. In the 2.5D case, MFR is levitating and unanchored while in the 3D case, it is anchored to the bottom boundary. The generation of MFR due to primary reconnections is identical for both cases in the two simulations. However, the subsequent evolution of MFRs is influenced by the Hall effect. In the 2.5D case, Hall MHD evolution depicts the local breakage of MFR, owing to the internal reconnections. When viewed favorably, the structure appears reminiscent of the “number eight

(8)". The temporal evolution of average magnetic energies, in the presence and absence of the Hall effect, is near-identical for both cases and consistent with the theoretical expectation that the Hall term does not affect the magnetic energy evolution. In the 3D case, the primary MFR gets generated in both simulations due to repetitive reconnections at 3D null points. Subsequently, Hall MHD evolution features the swirling motion of small-scale twisted structures in the vicinity of 3D null points. The intermittent reconnections within these structures lead to the formation of large-scale MFR which indicates the association of small-scale dynamics with large-scale structure formation—a key finding emphasizing the role of the Hall effect in 3D reconnection.

Based on the accomplished knowledge about the Hall effect in 3D magnetic reconnection, finally, in this thesis, the role of the Hall effect is explored for a solar flare. To achieve the aim, a C1.3 class flare on March 8, 2019 in the solar active region (AR) 12734 is selected as a test bed and the numerical model is employed to perform the data-based Hall MHD and MHD simulations. Analysis of multiwavelength observations from the AIA instrument on board SDO reveals an elongated extreme ultraviolet (EUV) counterpart of the eruption in the western part of the AR, a W-shaped flare ribbon, and the circular motion of chromospheric material in the eastern part. Subsequently, the magnetic field line morphologies over the AR are explored by employing the non-force-free field (non-FFF) extrapolation which uses the photospheric vector magnetogram from the HMI instrument on board SDO. The analysis of the extrapolated field reveals the presence of 3D nulls and quasi-separatrix layers (QSLs) which are favorable sites for 3D magnetic reconnection. A null point with fan-spine configuration is found in the middle of the active region whose Hall MHD evolution is in better agreement with the tip of the W-shaped flare ribbon. Further, the lower spine and fan remain anchored to the bottom boundary throughout the evolution, thus providing a pathway for post-reconnection plasma flow while in the MHD case, the lower spine gets disconnected. Notably, an MFR with QSLs as overlying field lines is found at the location of flare saturation in the SDO/AIA images. The Hall MHD simulation shows faster slipping reconnection of the flux-rope footpoints and overlying QSLs magnetic field lines. Consequently, the overlying magnetic field lines rise and re-

connect in the corona, thereby providing path for plasma ejection. This finding agrees with the observed eruption in the western part of AR. Contrarily, such a significant rise of the flux rope and overlying field lines is absent in the MHD simulation, thus signifying the reconnection to be slower in MHD. Interestingly, such field line dynamics suggest a distinct mechanism of flux rope eruption in 3D, which is not widely documented in the literature. The result further emphasizes that null points and true separatrices in 3D may not be required for eruptive flares. Additionally, a "fish-bone-like structure" surrounding a null line is found in the eastern part of the AR. A salient feature captured only in the Hall MHD is that rotating magnetic field lines agree remarkably with the observed circular plasma motion, both spatially and temporally.

Overall, investigations of the Hall effect on 3D magnetic reconnection employing the numerical simulations initiated with both the analytical and observed magnetic fields display significant changes in the magnetic structures around and on the reconnection site which subsequently alter the large-scale dynamics making the evolution faster. Therefore, this thesis provides the Hall MHD as a potential description to understand the faster reconnections in 3D with particular emphasis on the effects of structural dynamics at small-scale on large-scale structures.

Keywords: Magnetohydrodynamics, Hall magnetohydrodynamics, Magnetic reconnection, Solar active regions, Solar magnetic fields, Solar flares, Solar coronal mass ejections, and Numerical simulations.

List of Publications

1. **K. Bora**, R. Bhattacharyya, Avijeet Prasad, Bhuwan Joshi, Qiang Hu (2022): *"Comparison of the Hall Magnetohydrodynamics and Magnetohydrodynamics Evolution of a Flaring Solar Active Region"*. In: *The Astrophysical Journal*, 925, 197. DOI: https://doi.org/10.3847/1538-4357/ac3bce

2. **K. Bora**, R. Bhattacharyya, P. K. Smolarkiewicz (2021): *"Evolution of Three-dimensional Coherent Structures in Hall Magnetohydrodynamics"*. In: *The Astrophysical Journal*, 906, 102. DOI: https://doi.org/10.3847/1538-4357/abc8f7

Contents

List of Figures

List of Tables

Chapter 1

Introduction

Most of the observable matter in the universe is predominantly in the form of magnetized plasma. Generally, the astrophysical plasmas are magnetized, having high Lundquist number ($S = Lv_A/\lambda$; L being the length scale of magnetic field variation, v_A being the Alfvén speed, and λ being the magnetic diffusivity) causing the Alfvén's flux-freezing theorem (Alfvén, 1942) (discussed in detail later) to be satisfied. The dynamical evolution of such plasmas is often described by ideal magnetohydrodynamics (MHD). The validity of frozen-in condition on magnetic field lines being tied to plasma parcels makes it easier to study the dynamical evolution by tracking the motion of either one of them. However, unprecedented observations of explosive energy release phenomena such as flares and coronal mass ejections (CMEs) in various astrophysical systems reveal the diffusive nature of the plasma—breakdown of ideal MHD. The distinct fundamental process through which the magnetic energy is converted into other forms of energy *viz.* heat, the kinetic energy of plasma flow, and particle acceleration with the re-arrangement of magnetic field line connectivity is known as magnetic reconnection. In the presence of electrical resistivity, the flux-freezing condition gets violated and makes the plasma diffusive.

In this Chapter, we present a brief historical overview of magnetic reconnection and introduce the concept. The potential sites of magnetic reconnection in two-dimension (2D) and three-dimension (3D) are described along with the aspects of 2D and 3D reconnection. Then, we finally present the Hall magnetohydrodynamics (Hall MHD) as a potential description to understand the fast and impulsive

magnetic reconnection. The Chapter ends with a discussion of the thesis objectives and its organization.

1.1 Magnetic reconnection: Historical Overview

Historically, the notion of magnetic reconnection stems from the ideas, first introduced by Giovanelli (1946) motivated from the solar flare observations. Later on, the discussions between Giovanelli and Fred Hoyle, led Hoyle to propose the process occurring in Earth's magnetosphere (auroral substorms) due to the interaction between solar wind and Earth's magnetic field (Hoyle, 1949). Their realization that the electric fields near magnetic X-type neutral points are responsible for the heating and particle acceleration might be based on the fact that particle acceleration is only possible when a component of electric field is parallel to the magnetic field. Later, Cowling (1953) suggested that the solar flares owing to ohmic dissipation need a current sheet of only a few meters thick. Shortly, Dungey (1953) recognized that the magnetic reconnection process occurring in Earth's magnetic field is identical to the one in the solar flares. For the first time, Dungey (1953) demonstrated that the collapse of the X-type neutral points can actually form current sheets and proposed a cycle from magnetic reconnection at the magnetopause to reconnection at magnetotail in Earth's magnetosphere—specified as the 'Dungey cycle'. It was Dungey who introduced the concept of "lines of force can be broken and rejoined" for the first time. In his pioneering works on current sheets formation, Dungey treated the self-consistent nature of both plasma and magnetic fields rather than the simple motion of charged particles in electric and magnetic fields. Based on the fact that moving charged particles produce electric and magnetic fields, he used the MHD equations to investigate the effect of such fields where the Maxwell's equations are combined with Navier-Stokes equations.

Afterward, Sweet (1958) and Parker (1957) proposed a 2D steady-state theoretical model of magnetic reconnection within the MHD framework. Parker (1957) formulated the scaling laws for the model and coined the term "reconnection of field lines" or "merging of magnetic fields". The Sweet-Parker mechanism of reconnection is detailed in Section 1.3.1.1. The magnetic energy dissipation timescale

($\tau_d = L^2/\lambda \approx 10^6$ years, based on the global length-scale $L = 10^8$ m and diffusivity λ =1 $\mathrm{m^2 s^{-1}}$) is much too slow to explain the energy release during solar flares. Subsequently, Petschek (1964) developed a "fast reconnection" model to account for solar flares which, is discussed in Section 1.3.1.2.

Initial developments of magnetic reconnection models were in 2D within the MHD framework. A substantial amount of works have revealed important aspects of 2D reconnection over several decades. However, understanding magnetic reconnection in three dimensions (3D) is essential since the magnetic field in astrophysical plasmas is inherently 3D. Attempt to define magnetic reconnection have been made by Vasyliunas (1975); Sonnerup (1979), and Axford (1984) which will be discussed later in this chapter. These definitions are important in understanding existing scenarios of 3D magnetic reconnection and form the basis of the general magnetic reconnection (GMR) theory suggested by Schindler et al. (1988); Hesse & Schindler (1988).

1.2 Concept of Magnetic Reconnection: An MHD Approach

As described above, the dynamical evolution of astrophysical plasmas is given by the MHD description. Generally, the MHD equations are a set of coupled differential equations combining the Maxwell's equations of electromagnetism and Navier-Stokes equations of fluid dynamics. The MHD description of plasma is valid when the characteristic length and time scales of the system are much larger than the ion gyroradius and ion gyroperiod respectively—often referred to as collision-dominated plasma. The set of MHD equations and their physical interpretation are given as follows. Notably, here and hereafter, we use *SI* units except for numerical simulations carried out where cgs and dimensionless units are used.

1.2.1 MHD Equations

- Conservation of mass: Mass continuity equation

$$\frac{d\rho}{dt} + \rho(\nabla \cdot \mathbf{v}) = 0 \quad or \quad \frac{\partial \rho}{\partial t} + \nabla \cdot (\rho \mathbf{v}) = 0 \ , \tag{1.1}$$

where $\frac{d}{dt}$ is the total convective derivative or Lagrangian derivative, i.e., $\frac{d}{dt} = \frac{\partial}{\partial t} + \mathbf{v} \cdot \nabla$; ρ is the plasma density, and $\mathbf{v}$ is the plasma flow velocity. This equation implies that if mass flows into the system ($\nabla \cdot (\rho \mathbf{v}) < 0$) from the surrounding, the density increases $\left(\frac{\partial \rho}{\partial t} > 0\right)$ whereas if mass flows out of the system ($\nabla \cdot (\rho \mathbf{v}) > 0$) the density decreases $\left(\frac{\partial \rho}{\partial t} < 0\right)$.

- Conservation of momentum: Momentum balance or force balance equation for incompressible fluid

$$\rho \frac{d\mathbf{v}}{dt} = -\nabla p + \mathbf{J} \times \mathbf{B} + \rho \nu \nabla^2 \mathbf{v} \ , \tag{1.2}$$

where p is the thermal pressure, $\mathbf{J}$ is the current density, $\mathbf{B}$ is the magnetic field, and ν is the kinematic viscosity of the fluid.

- Electromagnetic induction equation

$$\nabla \times \mathbf{E} = -\frac{\partial \mathbf{B}}{\partial t} \ , \tag{1.3}$$

where $\mathbf{E}$ is the electric field.

- Ampere's law

$$\nabla \times \mathbf{B} = \mu_0 \mathbf{J} \ , \tag{1.4}$$

where μ_0 is the permeability of vacuum.

- Ohm's Law

$$\mathbf{E} + \mathbf{v} \times \mathbf{B} = \mathbf{N} \ , \tag{1.5}$$

where $\mathbf{N}$ includes the forcing terms which will be discussed shortly.

- Solenoidality of magnetic field

$$\nabla \cdot \mathbf{B} = 0 \ , \tag{1.6}$$

- Energy equation

$$\frac{d}{dt}\left(\frac{p}{\rho^\gamma}\right) = 0 \ , \tag{1.7}$$

where $\gamma = \frac{5}{3}$ is the specific heat ratio for an adiabatic equation of state. This form of energy equation assumes the plasma to be in an adiabatic state where it is thermally isolated (no exchange of heat) from its surroundings. More precisely, the time scale for the variation in p, ρ, and T is much smaller than the time scales for radiation, conduction, and heating—usually referred to as rapid changes in response to perturbations in the aforementioned parameters (Priest, 2014).

Combining Faraday-Maxwell's equation (Equation 1.3) and Ohm's law (Equation 1.5) essentially gives one of the fundamental MHD equations, namely, the *induction equation*. The induction equation for ideal Ohm's law $\mathbf{E} + \mathbf{v} \times \mathbf{B} = 0$ can be written as :

$$\frac{\partial \mathbf{B}}{\partial t} = \nabla \times (\mathbf{v} \times \mathbf{B}) \ . \tag{1.8}$$

If the resistive Ohm's law is considered $\mathbf{E} + \mathbf{v} \times \mathbf{B} = \eta \mathbf{J}$, where η is the electrical resistivity, then the induction equation takes the following form

$$\frac{\partial \mathbf{B}}{\partial t} = \nabla \times (\mathbf{v} \times \mathbf{B}) + \lambda \nabla^2 \mathbf{B} \ , \tag{1.9}$$

where $\lambda \equiv \frac{\eta}{\mu_0}$ is the spatially constant magnetic diffusivity. The first term on right-hand side of the above equation is the convective or advection term and the second term is resistive diffusion. The ratio of advection to resistive diffusion terms is known as magnetic Reynold's number, given by $R_M = L_0 V_0 / \lambda$; L_0 being the length scale over which the magnetic field varies and V_0 being the characteristic speed. It provides useful information about the flow and magnetic field coupling in plasma, e.g. if $R_M \gg 1$ (ideal limit) the advection processes govern the dynamics while the diffusion becomes unimportant, but if $R_M \ll 1$ (non-ideal limit) then the diffusive processes become significant.

1.2.2 Ideal limit ($R_M \gg 1$)

The concepts of magnetic flux and magnetic field line conservation are essential to understand magnetic reconnection. Central to the ideal MHD limit, both the magnetic flux and magnetic field lines are conserved which is discussed in the

following.

1.2.2.1 Conservation of magnetic flux

In the limit of large magnetic Reynold's number ($R_M \gg 1$), Alfvén's theorem (Alfvén, 1942) states that if magnetic flux through any closed curve is conserved then the magnetic field moves with the plasma as if the field is "frozen-in" or tied to the plasma parcels (Priest, 2014). Proof of this theorem can be presented by considering magnetic flux Φ through an area S of plasma restricted by a closed curve Γ :

$$\Phi = \iint_S \mathbf{B} \cdot d\mathbf{a} \ , \tag{1.10}$$

where $d\mathbf{a}$ is an infinitesimal area S. If $\mathbf{B}$ is an explicit function of time or/and the contour line of this plasma element changes, then the change in total magnetic flux can be due to the change of magnetic field strength following from the MHD equations ($\Phi^{'}$) and due to the area change of plasma element ($\Phi^{''}$) so that :

$$\frac{d\Phi}{dt} = \frac{d\Phi^{'}}{dt} + \frac{d\Phi^{''}}{dt} \ , \tag{1.11}$$

where

$$\frac{d\Phi^{'}}{dt} = \iint_S \frac{\partial \mathbf{B}}{\partial t} \cdot d\mathbf{a} \ . \tag{1.12}$$

Now, let us consider a small change of the area $d\mathbf{a}$ due to plasma motion with the velocity $\mathbf{v}$ in time interval dt, then:

$$d\mathbf{a} = \mathbf{v} \ dt \times d\mathbf{l} \ , \tag{1.13}$$

where $d\mathbf{l}$ is an infinitesimal length element on contour Γ. Then, the change in magnetic flux due to area change can be given as

$$d\Phi^{''} = \mathbf{B} \cdot d\mathbf{a} \ , \tag{1.14}$$

$$d\Phi^{''} = \mathbf{B} \cdot \mathbf{v} \times d\mathbf{l} \ dt \ , \tag{1.15}$$

using the vector identities $\mathbf{A}\cdot(\mathbf{B}\times\mathbf{C}) = \mathbf{B}\cdot(\mathbf{C}\times\mathbf{A}) = \mathbf{C}\cdot(\mathbf{A}\times\mathbf{B})$ and $\mathbf{A}\times\mathbf{B} = -\mathbf{B}\times\mathbf{A}$ leads to

$$d\Phi'' = -dt(\mathbf{v}\times\mathbf{B})\cdot d\mathbf{l}\ , \tag{1.16}$$

then the rate of change of flux due to area change is

$$\frac{d\Phi''}{dt} = -\int_{\Gamma}(\mathbf{v}\times\mathbf{B})\cdot d\mathbf{l}\ , \tag{1.17}$$

employing Stoke's curl theorem in Equation 1.17 and substituting values of $\frac{d\Phi'}{dt}$ from Equation 1.12 and $\frac{d\Phi''}{dt}$ in Equation 1.11

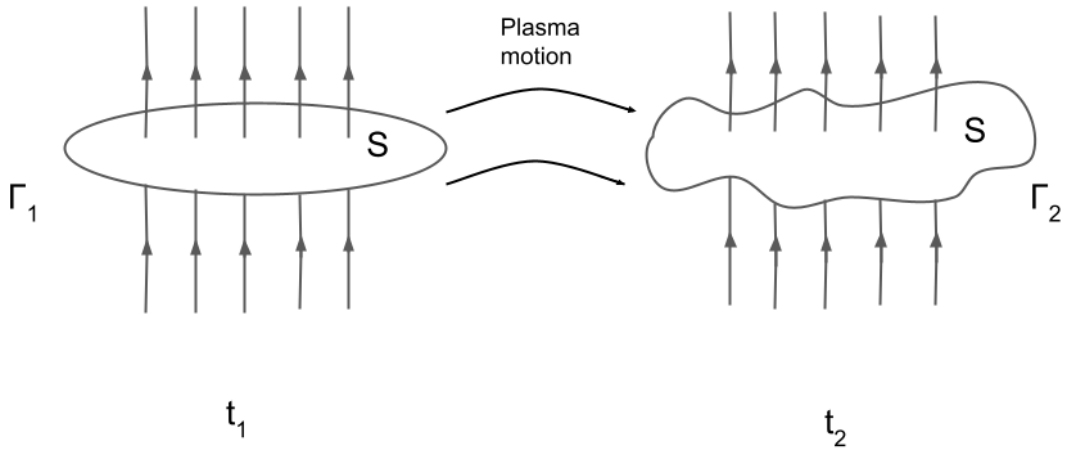

Figure 1.1: Conservation of magnetic flux through surface S, if the contour Γ_1 is deformed by plasma flow to make contour Γ_2, then the flux through Γ_1 at t_1 is equal to flux through Γ_2 at t_2.

$$\frac{d\Phi}{dt} = \iint_S\left(\frac{\partial\mathbf{B}}{\partial t} - \nabla\times(\mathbf{v}\times\mathbf{B})\right)\cdot d\mathbf{a}\ . \tag{1.18}$$

For an ideal plasma ($R_M \gg 1$), the right-hand side vanishes in the above equation, therefore implying the *conservation of magnetic flux* through S. Figure 1.1 depicts the flux-conservation through a surface S, where the field lines piercing the surface S within contour Γ_1 at t_1 remain on the same surface even after the deformation of Γ_1 into Γ_2 at t_2 by plasma motions.

1.2.2.2 Conservation of magnetic field lines

In ideal plasmas, the conservation of magnetic field lines follows from the conservation of magnetic flux. The concept of magnetic field lines can be illustrated by writing the induction equation in convenient form; using the vector identity* along with the solenoidality condition on magnetic field ($\mathbf{B}$)

$$\frac{\partial \mathbf{B}}{\partial t} + (\mathbf{v}\cdot\nabla)\mathbf{B} = (\mathbf{B}\cdot\nabla)\mathbf{v} - \mathbf{B}(\nabla\cdot\mathbf{v}) \ , \tag{1.19}$$

and combining it with the mass continuity Equation 1.1. In Equation 1.19, the first term on the right-hand side indicates the magnetic field strength increases owing to either accelerating plasma motion along the field or the shearing motion normal to the field causing the field to change direction by increasing the field component along the flow direction. The second term on the right-hand side suggests the decrease and increase in the field strength depending upon the expansion ($\nabla\cdot\mathbf{v} > 0$) and compression $\nabla\cdot\mathbf{v} < 0$) of plasma respectively. Substituting the value of $\nabla\cdot\mathbf{v}$ in Equation 1.19 from the mass-continuity equation

$$\frac{d}{dt}\left(\frac{\mathbf{B}}{\rho}\right) = \left(\frac{\mathbf{B}}{\rho}\cdot\nabla\right)\mathbf{v} \ , \tag{1.20}$$

To visualize Equation 1.20 resulting in field lines co-moving with plasma, let us take a length element $\delta\mathbf{r}$ along the magnetic field line moving with plasma. The plasma velocity at one end of length segment be $\mathbf{v}$ and at another end let the velocity be $\mathbf{v}+\delta\mathbf{v}$; then $\delta\mathbf{v}= (\delta\mathbf{r}\cdot\nabla)\mathbf{v}$. Then, the rate of change of the length element ($\delta\mathbf{r}$) within time interval dt can be expressed as

$$\frac{d\delta\mathbf{r}}{dt} = \delta\mathbf{v} = (\delta\mathbf{r}\cdot\nabla)\mathbf{v} \ , \tag{1.21}$$

which has the same form as Equation 1.20, thus indicating that if the vector $\dfrac{\mathbf{B}}{\rho}$ and length element $\delta\mathbf{r}$ are parallel at any time and will remain parallel at all time. Hence, implying any two plasma parcels connected by the magnetic field line will remain connected for all the time in ideal plasmas—conservation of magnetic field lines.

*$\nabla\times(\mathbf{v}\times\mathbf{B}) = (\mathbf{B}\cdot\nabla)\mathbf{v} + \mathbf{v}(\nabla\cdot\mathbf{B}) - (\mathbf{v}\cdot\nabla)\mathbf{B} - \mathbf{B}(\nabla\cdot\mathbf{v})$

1.2.3 Nonideal/diffusive limit ($R_M \ll 1$)

Any non-ideal term like resistive diffusion having form; $\mathbf{N} = \eta\mathbf{J} = \eta\nabla \times \mathbf{B}$ on the right-hand side of Equation 1.5, leads to the induction equation of form Equation 1.9. In the nonideal limit ($R_M \ll 1$), the induction equation has the following form

$$\frac{\partial \mathbf{B}}{\partial t} \approx \lambda \nabla^2 \mathbf{B} \ . \tag{1.22}$$

A straightforward integration of Equation 1.22 yields

$$B = B_0 \exp\left(-\frac{t}{\tau_D}\right) \ , \tag{1.23}$$

where $\tau_D \approx ({L_0}^2/\lambda)$ represents the diffusion time scale over which magnetic field lines diffuse out of the concerned plasma volume. Generalizing for non-ideal plasmas, a flux transport velocity can be defined with a constraint that it should have the same flux-preserving characteristics as that of ideal MHD, i.e., $\mathbf{w}$ should follow

$$\frac{\partial \mathbf{B}}{\partial t} = \nabla \times (\mathbf{w} \times \mathbf{B}) \ , \tag{1.24}$$

Nevertheless, using non-ideal Ohm's law (Equation 1.5) in Equation 1.3 leads to

$$\frac{\partial \mathbf{B}}{\partial t} = \nabla \times (\mathbf{v} \times \mathbf{B} - \mathbf{N}) \ . \tag{1.25}$$

On comparison of the right-hand sides of the above two equations, the non-ideal term can be expressed as

$$\mathbf{N} = \mathbf{u} \times \mathbf{B} + \nabla\Phi \ , \tag{1.26}$$

where $\mathbf{u}$ is the slippage velocity given by $\mathbf{u} = \mathbf{v} - \mathbf{w}$ and Φ is a scalar potential. Combining Equation 1.5 and Equation 1.26 gives

$$\mathbf{E} + \mathbf{w} \times \mathbf{B} = \nabla\Phi \ , \tag{1.27}$$

such that the flux velocity $\mathbf{w}$ is

$$\mathbf{w} = \mathbf{v} + \frac{(\mathbf{N} - \nabla\Phi) \times \mathbf{B}}{B^2} \ , \tag{1.28}$$

Since the flux transport velocity is not unique, its behavior depends on the particular magnetic field configuration under consideration which will be discussed in detail in Section 1.4. In the ideal case, $\mathbf{w} = \mathbf{v}$, but for any nonideal term $\mathbf{w} \neq \mathbf{v}$. The reconnection involves a localized region where diffusion occurs having global effects.

1.3 Magnetic reconnection in two dimensions (2D)

According to the historical overview presented in Section 1.1, features central to the concept of 2D magnetic reconnection are current sheets and magnetic neutral points. The current sheet is characterized as a narrow layer of current about which the direction of the magnetic field changes. The collapse of magnetic X-type neutral points leads to the formation of current sheet. We describe both the magnetic null point and current sheet one by one subsequently.

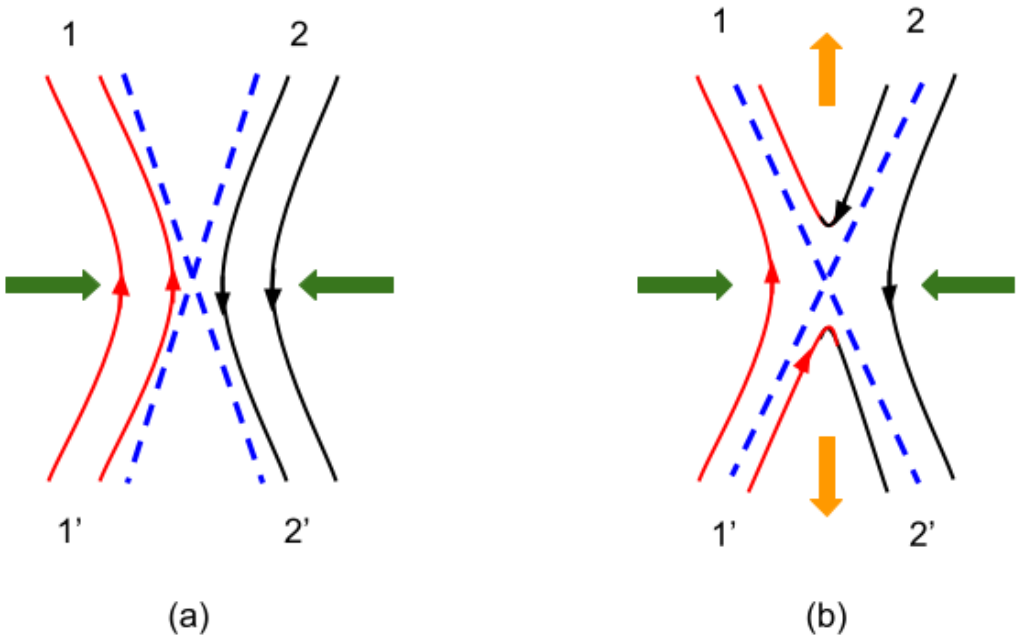

Figure 1.2: Panels (a) and (b) show the red and black field lines prior to and after the reconnection. In panel (a), red field lines connect region $1 \rightarrow 1^{'}$ and black field lines connect region $2 \rightarrow 2^{'}$. The blue dashed line is separatrix which separates topologically distinct regions. X-type null point is represented by the intersection of two separatrices in both the panels. The green arrows depict the converging plasma flow perpendicular to the magnetic field lines. Panel (b) depicts the topology of magnetic field lines after reconnection where the newly reconnected field lines connect the regions $2 \rightarrow 1$ and $1^{'} \rightarrow 2^{'}$.

Hyperbolic X-type null points are the preferential sites of magnetic reconnection in 2D. Figure 1.2 (a) and (b) depict the red and black field lines having different connectivities before and after the reconnection. Red field lines, directed from $1 \rightarrow 1^{'}$ and black field lines, directed from $2 \rightarrow 2^{'}$ (in panel (a)) are pushed by the converging plasma flows perpendicular to field lines. The blue dashed line, namely separatrix, separates the two distinct magnetic connectivity regions. The intersection of two separatrices is an X-type magnetic null point, where all components of the magnetic field vanish implying $|\mathbf{B}| = 0$. After reconnection at X-point, the resulting field lines connect the region $2 \rightarrow 1$ and $1^{'} \rightarrow 2^{'}$. Therefore, the reconnection is a topological re-arrangement of magnetic field lines in 2D.

The current sheets are intense volume current densities across which the magnetic field has a steep gradient (infinite in its mathematical limit). To elucidate, let us consider the magnetic field varying along $x-$direction and directed towards z, i.e., $\mathbf{B} = B_z(x)\hat{\mathbf{z}}$ then the associated current density from Ampere's law becomes

$$J_y = \frac{1}{\mu_0}\frac{\partial B_z}{\partial x} \ , \tag{1.29}$$

which signifies that a steep gradient in B_z with x gives rise to a strong current density along the sheet ($z-$direction) and perpendicular to the field lines. Spontaneous development of current sheets in an infinitely conducting plasma at equilibrium is expected from Parker's magnetostatic theorem (Parker, 1994). According to this theorem, the current sheets develop in the limit $L_0 \rightarrow 0$, causing the volume current density to intensify and get confined in a surface across which the magnetic field is discontinuous. A decrease in L_0 in the presence of finite but non-zero diffusivity λ locally reduces R_M and makes the plasma resistive; indicating the current sheet to be a potential site for magnetic field diffusion which can host reconnection.

1.3.1 Steady-state models of magnetic reconnection in 2D: MHD framework

As discussed in Section 1.1, primarily, the efforts to model magnetic reconnection theoretically were purely in 2D within the MHD framework. Here, we describe

two famous models of magnetic reconnection; Sweet-Parker and Petschek.

1.3.1.1 Sweet-Parker Model

The first ever theoretical model of magnetic reconnection in 2D describing the scaling laws for reconnection rate was developed by Sweet and Parker independently. This model uses an *order-of-magnitude* approach to derive the reconnection rate. Basic assumptions of the model consist of the incompressibility of fluid, low plasma$-\beta$ (where β is the ratio of kinetic pressure to magnetic pressure) and steady-state $\left(\frac{\partial}{\partial t} = 0\right)$ (Choudhuri, 1998), which leads to the reduced set of MHD equations are given as following

$$\mathbf{v} \cdot \nabla \rho = 0 \,, \tag{1.30}$$

$$\rho(\mathbf{v} \cdot \nabla)\mathbf{v} = \mathbf{J} \times \mathbf{B} \,, \tag{1.31}$$

$$0 = \nabla \times (\mathbf{v} \times \mathbf{B}) + \lambda \nabla^2 \mathbf{B} \,, \tag{1.32}$$

$$\nabla \cdot \mathbf{B} = 0 \,. \tag{1.33}$$

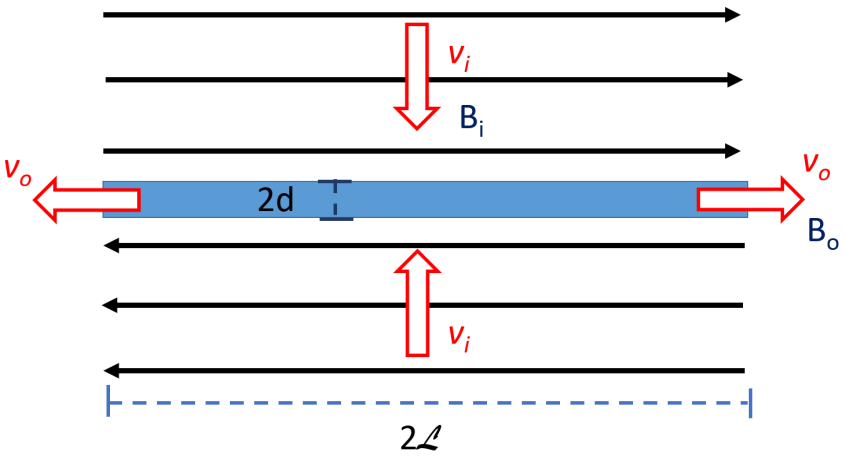

Figure 1.3: A schematic representation of the Sweet-Parker mechanism of magnetic reconnection. The blue shaded rectangular region is the diffusion region of width $2d$ and length $2\mathcal{L}$. Black lines represent magnetic field lines and the red arrows represent the plasma flow directions.

A diffusion region or current sheet of length $2\mathcal{L}$ and width $2d$, sandwiched

between the oppositely directed magnetic field $\pm B_i$ was considered. The plasma flow v_i is assumed in such a way that it pushes the oppositely directed magnetic field lines toward the diffusion region from both the sides (see Figure 1.3) and v_o is the outflow speed at both ends of the sheet. For a uniform mass density ρ, conservation of mass (from Equation 1.30) suggests that the rate at which mass enters the sheet $\rho(4\mathcal{L})v_i$ from both sides must be equal to the rate at which it leaves at both ends of the sheet $\rho(4d)v_o$, i.e.,

$$\mathcal{L}v_i = dv_o \ . \tag{1.34}$$

From the flux balance, we have

$$v_i B_i = v_o B_o \ . \tag{1.35}$$

By order-of-magnitude analysis, the current density is $\mathrm{J} \approx \dfrac{B_i}{\mu_o d}$ and the Lorentz force along the diffusion region is $(\mathbf{J}\times\mathbf{B})_x \approx JB_o = \dfrac{B_o B_i}{(\mu_o d)}$. Lorentz force accelerates the plasma from rest at the neutral point to v_o over a distance $\mathcal{L}$ and so, by Equation 1.31 where the plasma pressure gradient is neglected, we have

$$\rho\frac{v_o^2}{\mathcal{L}} \approx \frac{B_o B_i}{\mu_o d} \ . \tag{1.36}$$

Since the $\nabla \cdot \mathbf{B} = 0$ and dividing Equation 1.35 by Equation 1.34, gives

$$\frac{B_i}{\mathcal{L}} \approx \frac{B_o}{d} \ , \tag{1.37}$$

and Equation 1.36 then gives

$$v_o = \frac{B_i}{\sqrt{\rho\mu_o}} \approx v_A \ . \tag{1.38}$$

which is the expression for Alfvén speed v_A. From Equation 1.32, the advection term having order $\dfrac{v_i B_i}{\mathcal{L}}$ in the inflow region has to be balanced by the diffusion

term of the order $\frac{\lambda B_o}{d^2}$ in the outflow region and using Equation 1.37 leads to

$$v_i = \frac{\lambda}{d} \, . \tag{1.39}$$

From Equation 1.34, Equation 1.38, and Equation 1.39, the reconnection rate is defined as the ratio of inflow speed to outflow speed, given as

$$\boxed{M_A = \frac{v_i}{v_A} = \frac{1}{\sqrt{S}}}$$

where M_A is known as the Alfvén-Mach number and $S = \mathcal{L} v_A / \lambda$ is the Lundquist number[†]. For typical solar coronal parameters, i.e., $\mathcal{L} \equiv 10^8$m, $v_A \equiv 10^6$ ms^{-1}, and $\lambda \equiv 1$ m^{2}s^{-1} (Aschwanden, 2005), the reconnection rate is 10^{-7} which is too slow to explain the observed explosive transients on the Sun, such as solar flares.

1.3.1.2 Petschek Model

Petschek (1964) proposed that the rate at which magnetic flux enters the diffusion region can be much faster if the extent of diffusion region between the oppositely directed magnetic field is much smaller than the system or global length scale. He suggested that if L is the length of diffusion region and L_e is the system scale length then $L \ll L_e$. Let v_i and B_i be the plasma flow and magnetic field in the

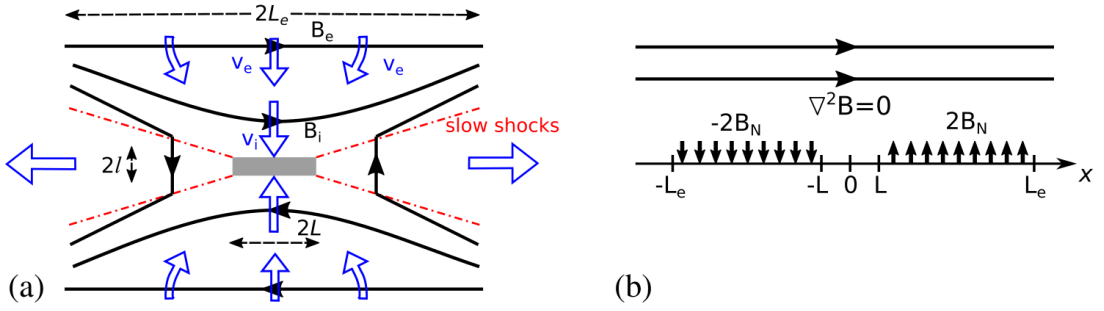

Figure 1.4: (a) A sketch of the Petschek reconnection mechanism. The external magnetic field (B_e) over a large distance L_e is carried towards the diffusion region (grey shaded) by a flow v_e towards a diffusion region (shaded) of width 2l and length 2L. Near the diffusion region, the inflow field is B_i, and the inflow speed is v_i. The slow shocks (red) heat and accelerate the plasma on the left and right sides of the diffusion region. (b) A schematic of the upper inflow region. (Figure adapted from Pontin & Priest (2022))

[†]For $v_o = v_A$, the Magnetic Reynolds number R_M is called the Lundquist number.

inflow region. The diffusion region is surrounded by an external region where the plasma flow is v_e and the magnetic field is B_e. Then the reconnection rate (M_e) and Lundquist number (S_e) in the external region will be

$$M_e = \frac{v_e}{v_{Ae}} , \tag{1.40}$$

$$S_e = \frac{L_e v_{Ae}}{\lambda} . \tag{1.41}$$

Assuming steady-state, magnetic flux conservation leads to $v_i B_i = v_e B_e$. Therefore,

$$\frac{M_i}{M_e} = \frac{B_e^2}{B_i^2} . \tag{1.42}$$

The magnetic field in the inflow region is assumed to be uniform and potential (current-free $\mathbf{J} = 0$). The specificity of the Petschek model is that the four slow-mode MHD shock waves (standing in the flow) are responsible for the plasma acceleration parallel to the shock front (as shown in Figure 1.4),i.e., $v_e = v_s$ where v_s is the shock speed.

As shown in Figure 1.4, B_i is weakly curved near the diffusion region in comparison to uniform B_e (far away from diffusion region) due to the normal component B_n of shocks on both sides. Let the shock speed be v_s which is given by $v_s = \frac{B_n}{\sqrt{\rho\mu_o}}$. Owing to shock in the region between L and L_e, $B_y = 2B_n$, and in the region between $-L$ and $-L_e$, $B_y = -2B_n$ on $x-$axis (Figure 1.4(b)), the shock inclination is negligible elsewhere. At the diffusion region (between $-L$ to L), B_n vanishes. The total magnetic field in the inflow region is the sum of two components, one is B_e along $x-$axis and the other is achieved by solving the Laplace's equation in the upper half of diffusion region. The magnetic field at the inflow region (B_i) can be given as

$$B_i = B_e - \frac{4B_n}{\pi} \log \frac{L_e}{L} . \tag{1.43}$$

Using $v_e = v_s$ relation and dividing the numerator and denominator of the second term on the right-hand side of the above expression by $\sqrt{\rho\mu_o}$ leads to

$$B_i = B_e \left(1 - \frac{4M_e}{\pi} \log \frac{L_e}{L}\right) . \tag{1.44}$$

An increase in reconnection rate M_e causes an increase in shock angle while the size of diffusion region decreases. Petschek suggested that if the value of M_e is large enough then the process chokes itself off. He derived the expression for reconnection rate ($M_e^{'}$)

$$M_e^{'} \approx \frac{\pi}{8 \log S} \ , \tag{1.45}$$

which is much faster than the reconnection rate given by the Sweet-Parker model. For solar flares, $M_e^{'} \approx$ 0.1-0.001. Hence, the Petschek model is also known as the *fast reconnection model*.

1.4 Magnetic reconnection in three dimensions (3D)

As described in Section 1.3, the 2D models of magnetic reconnection are primarily associated with the X-type null point geometry (Pontin & Priest, 2022), which is relatively simpler than the far more complex and richer variety of preferential reconnection sites in 3D. Toward the aim of this thesis to investigate the Hall effect in magnetic reconnection, an understanding of reconnection sites in 3D is essential. Therefore, in this section, we elaborate on the various aspects of 3D reconnection, which are essential for our works presented in Chapter 5 and Chapter 6. We begin with a brief historical development of the definition for 3D reconnection, followed by the description of reconnection sites in 3D such as null points, separators, quasi-separatrix-layers (QSLs), and hyperbolic flux tubes (HFTs).

Several definitions of magnetic reconnection in 3D exist in literature. For example, the attempts to define reconnection in 3D were primarily made by Vasyliunas (1975), Sonnerup (1979), and Axford (1984). According to Vasyliunas (1975), plasma flow across a separatrix surface is required for reconnection whereas Sonnerup (1979) suggested the electric field along the X-type neutral line or separator in 3D is necessary for reconnection. On the other hand, Axford (1984), proposed a change in the magnetic field line "connection" between plasma elements owing to the localized breakdown of the "frozen-in field" as the basis of magnetic reconnection. Here "connection" means that plasma elements that are at one time

connected by a single magnetic field line remain connected at subsequent times. Vasyliunas's and Sonnerup's definitions of magnetic reconnection require the identification of separatrix surfaces in 3D which needs the magnetic field line tracing to their origin. Identifying separator field line in 3D and distinguishing it from the surrounding field lines in realistic scenarios is difficult (Birn et al., 1997). Nevertheless, Axford's definition is general since it is not based on magnetic topology and does not require the tracing of field lines to their origin. However, it requires to track the temporal evolution of magnetic field line connection (Figure 1.5(a)) between plasma elements over a short time and possibly small distances. Axford's

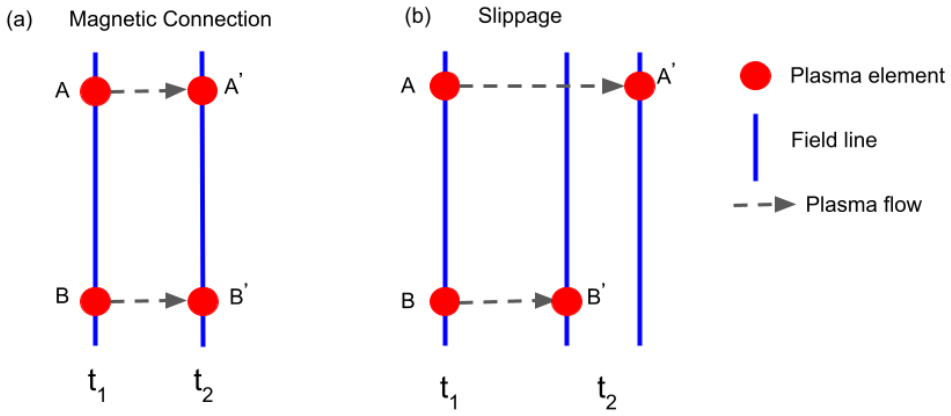

Figure 1.5: (a) Magnetic connection: Two plasma elements A and B connected by a magnetic field line at time t_1 remain connected by a magnetic field line at any other time t_2 under the plasma displacement. (b) Slippage: at time t_1 the plasma elements A and B are connected by a magnetic field line but at time t_2 plasma elements exchange the magnetic field lines and do not remain connected by a magnetic field line.

definition emphasizes the exchange of magnetic field lines between the plasma elements, i.e., the breakdown of magnetic connections—slippage of plasma elements from magnetic field lines. Later in 1988, this lead to the concept of general magnetic reconnection (GMR) (Schindler et al., 1988) which assumes the localized nonidealness. According to GMR, reconnection in 3D is classified into two categories: 1. Zero-B reconnection ($|B| = 0$ in the diffusion region), and 2. Finite-B reconnection ($|B| \neq 0$ in the diffusion region).

Following the aforementioned categorization of reconnection and central to the results presented in Chapter 5 and Chapter 6, further we discuss the 3D magnetic null (site for Zero-B reconnection) and its structure and QSLs (site for Finite-B reconnection).

- **3D null** A linear 3D null is a point in three-dimensional vector space, where all components of the magnetic field vanish ($\mathbf{B} = 0$) and the field increases linearly away from the null point (Parnell et al., 1996). For example, in Cartesian coordinates, the magnetic field $\mathbf{B}$ for a linear 3D null can be given as

$$\mathbf{B} = x\hat{i} + y\hat{j} - 2z\hat{k} \ , \tag{1.46}$$

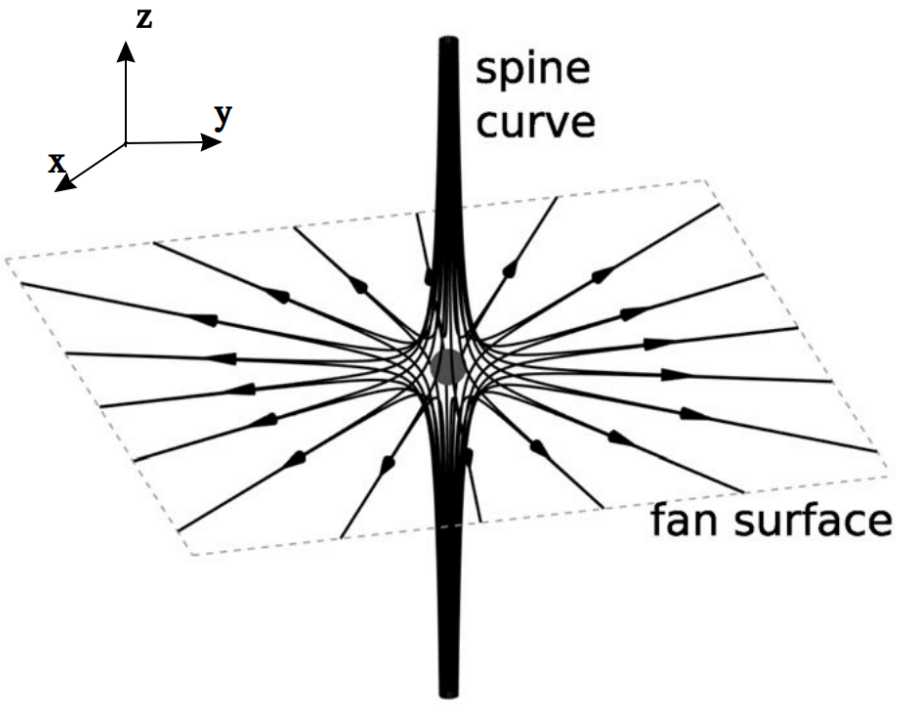

Figure 1.6: The magnetic structure around a 3D null point along with the spine curve and fan surface. (adapted from Pontin & Priest (2022))

such that $\nabla \cdot \mathbf{B} = 0$. The magnetic structure around a linear 3D null point consists of two families of field lines, namely, spine and fan (Priest & Titov, 1996). A schematic representation of the magnetic field line structure around a linear 3D null point is shown in Figure 1.6. The spine for the aforementioned field is along the $z-$axis along which the bundle of magnetic field lines approach asymptotically whereas the receding field lines are tangential

to a surface known as the fan plane (xy plane). Fan plane acts as separatrix surface since it separates the distinct topological domains of magnetic field lines connectivities. If the field lines on the fan plane radiate away from the null point then it is referred to a positive null point while if they approach the null point then it is referred to a negative null point (Pontin & Priest, 2022).

- **QSL** Reconnection in 3D can also take place without the null point. This idea was already conceptualized by Schindler et al. (1988) where the reconnection in the absence of null points was termed as finite-B reconnection. Following Schindler et al. (1988), if Ohm's law given by Equation 1.5 is considered where $\mathbf{N}$ is a finite non-ideal term due to either collisions, fluctuations, or particle inertia then this non-idealness can be important in a localized region with sharp gradients. In the convenient form, $\mathbf{N} = \eta\mathbf{J}$ can be assumed for Ohmic dissipation.

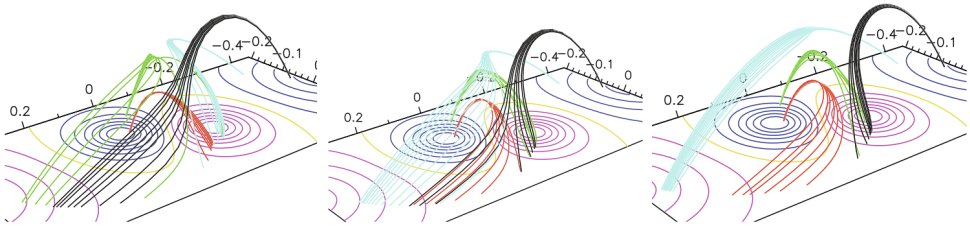

Figure 1.7: Illustration of the slip running or slipping reconnection of magnetic field lines in a numerical simulation of quasi-separator reconnection by Aulanier et al. (2006). Positive and negative polarities of the magnetic field are represented by the pink and blue contours respectively on the bottom boundary. Four sets of magnetic field lines (red, black, cyan, and green lines) are integrated from fixed footpoints, and their conjugate footpoints gradually slip along arc-shaped trajectories from one positive to other positive polarities.

For the finite-B reconnection to take place in 3D, the necessary and sufficient condition is that the magnetic field is nonzero in the diffusion region and $\mathbf{B}\times(\nabla\times\mathbf{N}) = 0$ (Schindler et al., 1988; Hornig & Schindler, 1996) at a given point located in the diffusion region. These locations of enhancement in current density (current sheets) can host the reconnection. Owing to the drastic change in magnetic field line connectivity (Demoulin et al., 1996, 1997; Titov,

2007) strong currents may arise, therefore, QSLs serve as preferential sites for 3D reconnection. In principle, this drastic change is quantified by the $Q-$value known as the squashing factor. For the explanation of Q-value calculation, let us consider two footpoints $P_1(x_1,\ y_1)$ and $P_2(x_2,\ y_2)$. The footpoints are mapped from P_1 to P_2 and the associated Jacobian is given by

$$D_{1,2} = \begin{pmatrix} \dfrac{\partial x_2}{\partial x_1} & \dfrac{\partial x_2}{\partial y_1} \\ \dfrac{\partial y_2}{\partial x_1} & \dfrac{\partial y_2}{\partial y_1} \end{pmatrix} = \begin{pmatrix} a & b \\ c & d \end{pmatrix} , \tag{1.47}$$

owing to

$$Q = \frac{a^2 + b^2 + c^2 + d^2}{|\mathbf{B}_{n,1}(x_1, y_1)/\mathbf{B}_{n,2}(x_2, y_2)|} , \tag{1.48}$$

where $\mathbf{B}_{n,1}(x_1, y_1)$ and $\mathbf{B}_{n,2}(x_2, y_2)$ are the components normal to the target planes. According to Liu et al. (2016), $Q > 2$ is a criterion on squashing degree to represent the location of QSLs. The regions having large $Q-$values are prone to *slip-running* or *slipping reconnection* (Aulanier et al., 2006). The illustration of slipping reconnection is given in Figure 1.7.

Following, the work of Aulanier et al. (2006), it can be seen in Figure 1.7 that the four sets of magnetic field lines (red, black, green, and cyan) change the connectivity from one positive to another positive polarity at the bottom boundary exhibiting the slipping reconnection.

1.5 Observed manifestations of magnetic reconnection

As mentioned in Section 1.1, the discovery of magnetic reconnection was primarily motivated from the spectacular observations of explosive transient events on the Sun and auroral substorms in Earth's magnetosphere. Since these events are the manifestation of magnetic reconnection, therefore we present a brief overview of the properties and nature of such phenomena on the Sun as well as on Earth.

1.5.1 Explosive activities on the Sun

For this thesis, the solar coronal plasma has been selected as a prototype astrophysical plasma which exhibits diffusive behavior in the form of solar flares and CMEs. Solar flares are observed as intense brightening of any emission across the electromagnetic spectrum occurring at a time scale of minutes (Benz, 2008). Typically, energy ranging from $10^{28} - 10^{32}$ erg is released during the solar flares

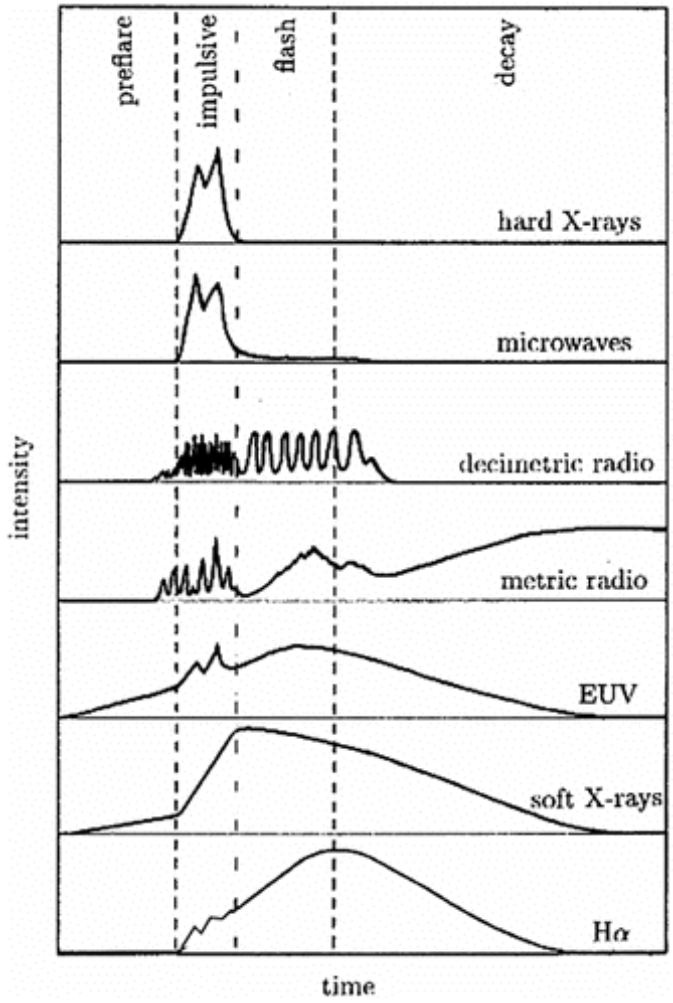

Figure 1.8: Illustration of intensity profile during a flare for several wavelengths. The four phases, namely, pre-flare, impulsive, flash, and decay phases are indicated at the top. The different phases have different temporal durations. (Figure adapted from (Benz, 2008))

within a time span of a few minutes (Benz, 2008). The temporal evolution of a flare is classified into four phases, namely the pre-flare, impulsive, flash, and decay phases. This characterization of different phases is based on the temporal evolution of different emission profiles across the electromagnetic spectrum during a flare. Pre-flare phase is characterized by the energy build along with the slow heating of

coronal plasma for which EUV and soft X-ray emission is detected. The impulsive phase of the flare is marked by the sudden peak in the hard X-ray emission where most of the energy is released and energetic particles are accelerated. Some high-energy particles get trapped and produce intensive emissions in the radio. The thermal soft X-ray and H_α emissions finally attain maxima after the impulsive phase, when energy is more smoothly released, manifest in decimetric pulsations. The flash phase is identified as the rapid increase in H_α intensity and line width and mostly coincides with the impulsive phase, although sometimes H_α may peak later. During the decay phase, the coronal plasma reaches the relaxed state except at the high corona ($> 1.2R_\odot$, where $R_\odot$ is the radius of the Sun), where plasma ejections and shock waves continue to accelerate particles, causing meter wave radio bursts. Aforementioned phases of solar flare have been shown in Figure 1.8, adapted from Benz (2008). Generally, magnetic reconnection is suggested to be

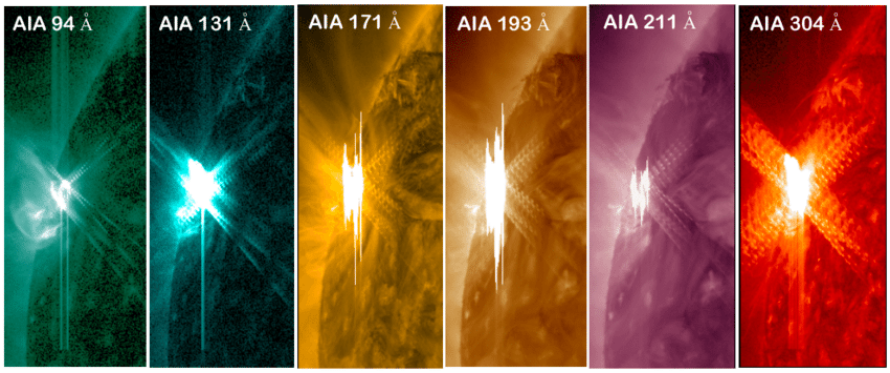

Figure 1.9: Multiwavelength observations of a solar flare as observed by SDO/AIA in six extreme ultraviolet (EUV) filters on the eastern limb of the Sun on March 9, 2011.

responsible for such sudden, rapid, and intense energy release (Shibata & Magara, 2011). The strong enhancement of H_α, ultraviolet (UV), and EUV emissions are the signature of reconnection driven processes in the solar corona. For example, one such enhancement in EUV emissions from Sun during a solar flare is shown in Figure 1.9.

Coronal Mass Ejections are gigantic clouds of magnetized plasma erupting from the solar corona into interplanetary space. The total mass and energy released during a typical CME ranges from 10^{15}-10^{16} g and 10^{27}-10^{33} erg respectively (Vourlidas et al., 2002; Gopalswamy et al., 2004). Generally, CMEs show up signatures in white light owing to Thomson scattering of photospheric light from

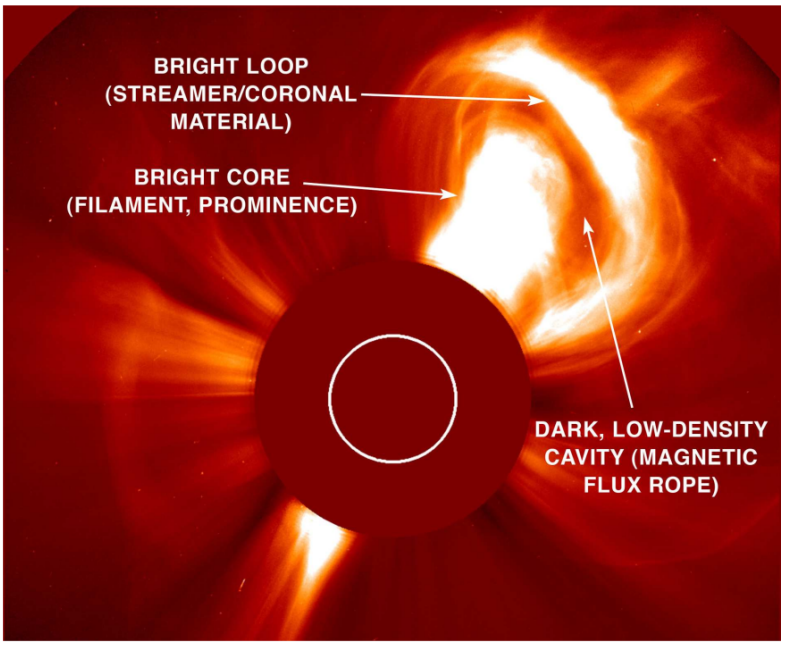

Figure 1.10: An observation of CME having classic three-part structure: (a) bright frontal loop or edge, (b) a dark cavity, and (c) bright core region as viewed by Large Angle and Spectrometric Coronagraph Experiment (LASCO) on board Solar and Heliospheric Observatory (SOHO) spacecraft. This figure is adapted from Müller et al. (2013).

the free electrons of coronal and heliospheric plasma (Vourlidas & Howard, 2006; Howard & Tappin, 2009) which can be observed using a coronagraph. In white light observations, mostly, CMEs have a three-part structure: a bright frontal loop (i.e., a leading edge (Illing & Hundhausen, 1985; Vourlidas & Howard, 2006), a dark cavity (low density, high magnetic field region (Low, 1996; Vourlidas et al., 2013) and a bright core embedded in the cavity (Illing & Hundhausen, 1985); cf. Figure 1.10. A near-consensus is that magnetic reconnection plays an important role in initiating CMEs (Low, 1996; Chen, 2011). It is widely accepted that most of the CMEs can be considered erupting flux-rope systems, generating the classic three-part structure. Therefore, in this thesis, we study the evolution of magnetic flux ropes owing to magnetic reconnection and present the results in Chapter 5.

1.5.2 Geomagnetic activity on Earth

Intense geomagnetic storms and substorms, observed near Earth are caused mainly by large-scale solar eruptions (*viz.* flares, CMEs) and disturb the space weather. Naturally, the magnetic field carried by these eruptions from Sun, couple the solar,

interplanetary, and magnetospheric system as shown in Figure 1.11. Generally,

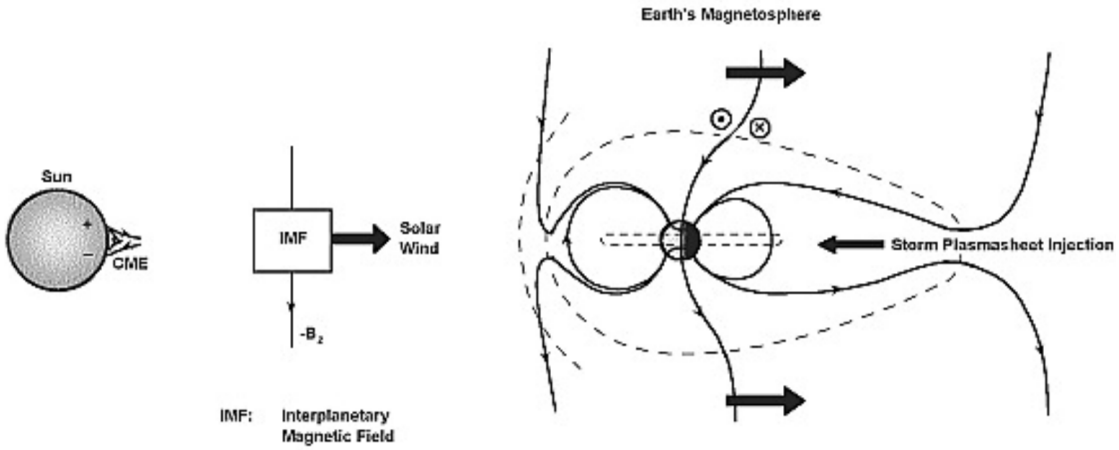

Figure 1.11: An illustration of coupling between magnetospheric and interplanetary magnetic field (IMF), depicting the magnetic reconnection and energy injection into the night side magnetosphere. This energy injection causes the development of the ring current. (Figure adapted from Gonzalez & Tsurutani (1992).

if the Earth-directed CMEs carrying southward magnetic field component (B_z) interact with the northward magnetic field of Earth on dayside (closest to the Sun), then the magnetic reconnection can take place (Dungey, 1961). Subsequently, the reconnected field is dragged by the solar wind—a continuous flow of plasma and magnetic field away from the Sun into interplanetary space, where it gets stretched on the night side. Here it deposits magnetic energy to the magnetotail—the thin elongated region facing away from the Sun. Consequently, at night side the magnetic fields are configured in such a way that they are oppositely directed on each side of the magnetotail's midplane, (on the right-hand side of Figure 1.11) so that they can reconnect. Then the superheated plasma from magnetotail region flows back toward Earth, where it can penetrate all the way down to Earth's atmosphere and dissipate its energy to give rise to *aurorae*. This cyclic process of magnetic reconnection at the magnetopause to reconnection at magnetotail is specified as the "Dungey cycle". The magnetotail reconnection causes the charged particles to get trapped in Earth's magnetic field where they gyrate following the Earth's magnetic field curvature and tend to move along the equatorial plane. The ions move westward (i.e. from midnight toward dusk) and electrons move eastward (i.e. from midnight toward dawn) ultimately generating the toroidal-shaped ring current in a westward direction surrounding the Earth. This ring current, in turn,

induces the magnetic field which tends to reduce the horizontal component of Earth's magnetic field, responsible for the geomagnetic storm.

1.6 Importance of the Hall effect during magnetic reconnection: Hall MHD

As mentioned in Section 1.3, the Sweet-Parker model is too slow to explain the reconnection rates for solar flares at the same time it does not account for the impulsive nature owing to steady-state assumption. While the Petschek model being steady-state gives fast reconnection rates but it can not explain the impulsive nature too and remains debatable since it is not realizable in the natural plasmas; see e.g., Biskamp (2000); Wang et al. (2000). Previous works (Terasawa, 1983; Scudder, 1997) suggest that in high-S plasmas, single-fluid MHD framework does not differentiate between the relative motions of different species. Considering Hall term ($\mathbf{J} \times \mathbf{B}$) in Ohm's law can be a useful attempt in this direction which leads to the Hall MHD description. In various astrophysical bodies, *viz.* dense molecular clouds, white dwarfs, or accretion disks, the Hall effect plays a key role in the magnetic field dynamics; see, e.g., Mininni et al. (2003) and references therein. Over the past few years, many studies (Ma & Bhattacharjee, 2001; Birn et al., 2001; Hesse et al., 2001; Otto, 2001) employing numerical simulation of Hall reconnection have found the fast reconnection rate or increase in reconnected flux. In the work of Bhattacharjee et al. (2003), the Hall MHD simulation exhibits impulsiveness.

Hall MHD recognizes the importance of the Hall effect in a generalized Ohm's law. Fundamentally magnetic reconnection is a multiscale process, so the identification of reconnection scale length is important which depends upon the particular system under consideration. To elucidate this, the reconnection scale length for a solar flare can be calculated by approximating the diffusion timescale (τ_d) with the impulsive rise time in hard X-ray emission which is of the order $10^2 - 10^3$ s. Thus, the reconnection scale length $L_\eta = \sqrt{\tau_d \lambda}$, for solar flare is ≈ 32 m where diffusion or reconnection time $\tau_d = 10^3$ s and $\lambda = 1$ m^{2}s^{-1}. Then the Lundquist number becomes $S \approx 10^7$. In solar corona, the ion-inertial scale length is $\delta_i = c/\omega_{pi} \approx 2.25$

m (Priest & Forbes, 2000) where $\omega_{pi} = \sqrt{\frac{ne^2}{m\epsilon_0}}$ being the plasma ion frequency, n is number density, m is mass and ϵ_0 is the permittivity of free space. For an electric field of form

$$\mathbf{E} + \mathbf{v} \times \mathbf{B} = \eta \mathbf{J} + \frac{\mathbf{J} \times \mathbf{B}}{ne} \ , \tag{1.49}$$

where $\left(\frac{\mathbf{J} \times \mathbf{B}}{ne}\right)$ is the Hall term, the dimensionless induction equation can be written as following

$$\frac{\partial \mathbf{B}}{\partial t} = \nabla \times (\mathbf{v} \times \mathbf{B}) - \frac{1}{S} \nabla \times \mathbf{J} - \frac{\delta_i}{L_\eta} \nabla \times (\mathbf{J} \times \mathbf{B}) \ , \tag{1.50}$$

using the following normalizations

$$\mathbf{B} \longrightarrow B_0 \mathbf{B}, \quad \mathbf{v} \longrightarrow v_A \mathbf{v}, \quad t \longrightarrow \tau_A t, \quad \nabla \longrightarrow \frac{\nabla}{L_0}, \quad \mathbf{J} \longrightarrow \frac{B_0}{\mu_0 L_0} \mathbf{J} \ . \tag{1.51}$$

An order analysis of the above dimensionless induction equation (Equation 1.50) at reconnection scale length (i.e., $L_0 = L_\eta$) leads to the order of dissipation term $1/S \approx 10^{-7}$ being much smaller than the order of Hall term $\delta_i / L_0 \approx 10^{-2}$. Magnetic reconnection being the underlying reason behind solar flares and other coronal transients, the Hall effect may play an important role during reconnection. According to Equation 1.26, Hall term $\left(\mathrm{N} = \frac{\mathbf{J} \times \mathbf{B}}{\mathrm{ne}}\right)$ alone cannot mediate the reconnection in the absence of dissipation ($\eta \mathbf{J}$). For a detailed discussion on the properties of the Hall effect on magnetic reconnection, see Section 1.7. From Equation 1.50, it can be emphasized that the resistive dissipation term and Hall terms are important only when strong current densities or magnetic field gradients exist. Since the order of magnitude for current density can be written as $J \approx B/L$ and the current (J) will be large only if the length scale L is sufficiently small. In the case of solar coronal plasma, if the characteristic scale length L is of the order of megameter (Mm) then the currents are very small and ignorable but if it is reconnection scale length the currents have sufficiently large values. This reduction in length scale, in turn leads to the reduction in the Lundquist number signifying the diffusion to be important and the order of the Hall effect being higher than the diffusion term should not be ignored.

1.7 Properties of Hall effect on magnetic reconnection

Standardly, if the magnetic field is applied to a current-carrying conductor in the direction perpendicular to the current then a transverse electric field is developed in the conductor and this phenomenon is known as the *Hall effect* (Ramsden, 2006). The Hall effect in reconnection physics is well known to give fast reconnection rates. In literature, the famous Geospace Environment Modelling (GEM) reconnection challenge by Birn et al. (2001) depicted the fast reconnection rates of the order of near Alfvènic inflow velocities with the Hall effect included in the different models ranging from fully particle-in-cell (PIC) codes to traditional resistive MHD codes. Numerical simulations in the GEM challenge assumed an

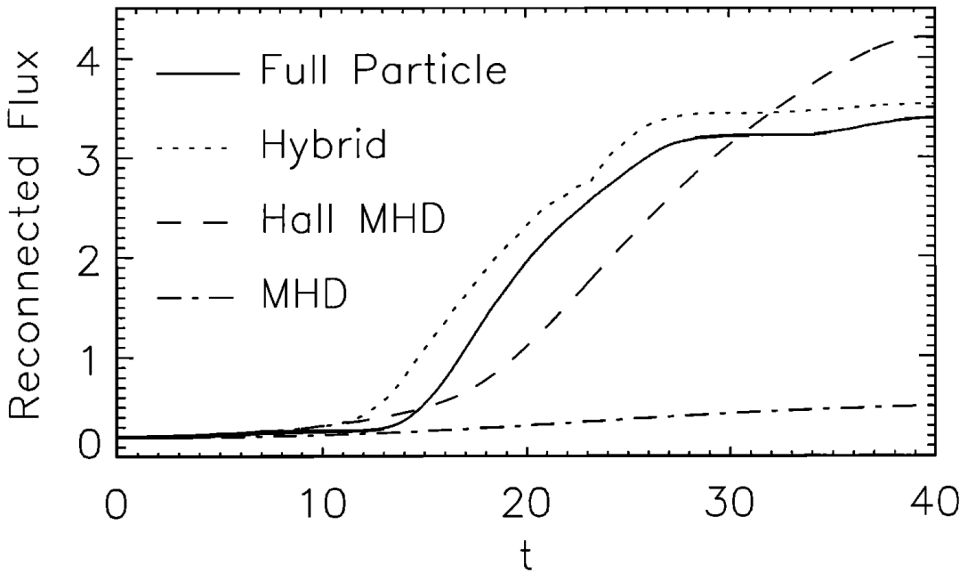

Figure 1.12: The temporal variation of reconnected magnetic flux from a range of numerical simulations with different models including full particle, hybrid, Hall MHD, and MHD, adapted from Birn et al. (2001).

initial Harris current sheet equilibrium perturbed by the magnetic island to initiate dynamics. The Figure 1.12, taken from Birn et al. (2001), shows the temporal variation of reconnected magnetic flux for different simulations from fully particle, hybrid, Hall MHD, and MHD models. The slope of reconnected magnetic flux versus the time curve gives the reconnection electric field. As evident from Figure 1.12, all the models including the Hall effect give the approximately same and larger reconnection rate as compared to the MHD. Noticeably, simulation results

for the models including the Hall effect emphasize that the reconnection rate is almost insensitive to the particular mechanism (thermal motion of particle, electron inertia, or resistivity) responsible for the breakdown of frozen-in condition.

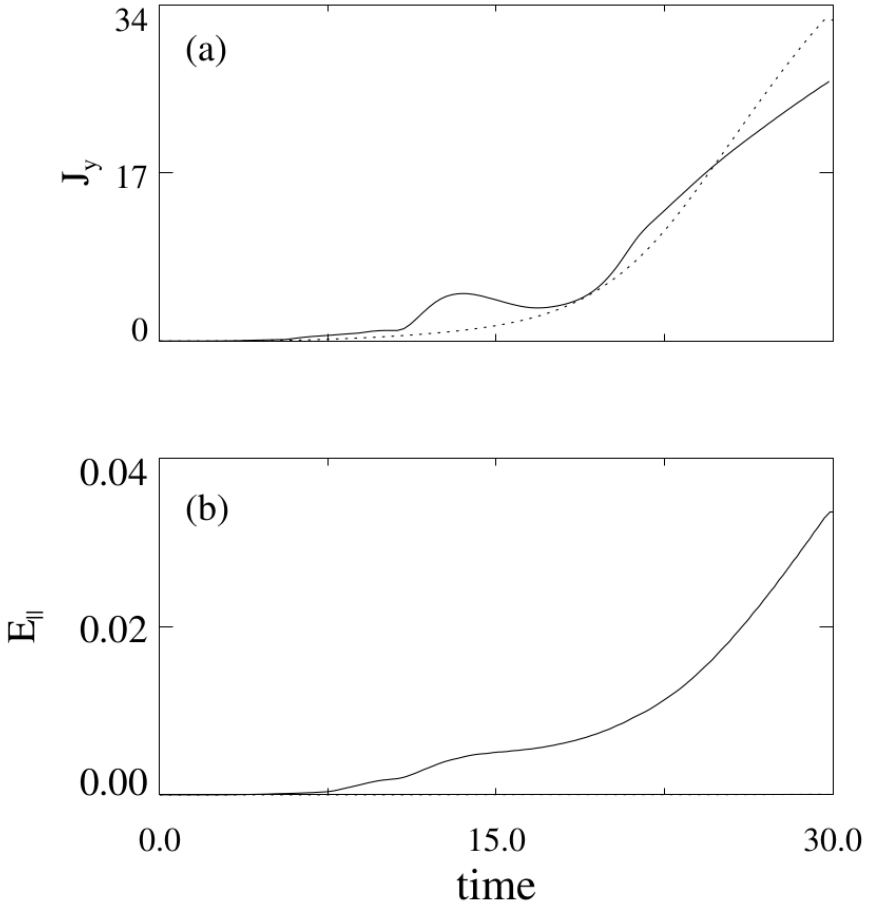

Figure 1.13: Growth rate (time evolution) of amplitudes of (a) current density J_y and (b) electric field $E_{||}$ for the Hall MHD and MHD simulations depicted by solid and dotted curves respectively from Bhattacharjee et al. (2003).

According to Bhattacharjee et al. (2003), the observed impulsive phase of a solar flare imposes an important constraint on any magnetic reconnection model explaining flare that not only the timescale of the growth rate of current density and electric field has to be fast but the time derivative should also increase abruptly. In their work, a comparative study of the Hall MHD and MHD simulations initiated with a 2D solar-like magnetic arcade configuration revealed the sudden and fast growth rate of current density and electric field during the Hall MHD evolution—signifying a greater degree of impulsiveness, as shown in Figure 1.13 (adapted from Bhattacharjee et al. (2003)).

The Hall effect being important at ion-inertial length scale causes the decou-

pling of ion and electron motion. Consequently, in the ion diffusion region, the ions diffuse out from the magnetic field line, and plasma flow is frozen into the electron fluid only. To elucidate, let us consider the induction equation (Equation 1.50) and ignoring the resistive diffusion term, then a velocity can be defined as $\left(\mathbf{v} - \frac{\delta_i}{L_\eta}\mathbf{J}\right)$ by combining the first and last terms on the right-hand side and then, the induction equation can be written as

$$\frac{\partial \mathbf{B}}{\partial t} = \nabla \times (\mathbf{w} \times \mathbf{B}) \ , \tag{1.52}$$

where $\mathbf{w} = \left(\mathbf{v} - \frac{\delta_i}{L_\eta}\mathbf{J}\right)$ is the electron flow velocity. Hall term, being ideal, does not cause any change in the magnetic energy and helicity rates (Priest & Forbes, 2000; Liu et al., 2022). However, following Hornig & Schindler (1996), the velocity $\mathbf{w}$ conserves magnetic flux (Schindler et al., 1988) and topology (Hornig & Schindler, 1996) since field lines are tied to it. The velocities $\mathbf{w}$ and $\mathbf{v}$ being different, field lines (moving with velocity $\mathbf{w}$) slip out from the plasma parcels moving with velocity $\mathbf{v}$—ion flow getting decoupled from field line motion. Consequently, two fluid parcels do not remain connected with the same field lines over time (see Figure 1.5). Quoting Schindler et al. (1988), such change in magnetic connections has been considered as the basis of magnetic reconnection by Axford (1984).

Additional slippage of field lines occurs in the presence of resistive diffusion term, but with a change in magnetic topology.

Apart from modeling efforts to explore the role of the Hall effect on magnetic reconnection, efforts have also been made to observe the magnetic reconnection in Earth's magnetosphere with an aim to probe the ion diffusion region physics. The Magnetospheric Multiscale Mission (MMS) has provided important insights into ion diffusion region physics. Mozer et al. (2002) proposed a model of magnetic reconnection including Hall effects which is purely based on the observations. A schematic picture of the diffusion region (Mozer et al., 2002) surrounding the reconnection site is depicted in Figure 1.14. In Figure 1.14, the magnetosheath on the left and magnetosphere on the right side have oppositely directed magnetic field lines (thick black lines directed along z) pointing southward (down) on the left and northward (up) on the right side. The magnetic field lines are convected

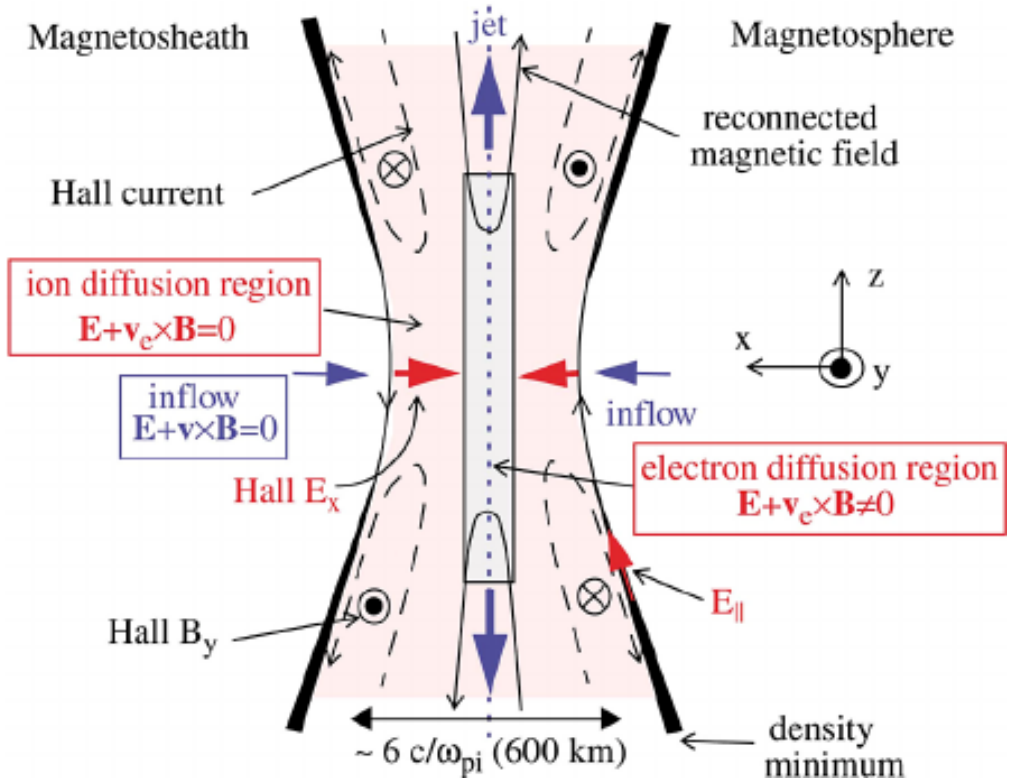

Figure 1.14: A sketch of the diffusion region around the magnetic reconnection site for a symmetric system (adapted from Mozer et al. (2002)).

along x direction toward magnetopause by inflow. When the field lines are in the white part (away from the diffusion region), the ideal MHD is satisfied and the electric field has a dominant contribution from the convection term such that the resultant electric field $-v_x B_z$ is in the positive $y-$direction and this out-of-reconnection plane field is known as reconnection electric field. In a region where the gyrating ions reach a distance apart that is equal to their gyroradius, they get demagnetized and decouple from the magnetic field but the electrons continue to be frozen to the magnetic field due to their gyroradius being smaller than that of ions, is known as ion diffusion region. There is a net current $\mathbf{J} = nq(\mathbf{v}_i - \mathbf{v}_e)$ generated by the bulk flow of electrons (shown by dashed curves in Figure 1.14) in the ion diffusion region along the $x-$direction, also known as *Hall current*. This in-plane (xz plane) Hall current generates an out-of-reconnection plane magnetic field component along the $y-$direction which is known as *Hall magnetic field*. The nature of this out-of-reconnection plane Hall magnetic field is quadrupolar owing to the in-plane current which wraps the associated magnetic field around it according to Ampere's law. Consequently, it causes the Hall magnetic field to point out of the

plane (along positive y direction) on the upper right and lower left while pointing into the plane (along negative y direction) on the upper left and lower right. Since the ion diffusion region has a width equal to the ion-inertial scale length δ_i, the Hall term $\mathbf{J} \times \mathbf{B}$ gives rise to an electric field in the positive $y-$direction which is equal to $J_x B_z$ which is in the same direction as that of the convective electric field. Alongside, the Hall magnetic field along the $y-$direction and current along z direction together produce *Hall electric field* along x direction which is depicted by two oppositely directed red arrows pointing toward the magnetopause on either side of it. In summary, the Hall effect plays a crucial role during magnetic reconnection by giving fast reconnection rates, a greater degree of impulsiveness, and altering the dynamics. The main properties of Hall-assisted reconnection are the generation of an out-of-reconnection plane quadrupolar Hall magnetic field, in-plane Hall current, and Hall electric field. Although, the Hall effect in 2D or 2.5D magnetic reconnection is well studied but the understanding of its role in 3D reconnection is lacking.

1.8 Motivation and Organization of the Thesis

In the above backdrop, presented in Section 1.6 and Section 1.7, the motivation of this thesis is to study the role of the Hall effect on magnetic reconnection in astrophysical plasmas, in general, and particularly in solar coronal plasma. To fulfill the aim, the specific objectives of this thesis are outlined below:

1. Development of a 3D Hall MHD solver by modifying the existing computational model EULAG MHD and benchmarking the model to validate the properties of Hall reconnection.

2. Understanding the Hall-assisted reconnection dynamics of a magnetic flux rope by means of Hall MHD simulation and its comparison with the MHD evolution.

3. Comparative study of the possible magnetic reconnections in 3D causing the observed flare brightening in the lower solar atmosphere employing the data-constrained Hall MHD and MHD simulations.

Based on the work carried out to accomplish the above mentioned objectives, the thesis is organized into seven chapters. A brief description of each chapter is given below.

Chapter 1: Introduction

This Chapter starts with a historical overview of magnetic reconnection followed by an introduction to the concept of magnetic reconnection. A revisit of the existing 2D models of magnetic reconnection and reconnection rates within the MHD framework is presented. Their limitations to explain the impulsive and fast nature of explosive events are described. Subsequently, the 3D magnetic reconnection and sites for reconnection in 3D are discussed. Then the observational manifestations of reconnection on the Sun and Earth are presented as examples. A brief overview of the previous efforts to achieve the fast reconnection rate is discussed briefly. Later, the motivation behind Hall MHD is described with an emphasis on the inevitability of the Hall effect in magnetic reconnection in the solar corona. The properties of the Hall effect on magnetic reconnection are described in detail. Lastly, the chapterwise organization is presented.

Chapter 2: Solar Coronal Magnetic Field Models and Coronal Transient Observations

The solar coronal plasma has been selected as a prototype astrophysical plasma due to the wealth of observational data. This Chapter focuses on the coronal magnetic field models depending upon the zero and non-zero Lorentz force ($\mathbf{J} \times \mathbf{B}$) on photosphere, i.e., force-free and non-force-free approaches are discussed in detail. To study reconnection the vector magnetic field is required which is obtained using the non-force-free extrapolation technique to initiate the data-based simulations in Chapter 6. The flare observations and magnetic field data utilized for extrapolations in this thesis are obtained from the Atmospheric Imaging Assembly (AIA) and Heliseismic Magnetic Imager (HMI) instruments onboard Solar Dynamic Observatory (SDO).

Chapter 3: Numerical model

In this Chapter, a detailed description of the EULAG MHD—a widely used computation model is presented. EULAG uses MPDATA advection and Implicit Large Eddy Simulation (ILES) schemes which are discussed in detail. Utilizing the ILES property and the flux conservative form of EULAG solver the Hall forcing term is incorporated in the model and discussed in detail in this Chapter.

Chapter 4: Benchmarking the 3D EULAG HMHD solver

This Chapter documents the benchmarking results of the 3D EULAG HMHD solver. As emphasized in the introduction, the focus here is to explore reconnection dynamics in the Hall MHD with its properties such as faster reconnection and impulsiveness. Both the properties are verified along with the key highlights of the 3D nature of magnetic field line evolution. Additionally, only the whistler wave modes are investigated. Since the model assumes incompressibility and homogeneous plasma density, Hall drift wave modes are not considered. There is a good agreement between the numerical and analytical whistler wave modes frequency, detailed in this Chapter. The description of the 3D Hall MHD solver and benchmark validation results are published in Bora et al. (2021).

Chapter 5: Investigation of the Hall effect on magnetic reconnection during the evolution of a magnetic flux rope

In this Chapter, the influence of the Hall forcing on the generation and ascend of a magnetic flux rope generated from bipolar sheared magnetic arcades is discussed for two cases. The first case uses initially axisymmetric (2.5D) while the second case uses initially 3D bipolar sheared magnetic arcade configurations for the simulations. The details of reconnection during the Hall MHD and MHD evolution of the rope along with the energetics are highlighted. The results of the first case of this work have been published in Bora et al. (2021). The results of the second case study are presently under preparation for communication in a peer-reviewed journal.

Chapter 6: Comparison of the magnetic reconnection in a flaring solar active region using data-constrained Hall MHD and MHD simulations

This Chapter contains a comparative study of possible magnetic reconnections causing the flare brightening in the lower solar atmosphere. The data-constrained Hall MHD model is employed to simulate a C1.3 class flare in active region NOAA 12734 as a test bed. The Chapter starts with a description of salient spatiotemporal features observed in the SDO/AIA multiwavelength channel images. Further, the non-force-free field (non-FFF) extrapolation utilizing the SDO/HMI vector magnetogram is discussed. A detailed numerical analysis to detect the favorable topologies for magnetic reconnections is presented. Finally, the differences in the magnetic reconnection dynamics during the Hall MHD and MHD evolution are presented. The results of this work have been published in Bora et al. (2022).

Chapter 7: Summary and Future Work

This Chapter presents the summary of the work carried out focusing on the major findings of the thesis. Further scope for future work is also discussed.

Chapter 2

Solar Coronal Magnetic Field Models and Coronal Transient Observations

2.1 Introduction

The importance of the Hall effect in magnetic reconnection has been illustrated in Chapter 1. The central aim of this thesis is to investigate the Hall effects on magnetic reconnection in astrophysical plasmas. Toward such an aim, magnetic reconnections leading to solar coronal transients can be used as a testbed. As an initial exploration, we select a solar flare (more details in Chapter 6) and perform data-constrained numerical simulations to explore the underlying mechanism of reconnection. In this regard, solar observations play an important role because: (a) multiwavelength imaging of the transient activity helps in the understanding various spatial features and their temporal evolution, (b) measurements of magnetic field allow one to understand the magnetic topology and field line dynamics in the solar corona. However, most of the ground and space-based observatories, provide the routine measurements of vector magnetic field only on the photosphere. Such extensive and accurate measurements are not available for the solar corona, leading to the necessity of coronal magnetic field modeling. Such model-based approaches are referred to as extrapolation techniques. In this thesis, the multiwavelength observations have been obtained from the Atmospheric Imaging Assembly (AIA)

instrument and the photospheric magnetic field is acquired from the Helioseismic Magnetic Imager (HMI) instrument, both on board the Solar Dynamics Observatory. In this Chapter, the description of coronal magnetic field extrapolation models is presented in detail, and a brief description of the aforementioned instruments, along with the details of their data acquisition techniques, is also provided.

2.2 Coronal magnetic field models

Since the routine measurements of the magnetic field are possible for the photosphere only, modeling of the coronal magnetic field is an essential and indispensable tool for understanding complex magnetic morphologies. In general, successful measurements of the magnetic field on the photosphere have been made possible using spectropolarimetry, which relies on the principle of the Zeeman effect. In the Zeeman effect, the magnetically sensitive spectral lines split into their components with circular and linear polarization in the presence of a strong magnetic field. These polarized signals are measured in the form of Stokes parameters (I, Q, U, and V), which describe the complete polarization state of light. The splitting is given by $\Delta\lambda \propto \lambda^2 gB$ where λ is the wavelength, g is the Lande's g-factor and B is the magnetic field strength. Measuring the magnetic field in the solar corona is challenging because (a) magnetic field strength is very low ($\sim 10-100$ G) as compared to the photosphere ($\sim 10^3$ G), (b) The million-degree Kelvin temperature in the corona (Aschwanden, 2005) results in thermal broadening. Extrapolation techniques have emerged as a viable and alternative solution for providing quantitative information about the coronal magnetic field. Such schemes are broadly classified into force-free and non-force-free, depending on whether they allow a zero or non-zero Lorentz force ($\mathbf{J} \times \mathbf{B}$) at the bottom boundary. We present a detailed description of these models in the following sections.

2.2.1 Force-free models

It is well established that the dynamical evolution of the coronal magnetofluid is given by the magnetohydrodynamics (MHD) description (see Chapter 1). Then, for a physical system characterized by length scale L and Alfvén transit time

$\tau_A = L/v_A$ (in SI units), where $v_A = \dfrac{B_o}{\sqrt{\mu_0 \rho}}$ is the Alfvén speed, the normalized force-balance equation along with the other ideal MHD equations can be written as follows:

$$\frac{L}{\tau_o v_o}\frac{\partial \bar{\rho}}{\partial \bar{t}} + \bar{\nabla}\cdot(\bar{\rho}\bar{\mathbf{v}}) = 0 \,, \tag{2.1}$$

$$\bar{\rho}\left(\frac{\tau_A}{\tau_o}\frac{\tau_o}{\tau_A}\frac{\partial \bar{\mathbf{v}}}{\partial \bar{t}} + \frac{{v_o}^2}{{v_A}^2}\bar{\mathbf{v}}\cdot\bar{\nabla}\bar{\mathbf{v}}\right) = \bar{\mathbf{J}}\times\bar{\mathbf{B}} - \frac{\beta}{2}\bar{\nabla}\bar{p} - \frac{\beta_g}{2}\bar{\rho}\bar{\nabla}\bar{\psi} \,, \tag{2.2}$$

$$\frac{L}{\tau_o v_o}\frac{\partial \bar{\mathbf{B}}}{\partial \bar{t}} = \bar{\nabla}\times(\bar{\mathbf{v}}\times\bar{\mathbf{B}}) \,, \tag{2.3}$$

$$\bar{\nabla}\cdot\bar{\mathbf{B}} = 0 \,, \tag{2.4}$$

where bars represent the dimensionless quantities. τ_o and v_o are the typical characteristic time scale and flow speed respectively, $\beta = 2\mu_o p_o/{B_o}^2$ is the plasma-β parameter which is the ratio of kinetic pressure (p_o) and magnetic pressure (${B_o}^2/2\mu_o$), $\beta_g = 2\mu_o\rho_o\psi_o/{B_o}^2$ is the ratio of gravitational energy density and magnetic pressure where $\mathbf{g} = \nabla\psi$, ψ being the gravitational potential. However, if the characteristic timescale over which the magnetic morphology of a region varies, is large compared to the Alfvén transit time, then the magnetohydrostatic approximation can be considered appropriate (Wiegelmann & Sakurai, 2021). In the limit of sub-Alfvénic flows, Equation 2.2 becomes

$$0 = \bar{\mathbf{J}}\times\bar{\mathbf{B}} - \frac{\beta}{2}\bar{\nabla}\bar{p} - \frac{\beta_g}{2}\bar{\rho}\bar{\nabla}\bar{\psi} \,. \tag{2.5}$$

Therefore, Equation 2.1 and Equation 2.3 now become inconsequential and Equation 2.5 is known as the magnetohydrostatic equation. Terms in this equation have varying strengths relative to each other in different layers of the solar atmosphere, which can be understood using the work of Gary (2001). In his work, a simple one-dimensional model for the magnetically and density stratified solar atmosphere was constructed. As shown in Figure 2.1, this model constrains the magnetic and plasma pressures based on the various observations at different heights in the solar atmosphere. Evidently, the magnetic field dominates the plasma dynamics in the mid-corona (β <1), whereas on the photosphere, the plasma dominates the dynamics (β >1), except in the active regions. According to Gary (2001)'s plasma

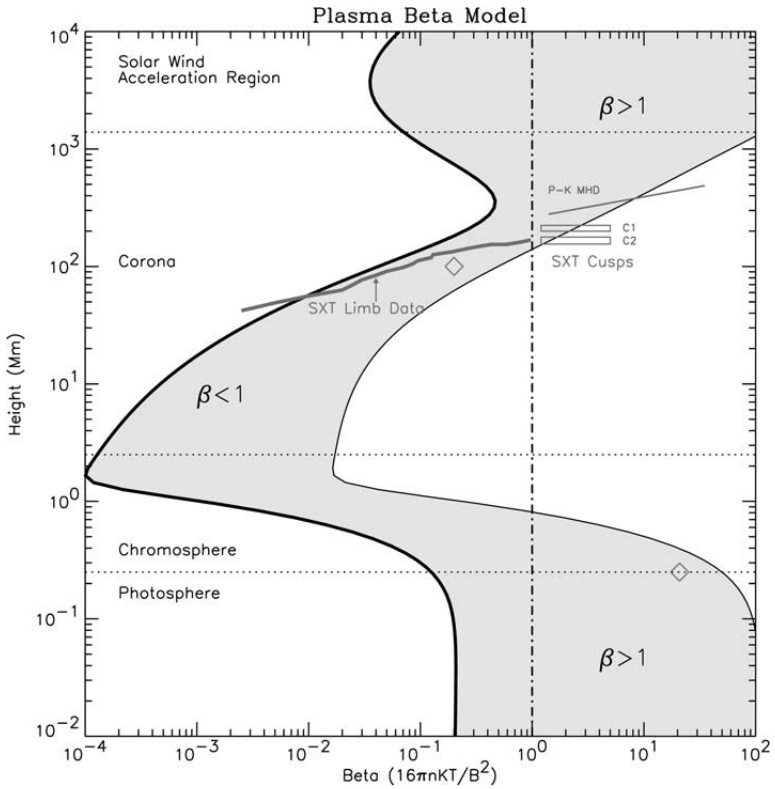

Figure 2.1: Plasma β variation in the solar atmosphere over an active region from Gary (2001).

β profile (Figure 2.1), for the region between 10-100 Mm height in the solar atmosphere, $\beta << 1$, which indicates that the Lorentz force is large compared to both plasma pressure gradient as well as gravitational force terms in Equation 2.5. Consequently, $\bar{\mathbf{J}} \times \bar{\mathbf{B}} = 0$, which implies that the force-free approximation is satisfied. Force-free assumption leads to two cases: either the current density $\mathbf{J}$ is zero (potential field) or the current density $\mathbf{J}$ is parallel to the magnetic field $\mathbf{B}$ (linear and nonlinear force-free fields). The solutions to force-free equations are discussed as follows.

2.2.1.1 Potential field

The easiest solution to $\mathbf{J} \times \mathbf{B} = 0$ is the current-free ($\mathbf{J} = 0$) magnetic field which is also known as the potential field. The current-free magnetic field, i.e., $\nabla \times \mathbf{B} = 0$, can be expressed as $\mathbf{B} = -\nabla\chi$ where χ is the scalar potential. The solenoidal condition $\nabla \cdot \mathbf{B} = 0$ leads to the partial differential equation (PDE), $\nabla^2\chi = 0$— the Laplace equation. Imposing Neumann boundary condition, i.e., the normal component of the magnetic field $\left(\frac{\partial\chi}{\partial n} = B_n\right)$ on the boundary of an enclosed

volume leads to a unique solution of the PDE. It can be readily visualized that the magnetic energy, $W = \int \frac{B^2}{2\mu_o} dV$ associated with the potential fields is the smallest. The magnetic energy of the non-potential magnetic fields ($\mathbf{J} \neq 0$) with the same B_n on the boundary is more than that of the potential fields (Priest, 2014). This holds good for a semi-infinite region, assuming no sources at infinity so that the magnetic field at the large distances R falls off faster than R^{-2}. A good example of such a system is the solar atmosphere above the photosphere where the normal field at the photosphere (line-of-sight component) is known, thus potential field extrapolations require only the line-of-sight magnetic field data.

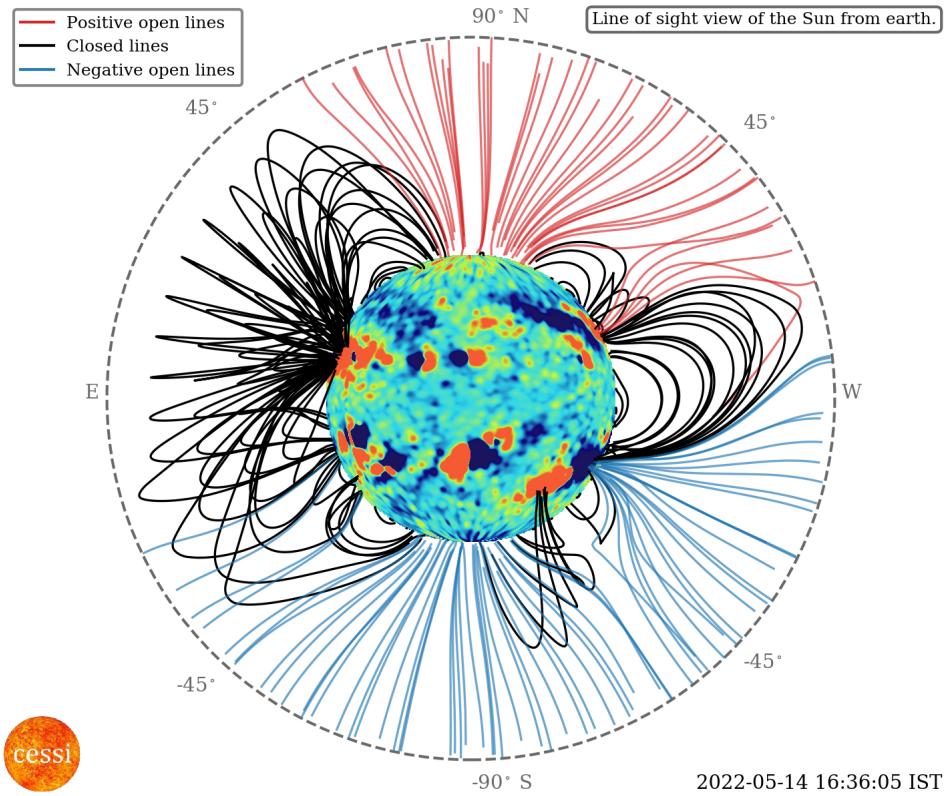

Figure 2.2: PFSS modeled magnetic field configuration of the Sun. Image courtesy: http://www.cessi.in/spaceweather/images/big/ori_corona_logo.png

A simplified but popular extrapolation model based on the current-free field approximation is known as the Potential Field Source Surface (PFSS) model. PFSS computes the magnetic field in the region bounded between the photosphere and an outer "source surface", i.e. between $R_\odot \leq r \leq R_s$ where $R_\odot$ is the radius of

the Sun and R_s is the distance of the source surface from the photosphere. The boundary conditions are imposed at R_s, and this is the only single free parameter in the PFSS model. The value of R_s is usually decided in accordance with either the observations of the white-light corona, coronal hole boundaries (in X-ray), or through the extrapolations from in situ interplanetary magnetic field (IMF) observations. The generally adopted value of R_s is equal to $2.5R_\odot$ but it can vary with the temporal variation of magnetic activity (Lee et al., 2011). Although the PFSS models are helpful in reconstructing the large-scale global structures in the corona but it has two major limitations: First, the transient phenomena can not be explained using PFSS due to its current-free nature since it does not account for the twist which plays a crucial role in coronal transients, and second is that actual coronal magnetic field is not entirely radial within the radius where electric currents may be ignored. Figure 2.2 shows an example of the magnetic field configuration obtained using the PFSS model.

2.2.1.2 Linear force-free

Another solution for the force-free approximation ($\mathbf{J} \times \mathbf{B} = 0$) follows by considering non-zero current density. This is possible if the current density is taken parallel to the magnetic field, satisfying the following relation

$$\mathbf{J} = \alpha_0 \mathbf{B} \quad \text{or} \quad \nabla \times \mathbf{B} = \alpha_0 \mathbf{B} \, , \tag{2.6}$$

where α_0 is a constant representing the twist of magnetic field lines. If, we consider the curl of Equation 2.6 and use the condition that $\nabla \cdot \mathbf{B} = 0$, we obtain the following vector Helmholtz equation

$$(\nabla^2 + \alpha_0^2)\mathbf{B} = 0 \, . \tag{2.7}$$

The theoretical and mathematical aspects of Equation 2.7 have been explored in earlier works such as Chandrasekhar & Kendall (1957) and Woltjer (1958). Further, the solution techniques for the determination of linear force-free field (LFFF) have been investigated in several previous works such as Nakagawa & Raadu (1972), followed by Chiu & Hilton (1977) and Seehafer (1978) using Green's func-

tion approach and by Alissandrakis (1981) employing the method of Fast Fourier transforms. Generally, linear force-free field extrapolation requires transverse field components in addition to the line-of-sight magnetogram for a unique solution (Gary, 1989). However, in special cases, using only line-of-sight magnetogram along with the estimation of α_0 provides physically realizable solutions. One of the methods for estimating α_0 utilizes the vector magnetic field data (in Cartesian coordinate) as

$$\alpha_0(x, y) = \mu_0 \frac{{J_z}^0}{{B_z}^0} \ , \tag{2.8}$$

where

$${J_z}^0 = \frac{\partial {B_y}^0}{\partial x} - \frac{\partial {B_x}^0}{\partial y} \ . \tag{2.9}$$

Though the linear force-free fields contain more energy than the potential magnetic field (Sakurai, 1981), their application to active region dynamics is limited. The reasoning behind this is the spatially varying α_0 in observations which contradicts the assumption of a constant α_0 force-free field. Additionally, due to the continuous injection of helicity from the photospheric surface, the magnetic field cannot relax to a linear force-free field (Wiegelmann & Sakurai, 2021). Therefore, the necessity of nonlinear force-free fields cannot be overlooked, which we will now discuss in the following section.

2.2.1.3 Nonlinear force-free

Having discussed the case of constant α force-free field and its limitations, now we consider the case where α is a function of position vector $\mathbf{r}$, satisfying the equation

$$\nabla \times \mathbf{B} = \alpha(\mathbf{r})\mathbf{B} \ . \tag{2.10}$$

Using solenoidality and taking divergence on both sides of Equation 2.10, we see that

$$\nabla\alpha \cdot \mathbf{B} = 0 \ , \tag{2.11}$$

which suggests that along each particular field line, the value of α is a constant but can vary among the field lines. Previous works such as Bineau (1972) and Amari et al. (2006) have explored the mathematical structure of Equation 2.10 re-

garding uniqueness and the existence of solutions. In the past two decades, several techniques have been developed to obtain a nonlinear force-free field such as the upward integration method (Nakagawa, 1974), the Grad-Rubin method (Sakurai, 1981, Amari et al., 1997 and Amari & Aly, 2010) and the optimization approach (Wheatland et al., 2000 and Wiegelmann, 2004). In general, the problem is challenging due to the intrinsic nonlinearity of the problem and the fact that transverse components of the magnetic field are required on the photosphere, which have more error compared to the line-of-sight field. Further, it should be emphasized that the photospheric boundary is not force-free, which contradicts Equation 2.10. To deal with this, particularly within the optimization approach, routines have been developed which artificially process the bottom boundary to make it compatible with the force-free assumption (e.g. Wiegelmann et al., 2006a) while ensuring that the changes are within the limit of measurement errors. Similarly, an additional effort has been directed to deal with regions lacking observational data in the vector magnetograms (Wiegelmann & Inhester, 2010). Due to the existence of several methods to obtain nonlinear force-free fields, many studies such as Schrijver et al. (2006) and De Rosa et al. (2009) have presented a comparative study of models, highlighting the differences and similarities. The nonlinear force-free model has been widely accepted as suitable for modeling active region dynamics. The success is due to adequate accounting of twisted magnetic field lines and the free magnetic energy, which is thought to be released during transient phenomena such as flares. A comparatively newer and alternate model to nonlinear modeling is the non-force-free model, which we now discuss in the next section.

2.2.2 Non-force-free model

As discussed previously, the observed vector magnetograms do not satisfy the force-free assumption. Therefore, a non-force-free model where the Lorentz force i.e. $\mathbf{J} \times \mathbf{B} \neq 0$ on the photospheric boundary but decreases with height, becoming force-free at coronal heights would be an apt choice for modeling magnetic fields in the solar atmosphere. The model that we are going to discuss in this section is based on the principle of the Minimum Dissipation Rate (MDR) hypothesis (see Bhattacharyya & Janaki, 2004 and reference therein for details). The fundamental

idea behind the MDR principle is that during an irreversible process, any system naturally evolves to those states (or relaxed states) in which the energy dissipation rate is minimum. In the context of coronal plasma, one can apply the MDR principle in the framework of single fluid MHD as well as two-fluid formalism. However, the two-fluid formulation is preferred due to the natural flow-field coupling and the inherent generality over single fluid MHD description. Further, to avoid the loss of a relaxed state in time, we also need to take into account the fact that the solar corona is an open system and is continuously driven by photospheric motions. Toward such an aim, in accordance with the selective decay principle (Hasegawa, 1985), by choosing total dissipation rate (ohmic and viscous) as the minimizer and generalized helicity dissipation rates (for ion and electron fluid) as invariants, Bhattacharyya & Janaki (2004) applied the MDR principle to obtain the corresponding relaxed state, represented by an inhomogeneous double-curl Beltrami equation as

$$\nabla \times (\nabla \times \mathbf{B}) + a\nabla \times \mathbf{B} + b\mathbf{B} = \nabla\phi \ , \tag{2.12}$$

where a and b are constants and ϕ is a scalar potential. The application of this idea in the solar coronal context was to model coronal arcades as minimum dissipative relaxed states (Bhattacharyya et al., 2007). Notice that Equation 2.12 can recasted into a homogeneous equation either by taking curl on both sides, which gives

$$\nabla \times [\nabla \times (\nabla \times \mathbf{B})] + a\nabla \times (\nabla \times \mathbf{B}) + b\nabla \times \mathbf{B} = 0 \ , \tag{2.13}$$

or by redefining the magnetic field vector as $\mathbf{B} = \mathbf{B}' + \dfrac{\nabla\phi}{b}$, which gives

$$\nabla \times (\nabla \times \mathbf{B}') + a\nabla \times \mathbf{B}' + b\mathbf{B}' = 0 \ . \tag{2.14}$$

In principle, Equation 2.13 and Equation 2.14 are equivalent. This can be seen by looking at the form of solution for Equation 2.13, given by

$$\mathbf{B} = \sum_{i=1}^{3} \mathbf{B}_i \ , \tag{2.15}$$

where $\mathbf{B}_i$ are the linear force-free Chandrasekhar-Kendall eigenfunctions (Chandrasekhar & Kendall, 1957), satisfying the relations

$$\nabla \times \mathbf{B}_i = \alpha_i \mathbf{B}_i \ , \tag{2.16}$$

where α_i are the constant twists and $\mathbf{B}_i$ form a complete set of orthonormal vectors for real eigenvalues (Yoshida & Giga, 1990). Using Equation 2.15 and Equation 2.16 in Equation 2.13, we have

$$\sum_{i=1}^{3} \alpha_i \left[\alpha_i^2 + a\alpha_i + b\right] \mathbf{B}_i = 0 \ , \tag{2.17}$$

which suggests that one of the $\alpha_i = 0$, thus corresponding to a potential field. Since $(\nabla\phi)/b$ is also a potential field, the equivalency is established. For more details, see Hu & Dasgupta (2008). Therefore, a superposition of two linear force-free fields with a potential magnetic field gives the required non-force-free solution. A practical approach toward obtaining such a solution in the case of the solar corona has been outlined in Hu et al. (2010). The stepwise methodology and procedure are described in detail as follows

Step-1 : Construction of the Vandermonde matrix

Consider Equation 2.15, then by taking additional curl operations, we have the following set of three equations

$$\mathbf{B} = \mathbf{B}_1 + \mathbf{B}_2 + \mathbf{B}_3 \ , \tag{2.18}$$

$$\nabla \times \mathbf{B} = \alpha_1 \mathbf{B}_1 + \alpha_2 \mathbf{B}_2 + \alpha_3 \mathbf{B}_3 \ , \tag{2.19}$$

$$\nabla \times (\nabla \times \mathbf{B}) = \alpha_1^2 \mathbf{B}_1 + \alpha_2^2 \mathbf{B}_2 + \alpha_3^2 \mathbf{B}_3 \ , \tag{2.20}$$

which can be transformed into a matrix form as follows

$$\begin{pmatrix} \mathbf{B} \\ \nabla \times \mathbf{B} \\ \nabla \times (\nabla \times \mathbf{B}) \end{pmatrix} = \begin{pmatrix} 1 & 1 & 1 \\ \alpha_1 & \alpha_2 & \alpha_3 \\ \alpha_1^2 & \alpha_2^2 & \alpha_3^2 \end{pmatrix} \begin{pmatrix} \mathbf{B}_1 \\ \mathbf{B}_2 \\ \mathbf{B}_3 \end{pmatrix} = \mathcal{V} \begin{pmatrix} \mathbf{B}_1 \\ \mathbf{B}_2 \\ \mathbf{B}_3 \end{pmatrix} \ ,$$

where $\mathcal{V}$ is said to be the Vandermonde matrix. Now, the constituent fields may be expressed as

$$\begin{pmatrix} \mathbf{B}_1 \\ \mathbf{B}_2 \\ \mathbf{B}_3 \end{pmatrix} = \mathcal{V}^{-1} \begin{pmatrix} \mathbf{B} \\ \nabla \times \mathbf{B} \\ \nabla \times (\nabla \times \mathbf{B}) \end{pmatrix} . \tag{2.21}$$

Step-2 : Obtain the z-component of constituent fields using the observed line-of-sight magnetogram

As evident from the term $\nabla \times (\nabla \times \mathbf{B})$ in the right-hand column of Equation 2.21, double derivatives are required for calculation. In the context of the solar corona, this translates into the requirement of two layers of magnetogram in the solar atmosphere. This criterion is not often met because routine observations of the magnetic field are available only for the photosphere and hence only one layer of magnetogram is possible. In order to get around this problem, Hu et al. (2008) introduced the following decomposition

$$\mathbf{B} = \mathbf{B}_1 + \mathbf{B}_2 + c\mathbf{B}_{\rm pot} \ , \tag{2.22}$$

where $\mathbf{B}_1$ and $\mathbf{B}_2$ are linear force-free fields, $\mathbf{B}_{\rm pot}$ is a potential magnetic field obtained using the line-of-sight magnetogram and c is an undetermined multiplier. Then, the z components of $\mathbf{B}_1$ and $\mathbf{B}_2$ can be obtained by taking the curl of Equation 2.22, as follows

$$\begin{aligned} (\nabla \times \mathbf{B})_z &= \alpha_1 \mathbf{B}_{1,z} + \alpha_2 \mathbf{B}_{2,z} \ , \\ (\nabla \times \mathbf{B})_z &= \alpha_1 \mathbf{B}_{1,z} + \alpha_2 (\mathbf{B}_z - \mathbf{B}_{1,z} - c\mathbf{B}_{\rm pot,z}) \ , \\ \mathbf{B}_{1,z} &= \frac{1}{\alpha_1 - \alpha_2} \left[(\nabla \times \mathbf{B})_z - \alpha_2 \mathbf{B}_z + \alpha_2 c \mathbf{B}_{\rm pot,z} \right] \ , \qquad (2.23) \\ \mathbf{B}_{2,z} &= \frac{1}{\alpha_2 - \alpha_1} \left[(\nabla \times \mathbf{B})_z - \alpha_1 \mathbf{B}_z + \alpha_1 c \mathbf{B}_{\rm pot,z} \right] \ . \qquad (2.24) \end{aligned}$$

Step-3 : Computation of transverse components of constituent fields and minimization of error

Having obtained the z components, we require the transverse fields i.e. the x and y components for a complete specification of the modeled field. For an initial choice of α_1, α_2, and c, Equation 2.24 and Equation 2.24 are solved. Then using a linear force-free solver, transverse components i.e. $\mathbf{B}_{1,x}$, $\mathbf{B}_{1,y}$ and $\mathbf{B}_{2,x}$, $\mathbf{B}_{2,y}$ are obtained. Now, denoting the modeled field as $\mathbf{b} = \mathbf{B}_1 + \mathbf{B}_2 + c\mathbf{B}_{\rm pot}$, the deviation between the modeled and observed magnetic field is evaluated by computing E_n, defined as

$$E_n = \sum_{i=1}^{M} \left(|\mathbf{B}_{t,i} - \mathbf{b}_{t,i}| \times |\mathbf{B}_{t,i}| \right) / \sum_{i=1}^{M} |\mathbf{B}_{t,i}| \ , \tag{2.25}$$

By varying the possible values of α_1, α_2, and c (see Hu & Dasgupta, 2008 for details), the process of calculating z components, followed by computation of transverse components and E_n is repeated until a minimum is obtained in the error. This state of minimum error corresponds to the optimized pair (α_1, α_2) and c. Hence, in principle, the non-force-free field in the solar atmosphere is obtained. However, further improvement was introduced by Hu et al. (2010) as described in the next step.

Step-4 : Improvements in the modeled field as described by Hu et al. (2010)

Considering the fact that the sum of potential fields is a potential field, Hu et al. (2010) proposed to modify the potential field $\mathbf{B}_2$ as

$$\mathbf{B}_2 = c\mathbf{B}_{\rm pot} + \mathbf{B}_2^{(1)} + \mathbf{B}_2^{(2)} + ... + \mathbf{B}_2^{(k)} + ... \ , \tag{2.26}$$

where $\mathbf{B}_2^{(k)}$ are iterative improvements of $\mathbf{B}_2$. Note that $\mathbf{B}_2^{(0)} = c\mathbf{B}_{\rm pot}$. Now, to calculate $\mathbf{B}_2^{(k)}$, first, a difference in transverse components of modeled and observed field is computed as

$$\triangle \mathbf{b}_t = \mathbf{B}_t - \mathbf{b}_t \ .$$

Then, the z component of $\mathbf{B}_2^{(k)}$ is computed (Venkatakrishnan & Gary, 1989) as

$$\mathbf{B}_{2,z}^{(k)} = \mathcal{F}^{-1} \left[\frac{iv\mathcal{F}(\triangle \mathbf{b}_y) + iu\mathcal{F}(\triangle \mathbf{b}_x)}{\sqrt{(u^2 + v^2)}} \right] \ , \tag{2.27}$$

where $\mathcal{F}(\mathcal{F}^{-1})$ denote the Fourier(inverse Fourier) transforms with u and v as

frequency domain variables. Having obtained z components, the transverse component of $\mathbf{B}_2^{(k)}$ is obtained by idealizing a periodic boundary and using Fast Fourier Transforms. Now, in an iterative scheme, $\mathbf{B}_2$ is improved and E_n is evaluated until an acceptable minimum is achieved. The number of iterations can be set manually until the profile of E_n saturates and no significant change is observed further.

2.3 Coronal Transient Observations

The coronal magnetic field extrapolation models described in the previous sections use observations of magnetic field vectors at the photosphere as input. Further, multiwavelength observations of the Sun, such as in the X-ray and EUV wavelength ranges, allow us to study the temporal evolution of transient activity at various heights in the solar atmosphere. The simultaneous use of multiwavelength observations and magnetic field provides a complete data set for effective analysis of any transient activity. For such an aim, we have extensively used the observations from a satellite, namely the Solar Dynamics Observatory (SDO).

2.3.1 Solar Dynamic Observatory (SDO)

The Solar Dynamics Observatory (SDO; Pesnell et al., 2012a) mission was launched on February 11, 2010 and it was the first space-based mission commissioned under the Living With a Star (LWS) program of NASA. The satellite is placed in a circular geosynchronous orbit, at an approximate altitude of 36,000 km and an inclination of 28°. The primary objective of this mission is to investigate the magnetic field of the Sun, its generation, evolution, and role in transient activities such as solar flares and coronal mass ejections. To achieve such an aim, it transmits nearly $\sim$ 1.5 Terabytes of data every day to the ground station, which is later processed into various data products such as dopplergrams, magnetograms, and spectra. Primarily, it consists of three instruments, namely the Atmospheric Imaging Assembly (AIA), Extreme Ultraviolet Variability Experiment (EVE), and the Helioseismic Magnetic Imager (HMI). In this thesis, we have used observations from AIA and HMI, which will be discussed in the following.

Channel	Primary ion(s)	Region of atmosphere	Char. log(T)
4500 Å	continuum	photosphere	3.7
1700 Å	continuum	photosphere	3.7
304 Å	He II	chromosphere, transition region	4.7
1600 Å	C IV + continuum	transition region, upper photosphere	5.0
171 Å	Fe IX	quiet corona, upper transition region	5.8
193 Å	Fe XII, XXIV	corona and hot flare plasma	6.2, 7.3
211 Å	Fe XIV	active-region corona	6.3
335 Å	Fe XVI	active-region corona	6.4
94 Å	Fe XVIII	flaring corona	6.8
131 Å	Fe VIII, XXI	transition region, flaring corona	5.6,7.0

Table 2.1: Different channels of AIA centered on specific lines and corresponding regions of the solar atmosphere with different characteristic temperatures (Lemen et al., 2012)

2.3.1.1 Atmospheric Imaging Assembly (AIA)

The Atmospheric Imaging Assembly (AIA: Lemen et al., 2012) observes the full-disk Sun in multiple wavelength channels. With 0.6″ pixel^{-1} spatial resolution and 12-second temporal resolution, it offers numerous, concurrent high-resolution images of the solar atmosphere up to 0.5 $R_{\odot}$ above the solar limb. Normal incidence and multi-layer coated optics-based telescopes of AIA allow narrow-band imaging in seven EUV channels, as summarized in Section 2.3.1.1. For each line, it describes the corresponding ion and region of the solar atmosphere, with a characteristic temperature in log scale. In this thesis, we have used the AIA images to understand the evolution of flaring activity in active region NOAA 12734, to identify salient features of the transient activity at different heights, and to correlate the observations with data-based MHD and Hall MHD simulations. In particular, we have used 94 Å to study the evolution of hot plasma in flare and to identify the location of flare. We have used 171 Å to identify post-flare loops and coronal loops in general. Other channels such as 131 Å and 304 Å have been used to define a W-shaped brightening (see Chapter 6) in the active region, which describes the overall geometry of the flaring region.

2.3.1.2 The Helioseismic and Magnetic Imager (HMI)

The Helioseismic Magnetic Imager (HMI; Scherrer et al., 2012) instrument on board SDO began operations in May 2010 and since then, it has been observing the Sun's entire visible disk continuously. Broadly speaking, the HMI data is categorized into three levels: (a) Level 0 - raw HMI images; (b) Level 1 - data from Level 0 at a particular wavelength and polarization, which has been corrected for various instrumental effects; and (c) Level 1.5 - the HMI observables, computed using Level 1 data (Couvidat et al., 2016). Furthermore, some higher-level data products such as vector magnetic field maps (Hoeksema et al., 2014) and active region patches (Bobra et al., 2014) are also produced. The HMI instrument acquires a series of polarized filtergrams at fixed cadence, using six wavelengths, centered on the Fe I spectral line (6173 Å). These observations are accomplished with the help of two cameras, each of which takes full-disk images at roughly 3.75 seconds and has 4096×4096 pixels along the x and y directions. Further, using two different processing pipelines (a) LoS Pipeline and (b) Vector Pipeline, the filtergrams are utilized to compute various observables corresponding to the photospheric surface. The LoS pipeline uses filtergrams (left or right circular polarization) from the HMI front camera to compute the dopplergrams, magnetograms, and continuum intensity at a cadence of 45 seconds in definitive and near-real-time (NRT) modes. In the NRT mode, data is available usually within three hours of the observation time, while in the definitive mode, data is available with a delay of three to four days. On the other hand, the Vector Pipeline uses filtergrams (linear and circular polarization) from the side camera to primarily compute the Stokes-vector elements, supplemented with line-of-sight dopplergrams, magnetograms, and continuum intensity, all at a cadence of 12 minutes (Couvidat et al., 2016). In this thesis, we have used the SHARP (Bobra et al., 2014) data series from HMI to obtain the vector magnetic field corresponding to the photospheric surface for active region NOAA 12734. It provides the magnetic field in a Cartesian coordinate system, which has been used as the bottom boundary to perform magnetic field extrapolation.

2.4 Summary

In this chapter, we have discussed the importance of solar observations to understand transient activities such as solar flares and coronal mass ejections. The multiwavelength imaging data from SDO/AIA and photospheric vector magnetic field measurements from SDO/HMI have been used to explore the C1.3 class solar flare in active region NOAA 12734, using data-constrained MHD and HMHD simulations (more details in Chapter 6). In this regard, we have briefly mentioned the details and workings of the aforementioned instruments, along with the data acquired from them. We have also emphasized the fact that since routine observations of the magnetic field are available for the photosphere only, extrapolation models are needed to obtain the magnetic field topology in the solar corona. Such models are broadly categorized into force-free and non-force-free models depending on whether they allow a zero or non-zero Lorentz force. Within the category of zero Lorentz force, three solutions are possible, namely (a) potential field (b) linear force-free field, and (c) nonlinear force-free field. The three solutions differ with respect to the force-free parameter (α), zero in the potential field model, constant throughout the computational domain for the LFFF model, and variable but constant for each individual field line in the NLFFF model. We have also discussed the theoretical and numerical aspects of the non-force-free model, which is based on the Minimum Dissipation Rate principle. We conclude this chapter with the idea that multiwavelength observations and magnetic field measurements (for magnetic field extrapolation) are essential tools for the exploration and understanding of transient activities, which are in turn a consequence of magnetic reconnection.

Chapter 3

Numerical model

3.1 Introduction

As mentioned in Chapter 1, to fulfill the aim of the thesis as a first step we develop a 3D HMHD* solver. Therefore, in this Chapter, we document the advancement of an already well-established MHD model to include Hall effects. In order to construct a numerical model that is consistent with the physics of astrophysical plasma, it must exactly maintain the flux-freezing by minimizing numerical dissipation and dispersion errors away from the reconnection regions, which are represented by steep gradients of the magnetic field (Bhattacharyya et al., 2010). This type of minimization is a distinguishing feature of a class of fundamentally nonlinear transport techniques that maintain field extrema along flow trajectories while guaranteeing higher-order accuracy away from steep gradients in advected fields. As discussed in Section 1.6, the Hall forcing term is only effective and localized to the regions of steep gradients of the magnetic field. As a result, we include the Hall forcing in the established high-resolution EULAG MHD model (Smolarkiewicz & Charbonneau, 2013; Charbonneau & Smolarkiewicz, 2013), a tailored variation of the general-purpose hydrodynamic model EULAG (Prusa et al., 2008), which is mostly used in atmospheric and climate research. MPDATA, a.k.a. Multidimensional Positive Definite Advection Transport Algorithm (Smolarkiewicz, 2006)—a spatiotemporally second-order-accurate nonoscillatory forward-in-time (NFT) advection scheme is important to the EULAG. The action of explicit subgrid-scale

*Everywhere in this thesis, the acronym HMHD is used for model name.

turbulence models is mimicked by MPDATA in EULAG. It has proven effectiveness in generating an intermittent and adaptive residual dissipation whenever the concerned advective field is under-resolved—a property inherent to implicit large eddy simulations (ILES) (Grinstein et al., 2007). The generation of steep gradients of the magnetic field in absence of magnetic diffusion provides an unbound sharpening of the corresponding field gradient and inevitably generates under-resolved scales. The unbound increase in field gradient is then smoothed out by this MPDATA produced locally effective residual dissipation of the second order, sufficient to sustain the monotonic nature of the solution. Consequently, the physical reconnections are mimicked at locations of maximal gradients by the ILES property of MPDATA. The ILES property of MPDATA has proven instrumental in a series of advanced numerical studies across a range of scales and physical scenarios, including studies related to coronal heating along with data-based simulations of solar transients (Bhattacharyya et al., 2010; Kumar & Bhattacharyya, 2011; Kumar et al., 2015b, 2017; Prasad et al., 2017, 2018; Nayak et al., 2019, 2020). Our development of a 3D HMHD solver benefits from the ILES property of MPDATA where we have tied the Hall term with the dissipation scale so that the increased local gradients cause the Hall term to be effective locally.

In this Chapter, we present the important features of the advection scheme MPDATA in Section 3.2, numerics of EULAG MHD and the advancement to include Hall forcing term in Section 3.3, and ILES property of MPDATA in Section 3.4.

3.2 Advection solver MPDATA scheme

MPDATA (Smolarkiewicz, 1983, 1984; Smolarkiewicz & Clark, 1986), a finite difference scheme, was originally designed by P. K. Smolarkiewicz in the early 1980s. The algorithm is at least second-order accurate, positive definite, conservative, and computationally efficient. The iterative use of upstream or upwind schemes allow for second order accuracy in MPDATA, where the first iteration is simply a donor cell differencing. Subsequently, the MPDATA algorithm improves the accuracy of the solution by compensating for the truncation error, obtained in the second iteration. In a similar fashion, further iterations may be executed to deal

with the residual errors, resulting from previous iterations, which further enhance the accuracy. In the past decades, MPDATA has been extended to accommodate curvilinear coordinates, full monotonicity preservation, third-order accuracy, and variable sign fields; for details cf. reviews Smolarkiewicz & Margolin (1998); Smolarkiewicz (2006). Here, by using Cartesian coordinates. We discuss the fundamental concepts underlying MPDATA design.

3.2.1 Derivation of MPDATA

To fix ideas, we consider a simple one-dimensional advection equation,

$$\frac{\partial \varphi}{\partial t} + \frac{\partial (k\varphi)}{\partial x} = 0, \tag{3.1}$$

for a scalar variable φ. The velocity k may also be a function of space and time. The donor cell discretization of the advection equation is given by,

$$\varphi_i^{n+1} = \varphi_i^n - \frac{\delta t}{\delta x}(k_{i+\frac{1}{2}}\varphi_r^n - k_{i-\frac{1}{2}}\varphi_l^n), \tag{3.2}$$

where φ_r^n and φ_l^n are chosen depending on the sign of $k_{i+\frac{1}{2}}$ and $k_{i-\frac{1}{2}}$:

$$\varphi_r^n = \begin{cases} \varphi_i^n, & k_{i+\frac{1}{2}} > 0, \\ \varphi_{i+1}^n, & k_{i+\frac{1}{2}} < 0, \end{cases} \tag{3.3}$$

and

$$\varphi_l^n = \begin{cases} \varphi_{i-1}^n, & k_{i-\frac{1}{2}} > 0, \\ \varphi_i^n, & k_{i-\frac{1}{2}} < 0, \end{cases} \tag{3.4}$$

with the integer and half-integer indices corresponding to cell centers and cell walls. In Equation 3.2, φ_i^{n+1} on the LHS is the solution sought at the grid point (t^{n+1}, x_i) with $\delta t = t^{n+1} - t^n$ and $\delta x = x_{i+1} - x_i$ representing temporal and spatial increments respectively. The above case distinctions can be avoided by writing the Equation 3.2 in the following form,

$$\varphi_i^{n+1} = \varphi_i^n - \frac{\delta t}{2\delta x}[k_{i+\frac{1}{2}}(\varphi_i^n + \varphi_{i+1}^n) - k_{i-\frac{1}{2}}(\varphi_{i-1}^n + \varphi_i^n) + \mid k_{i+\frac{1}{2}} \mid (\varphi_i^n - \varphi_{i+1}^n) - \mid k_{i-\frac{1}{2}} \mid (\varphi_{i-1}^n - \varphi_i^n)]. \tag{3.5}$$

Notably, if the sign of k determines the flow direction, this scheme always chooses the values of φ (for a given time) which lies in the upstream direction (Griebel et al., 1998). The donor cell approximation in flux form is expressed as,

$$\varphi_i^{n+1} = \varphi_i^n - [F(\varphi_i^n, \varphi_{i+1}^n, U_{i+\frac{1}{2}}) - F(\varphi_{i-1}^n, \varphi_i^n, U_{i-\frac{1}{2}})], \tag{3.6}$$

where the flux function F is

$$F(\varphi_L, \varphi_R, U) \equiv [U]^+ \varphi_L + [U]^- \varphi_R, \tag{3.7}$$

with $U \equiv \dfrac{a\delta t}{\delta x}$ represents the dimensionless local Courant number while, $[U]^+ \equiv 0.5(U + \mid U \mid)$ and $[U]^- \equiv 0.5(U - \mid U \mid)$ denoting the nonnegative and nonpositive parts of the Courant number (Smolarkiewicz & Margolin, 1998; Smolarkiewicz, 2006).

The donor cell scheme is conditionally stable and the corresponding stability condition, for every time step, has a form

$$\max\left(\frac{\mid k_{i+\frac{1}{2}} \mid \delta t}{\delta x}\right) \leq 1 \quad \forall i. \tag{3.8}$$

Moreover, under the condition Equation 3.8, the scheme is also positive definite, implying: if $\varphi_i^0 \geq 0 \quad \forall i$ then $\varphi_i^n \geq 0 \quad \forall i$ and n. These two properties as well as low computational cost and low phase error make the scheme Equation 3.6 attractive for the numerical evaluation of the advection equation. However, the scheme being first-order accurate (both in space and time) produces large implicit numerical diffusion.

Towards quantifying the diffusion in Equation 3.6, for simplicity we assume the k to be constant and φ to be nonnegative. A straightforward truncation analysis, expanding all dependent variables in a second-order Taylor series about the time level n and spatial point i, reveals that the scheme more accurately approximates

the advection-diffusion equation

$$\frac{\partial \varphi}{\partial t} + \frac{\partial (k\varphi)}{\partial x} = \frac{\partial}{\partial x}\left(K \frac{\partial \varphi}{\partial x}\right), \tag{3.9}$$

where the diffusion coefficient

$$K = \frac{\delta x^2}{2\delta t}(\mid U \mid - U^2). \tag{3.10}$$

In other words, the scheme estimates the solution of the advection equation with a second-order truncation error. The implicit diffusion term on the right-hand side of Equation 3.9 is crucial for the stability of the scheme and cannot be removed by simple subtraction. However, it is possible to minimize this error and improve the accuracy of the solution by re-writing the diffusive part of Equation 3.9 as

$$\frac{\partial \varphi}{\partial t} = \frac{\partial}{\partial x}\left(K \frac{\partial \varphi}{\partial x}\right) = -\frac{\partial}{\partial x}(u_d \varphi) \tag{3.11}$$

where $u_d = -\dfrac{K}{\varphi}\dfrac{\partial \varphi}{\partial x}$, an advection equation is obtained with velocity u_d, termed as the diffusion velocity. Now, utilizing the fact that solution of a diffusion equation is reversible, an anti-diffusion velocity is defined as $k^1 = -u_d = \dfrac{K}{\varphi}\dfrac{\partial \varphi}{\partial x}$ and hence the error term becomes

$$e^1 \equiv \frac{\partial}{\partial x}\left(K \frac{\partial \varphi}{\partial x}\right) = \frac{\partial (k^1 \varphi)}{\partial x}, \tag{3.12}$$

where e^1 symbolizes error term and $k^1 \equiv \dfrac{K}{\varphi}\dfrac{\partial \varphi}{\partial x}$ is termed pseudo velocity or anti-diffusion velocity.

$$\frac{\partial \varphi}{\partial t} + \frac{\partial (k\varphi)}{\partial x} = -\frac{\partial}{\partial x}\left(k^1 \varphi\right), \tag{3.13}$$

the superscript (1) is used to mark the first iteration for subtracting the error. To compensate for the error, we again use the donor cell scheme but this time with the pseudo velocity k^1 and the φ^{n+1} already available from Equation 3.6 in lieu of the physical velocity k and the φ^n. A first-order accurate estimate of the pseudo velocity is

$$k^1_{i+\frac{1}{2}} \equiv \frac{2K}{\delta x}\frac{\varphi^{(1)}_{i+1} - \varphi^{(1)}_i}{\varphi^{(1)}_{i+1} + \varphi^{(1)}_i} \tag{3.14}$$

where $\varphi^{(1)}$ represents the first-order accurate φ^{n+1} estimated from Equation 3.6. The modified Courant number is $V^1_{i+\frac{1}{2}} \equiv \dfrac{k^1_{i+\frac{1}{2}}\delta t}{\delta x}$. In the second iteration, we subtract a donor cell estimate of the error to improve the accuracy. The equation of the second iteration is

$$\varphi^2_i = \varphi^1_i - [F(\varphi^1_i, \varphi^1_{i+1}, V^1_{i+\frac{1}{2}}) - F(\varphi^1_{i-1}, \varphi^1_i, V^1_{i-\frac{1}{2}})], \tag{3.15}$$

which estimates φ^{n+1} which is the second-order accurate while preserving the sign of φ. It is an easy matter to show that, like the donor cell scheme, MPDATA is consistent and conditionally stable (Smolarkiewicz, 1983; Smolarkiewicz & Margolin, 1998; Smolarkiewicz, 2006). But, in contrast to the donor scheme, MPDATA does not contain strong numerical implicit diffusion because it compensates for strong implicit numerical diffusion with an anti-diffusion velocity.

The extension of MPDATA to multiple dimensions is straightforward. To demonstrate, we consider a simple two-dimensional advection equation,

$$\frac{\partial \varphi}{\partial t} + \frac{\partial (k\varphi)}{\partial x} + \frac{\partial (l\varphi)}{\partial y} = 0, \tag{3.16}$$

where k and l are velocities in $x-$ and $y-$directions. The corresponding donor cell approximation is then

$$\begin{aligned}\varphi^{n+1}_{i,j} = \varphi^n_{i,j} &- [F(\varphi^n_{i,j}, \varphi^n_{i+1,j}, U_{i+\frac{1}{2},j}) - F(\varphi^n_{i-1,j}, \varphi^n_{i,j}, U_{i-\frac{1}{2},j})] \\ &-[F(\varphi^n_{i,j}, \varphi^n_{i,j+1}, V_{i,j+\frac{1}{2}}) - F(\varphi^n_{i,j-1}, \varphi^n_{i,j}, V_{i,j-\frac{1}{2}})],\end{aligned} \tag{3.17}$$

where the flux function is similar to Equation 3.7 and, $U \equiv \dfrac{k\delta t}{\delta x}$ and $V \equiv \dfrac{l\delta t}{\delta y}$ are Courant numbers. Further, the Taylor series expansion of Equation 3.17 about the cell point (i, j) and the time level n with constant velocities yields the following advection-diffusion equation,

$$\frac{\partial \varphi}{\partial t} + \frac{\partial (k\varphi)}{\partial x} + \frac{\partial (l\varphi)}{\partial y} = K\frac{\partial^2 \varphi}{\partial x^2} + L\frac{\partial^2 \varphi}{\partial y^2} - \frac{UV\delta x\delta y}{\delta t}\frac{\partial^2 \varphi}{\partial x \partial y}, \tag{3.18}$$

with $K \equiv \frac{\delta x^2}{2\delta t}(\mid U \mid -U^2)$ and $L \equiv \frac{\delta y^2}{2\delta t}(\mid V \mid -V^2)$. To estimate the truncation error using the donor cell scheme, we rewrite the error terms, the right-hand side terms of Equation 3.18, in the following form

$$K\frac{\partial^2 \varphi}{\partial x^2} + L\frac{\partial^2 \varphi}{\partial y^2} - \frac{UV\delta x\delta y}{\delta t}\frac{\partial^2 \varphi}{\partial x \partial y} = \frac{\partial}{\partial x}(k^1\varphi) + \frac{\partial}{\partial x}(l^1\varphi) \tag{3.19}$$

where

$$k^1 \equiv \frac{K}{\varphi}\frac{\partial \varphi}{\partial x} - \frac{UV\delta x\delta y}{2\delta t}\frac{1}{\varphi}\frac{\partial \varphi}{\partial y} \quad \text{and} \quad l^1 \equiv \frac{L}{\varphi}\frac{\partial \varphi}{\partial y} - \frac{UV\delta x\delta y}{2\delta t}\frac{1}{\varphi}\frac{\partial \varphi}{\partial x} \tag{3.20}$$

are pseudo velocities in x and $y-$directions. Utilizing these velocities and the updated value of φ^{n+1} from Equation 3.17, the donor cell scheme is used to estimate the error. In the second iteration, the error is subtracted to enhance the accuracy.

3.2.2 Extension to the generalized transport equation

The general transport equation is

$$\frac{\partial \varphi}{\partial t} + \nabla \cdot (\mathbf{k}\varphi) = R, \tag{3.21}$$

where R combines all forcing and source terms. In general, both R and velocity $\mathbf{k}$ depends on the variable φ. The forward-in-time discretization of Equation 3.21 is assumed as,

$$\frac{\varphi^{n+1} - \varphi^n}{\delta t} + \nabla \cdot (\mathbf{k}^{n+\frac{1}{2}}\varphi^n) = R^{n+\frac{1}{2}}. \tag{3.22}$$

Expansion of Equation 3.22 into the second-order Taylor series about the time level n shows that the scheme Equation 3.22 approximates the equation

$$\frac{\partial \varphi}{\partial t} + \nabla \cdot (\mathbf{k}\varphi) = R - \nabla \cdot \Big[0.5\delta t \mathbf{k} (\mathbf{k} \cdot \nabla \varphi) + 0.5\delta t \mathbf{k} \varphi (\nabla \cdot \mathbf{k}) \Big] + \nabla \cdot (0.5\delta t \mathbf{k} R) + \mathcal{O}(\delta t^2). \tag{3.23}$$

In the right-hand side of Equation 3.23, all $\mathcal{O}(\delta t)$ truncation errors originated by uncentered time differencing in Equation 3.22 are already expressed by spatial derivatives. Specification of the time levels of both the advective velocity and the forcing term as $n + 1/2$ in Equation 3.22 eliminates $\mathcal{O}(\delta t)$ truncation errors which are proportional to their temporal derivatives (Smolarkiewicz & Clark, 1986). From Equation 3.23, it is clear that the formulation of a second-order accurate forward-in-time scheme for Equation 3.21 requires the compensation of $\mathcal{O}(\delta t)$ truncation errors to at least the second-order accuracy.

For such a formulation, we note that $\mathcal{O}(\delta t)$ error terms in Equation 3.23 have two distinct components. The first component is merely due to advection and does not involve the forcing R. In contrast, the second component depends on the forcing R. Towards compensating the first component, notable is the reduction of Equation 3.21 to homogeneous transport equation for $R = 0$. Then, the MPDATA scheme retains the form of the basic scheme (Section 3.2.1), where the first donor cell iteration utilizes the advective velocity $\mathbf{k}^{n+\frac{1}{2}}$ and φ^n, and subsequent iterations use pseudo velocities and φ calculated from the preceding iteration; for details cf. (Smolarkiewicz, 1991; Smolarkiewicz & Margolin, 1993, 1998; Smolarkiewicz, 2006). Compensation of the second component requires subtracting a first-order accurate approximation of the error from the right-hand side of Equation 3.22. A simple, efficient, and second-order accurate MPDATA for Equation 3.21 can then be symbolically written as,

$$\varphi_i^{n+1} = \mathcal{A}_i(\varphi^n + 0.5\delta t R^n, \mathbf{k}^{n+\frac{1}{2}}) + 0.5\delta t R_i^{n+1}, \tag{3.24}$$

where $\mathcal{A}$ denotes the basic MPDATA advection scheme (Smolarkiewicz, 1991; Smolarkiewicz & Margolin, 1993). In this equation, we assume $R^{n+\frac{1}{2}} = 0.5(R^n + R^{n+1})$ with R^{n+1} representing $\mathcal{O}(\delta t^2)$ accurate approximation of R at time level $(n + 1)$. Noticeably, the first donor cell iteration in the MPDATA scheme uses the auxiliary variable $\varphi^n + 0.5\delta t R^n$ in lieu of the physical variable φ^n with a physical

advective velocity $\mathbf{k}^{n+\frac{1}{2}}$. The advection of the auxiliary field is important for preserving the global accuracy and stability of the forward-in-time approximations (Smolarkiewicz, 1991; Smolarkiewicz & Margolin, 1993, 1997).

The advective velocity at intermediate $n+\frac{1}{2}$ time level may be approximated by linear interpolation or extrapolation

$$\mathbf{k}^{n+\frac{1}{2}} = \frac{1}{2}(\mathbf{k}^{n+1} + \mathbf{k}^{n}), \tag{3.25}$$

$$\mathbf{k}^{n+\frac{1}{2}} = \frac{1}{2}(3\mathbf{k}^{n} - \mathbf{k}^{n-1}), \tag{3.26}$$

either of which is sufficient to maintain second-order accuracy in Equation 3.24. For the subtleties involved in a particular choice of $\mathbf{k}^{n+\frac{1}{2}}$, readers are referred to (Smolarkiewicz & Clark, 1986).

3.2.3 Nonoscillatory MPDATA

The basic MPDATA scheme discussed above preserves sign[†] but not monotonicity of the advected variables (Smolarkiewicz, 1983, 1984; Smolarkiewicz & Clark, 1986), and in general, the solutions are not free of spurious oscillations, particularly in presence of steep gradients (Smolarkiewicz & Grabowski, 1990; Smolarkiewicz, 1991). However, MPDATA is made fully monotone (Smolarkiewicz, 1991) by adapting the flux-corrected-transport (FCT) methodology (Boris & Book, 1973; Book et al., 1975; Boris & Book, 1976). Actually, for a variety of reasons, MPDATA is appropriate for this sort of approach. First, the initial iteration in MPDATA is the donor cell scheme which is a low-order monotone scheme, generally used as the reference in the FCT design. Second, the overall accuracy of the resultant FCT scheme is improved by ensuring the monotonicity of successive iterations yielding a higher-order accurate reference solution for the next iteration. Third, the FCT scheme blends solutions with consistent phase errors since all MPDATA iterations have low phase errors that are typical features of the donor cell scheme (Smolarkiewicz & Clark, 1986). As a result, the overall accuracy of final

[†]We refer to this attribute in the preceding subsections as positive-definiteness for historical reasons.

FCT scheme (Smolarkiewicz & Grabowski, 1990) is benefited significantly.

3.3 Advancement of EULAG MHD to include Hall forcing

The numerical model EULAG is an established model for simulating fluid flows across a wide range of scales and physical scenarios (Prusa et al., 2008). The name EULAG alludes to the capability to solve fluid equations in either an Eulerian (Smolarkiewicz & Margolin, 1993) or a Lagrangian (Smolarkiewicz & Pudykiewicz, 1992) mode. The numerics of EULAG are unique, owing to a combination of MPDATA advection schemes, robust elliptic solver, and generalized coordinate formulation enabling grid adaptivity. The EULAG MHD is a spin-off of the numerical model EULAG (Smolarkiewicz & Charbonneau, 2013). Here, we describe the numerical apparatus of EULAG MHD utilized for our calculations.

3.3.1 Numerics of the EULAG MHD

In a non-rotating Cartesian coordinate system, the EULAG MHD model solves the MHD equations (in cgs unit[‡]) for an incompressible magnetofluid with zero physical resistivity (infinite electrical conductivity) which can be expressed in the form of a generalized transport equation Equation 3.21

$$\frac{\partial \mathbf{v}}{\partial t} + \nabla \cdot (\mathbf{vv}) = \mathbf{R^v}, \tag{3.27}$$

$$\frac{\partial \mathbf{B}}{\partial t} + \nabla \cdot (\mathbf{vB}) = \mathbf{R^B},, \tag{3.28}$$

$$\nabla \cdot \mathbf{v} = 0, \tag{3.29}$$

$$\nabla \cdot \mathbf{B} = 0, \tag{3.30}$$

where $\mathbf{R^v} = -\nabla\phi + \frac{1}{4\pi\rho_0}\mathbf{B}\cdot\nabla\mathbf{B} + \mathbf{F}_\nu$ and $\mathbf{R^B} = \mathbf{B}\cdot\nabla\mathbf{v}$. Assuming a constant density ρ_0, $\phi = (p + \mathbf{B}^2/8\pi)/\rho_0$ is the density normalized total pressure which is the sum of kinetic pressure (p) and magnetic pressure ($\mathbf{B}^2/8\pi$). F_ν symbolizes the viscous drag force. All other symbols have their usual meaning. On a general

[‡]EULAG MHD code uses either CGS, MKS, or dimensionless units

note, EULAG's governing equations are formulated and solved in transformed time-dependent generalized curvilinear coordinates

$$(\bar{t}, \bar{\mathbf{x}}) \equiv (t, F(t, \mathbf{x})). \tag{3.31}$$

The physical domain (t, x), where the physical problem is posed, is assumed to be any stationary orthogonal coordinate system. Moreover, the transformed horizontal coordinates $(\bar{x}, \bar{y})$ are assumed to be independent of the vertical coordinate z (Prusa & Smolarkiewicz, 2003). The physical domain used for the calculations carried out in this thesis is the Cartesian coordinate system and, therefore both the computational domain and the physical domain are identical, i.e., $(\bar{t}, \bar{x}) \equiv (t, x)$.

Here, we present the details of the EULAG MHD for the Cartesian domain. The generalized coordinate formulation of EULAG MHD utilizes the rigorous tensorial exposition of MHD equations; cf. (Smolarkiewicz & Charbonneau, 2013). In the following, the numerics of EULAG MHD are briefly discussed. In the discussion, the original notations used in Smolarkiewicz & Charbonneau (2013) are mostly retained to maintain homogeneity with the contemporary literature. Notably, using the vector identities

$$\mathbf{B} \cdot \nabla \mathbf{B} = \nabla \cdot \mathbf{B}\mathbf{B}, \qquad \mathbf{B} \cdot \nabla \mathbf{v} = \nabla \cdot \mathbf{B}\mathbf{v}, \tag{3.32}$$

equations 3.27 and 3.28 can be envisaged in a flux conservative form

$$\frac{\partial \mathbf{\Psi}}{\partial t} + \nabla \cdot (\mathbf{v}\mathbf{\Psi}) = \mathbf{R}, \tag{3.33}$$

where

$$\mathbf{\Psi} = \{\mathbf{v}, \mathbf{B}\}^T. \tag{3.34}$$

The forcing term on the right-hand side generally represents all possible forces, particularly for the simulations reported in the thesis,

$$\mathbf{R} = \{\mathbf{R}_\mathbf{v}, \mathbf{R}_\mathbf{B}\}^T \tag{3.35}$$

which are the forcing terms in Equation 3.27 and Equation 3.28. Additional to the

forcing term in the induction equation, an ad hoc term $-\nabla\phi^\star$ is added to right-hand side of the induction equation to enforce solenoidality of the numerically calculated magnetic field (discussed later). Notably, the total pressure ϕ (defined above) is similarly employed to make the velocity solenoidal. Notably, EULAG hydrodynamic solver (Prusa et al., 2008) integrates Equation 3.33 employing the nonoscillatory forward-in-time algorithm MPDATA, using the well-established EULAG template (cf. Equation 3.24)

$$\mathbf{\Psi}_i^{n+1} = \mathcal{A}_i(\mathbf{\Psi}^n + 0.5\delta t\mathbf{R}^n, \mathbf{v}^{n+\frac{1}{2}}) + 0.5\delta t\mathbf{R}_i^{n+1} \equiv \hat{\mathbf{\Psi}}_i + 0.5\delta t\mathbf{R}_i^{n+1}, \tag{3.36}$$

where $\mathbf{\Psi}_i^{n+1}$ is the solution sought at the grid point (t^{n+1}, x_i) where n and i are the temporal and spatial indices, respectively.

For inviscid dynamics (F_ν=0), the model template algorithm Equation 3.36 is implicit for all dependent variables in Equation 3.27 and Equation 3.28 because all forcing terms are assumed to be unknown at time level $n+1$. Importantly, the MHD equations add additional nonlinearity to the hydrodynamic forcings $\mathbf{R}$ through the terms $\nabla\cdot\mathbf{BB}$ and $\nabla\cdot\mathbf{Bv}$. To incorporate the nonlinearities while preserving the general structure of the EULAG template, Smolarkiewicz & Charbonneau (2013) anticipated

$$\mathbf{\Psi}_i^{n+1,q} = \hat{\mathbf{\Psi}}_i + 0.5\delta t\mathbf{L\Psi}\,|_i^{n+1,q} + 0.5\delta t\mathbf{N}(\mathbf{\Psi})\,|_i^{n+1,q-1} - 0.5\delta t\nabla\mathbf{\Phi}\,|_i^{n+1,q}, \tag{3.37}$$

where the forcing $\mathbf{R}$ on the right-hand side is the sum of a linear term $\mathbf{L\Psi}$ with $\mathbf{L}$ being a linear operator, a nonlinear part of forcing, i.e., $\mathbf{N}(\mathbf{\Psi})$, and a potential term $-\nabla\mathbf{\Phi}$ with $\mathbf{\Phi} \equiv (\phi, \phi, \phi, \phi^\star, \phi^\star, \phi^\star)$[§]. In Equation 3.37, $q = 1, 2, ..., m$ numbers fixed point iterations. The expression Equation 3.37 is implicit with respect to the forcing terms $\mathbf{L\Psi}$ and $-\nabla\mathbf{\Phi}$. To obtain a closed-form expression for ${\mathbf{\Psi}_i}^{n+1,q}$ Equation 3.37 is rearranged as

$$[\mathbf{I} - 0.5\delta t\mathbf{L}]\mathbf{\Psi}_i^{n+1,q} = \left(\hat{\mathbf{\Psi}} + 0.5\delta t\mathbf{N}(\mathbf{\Psi})\,|^{n+1,q-1} - 0.5\delta t\nabla\mathbf{\Phi}^{n+1,q}\right)_i, \tag{3.38}$$

[§]Here ϕ and ϕ^* are the same physical variable and numerical facilitator as defined above

which gives

$$\mathbf{\Psi}_i^{n+1,q} = [\mathbf{I} - 0.5\delta t\mathbf{L}]^{-1}\left(\hat{\hat{\mathbf{\Psi}}} - 0.5\delta t\nabla\mathbf{\Phi}^{n+1,q}\right)_i, \tag{3.39}$$

where the explicit element is modified to

$$\hat{\hat{\mathbf{\Psi}}} \equiv \hat{\mathbf{\Psi}} + 0.5\delta t\mathbf{N}(\mathbf{\Psi})\,|^{n+1,q-1}\,. \tag{3.40}$$

Taking divergence on both sides of Equation 3.39 and imposing solenoidality of $\mathbf{v}$ and $\mathbf{B}$, elliptic Poisson equations for ϕ and ϕ^* are generated. Under appropriate boundary conditions, these elliptic equations are solved iteratively using a preconditioned generalized conjugate residual (GCR) algorithm (Eisenstat et al., 1983; Eisenstat, 1983; Smolarkiewicz et al., 1997). The viscous forcing within this algorithm framework is incorporated by integrating explicitly to the first-order accuracy in time and then adding to the auxiliary argument of MPDATA operator $\mathcal{A}$. Now the argument modifies as $\tilde{\mathbf{\Psi}} \equiv \mathbf{\Psi}^n + 0.5\delta t(\mathbf{R}^n + 2\tilde{\mathbf{R}})$ where $\tilde{\mathbf{R}}$ symbolizing the first-order time accurate viscous forcing. All the dependent variables being spatially co-located in Equation 3.39, the time updated $\mathbf{\Psi}$ is obtained by solving two the discrete elliptic equations for ϕ and ϕ^* generated by the solenoidality constraints (Equation 3.29) and Equation 3.30 discretized consistently with the divergence operator implied by $\mathcal{A}$; see (Prusa et al., 2008). In EULAG MHD, the iterations carried out in GCR are termed as "inner" while the iterations executed to construct Equation 3.37 are called "outer". In the model, the time step controls the convergence of the outer iterations while being monitored by the convergence of inner iterations in the GCR solver (Smolarkiewicz & Szmelter, 2009, 2011). As the outer iterations complete, the solution gets updated. Consequently, the total implicit forcing $\mathbf{RI} = \mathbf{L\Psi} - \nabla\Phi$ in Equation 3.37 is returned as $\mathbf{RI}_i^n = \dfrac{2}{\delta t}(\mathbf{\Psi}_i^n - \hat{\hat{\mathbf{\Psi}}}_i)$. In the spirit of Equation 3.37 and Equation 3.39, total explicit forcing $\mathbf{RE} = \mathbf{N}(\mathbf{\Psi}) + \tilde{\mathbf{R}}$ is evaluated using the updated solution to give $\mathbf{RE}_i^n = \mathbf{RE}_i(\mathbf{\Psi}^n)$. The net forcing $\mathbf{R} = \mathbf{RI} + \mathbf{RE}$ is used in the subsequent time step in the argument of the MPDATA operator in Equation 3.36. In the following, we present the numerical implementation of the above discussed iterative formulation of Equation 3.36. The iterative steps to implement Equation 3.36 progresses sequentially so as to use the most current update of a dependent variable in the on-

going step, wherever possible. An individual outer iteration consists of two blocks: "hydrodynamic" and "magnetic". The hydrodynamic block emulates the standard EULAG solution of hydrodynamical equations (Prusa et al., 2008) by integrating the momentum balance equation with the magnetic field in the $\nabla \cdot \mathbf{BB}$ treated as supplementary. Being at the half of a single outer iteration, it is denoted by the index $q - 1/2$. In this block, the elliptic equation for ϕ (magnetic+kinetic pressure) is solved to obtain the final updated velocity. In the magnetic block, the induction equation is integrated using the final updated velocity obtained from the hydrodynamic block. This block returns the final updated magnetic field through the solution of the elliptic equation for ϕ^* (numerical facilitator to make magnetic field solenoidal).

Finally, the sequence of steps executed at each outer iteration for integrating the MHD equations Equation 3.27-Equation 3.30 is discussed below. Since all variables are at time $n+1$, hereafter the superscript $n+1$ is dropped to keep the expressions uncluttered. Additionally, at $q = 1$ the initial guess for $\mathbf{v}$ and $\mathbf{B}$ are based on the assumption: $\mathbf{v}^0 = 2\mathbf{v}^{n+1} - \mathbf{v}^n$ and $\mathbf{B}^0 = 2\mathbf{B}^{n+1} - \mathbf{B}^n$, respectively. The steps of the numerical scheme are described below.

- **Step 1:** As stated above, the hydrodynamic block requires an appropriate magnetic field to compute the forcing $\nabla \cdot \mathbf{BB}$ which enters the momentum transport equation in MHD. Therefore, as a first step, the magnetic field $\mathbf{B}^{q-1/2}$ at time t^{n+1} is estimated implicitly through inversion of the induction equation,

$$\mathbf{B}_i^{q-1/2} = \hat{\mathbf{B}}_i + 0.5\delta t \Big[\mathbf{B}^{q-1/2} \cdot \nabla \mathbf{v}^{q-1} - \mathbf{B}^{q-1/2} tr\{\nabla \mathbf{v}^{q-1}\} \Big]_i. \tag{3.41}$$

- **Step 2:** Subsequently, Equation 3.41 is utilized to obtain velocity by employing the standard EULAG procedure,

$$\mathbf{v}_i^q = \hat{\mathbf{v}}_i + \frac{0.5\delta t}{\rho_0 \mu_0} (\nabla \cdot \mathbf{BB})_i^{q-1/2} - 0.5\delta t (\nabla \phi)_i^q. \tag{3.42}$$

Following Equation 3.39, the above equation can be expressed in a closed

form,

$$\mathbf{v}_i^q = \hat{\hat{\mathbf{v}}}_i - 0.5\delta t(\nabla\phi)_i^q. \tag{3.43}$$

Employing solenoidality of the velocity on the above expression of $\mathbf{v}$,

$$\nabla \cdot (\hat{\hat{\mathbf{v}}}_i - 0.5\delta t(\nabla\phi)_i^q) = 0, \tag{3.44}$$

yields the elliptic equation for the total pressure ϕ which is solved through the GCR solver by imposing the appropriate boundary conditions on the normal component of $\mathbf{v}$ in Equation 3.43. Next, the solution of Equation 3.44 is used to calculate the velocity following the algorithm described in Smolarkiewicz & Margolin (1997). Finally, upon the completion of outer iterations in the hydrodynamics block the updated solenoidal velocity is obtained.

- **Step 3:** Using the updated velocity obtained from the hydrodynamic block in the previous step, initially the magnetic block calculates the magnetic field $\mathbf{B}^{q-1/4}$ at t^{n+1} implicitly (similar to Equation 3.41):

$$\mathbf{B}_i^{q-1/4} = \hat{\mathbf{B}}_i + 0.5\delta t\Big[\mathbf{B}^{q-1/4} \cdot \nabla\mathbf{v}^q - \mathbf{B}^{q-1/4} tr\{\nabla\mathbf{v}^q\}\Big]_i, \tag{3.45}$$

where $q - 1/4$ stands for the calculation at a quarter of iteration, i.e., before actually calculating the final updated $\mathbf{B}^q$ in the magnetic block.

- **Step 4:** The induction equation is solved in a way similar to the momentum transport equation by expressing the right-hand side forcing term in the flux conservative form:

$$\mathbf{B}_i^q = \hat{\mathbf{B}}_i + 0.5\delta t(\nabla \cdot \mathbf{B}^{q-1/4}\mathbf{v}^q)_i - 0.5\delta t(\nabla\phi^\star)_i^q. \tag{3.46}$$

The final updated magnetic field $\mathbf{B}$ is estimated from Equation 3.46 by imposing the solenoidality condition on the magnetic field and solving the elliptic equation for $\phi^\star$ through a procedure similar to **Step2**.

3.3.2 Inclusion of the Hall effect in the EULAG MHD

The inclusion of the Hall effect into the EULAG MHD model follows the principles of the outlined standard MHD integrator in Section 3.3.1. As discussed in Section 1.6, the Hall term enters the induction equation. The addition of the Hall term modifies the nonlinear part ($\mathbf{N}(\mathbf{\Psi})$) of forcing in Equation 3.37. Therefore, the Hall forcing is incorporated in the EULAG MHD by casting it in the induction equation in a flux conservative form which can be achieved via straightforward mathematical calculation presented below. Starting with the dimensionless generalized Ohm's law

$$\mathbf{E} + \mathbf{v} \times \mathbf{B} = \frac{\delta_i}{L} \mathbf{J} \times \mathbf{B} \ , \tag{3.47}$$

where $\mathbf{J} = \nabla \times \mathbf{B}$ is the dimensionless current density. The Hall term $\mathbf{J} \times \mathbf{B} = (\nabla \times \mathbf{B}) \times \mathbf{B} = -\mathbf{B} \times (\nabla \times \mathbf{B})$ can be written in the convenient form using the vector identity

$$-\mathbf{B} \times (\nabla \times \mathbf{A}) = \mathbf{A} \times (\nabla \times \mathbf{B}) - \nabla(\mathbf{A} \cdot \mathbf{B}) + (\mathbf{A} \cdot \nabla)\mathbf{B} + (\mathbf{B} \cdot \nabla)\mathbf{A}, \tag{3.48}$$

$$-\mathbf{B} \times (\nabla \times \mathbf{B}) = \mathbf{B} \times (\nabla \times \mathbf{B}) - \nabla(\mathbf{B} \cdot \mathbf{B}) + (\mathbf{B} \cdot \nabla)\mathbf{B} + (\mathbf{B} \cdot \nabla)\mathbf{B}. \tag{3.49}$$

Now using the identity given by Equation 3.32, we get

$$-2\mathbf{B} \times (\nabla \times \mathbf{B}) = -\nabla(\mathbf{B} \cdot \mathbf{B}) + 2\nabla \cdot (\mathbf{B}\mathbf{B}), \tag{3.50}$$

$$-\mathbf{B} \times (\nabla \times \mathbf{B}) = -\nabla \left(\frac{B^2}{2} \right) + \nabla \cdot (\mathbf{B}\mathbf{B}). \tag{3.51}$$

Substituting Equation 3.51 in Equation 3.47 and taking the curl on both sides leads to the induction equation

$$\frac{\partial \mathbf{B}}{\partial t} = \nabla \times (\mathbf{v} \times \mathbf{B}) - \frac{\delta_i}{L} \nabla \times \nabla \cdot \mathbf{B}\mathbf{B} \ . \tag{3.52}$$

For an incompressible flow, casting the above equation in the flux conservative form follows

$$\frac{\partial \mathbf{B}}{\partial t} + \nabla \cdot \mathbf{v}\mathbf{B} = \nabla \cdot \mathbf{B}\mathbf{v} - \frac{\delta_i}{L} \nabla \times \nabla \cdot \mathbf{B}\mathbf{B} \ . \tag{3.53}$$

Because the Hall term enters the induction equation as the curl of $\nabla \cdot \mathbf{B}\mathbf{B}$, it can

be judiciously updated and combined with the standard induction forcing, whenever the magnetic field is updated (i.e., before Equation 3.43 and Equation 3.46). In the current implementation, it enters the explicit (lagged) counterpart of the induction force and is updated after the inversion of the implicit evolutionary form of the induction equation in the "magnetic" block.

3.4 Implicit Large Eddy Simulation (ILES)

As discussed above, EULAG MHD is based on MPDATA advection scheme. Notably, the higher-order truncation terms of MPDATA provide an implicit turbulence model (Domaradzki et al., 2003; Margolin et al., 2006) and hence, allow to conduct large eddy simulations (LESs) without using explicit subgrid model (Smolarkiewicz & Prusa, 2002; Domaradzki et al., 2003; Domaradzki & Radhakrishnan, 2005; Rider, 2006; Prusa et al., 2008). Contrary to the typical LESs which filter out the under-resolved scales by employing explicit subgrid-scale models, MPDATA utilizes the residual dissipation—intermittent and adaptive to the generation of under-resolved scales—to filter out the under-resolved scales. The residual dissipation in MPDATA is produced via numerics which mimic the action of explicit subgrid-scale turbulence models. Such computations that rely on the characteristics of nonoscillatory numerics are named as implicit large eddy simulations (ILESs) in the literature. An extensive review on ILES along with various examples is given in the work published by Grinstein et al. (2007), including applications to local and global solar/stellar convection.

Under-resolved scales are recognized as the location of reconnection in a simulation having a fixed grid resolution. These under-resolved scales are then removed by MPDATA which generates locally effective residual dissipation, sufficient to preserve the monotonicity of solution. The residual dissipation, as discussed above, makes it easier for the model to execute ILESs since it is intermittent and adaptive. Such ILESs conducted using the model have already been successfully used to simulate typical solar cycles (Ghizaru et al., 2010), with the rotational torsional oscillations afterward described and investigated in (Beaudoin et al., 2013). The simulations performed with EULAG MHD continue to rely on the efficacy of ILES

in regulating the onset of magnetic reconnections, consistent and collocated with the reconnection sites (Kumar et al., 2013, 2015a; Kumar & Bhattacharyya, 2016).

3.5 Summary

To summarize, in this Chapter, the important features of the EULAG MHD model such as the MPDATA advection scheme and its dissipative property (ILES nature) have been discussed in detail. EULAG MHD is based on (at least) second-order accurate (both in space and time) nonoscillatory forward-in-time advection scheme MPDATA. The MPDATA basically utilizes the donor-cell scheme in an iterative manner to improve the accuracy of the solution while preserving the properties of the donor-cell scheme. The derivation of MPDATA along with its important aspects relevant to our calculations has been discussed in detail. Then, the numerics of EULAG MHD are discussed. The model employs an established framework of EULAG with an additional magnetic block to solve the induction equation. Notably, the proven property of MPDATA to produce locally adaptive residual dissipations in response to the generation of under-resolved scales facilitates the numerical model to carry out computations in the spirit of implicit large eddy simulations. Our development of a 3D HMHD solver by incorporating the Hall forcing term in the numerical model EULAG MHD capitalizes on the aforementioned property of the model.

Our reliance on EULAG MHD is based on its successful use in the simulation of solar coronal transients *viz.* flares and jets whereby the physical reconnections are mimicked using the residual dissipation of under-resolved scales at the locations of steep gradients. Away from steep gradients, the flux-freezing is satisfied to the high fidelity. Since the Hall effect plays a key role only at the locations where the gradients in the magnetic field are strong, therefore the Hall term is incorporated in the model such that it is tied with the dissipation scale (of the order of spatial stepsize in the model). Thus, the Hall term is incorporated in the induction equation as an explicit forcing term which is solved using the standard MHD integrator discussed in this Chapter. This 3D HMHD solver is benchmarked in Chapter 4 and further used to numerically simulate the Hall effect on the evolution

of magnetic flux ropes in Chapter 5 and an actual flaring active region in Chapter 6.

Chapter 4

Benchmarking the 3D HMHD solver

4.1 Introduction

With the EULAG MHD being extended to include the Hall effect in the previous Chapter, the aim of this Chapter is to benchmark the developed 3D HMHD solver toward the known properties of Hall-assisted reconnection including the following:

- out-of-reconnection plane magnetic field component generation,
- in-plane current generation,
- sharp changes in the current density rate,
- magnetic energy dissipation unaffected by Hall forcing.

Traditionally, the Hall MHD models are benchmarked against the known initial conditions involving either the Harris current sheet ($B_x = B_0 \tanh(z/\lambda), B_y = B_z = 0$) or the GEM challenge (described in Section 1.7), requiring very large spatiotemporal resolutions (spatial grid points $\geq (10^3)$ and $\Delta t \approx \mathcal{O}(10^{-5})$). Such high-resolution computations are beyond our computational resources at present. Consequently, we adopt an alternative approach by selecting a simple initial condition consisting of a unidirectional sinusoidal magnetic field with associated initial non-zero Lorentz force. In this case, sharp magnetic field gradients are not present initially but they develop gradually as the Lorentz force pushes the plasma. The

developed 3D EULAG HMHD numerical model has been employed to simulate the evolution of magnetic field lines in the presence and absence of Hall forcing term (i.e., Hall MHD and MHD, respectively). It solves the dimensional set of Hall MHD and MHD equations in cgs units invoked in Section 4.2. The magnetic reconnections in both the simulations are compared to investigate the Hall effect. It is well known that the Hall effect introduces two types of waves, namely whistler and Hall drift (Huba, 2003). In this Chapter, we also discuss wave modes in the framework of the HMHD version of EULAG.

4.2 Numerical Model

The two sets of numerical experiments presented in this Chapter use a dimensional and dimensionless set of equations which we describe in this section. The numerical experiment to benchmark the 3D EULAG HMHD solver solves the dimensional equations while the wave exploration experiment utilizes the dimensionless equations. Using a conservative flux form and dyadic notation, the dimensional incompressible Hall MHD equations are compactly written (in cgs units) as

$$\frac{\partial \mathbf{v}}{\partial t} + \nabla \cdot \mathbf{vv} = -\nabla\phi + \frac{1}{4\pi\rho_0}\nabla \cdot \mathbf{BB} + \boldsymbol{\nu}\nabla^2\mathbf{v} \ , \tag{4.1}$$

$$\frac{\partial \mathbf{B}}{\partial t} + \nabla \cdot \mathbf{vB} = \nabla \cdot \mathbf{Bv} - \frac{d_0}{4\pi}\left(\nabla \times \nabla \cdot \mathbf{BB}\right) - \nabla\phi^* \ , \tag{4.2}$$

$$\nabla \cdot \mathbf{v} = 0 \ , \tag{4.3}$$

$$\nabla \cdot \mathbf{B} = 0 \ , \tag{4.4}$$

where ρ_0 and $\boldsymbol{\nu}$ denote constant density and kinematic viscosity respectively, $\phi = \left(p + \mathbf{B}^2/8\pi\right)/\rho_0$ is the density normalized total pressure, and $d_0 = \sqrt{4\pi}\delta_i/\sqrt{\rho_0}$; the $-\nabla\phi^*$ term on the right-hand side is already explained in Section 3.3.1.
The dimensionless equations

$$\frac{\partial \mathbf{v}}{\partial t} + \nabla \cdot \mathbf{vv} = -\nabla\phi + \nabla \cdot \mathbf{BB} + \frac{\tau_A}{\tau_\nu}\nabla^2\mathbf{v} \ , \tag{4.5}$$

$$\frac{\partial \mathbf{B}}{\partial t} + \nabla \cdot \mathbf{vB} = \nabla \cdot \mathbf{Bv} - \frac{\delta_i}{L_0}\left(\nabla \times \nabla \cdot \mathbf{BB}\right) - \nabla\phi^* \ , \tag{4.6}$$

$$\nabla \cdot \mathbf{v} = 0 \ , \tag{4.7}$$

$$\nabla \cdot \mathbf{B} = 0 \ , \tag{4.8}$$

are achieved using the following normalizations used in Equation 4.1 - 4.4

$$\mathbf{B} \longrightarrow \frac{\mathbf{B}}{B_0}, \quad \mathbf{v} \longrightarrow \frac{\mathbf{v}}{v_A}, \quad L \longrightarrow \frac{L}{L_0}, \quad t \longrightarrow \frac{t}{\tau_A}, \quad p \longrightarrow \frac{p}{\rho {v_A}^2} \ , \tag{4.9}$$

The ratio τ_A/τ_ν is an effective viscosity of the system which, along with the other forces, influences the magnetofluid evolution. The constant B_0 is kept arbitrary, whereas L_0 is fixed to the system size. Further, $v_A \equiv B_0/\sqrt{4\pi\rho_0}$ is the Alfvén speed, where ρ_0 is a constant mass density. The τ_A and τ_ν are respectively the Alfvén transit time ($\tau_A = L_0/v_A$) and viscous diffusion time scale ($\tau_\nu = L_0^2/\nu$). The kinematic viscosity is denoted by ν. The equations are numerically integrated using the 3D HMHD solver and the model assumes the magnetofluid to be thermodynamically inactive and incompressible, having zero physical resistivity.

4.3 Results

4.3.1 Benchmarking the 3D HMHD solver

To benchmark the HMHD solver, the initial field is selected as

$$\mathbf{B} = 2.5 \sin(x) \hat{\mathbf{z}} \ , \tag{4.10}$$

with $x, y, z \in [-2\pi, 2\pi]$ cm, respectively, in each direction of a 3D Cartesian domain. This selection has two merits: first, the magnetic field reverses at x=0; and second, the Lorentz force

$$(\mathbf{J} \times \mathbf{B}) = -6.25 \cos(x) \sin(x) \, \hat{\mathbf{x}} \ , \tag{4.11}$$

generates a converging flow that onsets magnetic reconnections.

Equations 4.1-4.4 are solved for $d_0 = 0,\ 2$ cm g$^{-1/2}$*. The latter selection of d_0 optimizes the computation time and a tractable development of magnetic structures for the employed spatiotemporal resolution. The corresponding $\delta_i = 0.56$ cm is slightly higher than the spatial stepsize $\delta\mathbf{x} \approx 0.40$ cm set for the simulation. Consequently, the Hall forcing kicks in near the dissipation scale, thereby

*Hereafter, we drop the units of d_0 in discussions to avoid repetition.

directly affecting the overall dynamics only in the vicinities of the reconnection regions. With the large-scale $L = 4\pi$ cm of the magnetic field variability, the resulting $\delta_i/L \approx 0.04$ is of the order of solar coronal value. The simulations are then expected to capture the dynamics of the Hall MHD and the intermittently diffusive regions of corona-like plasmas, thus shedding light on the evolution of neighboring frozen-in magnetic field lines. Moreover, $1/S < \delta_i/L$ as discussed in the Introduction. The physical domain is resolved with a $32 \times 32 \times 32$ grid. A coarse resolution is selected for an earlier onset of magnetic reconnections and to expedite the overall evolution. The kinematic viscosity and mass density are set to $\nu = 0.005$ cm^{2}s^{-1} and $\rho_0 = 1$ g, respectively. All three boundaries are kept open. The initial magnetic field is given by Equation 4.10 and the fluid is evolved from an initially static state having zero pressure.

The overall evolution is depicted in different panels of Figure 4.1. The initial Lorentz force, given by Equation 4.11, pushes segments of the fluid on either side of the field reversal layers—toward each other. Consequently, magnetic energy gets converted into kinetic energy of the plasma flow: panels (a) and (b). Panels (c) and (d) show the history of grid-averaged magnitude of the out-of-plane (along y) and in-plane (xz plane) magnetic fields. Notably, for $d_0 = 0$ (MHD) the out-of-plane field is negligibly small compared to its value for $d_0 = 2$ (Hall MHD). Such generation of the out-of-plane magnetic field is inherent to Hall MHD and is in conformity with the result of another simulation (Ma & Bhattacharjee, 2001). Panels (e) and (f) illustrate the variation of the rate of change of out-of-plane current density and total volume current density. Importantly, in contrast to the $d_0 = 0$ curve, the rate of change of volume current density shows an early bump at ($\approx$ 7.5 s) and a well-defined peak ($t \approx 9.75$ s) for $d_0 = 2$. Such peaks in the current density are expected in the impulsive phase of solar flares, and they manifest magnetic reconnections in the presence of the Hall term (Bhattacharjee, 2004).

Figure 4.2 plots magnetic field lines tangential to pre-selected planes during different instances of the evolution for $d_0 = 0$. Panel (a) plots the initial magnetic field lines for reference. The initial Lorentz force pushes anti-parallel magnetic field lines (depicted in the inset) toward each other. With time, two counter-

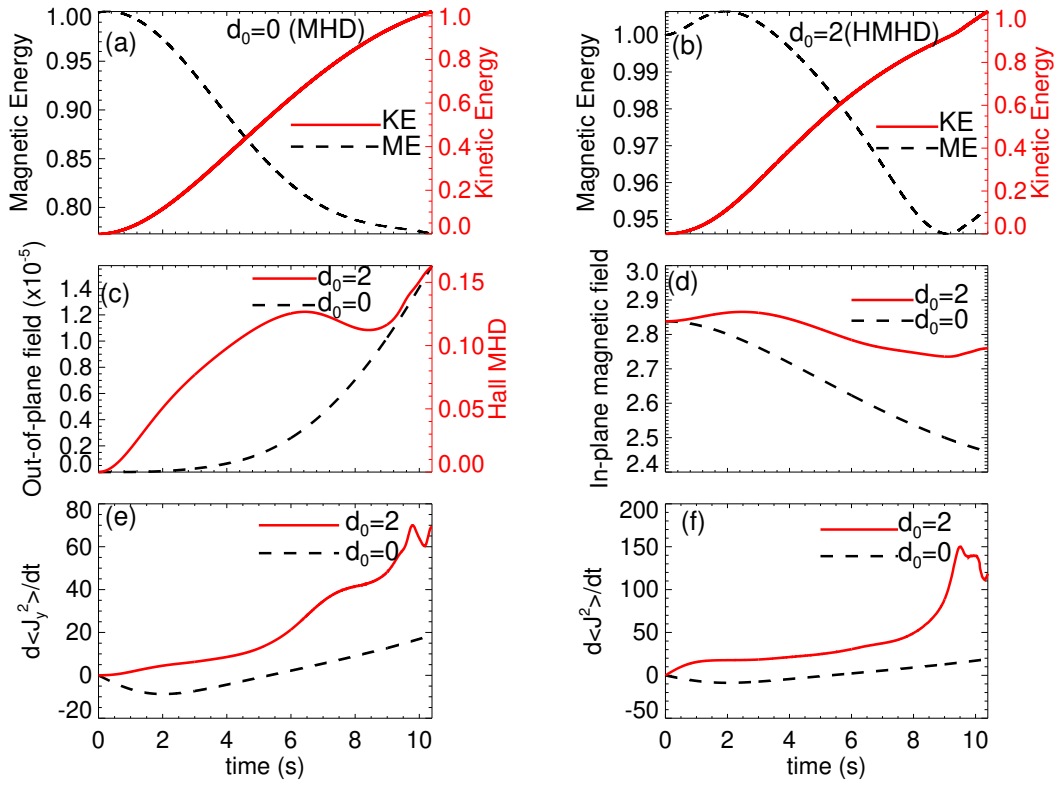

Figure 4.1: Panels (a) and (b) show the evolution of the magnetic energy (black dashed curve) and kinetic energy (red solid curve) for $d_0 = 0$ (MHD) and $d_0 = 2$ (Hall MHD) respectively. Panel (c) shows the evolution of the out-of-plane magnetic field for $d_0 = 0$ (MHD) with a black dashed curve and $d_0 = 2$ (Hall MHD) with a red solid curve respectively. Also in panels (a) to (c), the scales for the solid and the dashed curves are spaced on the right and left respectively. Panels (d) to (f) represent the in-plane magnetic field, amplitudes of the rate of change of out-of-plane, and total current densities for $d_0 = 0$ (black dashed curve) and $d_0 = 2$ (red solid curve) respectively. The variables in panels (a) and (b) are normalized with the initial total energies. All the variables are averaged over the computational domain. Important is the generation of the out-of-plane magnetic field along with sharp changes in time derivatives of the out-of-plane and total volume current densities in Hall MHD simulation.

rotating vortices develop on each side of the polarity reversal line (see Figure 4.3). As a result, two segments of the oppositely directed field lines approach each other while another two segments of the same field lines recede from each other—generating the X-type neutral points near $z = \pm 2\pi$. The consequent magnetic reconnections generate a complete magnetic island which maintains its identity beyond $t = 10$ s. Such islands, stacked on each other along the y, generate an extended magnetic flux tube (MFT) at the center, which in its generality is a magnetic flux surface. Further evolution breaks the MFT such that the cross-section of the broken tube yields two magnetic islands. The point of contact

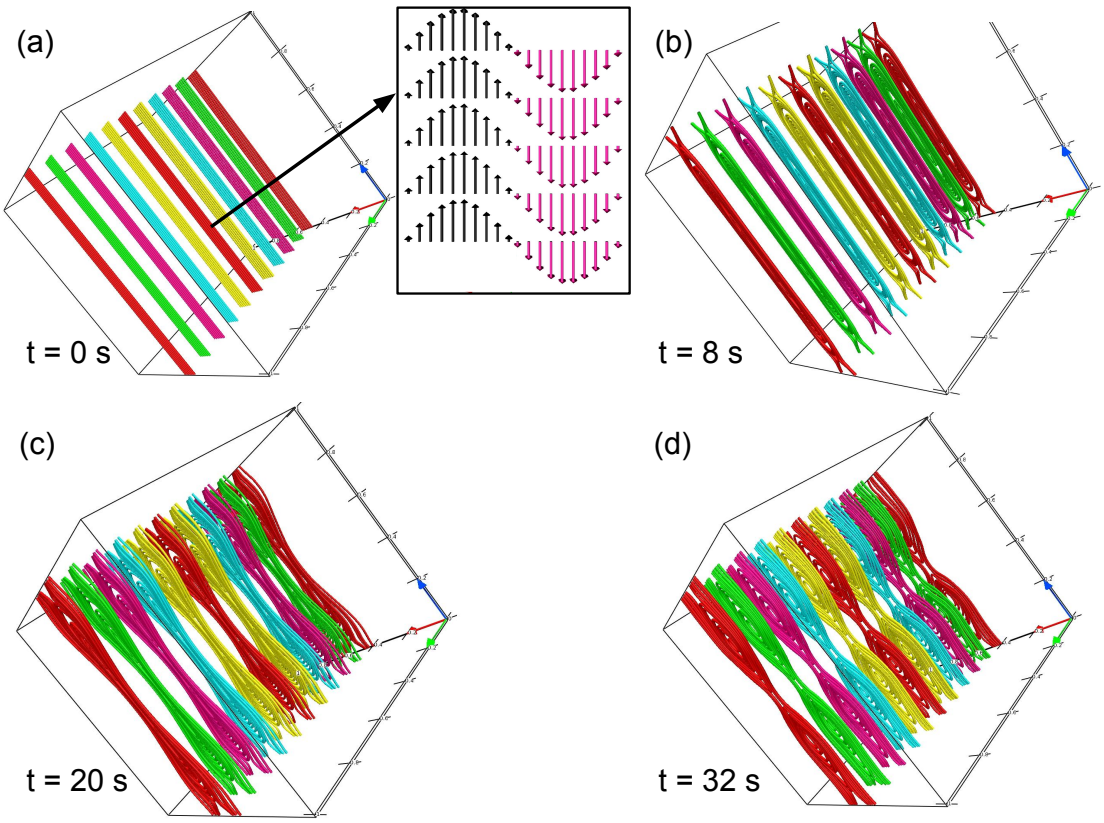

Figure 4.2: Snapshots of preselected magnetic field lines for the $d_0 = 0$ (MHD) simulation, plotted on equidistant y-constant planes. In all figures (this and hereafter), the red, green, and blue arrows represent the $x-$, $y-$, and $z-$axis respectively. The inset in panel (a) highlights the polarity reversal of the initial magnetic field vectors (arrows depict the direction and the length of the arrows depict the magnitude of vectors). The plots illustrate the formation of a primary flux tube (panel (b)) made by stacking of the depicted magnetic field lines. Notably, symmetry is preserved throughout evolution.

between the two tear-drop-shaped magnetic field lines generates an X-type neutral point. Notably, within the computational time, no field is generated along the y direction and the corresponding symmetry is exactly preserved.

In Figure 4.4 we provide the 2D projection of the magnetic field lines on the $y = 0.5$ plane, for later comparison with a similar projection for the $d_0 = 2$ case.

The panels (a) to (b) and (c) to (d) of Figure 4.5 show magnetic field lines evolution for $d_0 = 2$ from two different vantage points.

The field lines are plotted on different $y-$constant planes centered at $x = 0.5$ and $x = 0.74435$. The planes are not connected by any field lines at $t = 0$. Importantly the out-of-plane magnetic field is generated with time in both sets of field lines (at $x = 0.5$ and $x = 0.74435$), which connects two adjacent planes (cf. panel

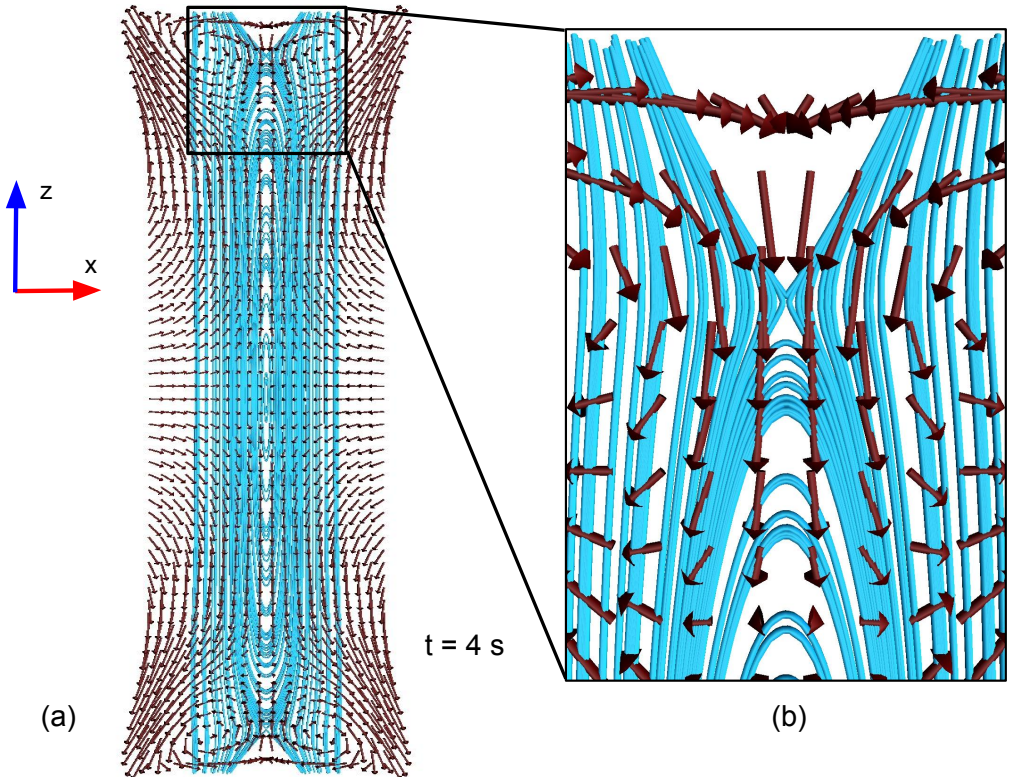

Figure 4.3: Velocity flow vectors (panel (a)) profile to form the X-type geometry of reconnection. Panel (b) shows the zoomed view of the region marked in the black box (panel (a)).

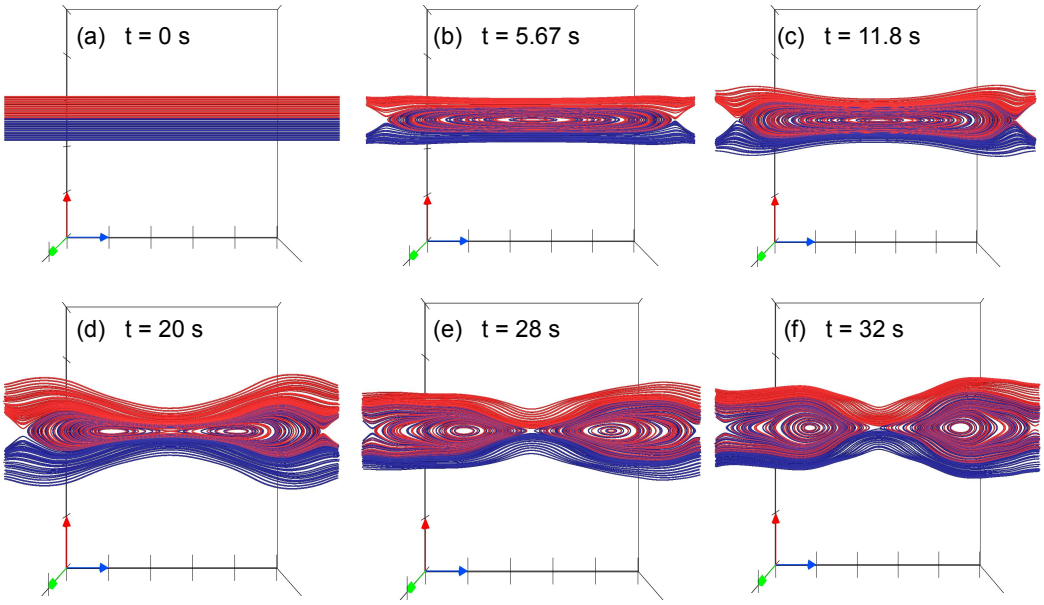

Figure 4.4: Projection of magnetic field lines depicted in Figure 4.2 on a $y-$constant plane during their evolution. Notable is the formation of a primary magnetic island having a single O-type neutral point. Subsequently, the primary island breaks into two secondary islands which are separated by an X-type neutral point.

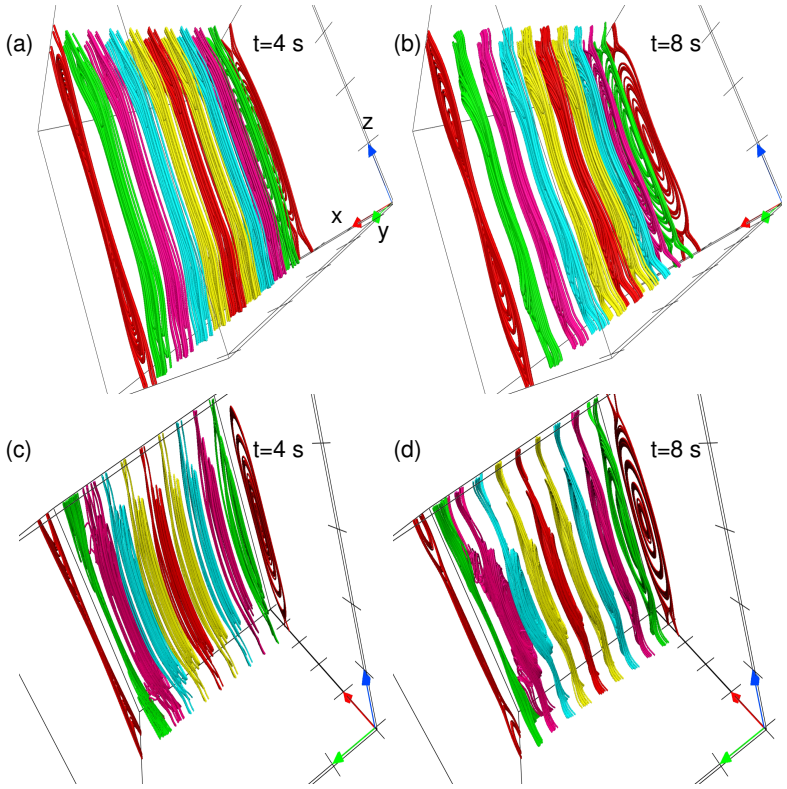

Figure 4.5: Magnetic field lines evolution for $d_0 = 2$ (Hall MHD) case, from two vantage points. The field lines are plotted on planes centered at $x = 0.5$ and $x = 0.74435$ and equidistant along y. Important is the symmetry breaking, cf. field lines at $y = -2\pi$ and $y = 2\pi$ of the panel (b) and (d). The out-of-plane magnetic field is generated throughout the domain.

(b) of Figure 4.2 and Figure 4.5 and breaks the y symmetry that was preserved in the $d_0 = 0$ case—asymmetry in reconnection planes. Consequently, the evolved $\mathbf{B}$ is three-dimensional. Also, the out-of-plane component (B_y) has a quadrupole structure, shown in Figure 4.6, which is in congruence with observations and models (Mozer et al., 2002).

For better clarity, the magnetic field lines evolution is further detailed in Figure 4.7 and Figure 4.8. In Figure 4.7, important is the development of two MFTs constituted by disjointly stacked magnetic islands. The islands are undulated and appear much earlier compared to the $d_0 = 0$ case, indicating the faster reconnection. Notable is also the creation of flux ropes where a single helical field line makes a large number of turns as the out-of-plane field B_y develops (Figure 4.8). In principle, the magnetic field line may ergodically span the MFS, if the "safety factor" $q = rB_y/\mathcal{L}B_T$ is not a rational number (Freidberg, 1982); here r and $\mathcal{L}$ are the radius and length of the rope, respectively, and $B_T = \sqrt{B_x^2 + B_y^2}$. Fur-

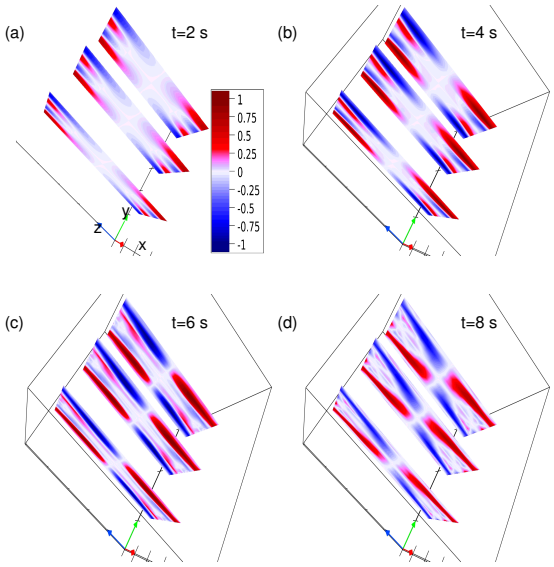

Figure 4.6: Contour plots of $B_y(x, z)$ (out-of-plane component) on y-constant planes for $d_0 = 2$ (Hall MHD), with time. The plots confirm the quadrupolar nature of the out-of-plane component of the magnetic field.

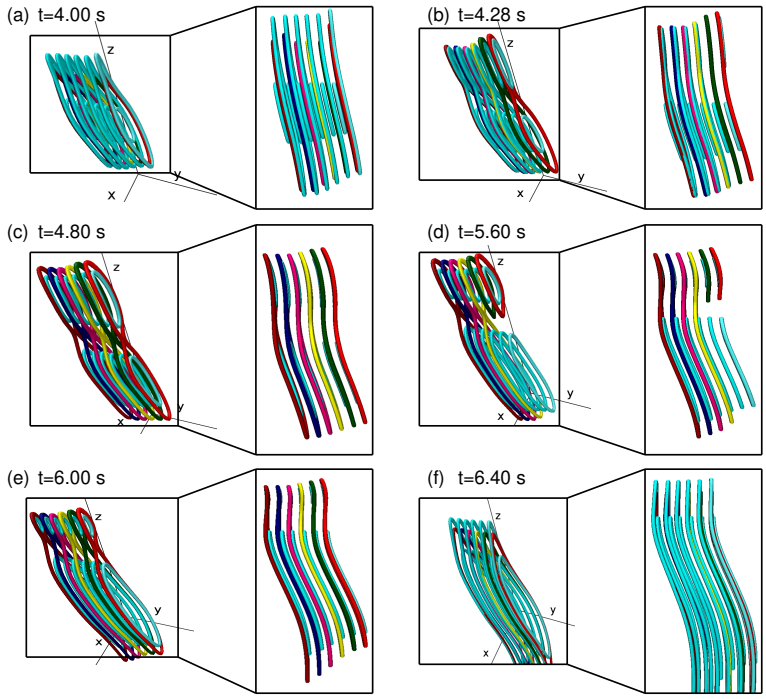

Figure 4.7: Panels (a) to (f) show the magnetic field lines evolution for $d_0 = 2$ (Hall MHD) case, from two different angles to highlight the generation of two MFTs constituted by disjoint field lines. The islands look like "figure 8" structure; Panels (b) to (d). The side views of the field lines are shown in the insets, highlighting their undulated geometry. The three black lines in the background represent the three axes.

ther evolution breaks the flux rope into secondary ropes by internal magnetic reconnections—i.e., reconnections between magnetic field lines constituting the

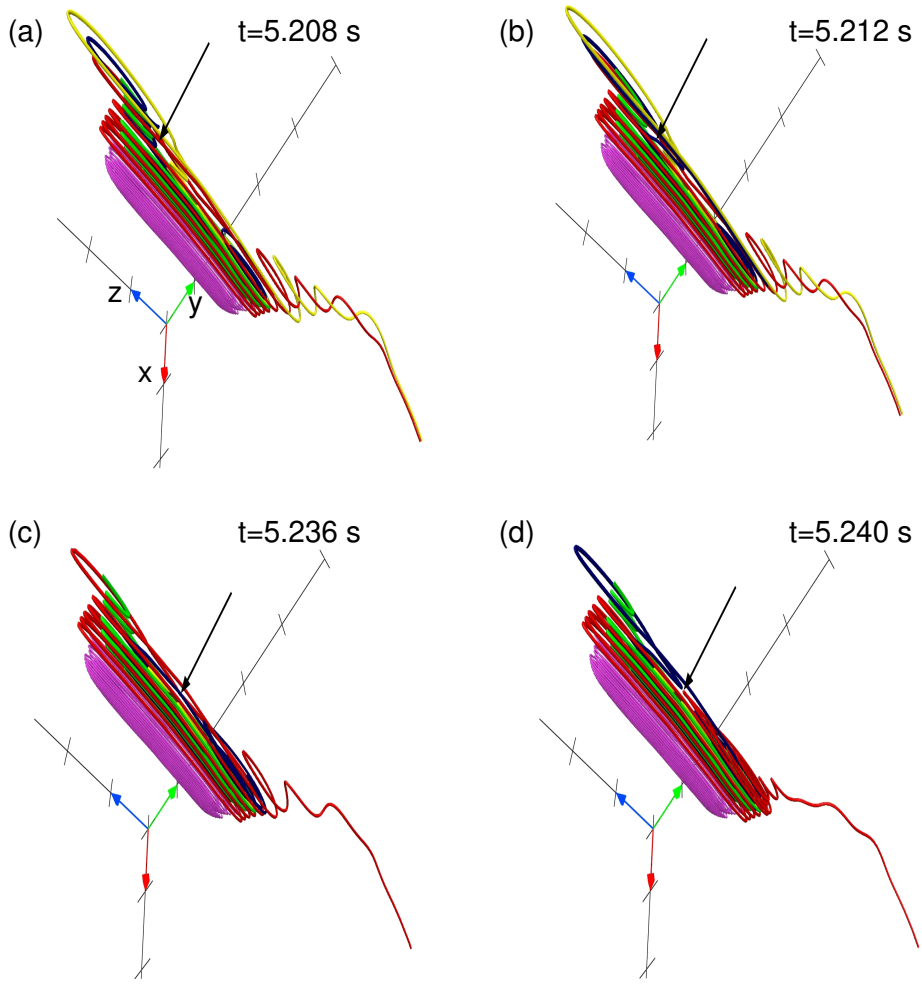

Figure 4.8: Panels (a) and (b) show the topology of the magnetic field lines for the $d_0 = 2$ (Hall MHD) evolution, prior to and after the internal reconnection of the dark blue colored field line (marked by the arrow). Panels (c) and (d) depict the topology of field lines prior to and after the internal reconnection of blue and red color field lines within the rope, marked by the arrow.

rope—shown in panels (a) to (d) of Figure 4.8, where two oppositely directed sections of the given magnetic field lines reconnect (location marked by arrows in the Figure 4.8). Since most of the contemporary Hall simulations are in 2D, in Figure 4.9 we plot the projection of field lines depicted in Figure 4.5 on $y = 0.5$ plane. The corresponding evolution is visibly similar to the generation of secondary islands (Shi et al., 2019), and their later coalescence as envisioned by Shibata & Tanuma (2001).

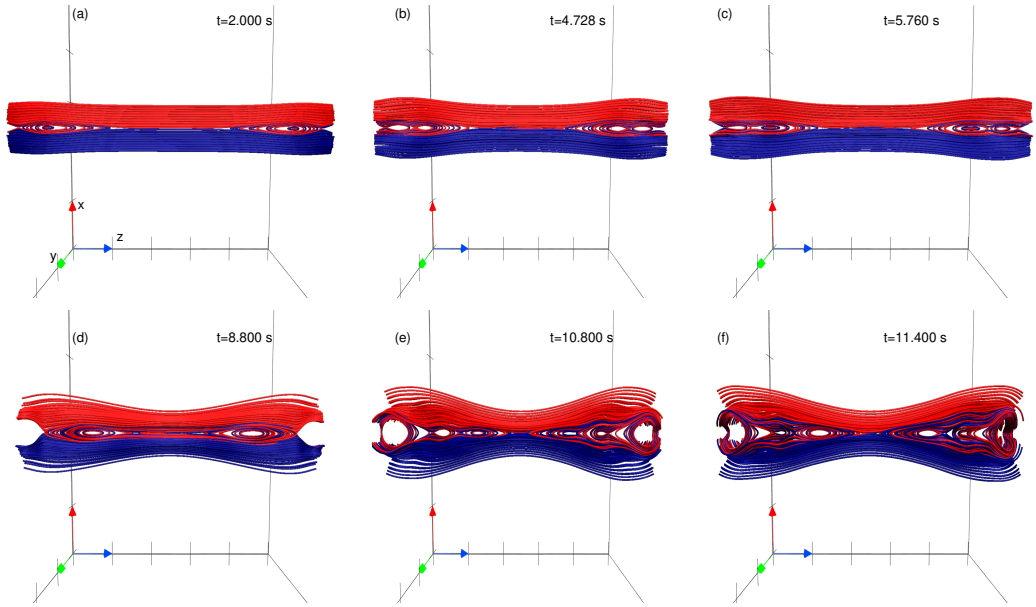

Figure 4.9: Magnetic field lines evolution for $d_0 = 2$ (Hall MHD), projected on y constant plane. Panel (a) depicts the development of two primary magnetic islands. Panels (b) and (c) show their further breakage into secondary islands. Panels (d) to (f) show the field lines evolution toward the generation of an X-type geometry at the center by $t = 11.4$ s (panel (f)). The central X-type is formed as a result of the subsequent merging of the two islands (innermost in panels (e) and (f)) heading toward each other.

4.3.2 Investigation of the whistler wave modes using the 3D HMHD solver

The addition of the Hall term in the standard MHD introduces modified wave modes in the system, namely whistler and Hall drift wave (Huba, 2003). These wave modes can be derived through the linearization of the magnetic induction equation. Following Huba (2003), the induction equation can be written as

$$\frac{\partial \mathbf{B}}{\partial t} = -\frac{1}{ne}\nabla \times (\mathbf{J} \times \mathbf{B}) + \frac{1}{n^2 e}\nabla n \times (\mathbf{J} \times \mathbf{B}) \ , \tag{4.12}$$

to identify each wave mode. The first term on the right-hand side of Equation 4.12 gives the whistler wave mode while the second term gives the Hall drift mode. Noticeably, the Hall drift wave can only exist in the inhomogeneous plasma (since $\nabla n \neq 0$). However, the developed HMHD solver being incompressible and assuming plasma to be homogeneous, the Hall drift mode can not be explored and we only concentrate on the whistler modes.

To complete the benchmarking, we repeat the numerical experiment described in Huba (2003), where wave propagation in the presence of the Hall forcing is explored. Let us consider the induction equation in its dimensionless form

$$\frac{\partial \mathbf{B}}{\partial t} = -\frac{\delta_i}{L_0}\nabla \times (\mathbf{J} \times \mathbf{B}) \ ,$$

which can also be written as

$$\frac{\partial \mathbf{B}}{\partial t} = -\frac{\delta_i}{L_0}\nabla \times ((\nabla \times \mathbf{B}) \times \mathbf{B}) \ , \tag{4.13}$$

Now assuming that the time-independent ambient magnetic field is in the z direction and the perturbations are along x and y directions, we have

$$\mathbf{B} = \delta\boldsymbol{\mathcal{B}} + \boldsymbol{\mathcal{B}}_{\boldsymbol{z}}$$

where $\delta\boldsymbol{\mathcal{B}} = \delta B_x\hat{\boldsymbol{i}} + \delta B_y\hat{\boldsymbol{j}}$ and $\boldsymbol{\mathcal{B}}_{\boldsymbol{z}} = B_0\hat{\boldsymbol{k}}$.
A first-order linear analysis yields

$$\frac{\partial(\delta\boldsymbol{\mathcal{B}})}{\partial t} = -\frac{\delta_i}{L_0}\nabla \times [(\nabla \times \delta\boldsymbol{\mathcal{B}}) \times \boldsymbol{\mathcal{B}}_{\boldsymbol{z}}] \ , \tag{4.14}$$

since

$$\nabla \times \delta\boldsymbol{\mathcal{B}} = -\hat{\boldsymbol{i}}\frac{\partial \delta B_y}{\partial z} + \hat{\boldsymbol{j}}\frac{\partial \delta B_x}{\partial z} \ ,$$

and

$$(\nabla \times \delta\boldsymbol{\mathcal{B}}) \times \boldsymbol{\mathcal{B}}_{\boldsymbol{z}} = \hat{\boldsymbol{j}}B_0\frac{\partial \delta B_y}{\partial z} + \hat{\boldsymbol{i}}B_0\frac{\partial \delta B_x}{\partial z} \ .$$

The right-hand side of Equation 4.14 can be expressed by taking the curl of the above equation

$$\nabla \times [(\nabla \times \delta\boldsymbol{\mathcal{B}}) \times \boldsymbol{\mathcal{B}}_{\boldsymbol{z}}] = -\hat{\boldsymbol{i}}B_0\frac{\partial^2 \delta B_y}{\partial z^2} + \hat{\boldsymbol{j}}B_0\frac{\partial^2 \delta B_x}{\partial z^2} \ .$$

Now Equation 4.14 can be written as

$$\frac{\partial(\delta\boldsymbol{\mathcal{B}})}{\partial t} = -\frac{\delta_i}{L_0}\left(-\hat{\boldsymbol{i}}B_0\frac{\partial^2 \delta B_y}{\partial z^2} + \hat{\boldsymbol{j}}B_0\frac{\partial^2 \delta B_x}{\partial z^2}\right) \ .$$

The magnetic field perturbation is assumed to be a plane wave, with δB_x and

$\delta B_y \propto \exp(ik_z z - i\omega t)$, then $\frac{\partial}{\partial t} \rightarrow i\omega$, $\nabla_z \rightarrow (-ik_z)$ and ${\nabla_z}^2 \rightarrow -{k_z}^2$.

$$i\omega \left(\delta B_x \hat{\boldsymbol{i}} + \delta B_y \hat{\boldsymbol{j}}\right) = -\frac{\delta_i}{L_0}\left(\hat{\boldsymbol{i}} B_0 {k_z}^2 \delta B_y - \hat{\boldsymbol{j}} B_0 {k_z}^2 \delta B_x\right) \ , \tag{4.15}$$

$$\omega \delta B_x = i\frac{\delta_i}{L_0} B_0 {k_z}^2 \delta B_y \ , \tag{4.16}$$

$$\omega \delta B_y = -i\frac{\delta_i}{L_0} B_0 {k_z}^2 \delta B_x \ , \tag{4.17}$$

$$\omega^2 = -i^2 \left(\frac{\delta_i}{L_0}\right)^2 {B_0}^2 {k_z}^4 \ , \tag{4.18}$$

Finally, the dimensionless dispersion relation of the whistler wave is obtained as

$$\boxed{\omega = \left(\frac{\delta_i}{L_0}\right) B_0 {k_z}^2}$$

Following Huba (2003), the ambient field is set up as

$$B_z = B_0 \ , \tag{4.19}$$

whereas the perturbations are

$$\delta B_x = \delta B_0 \sin\left(\frac{2\pi m z}{L_0}\right) \ , \tag{4.20}$$

$$\delta B_y = \delta B_0 \cos\left(\frac{2\pi m z}{L_0}\right) \ , \tag{4.21}$$

where L_0 is the size of the system which is set equal in all three directions x, y, and z of a Cartesian coordinate system, and m is the wave mode number. According to the perturbation expressions Equation 4.21, the total length (L_z) on each plane in the computational domain will satisfy $L_z = m\lambda$. The parameters set for simulation are $B_0 = 1000$, $\delta B_0 = 10$, and $L_0 = 7\pi$. The simulations are carried out on a computational domain of size $128 \times 128 \times 128$ and the dimensionless Hall MHD equations are employed. The analytical wave propagation number is given by $k_z^A = \frac{2\pi m}{L_0}$ and the numerical wave propagation number is given by $k_z^N = \frac{2\pi}{\lambda_N}$. λ_N is the wavelength—twice the distance between two consecutive nodes ($\Delta z = z_2 - z_1$)—calculated from the simulation outcomes as depicted in Figure 4.10, Figure 4.11, and Figure 4.12. The analytical and the numerical frequencies obtained for a few

modes are listed in Table 4.1, confirming the simulations to replicate the analytical calculations fairly well.

m	Analytical frequency (ω_A)	Numerical frequency (ω_N)
2	26.12	27.50
3	132.237	141.88
4	417.92	430.04

Table 4.1: Estimated values of analytical and numerical frequencies for different modes.

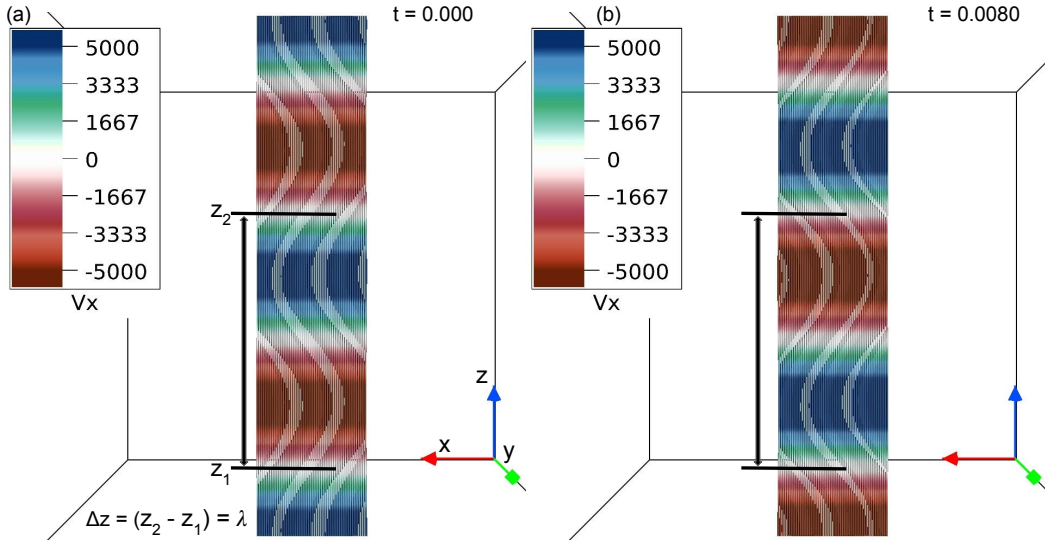

Figure 4.10: Whistler wave amplitude variation from $t = 0$ (panel (a)) to $t = 0.0080$ (panel (b)) for mode number $m = 2$. The color bar on the left-hand side depicts x component of the velocity ranging from -5000 to 5000. The length of the region between black arrows (in panels (a) and (b)), i.e., twice the distance between two consecutive nodes (white regions marked by horizontal black lines) is a wavelength λ_N. Notable is the amplitude variation from successive negative-positive (at $t = 0$) to positive-negative (at $t = 0.0080$) respectively.

Notably, the numerical frequencies are systematically higher than their analytical counterparts which can be speculated because of a systematic error in visually approximating the distance between two consecutive nodes.

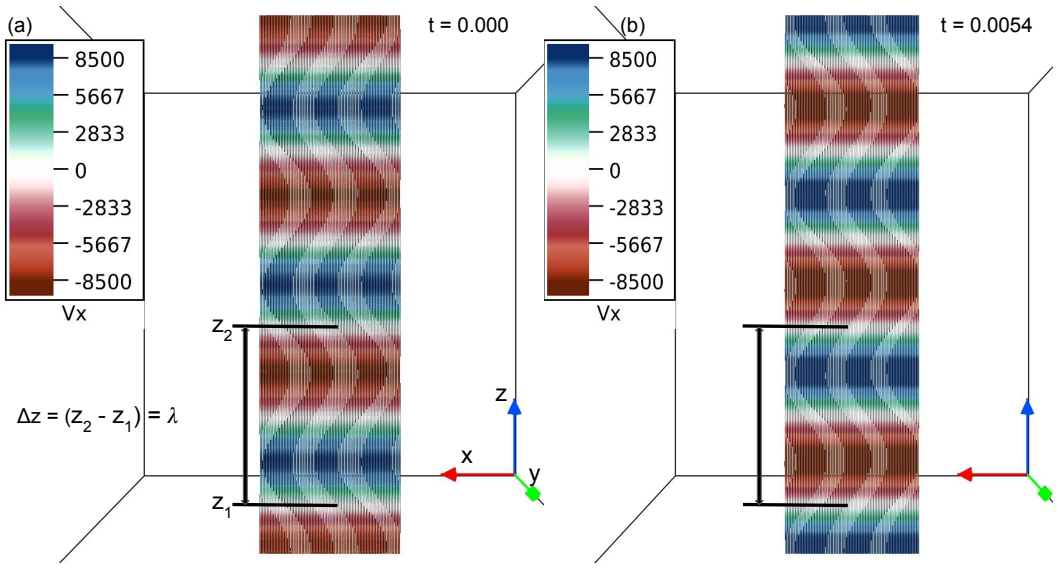

Figure 4.11: Whistler wave amplitude variation from $t = 0$ (panel (a)) to $t = 0.0054$ (panel (b)) for mode number $m = 3$. The color bar on the left-hand side depicts x component of velocity ranging from -8500 to 8500. The length of the region between black arrows (in panels (a) and (b)), i.e., twice the distance between two consecutive nodes (white regions marked by horizontal black lines) is the wavelength λ_N. Notable is the amplitude variation from successive positive-negative (at $t = 0$) to negative-positive (at $t = 0.0054$) respectively.

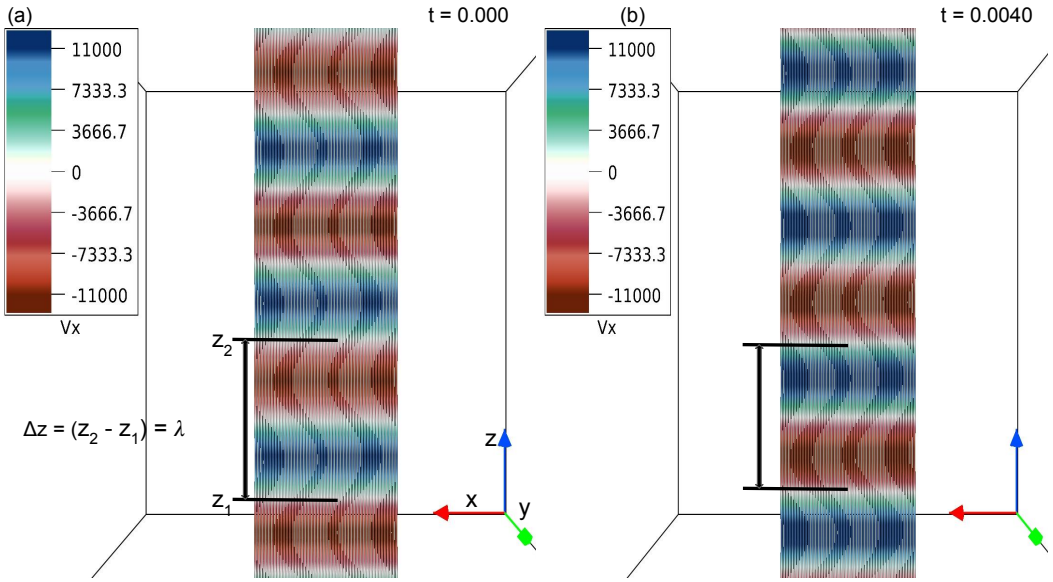

Figure 4.12: Whistler wave amplitude variation from $t = 0$ (panel (a)) to $t = 0.0040$ (panel (b)) for mode number $m = 4$. The color bar on the left-hand side depicts x component of velocity ranging from -11000 to 11000. The length of the region between black arrows (in panels (a) and (b)), i.e., twice the distance between two consecutive nodes (white regions marked by horizontal black lines) is the wavelength λ_N. Notable is the amplitude variation from successive positive-negative (at $t = 0$) to negative-positive (at $t = 0.0040$) respectively.

4.4 Summary and Conclusion

In this Chapter, the developed 3D HMHD solver has been benchmarked with an initially sinusoidal magnetic field, symmetric in the y direction of the employed Cartesian coordinate system. The choice of the field is based on its simplicity and non-force-free property to exert Lorentz force on the magnetofluid at $t = 0$. Moreover, the selected field provides an opportunity to independently verify the physics of Hall MHD without repeating the more traditional computations related to the Harris equilibrium or the GEM challenge. Simulations are carried out in the absence and presence of the Hall term. In the absence of the Hall term, the magnetic field maintains its symmetry as magnetic reconnections generate magnetic flux tubes made by disjoint magnetic field lines. With the Hall term, the evolution becomes asymmetric and 3D due to the development of a magnetic field which is directed out of the reconnection plane. This is in concurrence with earlier simulations. Along with the flux tube, magnetic reconnections also generate a magnetic flux rope in the Hall MHD. When viewed along the negative $y-$direction, the rope, and the tube appear as magnetic islands. Further evolution, leads to breakage of the primary islands into secondary islands and later, their coalescence. The results, overall, agree with the existing scenarios of Hall-reconnection based on physical arguments and other recent simulations including those on the GEM challenge. An important finding is the formation of complex 3D magnetic structures which can not be apprehended from 2D models or calculations although their projections agree with the latter. Alongside, we have numerically explored the Whistler mode propagation vis-a-vis its analytical model and found the two to be matching reasonably well.

The overall simulation results with the 3D HMHD solver give us the confidence to use it to model naturally observed magnetic structures further.

Chapter 5

Investigations of the Hall effect on magnetic reconnection during the evolution of a magnetic flux rope

5.1 Introduction

The results presented in Section 4.3.1 depict the magnetic flux rope (MFR) formation owing to the generation of an out-of-plane (reconnection plane) magnetic field component—one of the well-known features of the Hall-assisted magnetic reconnection. MFR is defined as a bundle of helically twisted magnetic field lines wrapped along a common axis (Zhong et al., 2021). MFR is often regarded as the fundamental structure associated CMEs on the Sun. There are two concepts of MFR eruption associated with CMEs; one considers the pre-existing MFR in the solar atmosphere confining the plasma material and the another assumes MFR formation as a consequence of magnetic reconnection from initially highly sheared magnetic arcades. Models based on observations and theory, such as CSHKP (Carmichael, 1964; Sturrock, 1966; Hirayama, 1974; Kopp & Pneuman, 1976), tether cutting (Moore et al., 2001) and breakout (Antiochos et al., 1999)—irrespective of their applicability to explain successful CME—suggest that magnetic reconnections beneath the MFR essentially reshape it by adding reconnected magnetic field to the envelope of MFR. In brief, the CME models require MFRs to confine the plasma. Destabilized from its equilibrium, as the MFR ascends with height—it stretches

the overlaying magnetic field lines. The ascend of the rope decreases the magnetic pressure below it which, in turn, sucks in more field lines below the rope. These non-parallel field lines reconnect and the generated outflow further pushes the MFR up. It is then imperative to study the effects of Hall forcing on such magnetic reconnections during the evolution of an MFR. For this purpose, in this Chapter, the developed 3D EULAG solver is employed to simulate the evolution of MFRs in the presence and absence of the Hall forcing. The aim of this work is to explore the topological changes owing to the Hall effect on magnetic reconnections by investigating simulated magnetic field lines dynamics and their comparison in the Hall MHD and MHD. To ascertain the MFR generation, the simulations are initiated with the initial conditions of Kumar et al. (2016). The work presented in this Chapter is mainly divided into two case studies where the first one uses an axisymmetric (2.5D) and the second one uses fully 3D initial bipolar sheared magnetic field configurations. In this Chapter, the efficient and faster reconnections along with the magnetic topological changes during the Hall MHD simulations are reported. A comprehensive analysis of reconnection-assisted MFR evolution for the two cases is presented below.

5.2 Case-I: MFR generated from a 2.5D initial analytical magnetic field

The simulations are initiated with an axisymmetric (2.5D) magnetic field given in Kumar et al. (2016)

$$B_x = k_z \sin(k_x x) \exp\left(\frac{-k_z z}{s_0}\right) , \tag{5.1}$$

$$B_y = \sqrt{k_x^2 - k_z^2} \sin(k_x x) \exp\left(\frac{-k_z z}{s_0}\right) , \tag{5.2}$$

$$B_z = s_0 k_x \cos(k_x x) \exp\left(\frac{-k_z z}{s_0}\right) , \tag{5.3}$$

with $k_x = 1.0$, $k_z = 0.9$ and $s_0 = 6$.

The dynamical evolution of the above initial field is governed by Equation 4.1 - Equation 4.4 given in Section 4.2 of the previous Chapter. The effective viscosity

and mass density are set to $\tau_A/\tau_\nu = 2\times10^{-5}$ and $\rho_0 = 1$, respectively. Equation 4.1 - Equation 4.4 are numerically integrated using the 3D HMHD solver described in Chapter 3.

The magnetic field lines are depicted in panel (a) of Figure 5.2 which are sheared bipolar loops having a straight Polarity Inversion Line (PIL) and no field-line twist. For simulations, a physical domain of the extent $[\{0, 2\pi\}, \{0, 2\pi\}, \{0, 8\pi\}]$ is resolved on the computational domain of size $64 \times 64 \times 128$, making the spatial step sizes $\delta x = \delta y = 0.0997$, $\delta z = 0.1979$. The temporal step size is $\delta t = 16\times10^{-4}$. The initial state is assumed to be motionless and open boundary conditions are employed. The simulations are carried out for $\delta_i/L_0 = 0$ and $\delta_i/L_0 = 0.04$, having a simulated physical time of $7000\tau_A\delta t$. The arbitrary B_0 can be selected such that the Alfvén transit time, $\tau_A \in \{1, 10\}$ s makes the simulated time, 11.2 s to 112 s consistent with the beginning of the impulsive phase of a flare 100 s to 1000 s.

The evolution onsets as the Lorentz force (as depicted in Figure 5.1)

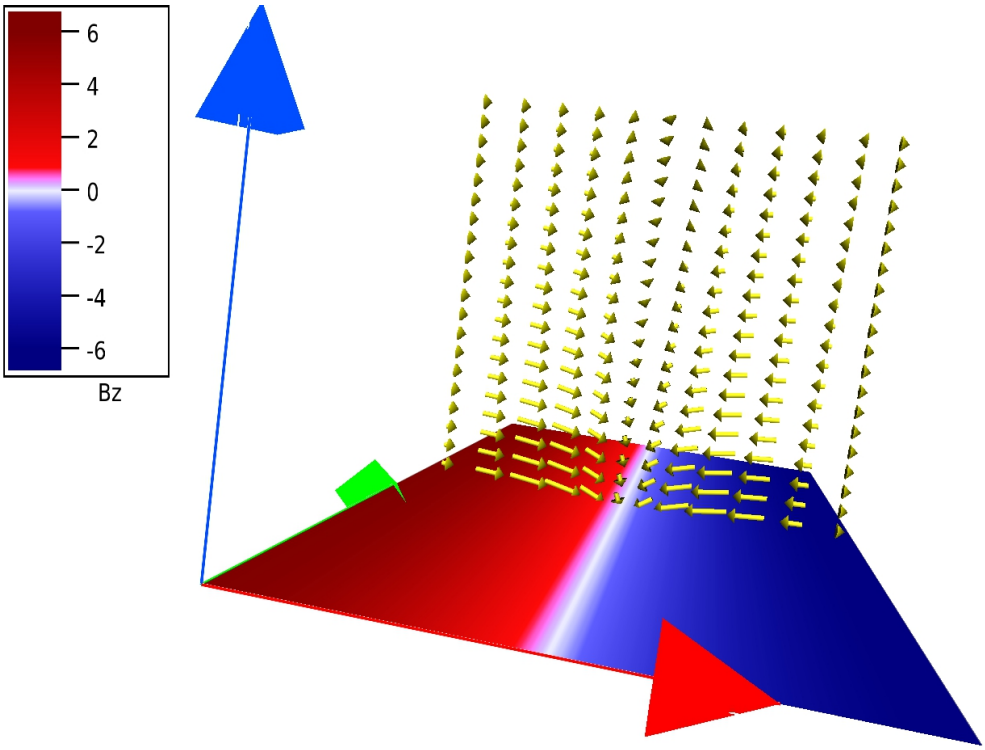

Figure 5.1: Initial Lorentz force vectors (yellow) associated with the magnetic field. Notably, due to the field being initially axisymmetric, the Lorentz force on all $y-$constant planes has the same profile at $t = 0$. Therefore, for clarity, we present the Lorentz force profile on a single $y-$constant plane at $t = 0$ here. The bottom boundary shows the value of $z-$component of the magnetic field.

$$(\mathbf{J}\times\mathbf{B})_x = \left[-k_x(k_x^2-k_z^2)+k_x s_0\left(s_0k_x^2-\frac{k_z^2}{s_0}\right)\right] \times \sin^2(k_x x)\exp\left(-\frac{2k_z z}{s_0}\right), \tag{5.4}$$

$$(\mathbf{J}\times\mathbf{B})_y = 0, \tag{5.5}$$

$$(\mathbf{J}\times\mathbf{B})_z = \left[\frac{k_z}{s_0}(k_x^2-k_z^2)-k_z\left(s_0k_x^2-\frac{k_z^2}{s_0}\right)\right] \times \frac{\sin(2k_x x)}{2}\exp\left(-\frac{2k_z z}{s_0}\right), \tag{5.6}$$

pushes oppositely directed segments of magnetic field lines toward each other, generating the neck at $t = 3.264$, panel (b) of Figure 5.2—demonstrating the magnetic field line dynamics for $(\delta_i/L_0) = 0$. The reconnections at the neck

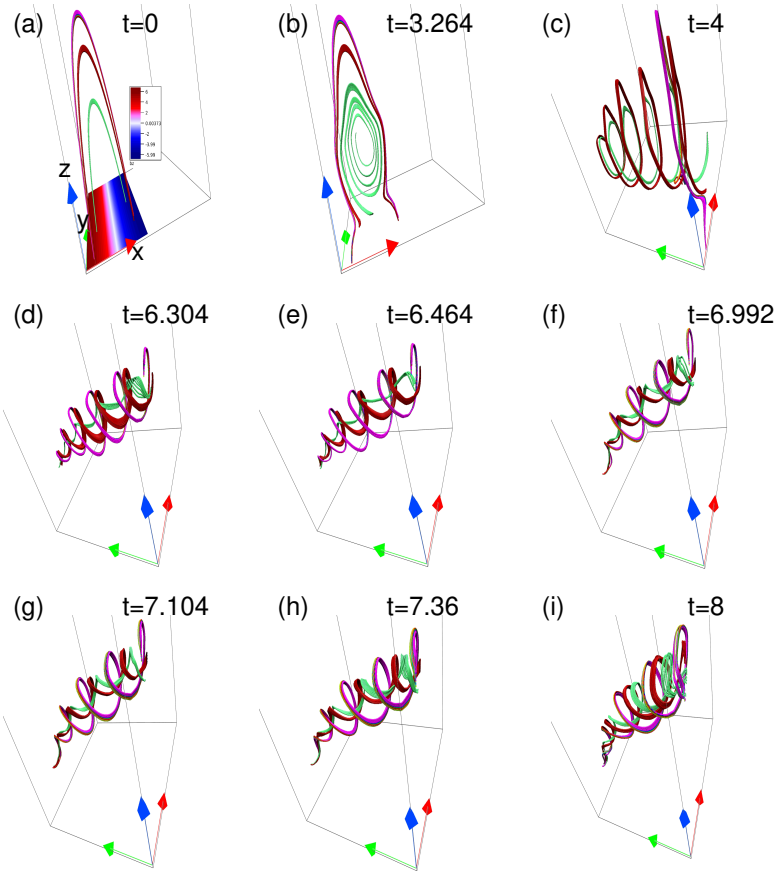

Figure 5.2: Panel (a) shows the initial bipolar sheared arcade configuration along with the polarity inversion line, Panels (b) and (c) show the formation of the magnetic flux rope. Panels (d) to (i) represent the further evolution of the magnetic flux rope with a tilted axis (along y) of it for $\delta_i/L = 0$ (MHD) case.

generate the MFR—which we refer to the primary MFR (panel (c) of Figure 5.2). Further evolution preserves the primary MFR by not allowing it to go through

any internal reconnections. Notably, the rope loses its initial symmetry along the y direction by a marginal amount which, we attribute to the open boundary conditions. Nevertheless, the rope rises uniformly about a slightly inclined axis.

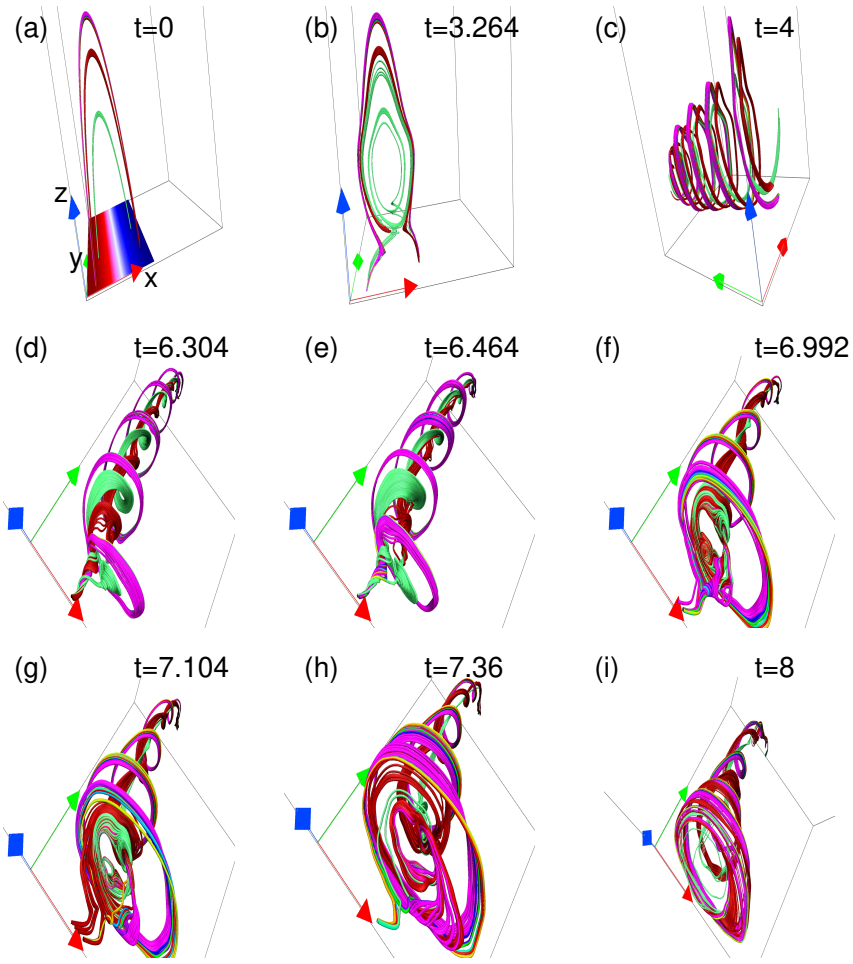

Figure 5.3: Panels (a) to (i) show the topology of magnetic field line s in their evolution for $\delta_i/L = 0.04$ under the Hall forcing. Important is the similarity of the dynamics leading to the formation of primary MFR which occurs at a similar instant as the primary MFR in the absence of the Hall forcing.

The magnetic field line evolution for $\delta_i/L = 0.04$ is exhibited in Figure 5.3. The selected value is on the order of the coronal value quoted in the Introduction and optimizes the computation. The primary MFR develops at $t = 4$, which is similar to the instant at which the primary MFR was generated for the $\delta_i/L = 0$ case. The overall dynamics leading to the primary MFR also remains similar to the one without the Hall forcing. The similar dynamics and the near-simultaneity in the onset of the primary MFR in both cases indicate the large-scale dynamics, i.e., the dynamics before or away from reconnections, to be insensitive to the particular

Hall forcing.

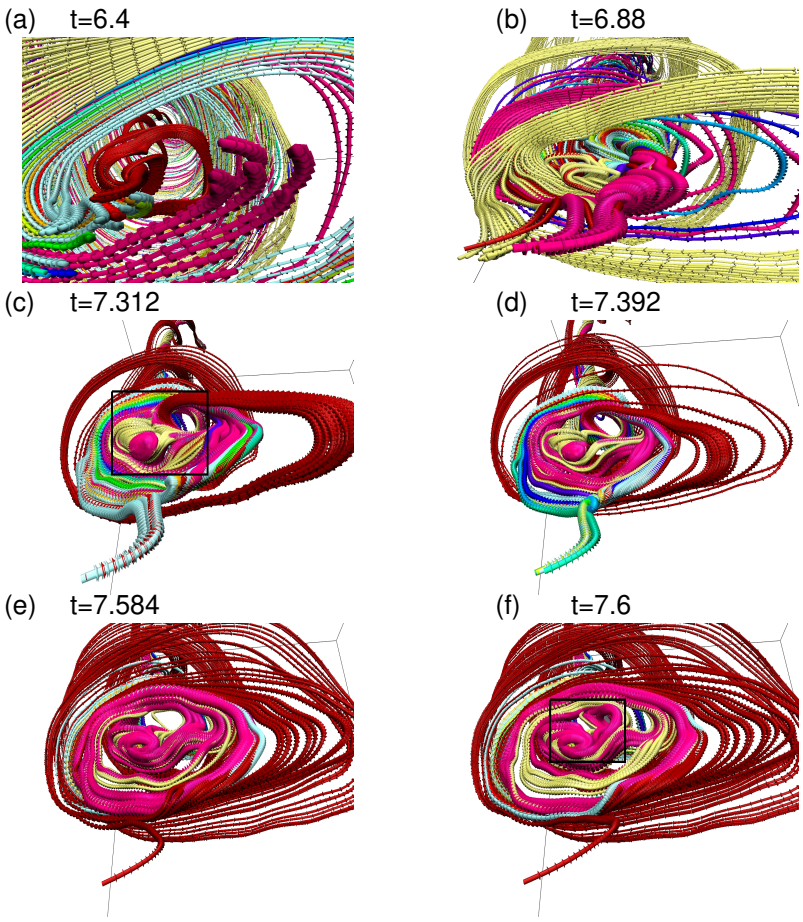

Figure 5.4: Sequence of magnetic field lines evolution under the Hall forcing ($\delta_i/L = 0.04$ case), zoomed to reveal intricate magnetic topologies generated by the reconnections. Formation of the "number 8" like magnetic structure starts to develop at $t = 7.312$ (panel (c)) and is the most pronounced at $t = 7.6$ (panel (f)). For easy identification, the structure is marked by rectangles. Importantly, such intricate topologies are absent in the MFR evolution without the Hall forcing.

However, there are conspicuous differences between the MHD and Hall MHD realizations of the MFR morphology. In the Hall MHD case, the primary MFR undergoes multiple internal reconnections highlighted in Figure 5.4, leading to magnetic field line morphologies which when projected favorably look like magnetic islands similar to those found in the sinusoidal simulation. A swirling motion is also observed; cf. panels (a) to (f) of Figure 5.4. Noteworthy, swirling motion during the evolution of a prominence eruption has been observed (Pant et al., 2018). To complete the analyses, we plot the overall evolution of magnetic and kinetic energies, the amplitude of the out-of-plane field, and the rate of change of the total volume current density in panels (c) and (d) of Figure 5.5. The similarity

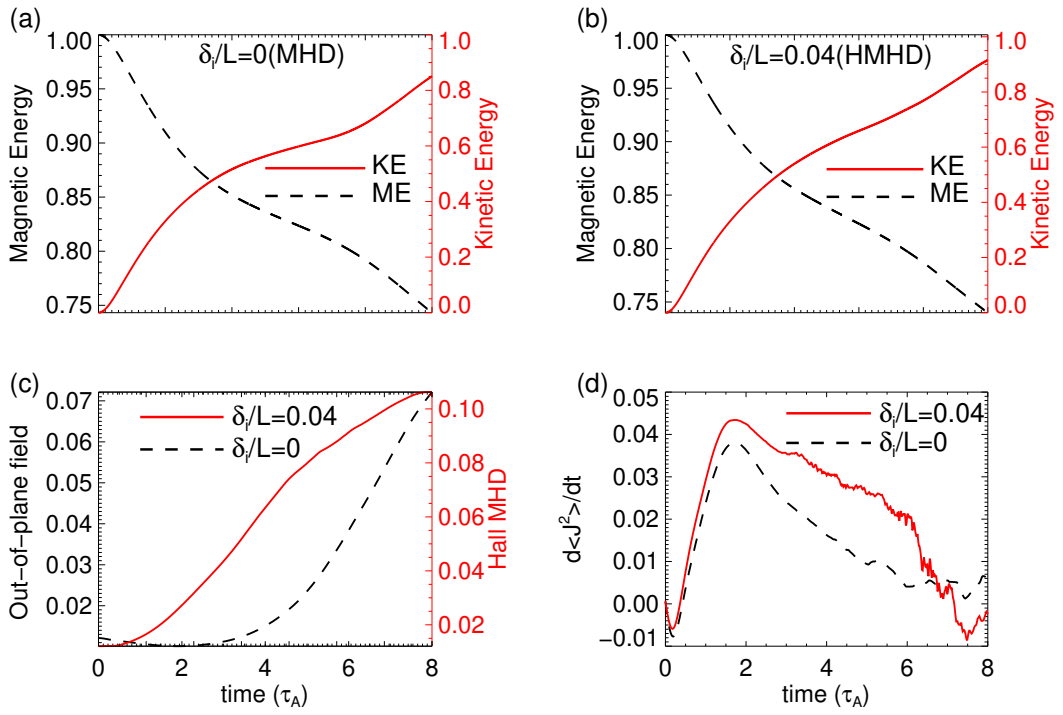

Figure 5.5: Panels (a) and (b) show the evolution of normalized (with the initial total energy) grid averaged magnetic energy (black dashed curve) and kinetic energy (red solid curve) for $\delta_i/L = 0$ (MHD) and $\delta_i/L = 0.04$ (Hall MHD) respectively. Panel (c) shows the evolution of grid averaged out-of-plane magnetic field for $\delta_i/L = 0$ (MHD) with a black dashed curve and $\delta_i/L = 0.04$ (Hall MHD) with a red solid curve respectively. Also in Panels (a) to (c), the scales for the solid and the dashed curves are spaced on the right and left respectively. Panel (d) represents the grid averaged rate of change of total current density for $\delta_i/L = 0$ (black dashed curve) and $\delta_i/L = 0.04$ (red solid curve) respectively. Important is the generation of the out-of-plane magnetic field along with small but abrupt changes in time derivative of the total volume current density in Hall MHD simulation.

of the energy curves in the presence and absence of the Hall forcing agrees with the fact that the Hall term does not affect the system energetics directly. Importantly, the out-of-plane magnetic field (approximated by the axial magnetic field B_y) is larger than that in the absence of the Hall forcing, in accordance with the expectation. Further, contrary to its smooth variation in the MHD case, the rate of change of total volume current density in Hall MHD goes through small but abrupt changes. Such abrupt changes may correspond to a greater degree of impulsiveness (Bhattacharjee, 2004).

To check the dependence of the above findings on the grid resolution, we have carried out auxiliary simulations with $32 \times 32 \times 64$ grid resolution, spanning the same physical domain with all the other parameters kept identical (not shown).

The findings are similar to those at higher resolution. In particular, they evince the nearly simultaneous formation of the primary MFR, with and without the Hall forcing, through a similar dynamical evolution. Also, breakage of the primary MFR through internal reconnections is found in presence of Hall forcing whereas no such breakage is seen in the absence of the Hall forcing. The identical dynamics in two separate resolutions indicate the findings to be independent of the particular resolution used.

5.3 Case-II: MFR generated from a 3D initial analytical magnetic field

The magnetic field lines dynamics responsible for flares and CMEs are 3D owing to their inherent twist. It is then imperative to complement the above work by exploring Hall MHD evolution of an initially 3D magnetic configuration toward the creation and further evolution of MFR. For this purpose, a comprehensive analysis of 3D Hall-assisted magnetic reconnection during the evolution of an anchored MFR is presented here. Importantly, anchored MFRs are observationally more relevant to solar coronal transients than non-anchored levitating ones, as idealized in Bora et al. (2021); Kumar et al. (2016). The simulations are initiated with a 3D bipolar sheared field (Kumar et al., 2016) $\mathbf{B}^*$ having a sigmoid-shaped polarity inversion line (PIL) (shown in Figure 5.6). The $\mathbf{B}^* = \mathbf{B} + a_0\mathbf{B}^{'}$ where $\mathbf{B}$ is given by equations 5.1-5.3 and $\mathbf{B}^{'}$ is

$$B_x^{'} = (\sin x \cos y - \cos x \sin y) \exp\left(\frac{-z}{s_0}\right) , \tag{5.7}$$

$$B_y^{'} = -(\cos x \sin y + \sin x \cos y) \exp\left(\frac{-z}{s_0}\right) , \tag{5.8}$$

$$B_z^{'} = 2s_0 \sin x \sin y \exp\left(\frac{-z}{s_0}\right) . \tag{5.9}$$

The parameters k_x, k_y, k_z, and s_0 used in simulations are the same as mentioned for Case-I in Section 5.2. Equation 4.1 - Equation 4.4 are numerically integrated using the 3D HMHD solver (already described in Chapter 3) to get the dynamical evolution of the 3D initial field given above.

The simulations are conducted by assuming the plasma to be incompressible, thermodynamically inactive, and explicitly non-resistive. A physical domain of extent [{0,2π}, {0,2π}, {0,8π}] is resolved by a computational domain of size 64×64×128, making the spatial step sizes $\Delta x = \Delta y$ =0.0997, and Δz =0.1979 (in dimensionless units). The simulations start with a motionless state, i.e. initial flow velocity field ($\mathbf{v}$) is set to zero. The mass density ρ_0 is set to 1 and the effective viscosity τ_A/τ_ν is set to 2×10^{-5}. All the parameters are the same for the Hall MHD and MHD simulations except for δ_i/L_0.

For the MHD simulation, the value of δ_i/L_0 is set to 0. In conformity with the order of δ_i/L_0 in the solar corona, it is set to 0.04 for the Hall MHD simulation. Notably, the ion inertial scales are greater than the dissipation scale (the spatial step sizes). As a result, reconnections because of both the Hall effect and the MPDATA-assisted residual dissipation are expected to be near-simultaneous in the presented simulations and onset with a steepening of current density.

The simulation results presented herein correspond to a total run of $7000\Delta t$ with the dimensionless temporal step size $\Delta t = 16 \times 10^{-4}$. The total simulated physical time is $7000\Delta t\tau_A = 11.2\tau_A$, where τ_A is in seconds. For convenience, hereafter (including figures) the time is presented in units of τ_A. The B_z at the bottom boundary (at z = 0) is kept fixed throughout the simulation while all other field variables are allowed to vary. At all other boundaries, all variables including B_z, vary with time with their values at a given spatial location on the boundary being mapped from the immediate spatial neighborhood. Importantly, the boundary condition used here is entirely different from the periodic boundary used in Kumar et al. (2016) and allows for the generated flux rope to be anchored.

Our investigation of the reconnection sites toward the generation of initial MFR reveals the repetitive 3D reconnections occurring at null points in Hall MHD as well as MHD simulation. The presence and location of such null points is confirmed by utilizing the well-established and tested trilinear method of null detection in three-dimensional vector space; see Haynes & Parnell (2007) for details. For the null detection we have used a python code based on the trilinear method, developed by Federica Chiti, David Pontin, Roger Scott and available at https://zenodo.org/record/4308622#.YByPRS2w0wc. Null detection shows

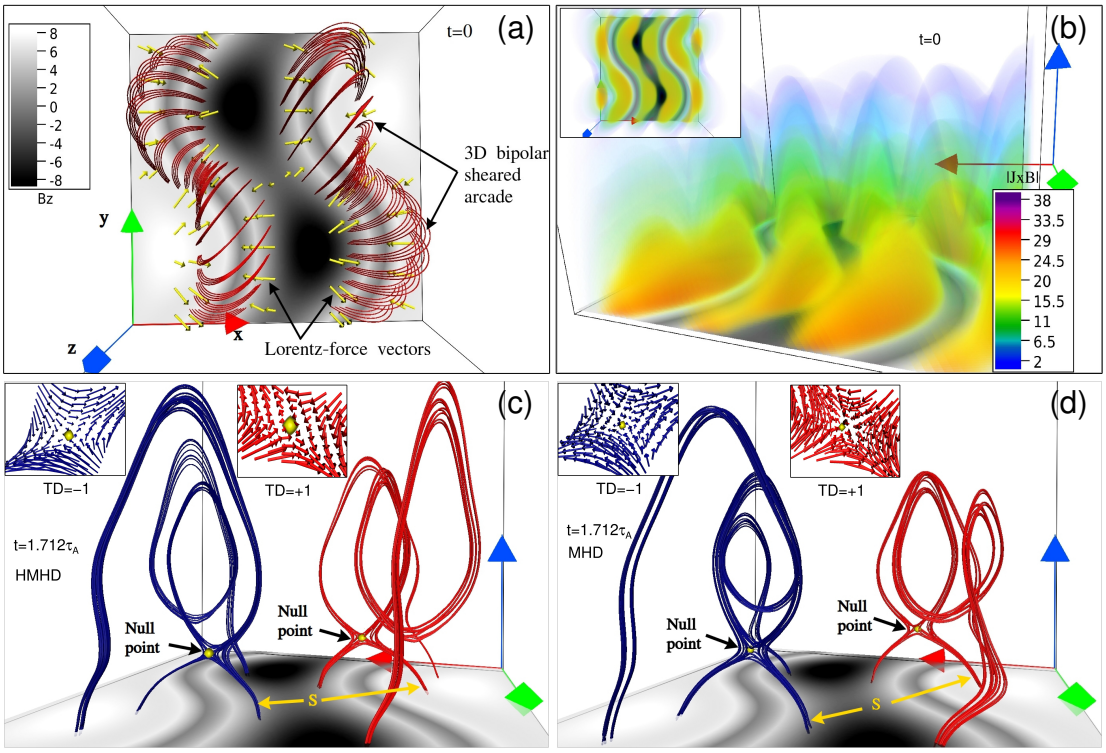

Figure 5.6: (a) Initial 3D sheared magnetic field lines (red) along with the oppositely directed Lorentz force vectors (yellow) around the sigmoid-shaped polarity inversion line (PIL). (b) The magnitude of Lorentz force ($|\mathbf{J}\times\mathbf{B}|$) and its top-down view (inset image in the top left corner). (c) and (d) Two 3D nulls (yellow) of topological degrees -1 (blue) and +1 (red) during the Hall MHD and MHD simulations respectively. The spine is indicated by the yellow arrows. The bottom boundary in all the panels of this figure and subsequent figures shows the B_z maps in grayscale, where the lighter shade represents positive-polarity regions and the darker shade indicates the negative-polarity regions. The red, green, and blue arrows in each panel represent the x, y, and z axis of the Cartesian coordinate system respectively.

that there are no null points present initially at $t = 0$. The reconnections onset as the initial non-zero Lorentz force (direction and magnitude around the PIL is shown in panels (a) and (b) of Figure 5.6) pushes the oppositely directed segments of magnetic field lines toward each other to generate the neck (panels (c) and (d) of Figure 5.6). At the neck the null points are detected and one such instance of the reconnections at null points from each simulation (at $t = 1.712\tau_A$) is presented in the panels (c) and (d) of Figure 5.6. Since there are no null points present at $t = 0$, the net topological degree is zero. Subsequently, careful analysis of the magnetic field vectors around null points reveals the blue magnetic field lines have a topological degree -1 (magnetic field lines approaching the null along the spine) while the red magnetic field lines have a topological degree +1 (magnetic field lines

receding from the null along the spine); see Figure 5.6 (c) and (d). Hence the net topological degree is zero, implying the topological degree to be conserved (Wyper & Pontin, 2014) because the net topological degree is zero initially. Determining the topological degree of all the nulls detected with the trilinear method is difficult and beyond the scope of this work, since the maximum number of null points detected in Hall MHD is ≈ 650 and in MHD it is ≈ 500. Noticeably, the initial magnetic field configuration is symmetric about $x = \pi$ (Figure 5(a)), i.e., in the $x \in \{0, \pi\}$ and $x \in \{\pi, 2\pi\}$ domain. Dynamical evolution and structures are the same about $x = \pi$; as evident from panels (c) and (d) of Figure 5.6. Therefore, for relevant illustrations and to avoid much dynamical complications, we focus only on the $x \in \{\pi, 2\pi\}$ domain here.

Figure 5.7 and Figure 5.8 illustrate the instances of the evolution of selected magnetic field line sets from the Hall MHD and MHD simulation respectively. To highlight the differences in the magnetic field lines dynamics around the reconnection sites and subsequent large-scale structural changes, we compare panels (a)-(d) of Figure 5.7 and Figure 5.8. Panels (a) of Figure 5.7 and Figure 5.8 depict an identical twisted MFR (cyan color), overlying stretched field lines, and the reconnection site below MFR during the Hall MHD and MHD simulations. An indistinguishable initial MFR creation in both the simulations is evident from panels (c) and (d) of Figure 5.6. However, the red and lavender magnetic field lines approach each other apparently during the Hall MHD (marked by the yellow rectangle in Figure 5.6(a)) at $t = 2.256\tau_A$ but during the MHD the two magnetic field lines set are farther, and red magnetic field lines reconnects with itself below the MFR. Panels (b) of Figure 5.7 and Figure 5.8 show the similarity of cyan color MFR and red magnetic field lines post reconnection arcade during the Hall MHD and MHD simulations respectively. It is only the lavender magnetic field lines that exhibit different structures during the Hall MHD and MHD from $t = 6.448\tau_A$ onwards, hence we focus mainly on the instances of lavender magnetic field lines dynamics in panels (c) and (d) of Figure 5.7 and Figure 5.8 further. Panels (c) of Figure 5.7 and Figure 5.8 depict the main difference in the lavender magnetic field lines structure since during the Hall MHD at $t = 6.736\tau_A$ the lavender magnetic field lines have formed a large-scale MFR (marked by the yellow arrow in Figure 5.7(c)) with the

associated twisted magnetic field lines region below MFR (marked by the yellow rectangle in Figure 5.7(c)). Contrary to the Hall MHD, Figure 5.8(c) depicts no large-scale MFR formation by lavender magnetic field lines. Notably, panels (d) of Figure 5.7 and Figure 5.8 show the post-reconnection arcade (Lavender magnetic field lines marked with the yellow arrow) in the Hall MHD simulation develops earlier than in the MHD simulation which, yet lacks the arcades to get developed by $t = 7.568\tau_A$. Faster development of a post-reconnection arcade clearly indicates faster reconnection dynamics in Hall MHD. Notably, the post-reconnection wavy arcade is twisted in Figure 5.7(d). Interestingly, if the twisted magnetic field lines confine the plasma, they are usually observed as filament (against solar disk) or prominence (against solar limb) on the Sun.

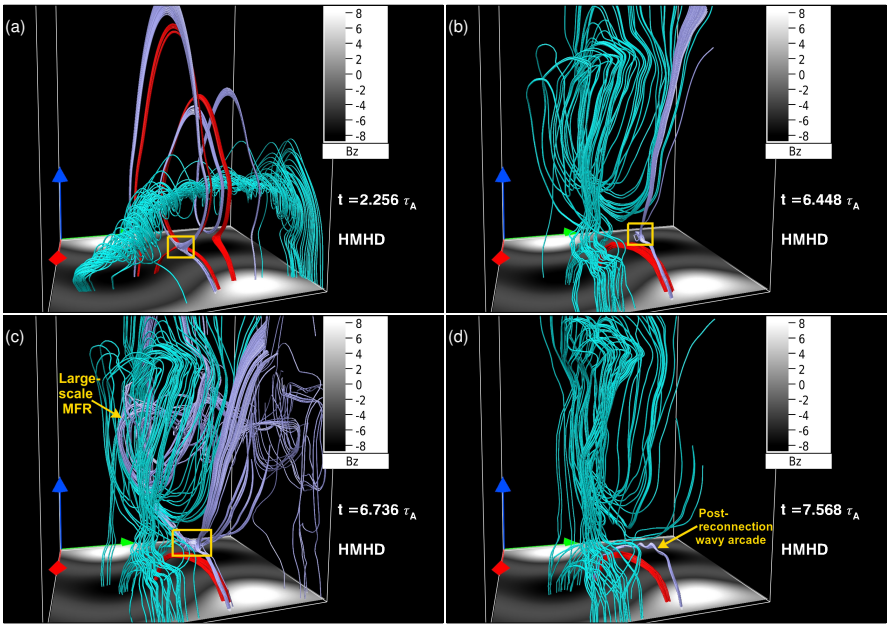

Figure 5.7: Snapshots from the Hall MHD evolution of a 3D MFR. (a) The two sets of field lines (red from the left and lavender from the right side) approaching each other (marked in a yellow rectangular box) below the MFR (cyan color) at $t = 2.256\tau_A$. (b) The structure formed by lavender color magnetic field lines (marked by the yellow rectangle) and the post reconnection arcade formed by red magnetic field lines at $t = 6.448\tau_A$. (c) Large-scale MFR formed by lavender color magnetic field lines and associated small-scale structure around reconnection site (marked by the yellow rectangle) at $t = 6.736\tau_A$). (d) Post-reconnection wavy arcade generated by lavender magnetic field lines at $t = 7.568\tau_A$.

All the differences mentioned above are purely on the basis of magnetic field lines dynamics and structural changes around possible reconnection sites, which we further analyze using the trilinear method of null points detection and twist

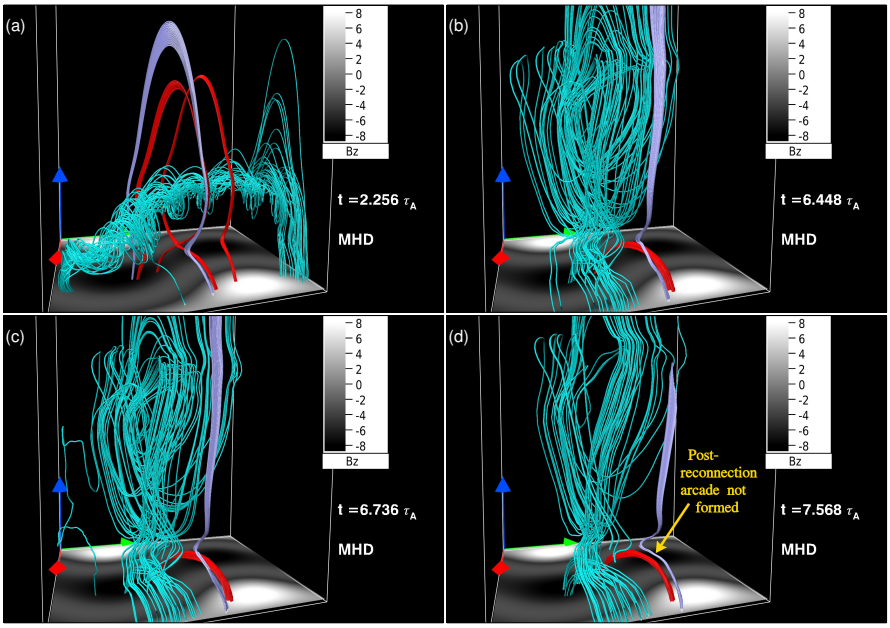

Figure 5.8: Snapshots from the MHD evolution of a 3D MFR. Panel (a) shows the MFR (cyan color) structure with two other sets of magnetic field lines (red and lavender) overlying the MFR. Notably, red and lavender color magnetic field lines are relatively farther compared to the Hall MHD instance of the same at $t = 2.256\tau_A$. Panels (b)-(d) highlight the morphology of lavender magnetic field lines. Noticeably, the lavender magnetic field lines do not exhibit any twisted structure formation near the reconnection site (cf. panels (b)-(d) of Figure 5.7.)

analysis. In Figure 5.9, we present the temporal evolution and the detailed zoomed view of the magnetic field lines morphology marked in Figure 5.7(a). Panels (a)-(c) and panels (d)-(f) show the snapshots from the HMHD and MHD simulations respectively. Inset images in panels (a)-(c) show the frontal view of red magnetic field lines (color coded with the twist $\alpha = \mathbf{j}\cdot\mathbf{B}/|B|^2$) around the null point (yellow point marked by arrow). Interestingly, the development of high twist value $\alpha \sim 10$ in the neighborhood of the null point is evident from inset images in Figure 5.9 (b) and (c). Such twisting of field lines around the reconnection site is not found during the MHD simulation. Since the red field lines form the post-reconnection arcade by $t = 6.448\tau_A$ and do not reconnect further, so we drop it and focus on the dynamics of lavender field lines. The lavender color field lines form intermediate small-scale* structure during the HMHD evolution (marked within the yellow rectangle in Figure 5.7 (b) and (c)). We present the detailed zoomed frontal view of these structures in Figure 5.10. In panel (a), we have plotted additional field lines left to 3D null. These field lines are color coded with the value of twist and show the high

*Size compared to large-scale MFR

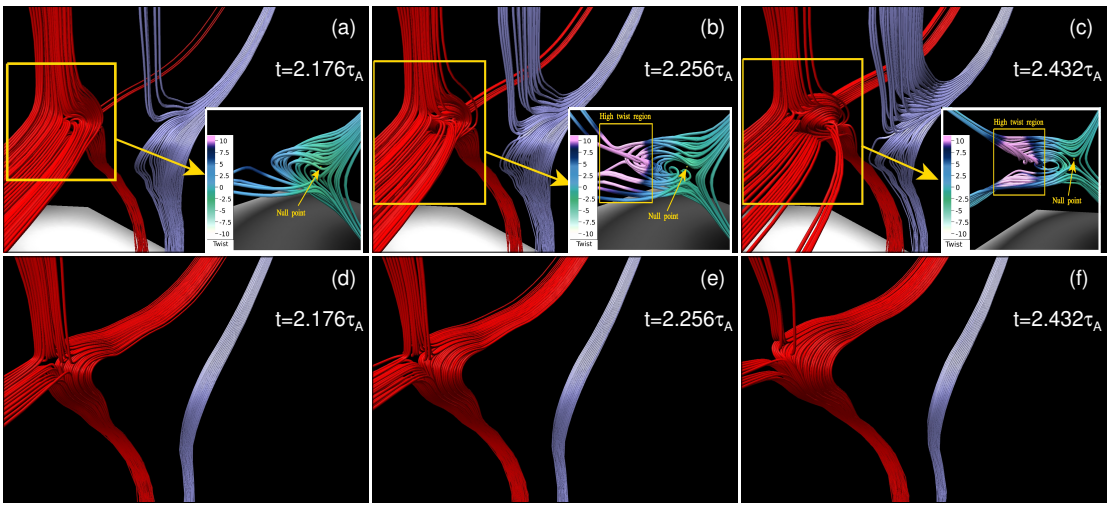

Figure 5.9: Detailed side view of the magnetic field lines marked in Figure 5.7 (a). Panels (a)-(c) depict the snapshots from the HMHD simulation and panels (d)-(f) depict the snapshots from the MHD simulation. Formation of the twisted magnetic structure by red field lines is evident during the HMHD in panels (a)-(c), whereas no such structure is found during the MHD simulation(c.f. panels (d)-(f)). The inset images in panels (a)-(c) show the presence of a 3D null point and the development of twist in the neighborhood of the null point. Field lines in inset images are the red field lines (marked by the yellow rectangular box) color-coded with the value of twist ($\alpha = \mathbf{j} \cdot \mathbf{B}/|\mathbf{B}|^2$).

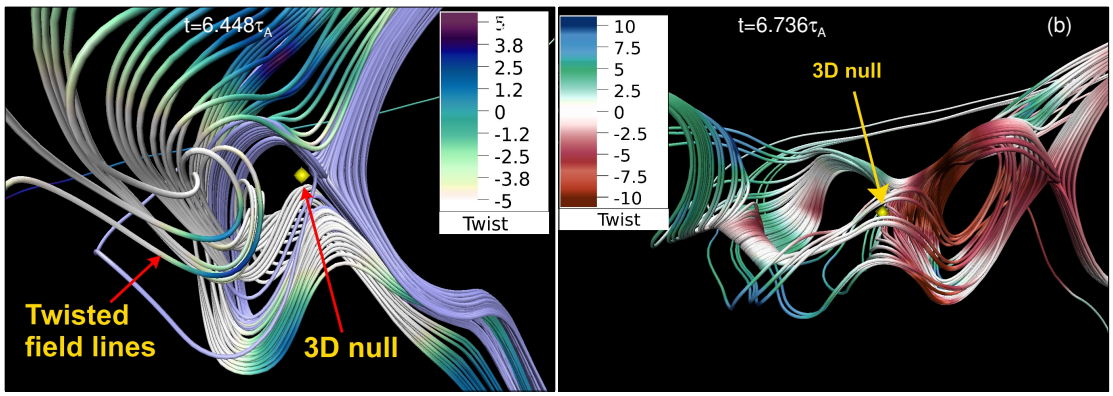

Figure 5.10: Panels (a) and (b) show the zoomed frontal view of the lavender field lines structure (marked in Figure 5.7 (b) and 5.7(c)) highlighting the presence of a 3D null at $t = 6.448\tau_A$ and $t = 6.448\tau_A$ during the HMHD evolution. In panel (a) additional field lines (left to 3D null and color-coded with the twist value α) show the twist value ~ -5 around the 3D null. Notably, in panel (b), the field lines have twist $\alpha \sim -10$ on the right and $\alpha \sim (5 - 7.5)$ on the left to the 3D null.

twist value around 3D null, i.e., $\alpha \sim -5$ This figure highlights the presence of null points in both the panels and mini twisted flux rope in panel (b). The lavender color large-scale MFR (Figure 5.7(c)) is formed as a result of reconnections in the region shown in Figure 5.10(b). This small-scale complex and twisted structure is associated with the large-scale MFR formation during the HMHD but no such

structures were found in the MHD.

Temporal variation of the volume-averaged magnetic and kinetic energies is presented in panels (a) and (b) of Figure 5.11. The solid blue and dashed black curves represent the kinetic and magnetic energy variations respectively. Noticeably, the magnetic energy is decreasing identically in both the simulations, hence the results are in agreement with the general theoretical expectation that the Hall effect does not cause changes in the magnetic energy dissipation rates (Liu et al., 2022).

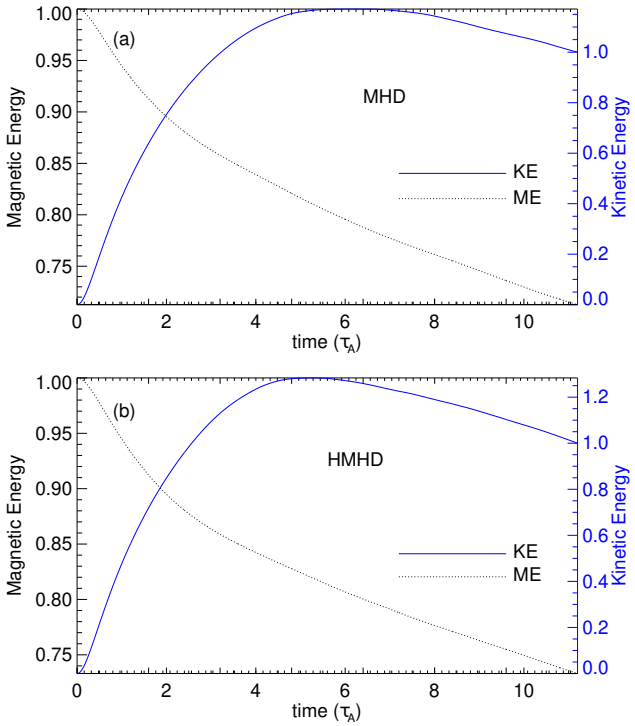

Figure 5.11: Panels (a) and (b) show the temporal variation of the volume-averaged magnetic (black dashed curve) and kinetic energies (blue solid curve) during the MHD and Hall MHD evolution respectively.

In summary, the ubiquitous twisting of magnetic field lines in the vicinity of null points is unique to the Hall MHD evolution of the 3D MFR. Owing to the local enhancements of the strong gradients of the magnetic field, the Hall effects cause magnetic field lines morphological changes, (e.g., twisting) around the reconnection sites which further affects the large-scale dynamics during the Hall MHD simulations.

5.4 Summary

In this Chapter, for the first time, the newly developed 3D HMHD EULAG model has been employed to investigate the Hall effect on magnetic reconnections during the evolution of MFR. Particularly, the topological changes during the MFR creation and evolution are analyzed in the presence and absence of the Hall term in the induction equation. Following the model equations, simulations presented in this Chapter use a dimensionless set of equations along with the description of normalization. A detailed analysis of the magnetic reconnections for the MFRs generated from two sets of initial conditions is carried out. The results presented in this Chapter, clearly depict that the initial MFR formation mechanism through reconnections is identical in the Hall MHD as well as MHD, but the further evolution in two simulations is illustrative in terms of repetitive formation of intermediate structures during the Hall MHD evolution. Key highlights of the work presented in this Chapter include the faster, efficient, and complex reconnections during the Hall MHD simulation and identical volume-averaged temporal evolution of magnetic and kinetic energies in the Hall MHD and MHD simulations. The reconnections in our simulations occur owing to the numerical dissipation of the under-resolved magnetic field variables (ILES property of the model, described in Chapter 3). These reconnections being intermittent and local, successfully mimic the physical reconnections. With the Hall scale being tied together with the dissipation scale (where the current density is highest), the Hall forcing gets enhanced. This enhanced Hall forcing may further modify the dynamics around the reconnection site and yield the more efficient and faster reconnections reported in this Chapter.

At last, we want to emphasize the fact that we have only considered the Hall effect on magnetic reconnections during the evolution of MFR generated through the reconnections from initially bipolar sheared magnetic arcades. Whereas, presently, there are two different concepts of CMEs on the Sun; one considers that the MFR is absent prior to eruption and it is eventually generated through magnetic reconnections (tether cutting or breakout models); another assumes the pre-existence of MFR emerged from below the photosphere (i.e., from the convection zone) and undergoes the ideal MHD instabilities (torus and kink instabilities) which initiate

eruptions. Available observations of the CMEs on Sun suggest the possibility of both the ideas. Regardless of which idea is admissible in the real eruptions on Sun, the general agreement is that the reconnection shapes the erupting MFR. In order to understand the CMEs happening due to the successful prominence or filament eruption, is then crucial to also investigate the role of Hall forcing on magnetic reconnetctions driving the dynamics of a pre-existing 3D MFR further.

Chapter 6

Data-based Hall MHD and MHD simulations of a flaring solar active region

6.1 Introduction

In Section 1.6, a straightforward calculation based on the observed impulsive rise time of hard X-ray emission ($\approx$ a few minutes) during the solar flares, suggests that reconnection length scale is of the order of a few tens of meters in the solar corona. Notably, a single reconnection site or current sheet has been assumed for the calculation. An order-of-magnitude analysis of the induction equation at reconnection scale length indicates the inevitability of Hall effects during dissipative processes or magnetic reconnection on the Sun (Bhattacharjee, 2004; Bora et al., 2021). Chapter 5 clearly illustrates that contrary to the standard MHD, the presence of the Hall term leads to faster reconnection while also capturing the effects of small-scale processes over large length scale magnetic field line dynamics. Modeling magnetic reconnection in solar corona at small length scales and capturing its effects on large-scale dynamics together is challenging and is an open problem. It is compelling to study the Hall MHD evolution in a more realistic scenario with the initial magnetic field obtained from a solar magnetogram. In this Chapter, we present the data-based Hall MHD and MHD simulations of a flaring solar active region as a test bed. The main objective of this work is to explore the significance

of the Hall effect on magnetic reconnection to understand the spatiotemporal development of the observed solar flare ribbon brightening. To attain the objective, we select the recently reported active region (AR) NOAA 12734 by Joshi et al. (2021) that produced a C1.3 class flare. In absence of reliable direct measurement of the coronal vector magnetic field, several extrapolation models such as nonlinear force-free field (NLFFF) (Wiegelmann, 2008; Wiegelmann & Sakurai, 2012) and non-force-free field (non-FFF) (Hu & Dasgupta, 2008; Hu et al., 2010) have been developed to construct the coronal magnetic field using photospheric magnetograms. The standard is the NLFFF, and the recent data-based MHD simulations initialized with it have been reasonably successful in simulating the dynamics of various coronal transients (Jiang et al., 2013; Amari et al., 2014; Inoue et al., 2014; Savcheva et al., 2016). However, the NLFFF extrapolations require to treat the photosphere as force-free, while it is actually not so (Gary, 2001). Hence, a "preprocessing technique" is usually employed to minimize the Lorentz force on the photosphere in order to provide a boundary condition suitable for NLFFF extrapolations (Wiegelmann et al., 2006b; Jiang & Feng, 2014) and thereby artificially modifying the photosphere. Recently, the non-Force Free Field (non-FFF) model, based on the principle of minimum energy dissipation rate (Bhattacharyya & Janaki, 2004; Bhattacharyya et al., 2007), has emerged as a plausible alternative to the force-free models (Hu & Dasgupta, 2008; Hu et al., 2008, 2010). In the non-FFF model, the magnetic field $\mathbf{B}$ satisfies the double-curl-Beltrami equation (Mahajan & Yoshida, 1998), and the corresponding Lorentz force on the photosphere is non-zero while it decreases to small values at the coronal heights (Prasad et al., 2018; Nayak et al., 2019; Prasad et al., 2020)—concurring with the observations. In this Chapter, we use non-FFF extrapolation (Hu et al., 2010) to obtain the magnetic field in the corona using the photospheric vector magnetogram obtained from the Helioseismic Magnetic Imager (HMI) (Schou et al., 2012) onboard the Solar Dynamics Observatory (SDO) (Pesnell et al., 2012b).

The Chapter is organized as follows. Section 6.2 describes the flaring event in AR NOAA 12734, and Section 6.3 presents the magnetic field lines morphology of AR NOAA 12734 along with the preferable sites for magnetic reconnections such as QSLs, 3D null point, and null-line found from the non-FFF extrapolation.

Section 6.4 focuses on the numerical model, numerical set-up, and the evolution of magnetic field lines obtained from the extrapolation along with their realizations in observations. Section 6.5 highlights the key findings.

6.2 Salient features of the observed C1.3 class flare in AR NOAA 12734

The AR NOAA 12734 produced an extended C1.3 class flare on March 08, 2019 (Joshi et al., 2021). The impulsive phase of the flare started at 03:07 UT as reported in Figure 3 of Joshi et al. (2021) and also shown in Figure 6.1, which shows the X-ray flux in the 1-8 Å and 0.5-4 Å detected by the Geostationary Operational Environmental Satellite (GOES) (Garcia, 1994). The flux evinces two subsequent peaks after the onset of the flare, one around 03:19 UT and another roughly around 03:38 UT. Joshi et al. (2021) suggested the eruptive event to take place in a coronal sigmoid with two distinct stages of energy release.

Additional observations using the multiwavelength channels of Atmospheric Imaging Assembly (AIA) (Lemen et al., 2012) onboard SDO are listed below to highlight important features pertaining to simulations reported in this Chapter. Figure 6.2 illustrates a spatiotemporal observational overview of the event. Panel (a) shows the remote semicircular brightening (C1) prior to the impulsive phase of the flare (indicated by the yellow arrow). Panels (b) to (d) indicate the flare by the yellow arrow and the eruption by the white arrow in the 94 Å, 171 Å, and 131 Å channels respectively. Notably, the W-shaped brightening appears in panels (b) to (d) along with the flare in different wavelength channels of SDO/AIA. Panel (e) shows the circular structure of the chromospheric material (C2) during the impulsive phase of the flare. It also highlights the developed W-shaped flare ribbon (enclosed by the white box) which has a tip at the center (marked by the white arrow). Panel (f) depicts the post-flare loops in 171 Å channel, indicating the post-flare magnetic field line connectivity between various negative and positive polarities on the photosphere.

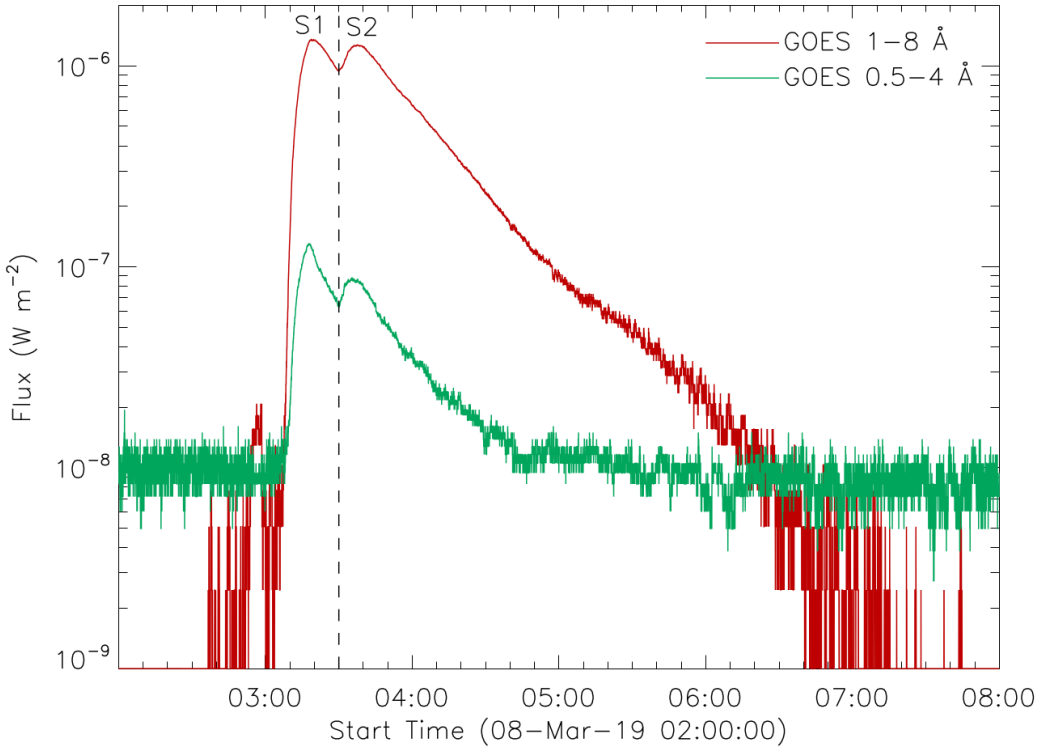

Figure 6.1: GOES light curves depicting X-ray flux in 1-8 Å (red) and 0.5-4 Å (green) wavelength bands corresponding to disk-integrated X-ray emission in energy ranges 1.5-12.5 keV and 3-25 keV, respectively. A two-step process of energy release during a C-class flare in active region NOAA 12734 is suggested by the two different episodes of energy release (labeled as S1 and S2) that are visible in GOES profiles having peak at 03:19 and 03:38 UT, respectively. (Figure adapted from Joshi et al. (2021).)

6.3 Coronal magnetic field construction and the morphology of AR NOAA 12734

As stated in Chapter 2, the non-FFF extrapolation technique proposed by Hu & Dasgupta (2008) and based on the minimum dissipation rate theory (MDR) (Bhattacharyya & Janaki, 2004; Bhattacharyya et al., 2007) is used to obtain the coronal magnetic field for the AR NOAA 12734. The vector magnetogram is selected for 2019 March 08, at 03:00 UT ($\approx$ 7 minutes prior to the start of flare). The original magnetogram cut out of dimensions 342×195 pixels with pixel resolution 0.5 arcsec per pixel having an extent of 124 Mm × 71 Mm from "hmi.sharp_cea_720s" series is considered, which ensures an approximate magnetic flux balance at the bottom boundary. To optimize the computational cost with the available resources, the original field is re-scaled and non-FFF extrapolated over a volume of 256×128×128

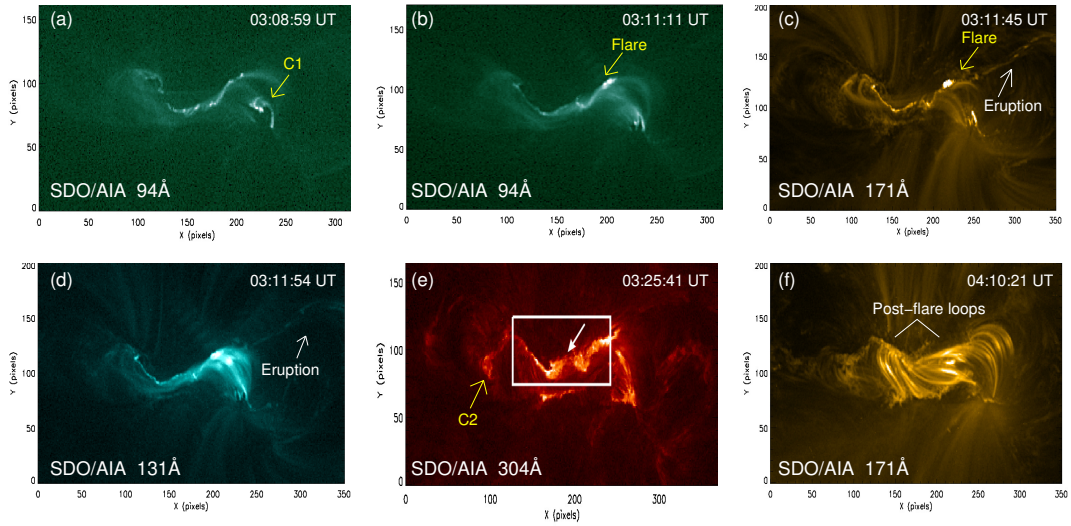

Figure 6.2: Panels (a)-(f) are SDO/AIA images showing the multiwavelength observations of the flaring active region AR NOAA 12734. Panel (a) shows the quasi-circular brightening at the western part of AR prior to the flare (marked by C1). Panels (b)-(d) show the initiation of the flare followed by the eruption (indicated by a yellow arrow). Panel (e) shows the circular structure after the eruption at the eastern part of AR (marked by C2) and the W-shaped flare ribbon (enclosed by the white box). Panel (f) shows the post-flare loops.

pixels while keeping the physical extent same and preserving all magnetic structures throughout the region. The reduction, in effect, changes the conversion factor of 1 pixel to ≈ 0.484 Mm along x and ≈ 0.554 Mm along y and z directions of the employed Cartesian coordinate system.

Panel (a) of Figure 6.3 shows E_n in the transverse field, defined in Section 2.2.2, as a function of number of iterations. It shows that E_n tends to saturate at the value of $\approx$0.22. Panel (b) of Figure 6.3 shows logarithmic decay of the normalized horizontally averaged magnetic field, current density, and Lorentz force with height. It is clear that the Lorentz force is appreciable on the photosphere but decays off rapidly with height, agreeing with the general perception that the corona is force-free while the photosphere is not (Liu et al., 2020; Sarp Yalim et al., 2020). Panel (c) shows that the Pearson-r correlation between the extrapolated and observed transverse fields is $\approx$0.96, implying a strong correlation. The direct volume rendering of the Lorentz force in panel (d) also reveals a sharp decay of the Lorentz force with height, expanding on the result of panel (b).

To facilitate description, Figure 6.4 (a) shows the SDO/AIA 304 Å image at 03:25 UT, where the flare ribbon brightening has been divided into four segments

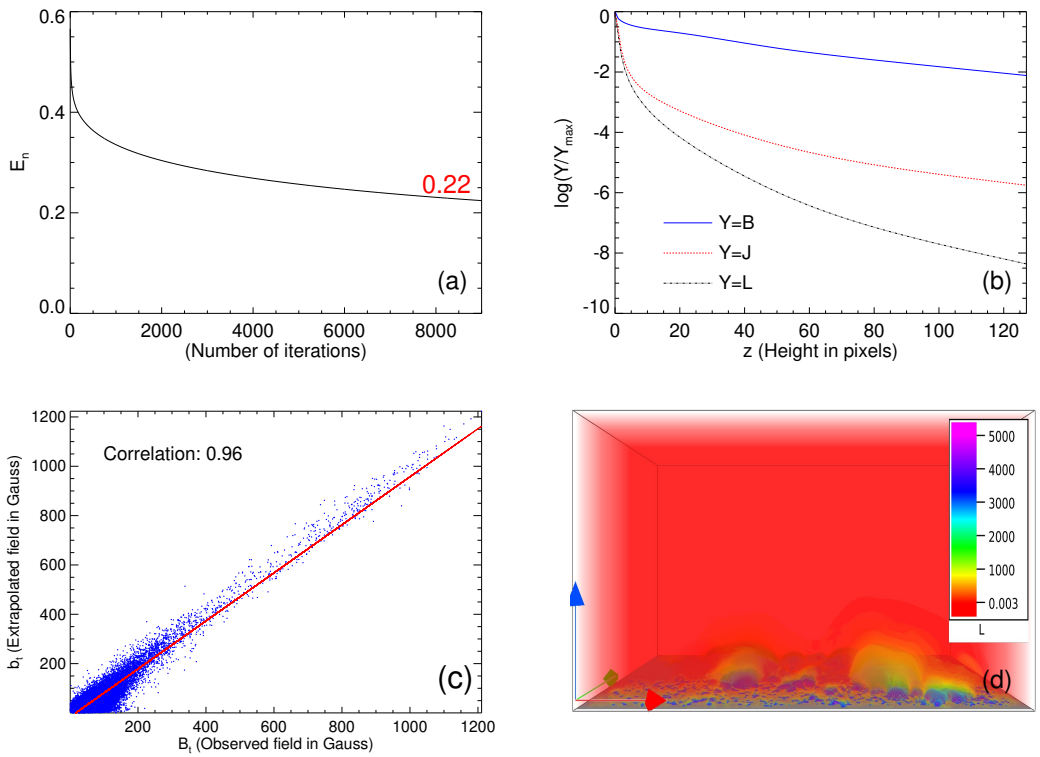

Figure 6.3: Panel (a) shows the variation of the deviation E_n with number of iterations in non-FFF extrapolation. Panel (b) shows the logarithmic variation of horizontally averaged magnetic field (Y=B), the current density (Y=J), and the Lorentz force (Y=L) with height z in pixels. All the quantities plotted in panel (b) are normalized with their respective maximum values. Panel (c) shows the scatter plot of the correlation between the observed and extrapolated magnetic field. The red line is the expected profile for perfect correlation. Distribution of the magnitude of the Lorentz force for an initial extrapolated field is shown in panel (d) using direct volume rendering (DVR). The distribution clearly shows that the Lorentz force is maximum at the bottom boundary and decreasing with the height in computational volume. The red, green and blue arrows on the bottom left corner represent x, y and $z-$directions respectively here and hereafter. The color bars on the right side of the panel represent the magnitude of the strength of Lorentz force .

marked as B1-B4. Figure 6.4 (b) shows the initial global magnetic field line morphology of AR NOAA 12734, partitioned into four regions R1-R4, corresponding to the flare ribbon brightening segments B1-B4. The bottom boundary of panel (b) comprises of B_z maps in grayscale where the lighter shade indicates positive polarity regions and the darker shade marks the negative polarity regions. The magnetic field lines topologies and structures belonging to a specific region and contributing to the flare are documented below.

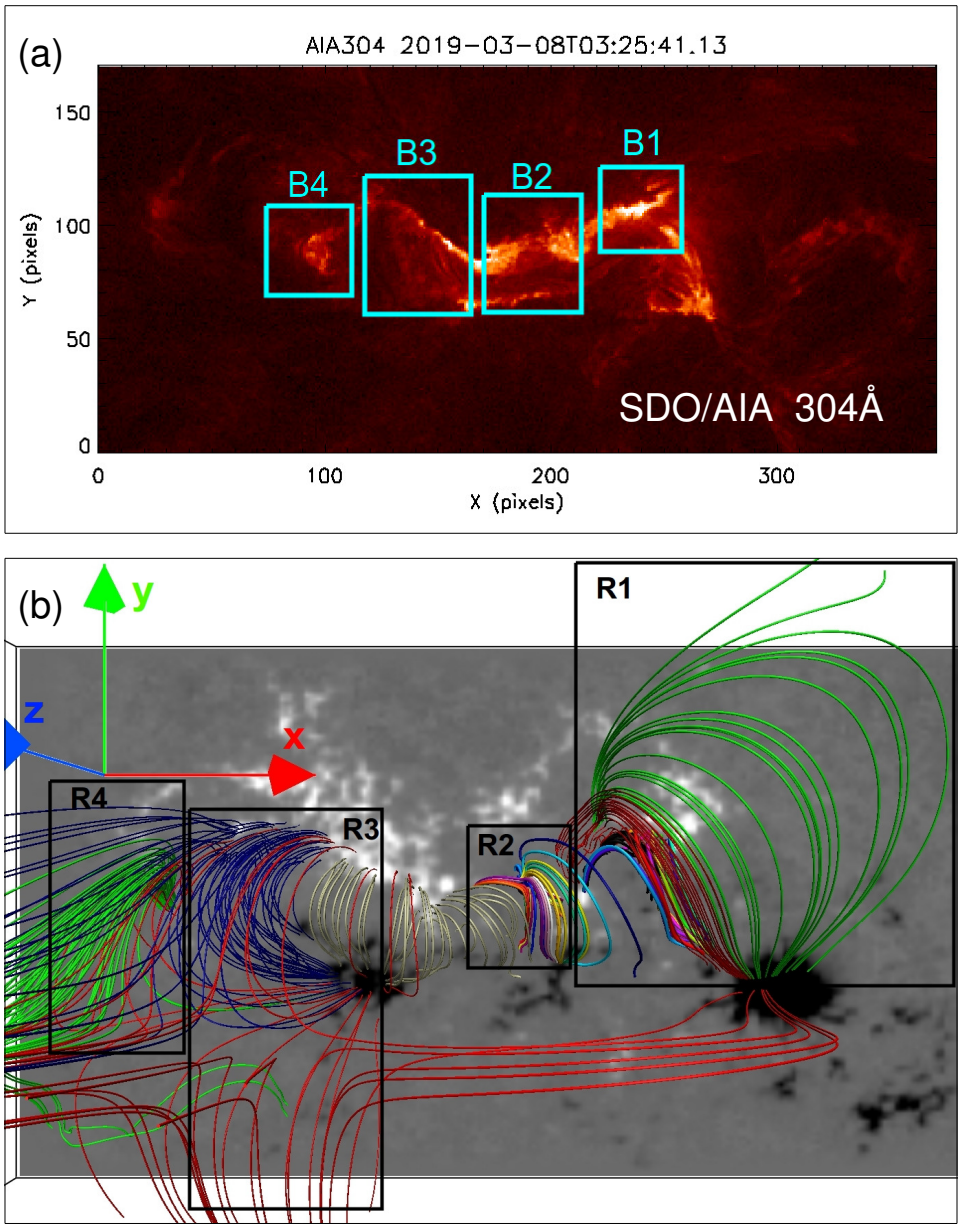

Figure 6.4: Panel (a) shows the SDO/AIA 304Å image where the flare ribbon brightening has been divided into four parts B1, B2, B3, and B4 (enclosed by boxes). Panel (b) shows an overall extrapolated magnetic field lines morphology of AR NOAA 12734 with the B_z-component of magnetogram at the bottom boundary. Foot points of the magnetic structures contained in regions R1, R2, R3, and R4 correspond to the brightening B1, B2, B3, and B4 respectively.

Region R1: The top-down view of the global magnetic field line morphology is shown in panel (a) of Figure 6.5. To help locate QSLs, the bottom boundary is overlaid with the $\log Q$ map of the squashing factor Q (Liu et al., 2012) in all panels of the figure. Distribution of high Q values along with B_z on the bottom boundary helps in identifying differently connected regions. The region with a

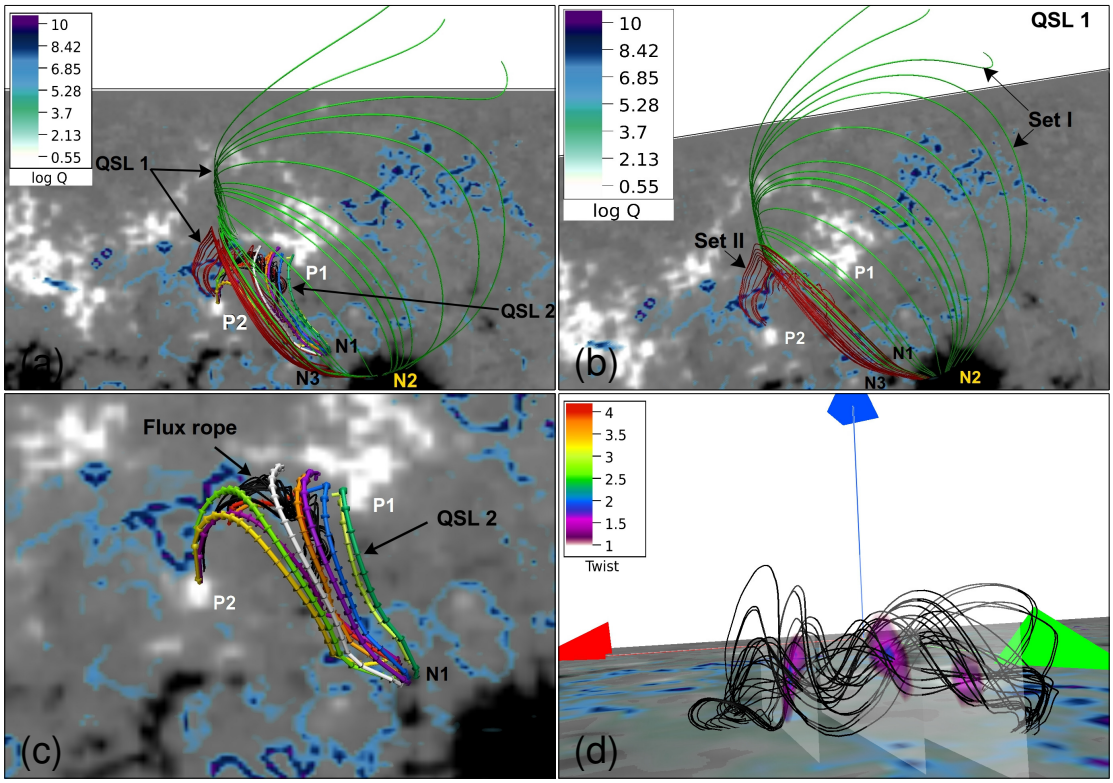

Figure 6.5: Panel (a) shows magnetic field lines morphology of region R1 between positive and negative polarities P1, P2, N1, N2, and N3 respectively. Panel (b) highlights the structure of QSL 1 comprised of magnetic field lines Set I (green) and Set II (maroon). Panel (c) shows the zoomed top view of the flux rope structure (black) and an overlying QSL 2 (multi-color arrowed magnetic field lines), between the positive and negative polarities P1, P2, and N1 respectively. Panel (d) shows the side view of the flux rope where three vertical planes along the cross-section of the flux rope show the twist value T_w at different locations along the flux rope. In all the panels the log Q between 5 and 10, is overlaid on B_z-component of magnetogram at the bottom boundary.

large Q is prone to the onset of slipping magnetic reconnections (Démoulin, 2006). Foot points of magnetic field lines constituting QSL1 and QSL2 trace along the high Q values near the bottom boundary. QSL1, involving the magnetic field lines Set I (green) and Set II (maroon), is shown in panel (b). Particularly, magnetic field lines Set I (green) extends higher in the corona forming the largest loops in R1. Panel (c) illustrates a closer view of QSL2 (multicolored) and the flux rope (black) beneath, situated between the positive and negative polarities P1, P2, and N1, respectively. In panel (d), the flux rope (constituted by the twisted black magnetic field lines) is depicted using the side view. The twist value T_w (Liu et al., 2012) in the three vertical planes along the cross-section of the flux rope is also overlaid. Notably, the twist value is 2 at the center of the rope and decreases

outward (cf. vertical plane in the middle of the flux rope in panel (d)).

Region R2: Figure 6.6 (a) shows the side view of a 3D null point geometry of magnetic field lines and the bottom boundary B_z overlaid with log Q ranging between 5 and 10. Panel (b) depicts an enlarged view of the 3D null location,

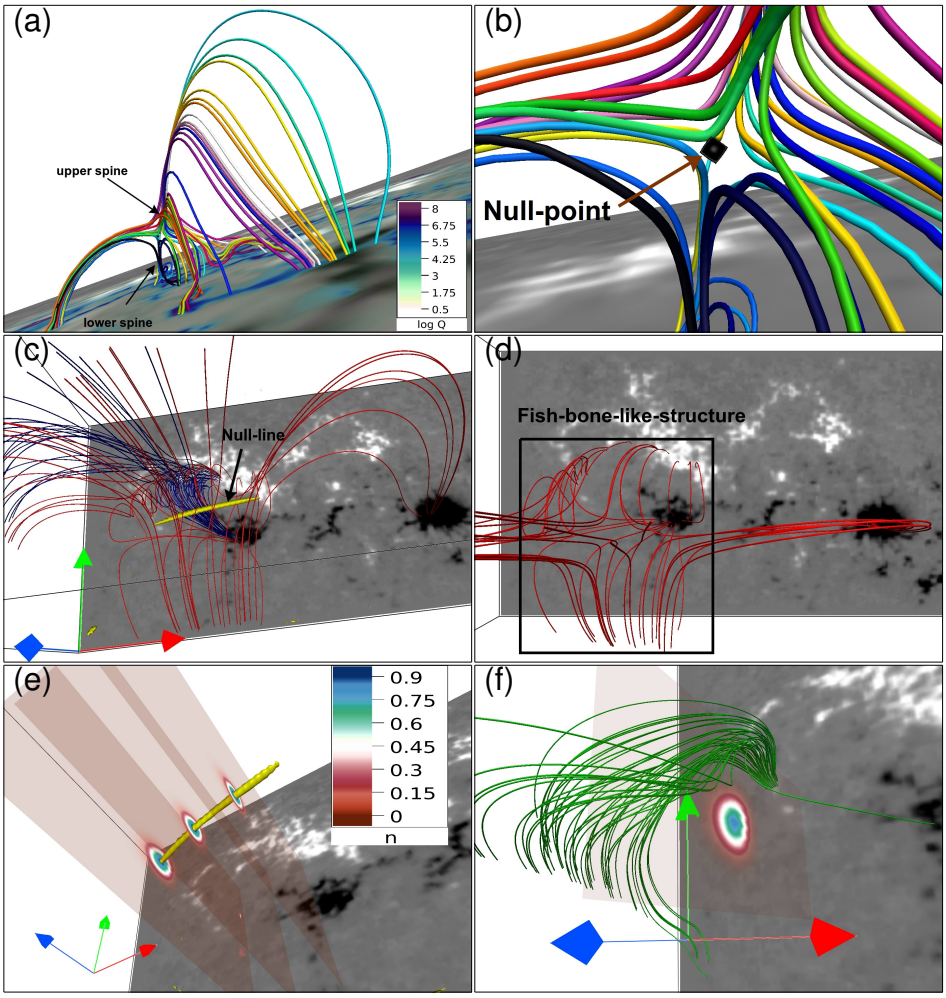

Figure 6.6: Panel (a) shows a 3D null spine-fan configuration in region R2 with the B_z as the bottom boundary overlaid with log Q between 5 and 10. Panel (b) is zoomed view of (a), highlighting the 3D null point (in black)—an iso surface of $n = 0.6$ indicated by an arrow. Panel (c) shows the side view of the magnetic field lines structure in region R3 along with the yellow surface representing the null-line corresponding to $n = 0.9$. Panel (d) shows the top-down view of red magnetic field lines of (c) forming a fish-bone-like structure. In panel (e) we show the value of n on the three different vertical planes passing through the cross-sections of the null-line surface. Notably, the planes show circles in the cross-section at different locations which indicates that the yellow surface is a null line. Panel (f) depicts magnetic field lines morphology in region R4 along with the value of n on a vertical plane where the green circular contour corresponds to $n = 0.6$ suggesting the right part of magnetic field lines morphology may be a part of the null-line geometry (shown in panel (c)).

marked black. The height of the null is found to be ≈ 3 Mm from the photosphere. The null is detected using the bespoke procedure (Kumar & Bhattacharyya, 2011; Nayak et al., 2020) approximates the Dirac delta on the grid as

$$n(B_i) = \exp\left[-\sum_{i=x,y,z}(B_i - B_o)^2/d_o^2\right], \tag{6.1}$$

where small constants B_o and d_o correspond to the isovalue of B_i and the Gaussian spread. The function $n(B_i)$ takes significant values only if $B_i \approx 0\ \forall i$, whereupon a 3D null is a point where the three isosurfaces having isovalues $B_i = B_o$ intersect.

Region R3: A side view of the magnetic field line morphology in region R3 is shown in Figure 6.6 (c), where the yellow surface corresponds to $n = 0.9$. Panel (d) highlights a "fish-bone-like" structure, similar to the schematic in Figure 5 of Wang et al. (2014). To show that in the limiting case $n = 0.9$ reduced to a null line, we plot corresponding contours in the range $0.6 \leq n \leq 0.9$ on three pre-selected planes highlighted in panel (e). The size reduction of the contours with increasing n indicates the surface converging to a line. Such null lines are also conceptualized as favorable reconnection sites (Wang et al., 2014).

Region R4: Figure 6.6 (f) shows magnetic field lines relevant to plasma rotation in B4. Notably, the null line from the R3 intrudes into R4 and the extreme left plane in R3 (Figure 6.6 (e)) is also shared by the R4.

6.4 Results: Comparison of the reconnections in the Hall MHD and MHD simulations of the flaring active region NOAA 12734

In the spirit of earlier related works (Prasad et al., 2018; Nayak et al., 2019; Prasad et al., 2020), the plasma is idealized to be incompressible and thermodynamically inactive as well as explicitly non-resistive. While this relatively simple idealization is naturally limited, it exposes the basic dynamics of magnetic reconnections unobscured by the effects due to compressibility and heat transfer. Albeit the

latter is important for coronal loops (Ruderman & Roberts, 2002), they do not directly affect the magnetic topology—in focus of this Chapter. Historically rooted in classical hydrodynamics, such idealizations have a proven record in theoretical studies of geo/astrophysical phenomena (Rossby et al., 1938; Dahlburg et al., 1991; Bhattacharyya et al., 2010; Bora et al., 2021). Inasmuch as their cognitive value depends on an a posteriori validation against the observations, the present study offers yet another opportunity to do so. The Hall forcing has been incorporated (Bora et al., 2021) in the computational model EULAG MHD (Smolarkiewicz & Charbonneau, 2013) to solve the dimensionless Hall MHD equations,

$$\frac{\partial \mathbf{v}}{\partial t} + (\mathbf{v}\cdot\nabla)\mathbf{v} = -\nabla p + (\nabla\times\mathbf{B})\times\mathbf{B} + \frac{1}{R_F^A}\nabla^2\mathbf{v}\ , \tag{6.2}$$

$$\frac{\partial \mathbf{B}}{\partial t} = \nabla\times(\mathbf{v}\times\mathbf{B}) - d_H\nabla\times((\nabla\times\mathbf{B})\times\mathbf{B})\ , \tag{6.3}$$

$$\nabla\cdot\mathbf{v} = 0\ , \tag{6.4}$$

$$\nabla\cdot\mathbf{B} = 0\ , \tag{6.5}$$

where $R_F^A = (v_A L_0/\nu)$, ν being the kinematic viscosity—is an effective fluid Reynolds number, having the plasma speed replaced by the Alfvén speed v_A. Hereafter R_F^A is denoted as a fluid Reynolds number for convenience. The transformation of the dimensional quantities (expressed in cgs-units) into the corresponding non-dimensional quantities,

$$\mathbf{B}\longrightarrow\frac{\mathbf{B}}{B_0},\quad \mathbf{x}\longrightarrow\frac{\mathbf{x}}{L_0},\quad \mathbf{v}\longrightarrow\frac{\mathbf{v}}{v_A},\quad t\longrightarrow\frac{t}{\tau_A},\quad p\longrightarrow\frac{p}{\rho_0 {v_A}^2}\ , \tag{6.6}$$

assumes arbitrary B_0 and L_0 while the Alfvén speed $v_A \equiv B_0/\sqrt{4\pi\rho_0}$. Here ρ_0 is a constant mass density, and d_H is the Hall parameter. In the limit of $d_H = 0$, Equation 6.2 - Equation 6.5 reduce to the MHD equations (Prasad et al., 2018).

The governing equations (Equation 6.2 - Equation 6.5) are numerically integrated using the 3D HMHD solver described in Chapter 3.

The simulations are carried out by mapping the physical domain of $256\times128\times128$ pixels on the computational domain of $x\in\{-1,1\}$, $y\in\{-0.5,0.5\}$, $z\in\{-0.5,0.5\}$ in a Cartesian coordinate system. The dimensionless spatial step sizes are $\Delta x=\Delta y=\Delta z\approx 0.0078$. The dimensionless time step is $\Delta t = 5\times10^{-4}$,

set to resolve whistler speed—the fastest speed in incompressible Hall MHD. The rationale is briefly presented in Appendix A. The corresponding initial state is motionless ($\mathbf{v} = 0$) and the initial magnetic field is provided from the non-FFF extrapolation. The non-zero Lorentz force associated with the extrapolated field pushes the magnetofluid to initiate the dynamics. Since the maximal variation of magnetic flux through the photosphere is only 2.28% of its initial value during the flare (not shown), the B_z at the bottom boundary (at $z = 0$) is kept fixed throughout the simulation while all other boundaries are kept open. For velocity, all boundaries are set open. The mass density is set to $\rho_0 = 1$.

The fluid Reynolds number is set to 500, which is roughly two orders of magnitude smaller than its coronal value ≈ 25000 (calculated using kinematic viscosity $\nu = 4 \times 10^9$ m^{2}s^{-1} (Aschwanden, 2005) in the solar corona). Without any loss in generality, the reduction in R_F^A can be envisaged to cause a reduction in computed Alfvén speed, $v_A|_{\text{computed}} \approx 0.02 \times v_A|_{\text{corona}}$ where the L for the computational and coronal length scales are set to 71 Mm and 100 Mm respectively. This diminished Alfvén speed reduces the requirement of computational resources and also relates it with the observation time. The results presented herein pertain to a run for $1200\Delta t$ which along with the normalizing $\tau_A \approx 3.55 \times 10^3$ s roughly corresponds to an observation time of $\approx$ 35 minutes. For ease of reference in comparison with observations, we present the time in minutes (03:00 UT onwards) in the discussions of the figures given in this chapter. Although the coronal plasma idealized to have reduced Reynolds number is inconsequential here, in a comparison of MHD and Hall MHD evolution, we believe the above rationale merits further contemplation. Undeniably such a coronal plasma is not a reality. Nevertheless, the reduced R_F^A does not affect the reconnection or its consequence, but slows down the dynamics between two such events and importantly—reduces the computational cost, making data-based simulations realizable even with reasonable computing resources. A recent work by Jiang et al. (2016) used a homologous approach toward simulating a realistic and self-consistent flaring region.

In the present simulations, all parameters are identical for the MHD and the Hall MHD except for the d_H, respectively set to 0 and 0.004. The value 0.004 is motivated by recognizing ILES dissipation models intermittent magnetic recon-

nections at the $\mathcal{O}(\| \Delta\mathbf{x} \|)$ length scales, consistent with the thesis put forward in Introduction, we specify an appreciable Hall coefficient as $d_H = 0.5\Delta z/L \approx 0.004$, where $L = 1 \equiv$ smallest extent of the computational volume, having $\Delta y = \Delta z \approx 0.0078$ as the dissipation scales because of the ILES property of the model. Correspondingly, the value is also at the lower bound of the pixel or scale order approximation and, in particular, an order of magnitude smaller than its coronal value valid at the actual dissipation scale. An important practical benefit of this selection is the optimization of the computational cost while keeping magnetic field line dynamics tractable. Importantly, with dissipation and Hall scales being tied, an increased current density at the dissipation scale introduces additional slippage of field lines in Hall MHD over MHD (due to the Hall term) and, may be responsible for more effective and faster reconnections found in the Hall simulation reported below.

The simulated Hall MHD and MHD dynamics leading to the flare show unambiguous differences. Here we document these differences by comparing methodically simulated evolution of the magnetic structures and topologies in the AR NOAA 12734—namely, the flux rope, QSLs, and null points—identified in the extrapolated initial data in the regions R1-R4.

6.4.1 Region R1

The dynamics of region R1 are by far the most complex among the four selected regions. To facilitate future reference as well as to outline the organization of the discussion that follows, Table 6.1 provides a brief summary of our findings—in a spirit of theses to be proven by the simulation results. The global dynamics of magnetic field lines in region R1 is illustrated in Figure 6.7; consult Figure 6.5 for the initial condition and terminology. The snapshots from the Hall MHD and MHD simulations are shown in panels (a)-(d) and (e)-(f), respectively. In panels (a) and (b), corresponding to $t = 5.6$ min and $t = 13.6$ min, the foot points of magnetic field lines Set II (near P2, marked maroon) exhibit slipping reconnection along high values of the squashing factor Q indicated by black arrows. Subsequently, between $t = 23.7$ min and 24.0 min in panels (c) and (d), the magnetic field lines Set II rise in the corona and reconnect with magnetic field lines Set I to

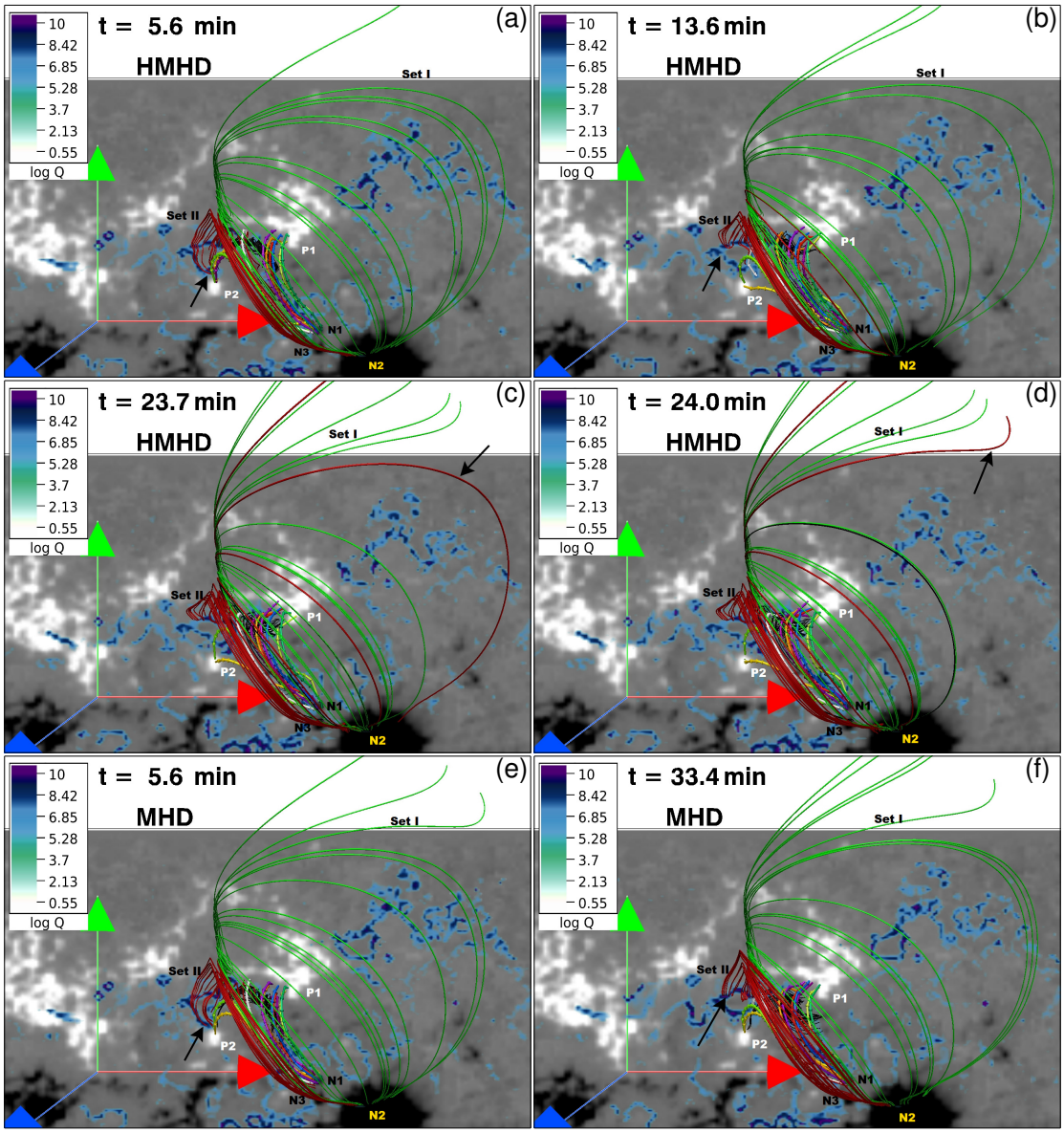

Figure 6.7: Snapshots of the global dynamics of magnetic field lines in region R1 during the Hall MHD and MHD simulations are shown in panels (a)-(d) and panels (e)-(f) respectively. Panels (a) and (b) show the departure of foot points of magnetic field lines Set II (maroon) away from polarity P2 between $t = 5.6$ min and 13.6 min on the bottom boundary (marked by black arrow). Panel (c) depicts the rising magnetic field lines Set II (maroon) higher up in the solar corona at $t = 23.7$ min (marked by black arrow) and (d) shows subsequent connectivity change of rising magnetic field lines at $t = 24.0$ min, due to reconnection with the Set I (green) magnetic field lines. Panels (e) and (f) depict the departure of foot points of magnetic field lines Set II (maroon) away from P2 between $t = 5.6$ min to 33.4 min which is similar to the Hall MHD but delayed in time—indicating the slower dynamics in the MHD. Notably, a significant rise of magnetic field lines Set II and consequent reconnection of it with magnetic field lines Set I higher up in the solar corona is absent in the MHD simulation.

change connectivity. The MHD counterpart of the slipping reconnection in panels (e) and (f), corresponds to magnetic field lines Set II between $t = 5.6$ min and $t = 9.8$ min. It lags behind the Hall MHD displays, thus implying slower dynamics. Furthermore, the magnetic field lines Set II, unlike for the Hall MHD, do not reach up to the magnetic field lines Set I constituting QSL1 and hence do not reconnect. The decay index is calculated for each time instant for both the simulations and is found to be less than 1.5 above the flux rope, indicating an absence of the torus instability (Kliem & Török, 2006). For more detail, Figure 6.8 and Figure 6.9 illustrate the evolution of QSL2 and flux rope separately.

Magnetic field lines structure	Hall MHD	MHD
QSL1	Fast reconnection followed by a significant rise of loops, eventually reconnecting higher in the corona.	Slow reconnection followed by a limited rise of loops.
QSL2	Fast reconnections cause the magnetic field lines to entirely disconnect from the polarity P2.	Due to slow reconnection magnetic field lines remain connected to P2.
Flux rope	Fast slipping reconnection of the flux-rope foot points, followed by the expansion and rise of the rope envelope.	Slow slipping reconnection and rise of the flux-rope envelope; the envelope does not reach the QSL1.

Table 6.1: Salient features of magnetic field lines dynamics in R1

Figure 6.8 panels (a)-(b) and (c)-(d) show, respectively, the instants from the Hall MHD and MHD simulations of QSL2 between P1, P2, and N1. The Hall MHD instants show magnetic field lines that were anchored between P2 and N1 at $t = 3.0$ min and have moved to P1 around $t = 3.0$ min, marked by black arrows in both panels. The magnetic field lines anchored at P2 moved to P1 along the high Q values—signifying the slipping reconnection. The MHD instants in panels (c)-(d) show the connectivity changes of the violet and white colored magnetic

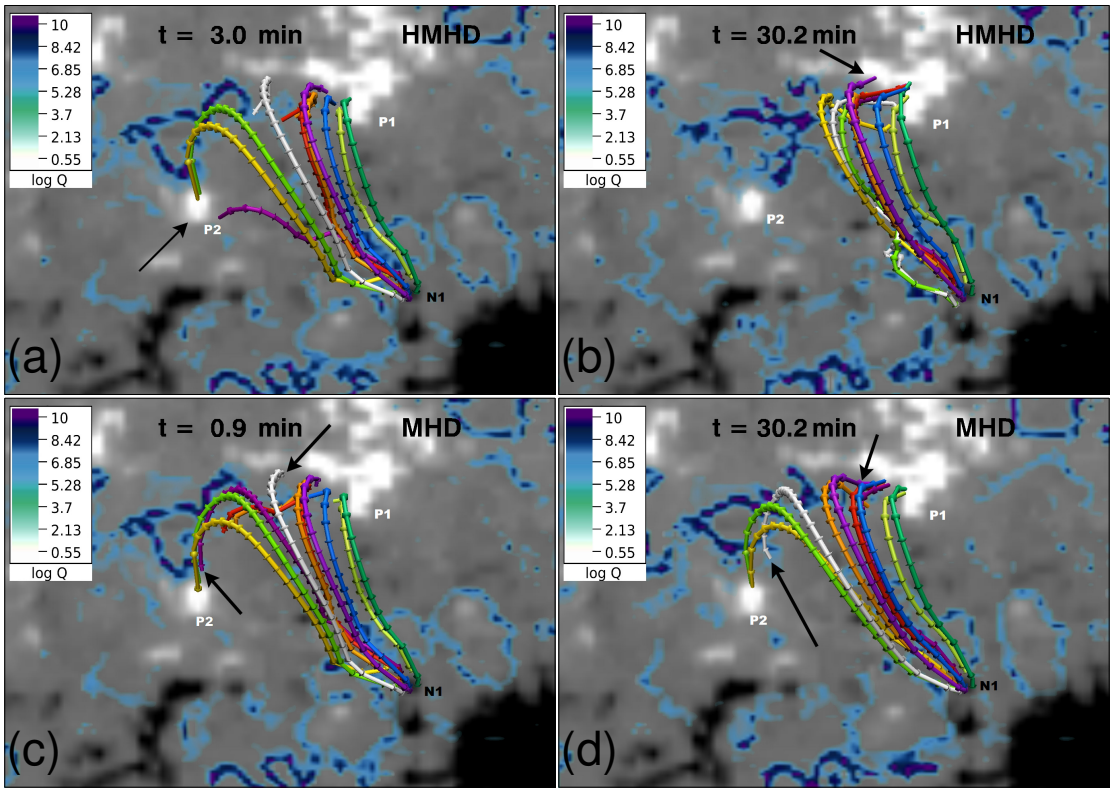

Figure 6.8: Snapshots of the Hall MHD and MHD evolution of QSL2 (Figure 6.5 (c)) are shown in panels (a)-(b) and panels (c)-(d) respectively. Panels (a)-(b) show magnetic field lines anchored in the positive polarity P2 at $t = 3.0$ min have moved to the polarity P1 by $t = 3.0$ min and changed their connectivity (marked by black arrow) due to reconnection along QSL during the Hall MHD. Panels (c)-(d) show the connectivity changes of the violet and white color magnetic field lines during the MHD evolution. The white field line was initially connecting the polarities P1 and N1 whereas the violet field line was connecting P2 and N1. As a result of reconnection along QSL, the white field line changes its connectivity from P1 to P2 and the violet field line changes the connectivity from P2 to P1 (marked by black arrows). Notably, unlike the Hall MHD simulation, not all magnetic field lines move to P1 from P2 due to reconnection along QSL during the MHD which indicates slower dynamics.

field lines. The white field line was initially connecting P1 and N1, whereas the violet field line was connecting P2 and N1. As a result of reconnection along QSL, the white field line changed its connectivity from P1 to P2, and the violet field line changes its connectivity from P2 to P1 (marked by black arrows). Notably, in contrast to the Hall MHD evolution, all magnetic field lines initially anchored in P2 do not change their connectivity from P2 to P1 during the MHD evolution, indicating slower dynamics. The flux rope has been introduced in panels (c) and (d) of Figure 6.5, respectively, below the QSL2 and in enlargement. Its Hall MHD and MHD evolutions along with the twists on three different vertical cross sections

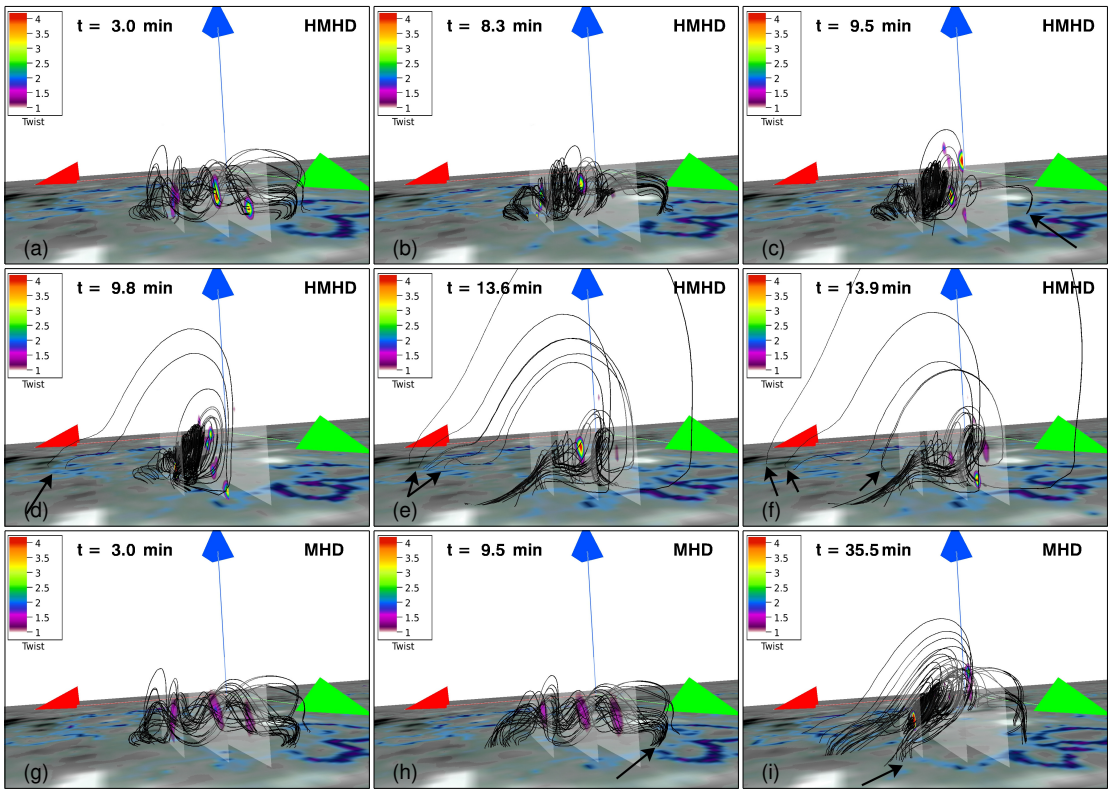

Figure 6.9: Time sequence showing the Hall MHD (panels (a)-(f)) and MHD (panels (g)-(i)) evolution of the flux rope (shown in Figure 6.5(c)) along with the twist T_w. Panel (a) shows the twist on the middle and the right plane on the flux rope is higher than initial values (c.f. Figure 6.5(d)) and reduced with time in panel (b). Panels (c)-(d) depict the connectivity change of the foot point of the rope from right to left (indicated by the black arrow) due to reconnection along QSL. Panels (e)-(f) show the connectivity change of magnetic field lines on left-hand side (indicated by the black arrow). Panels (g)-(i) depict the dynamic rise of the flux rope between $t = 3.0$ min and $t = 35.5$ min during the MHD simulation. Notably, the foot points of the rope on the right side (marked by black arrow) at $t = 9.5$ min in (h) have moved towards left by $t = 35.5$ min in (i) as a result of reconnection along QSL.

are shown in panels (a)-(f) and (g)-(i) of Figure 6.9, respectively. Magnetic field lines constituting the rope, rise substantially higher during the Hall MHD evolution as a result of slipping reconnection along the high Q in panels (c)-(f). In panel (c) at $t = 9.5$ min, the foot points of the rope that are anchored on the right side (marked by the black arrow) change their connectivity from one high Q regime to another in panel (d) at $t = 9.8$ min; i.e., the foot points on the right have moved to the left side (marked by black arrow). Afterward, the magnetic field lines rise because of the continuous slipping reconnection, as evidenced in panels (e) to (f). Comparing panels (a) with (g) at $t = 3.0$ min and (c) with (h) at $t = 9.5$ min, we

note that the twist value T_w is higher in the Hall MHD simulation. Panels (h)-(i) highlight the displaced foot points of flux rope due to slipping reconnection at $t = 9.5$ min and $t = 35.5$ min (cf. black arrow). The rope is preserved throughout the Hall MHD and MHD simulations. The rise and expansion of the flux-rope envelope owing to slipping reconnection is remarkable in the Hall MHD simulation. Dudík et al. (2014) have already shown such a flux-rope reconnection along QSL in a J-shaped current region, with slipping reconnection causing the flux rope to form a sigmoid (S-shaped hot channel observed in EUV images of SDO/AIA) followed by its rise and expansion. Further insight is gained by overlaying the flux rope evolution shown in Figure 6.9 with direct volume rendering of $|\mathbf{J}|/|\mathbf{B}|$ (Figure 6.10 and Figure 6.11) as a measure of magnetic field gradient for the Hall MHD and MHD simulations. In the Hall MHD case, the appearance of large values of $|\mathbf{J}|/|\mathbf{B}| > 475$ inside the rope (panels (a) to (c)) and foot points on the left to the rope (panels (d) to (e)) are apparent. The development of the large $|\mathbf{J}|/|\mathbf{B}|$ is indicative of reconnection within the rope. Contrarily, MHD simulation lacks such high values of $|\mathbf{J}|/|\mathbf{B}|$ in the same time span (panels (a)-(b)) and the field lines show no slippage—agreeing with the proposal that large currents magnify the Hall term, resulting into more effective slippage of field lines.

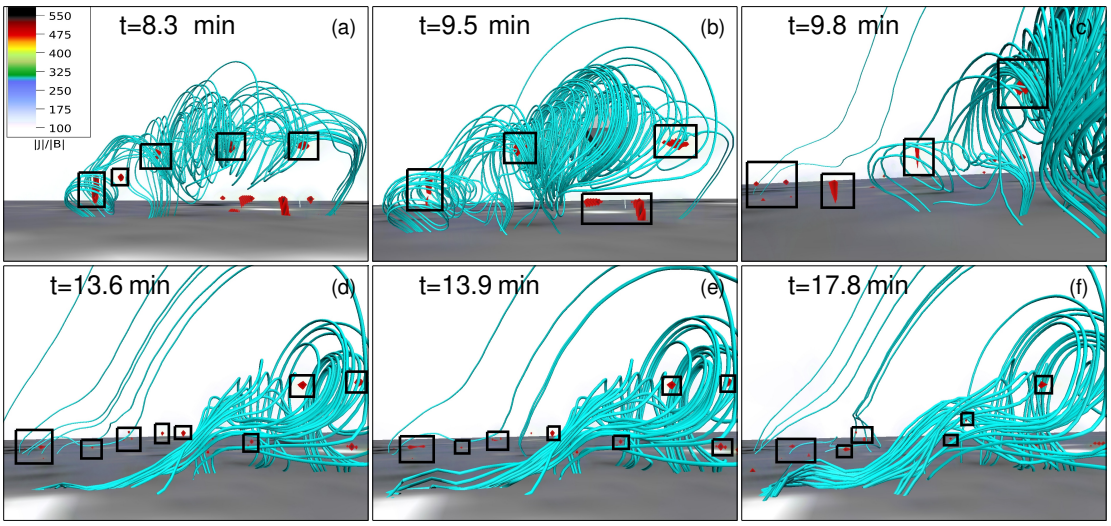

Figure 6.10: Temporal variation of the direct volume rendering of ($|\mathbf{J}|/|\mathbf{B}|$) along with the flux rope is shown during the Hall MHD simulation. Noticeably, the high magnetic field gradient regions with ($|\mathbf{J}|/|\mathbf{B}|$) ≥ 475 develop within (panels (a) to (c)) and on the left side of the flux rope (panels (d) to (f)). The values ($|\mathbf{J}|/|\mathbf{B}|$) ≥ 475 in each panel are enclosed within the black rectangular boxes.

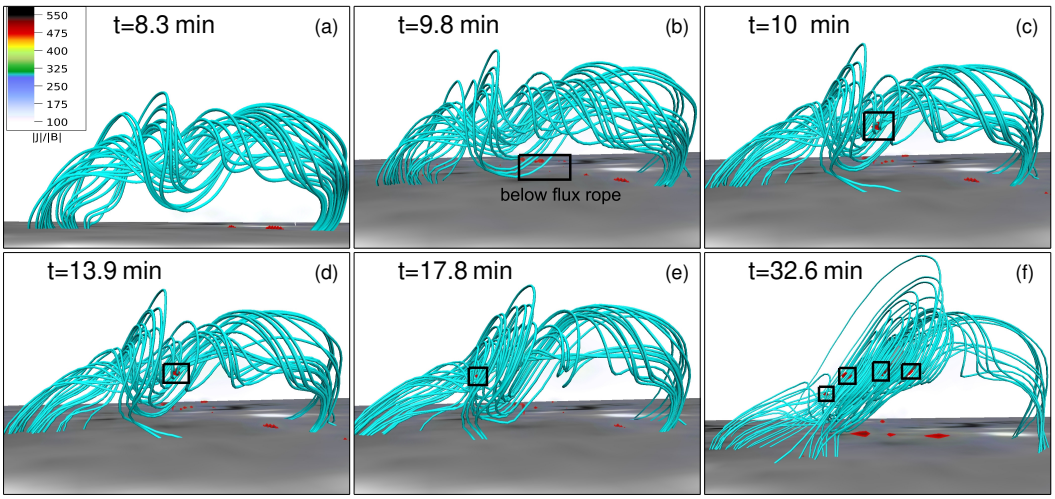

Figure 6.11: Temporal variation of the direct volume rendering of ($|\mathbf{J}|/|\mathbf{B}|$) along with the flux rope is shown during the MHD simulation. Panels (a) and (b) shows the absence of high values of ($|\mathbf{J}|/|\mathbf{B}|$) within the rope at $t = 8.3$ min and $t = 9.5$ min but in later panels (c) to (f) ($|\mathbf{J}|/|\mathbf{B}|$) ≥ 475 appears (enclosed by the black rectangular boxes). Notably, as compared to the Hall MHD case (Figure 6.10), the development of ($|\mathbf{J}|/|\mathbf{B}|$) is not significant in the region R1 during the MHD.

6.4.2 Region R2

To compare the simulated magnetic field lines dynamics in region R2 with the observed tip of the W-shaped flare ribbon B2 (Figure 6.4 (a)) during the Hall MHD and MHD evolution, we present the instants from both simulations at $t = 20.7$ min in panels (a) and (b) of Figure 6.12 respectively. Importantly, the lower

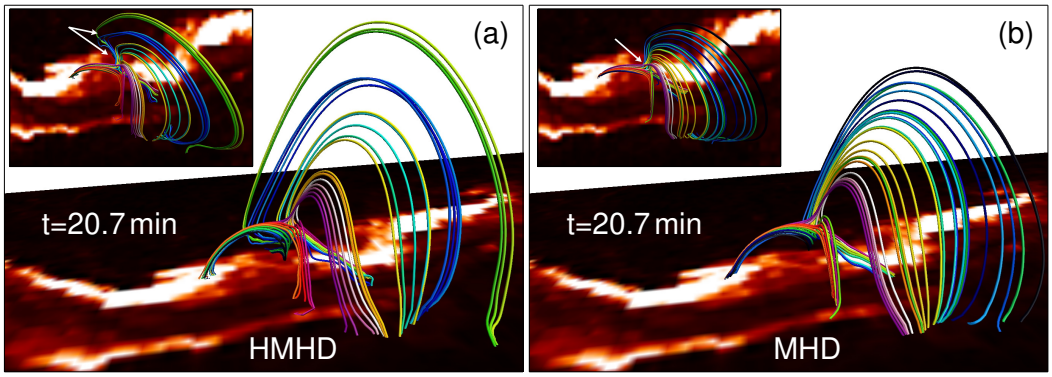

Figure 6.12: Panels (a) and (b) show the comparison of magnetic field lines topology in region R2 at $t = 20.7$ min with the flare ribbons observed in the SDO/AIA 304 Å channel (side views) during the Hall MHD and MHD simulations respectively. The inset images on the top left corner of each panel show the top view of the same magnetic field lines topology. Notably, the spine is anchored in the Hall MHD while it is not connected to the bottom boundary in the MHD at $t = 20.7$ min (marked by the white arrow in inset images).

spine remains anchored to the bottom boundary during the Hall MHD simulation.

Further, Figure 6.13 shows the evolution of the lower spine along with the $|\mathbf{J}|/|\mathbf{B}|$ on the bottom boundary for the Hall MHD (panels (a) to (d)) and MHD (panels (e) to (h)) cases. In the Hall MHD case, noteworthy is the slipping motion of the lower spine (marked by the black arrows) tracing the $|\mathbf{J}|/|\mathbf{B}| > 350$ regions on the bottom boundary (panels (a) to (b)). Whereas, in the MHD such high values of

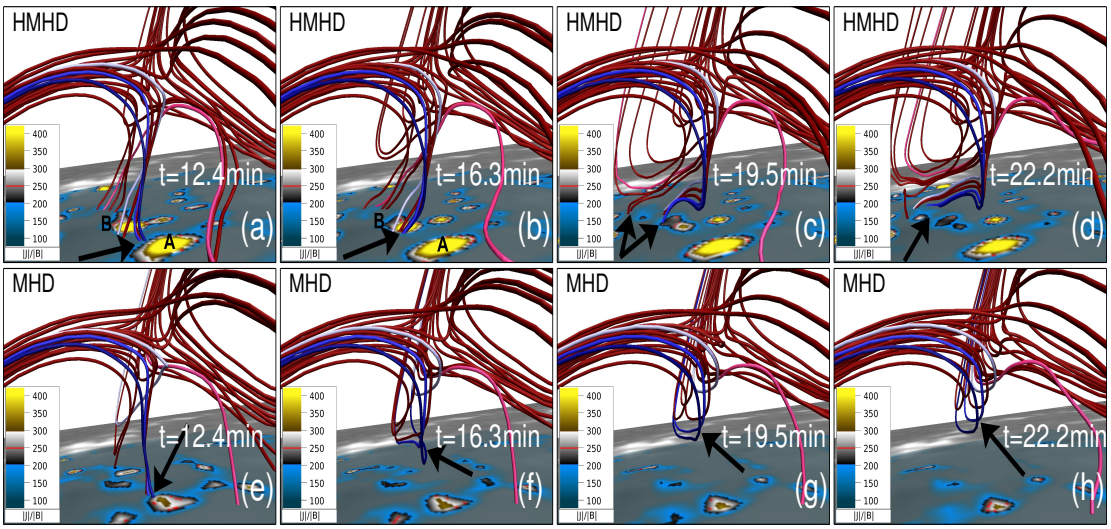

Figure 6.13: Panels (a) to (d) depict the slipping motion of the lower spine field lines (also shown in Figure 6.6) overlaid with the $|\mathbf{J}|/|\mathbf{B}|$ on the bottom boundary during the Hall MHD evolution. The motion is marked by the black arrows in all the panels indicating the successive change in the location of field lines on the bottom boundary. A and B (in panels (a) and (b)) are the two regions with $|\mathbf{J}|/|\mathbf{B}| > 350$ on the bottom boundary (just below the lower spine). Notably, the field lines follow the high values of $|\mathbf{J}|/|\mathbf{B}|$ on the bottom boundary and remain anchored. Panels (e) to (h) show the evolution of the same lower spine field lines during the MHD simulation. The large values of $|\mathbf{J}|/|\mathbf{B}|$ do not appear below the lower spine (on the bottom boundary) and it does not remain anchored from $t \approx 55$ onward (panels (f) to (h)).

$|\mathbf{J}|/|\mathbf{B}|$ are absent on the bottom boundary—suggesting the slippage of the field lines on the bottom boundary to be less effective in contrast to the Hall MHD. The finding is in agreement with the idea of enhanced slippage of field lines due to high current densities as conceptualized in the introduction. The anchored lower spine provides a path for the plasma to flow downward to the brightening segment B2. In the actual corona, such flows result in flare brightening (Benz, 2008). In contrast, the lower spine (the bunch of traced field lines) gets completely disconnected from the bottom boundary (Figure 6.12 (b) and Figure 6.13(h)) in the MHD simulation, hence failing to explain the tip of the W-shaped flare ribbon in B2. The anchored lower spine in the Hall MHD simulation is caused by a complex series of magnetic

field line reconnections at the 3D null and along the QSLs in R2.

6.4.3 Region R3

Hall MHD and MHD simulations of magnetic field lines dynamics around the null-line are shown in Figure 6.14 and Figure 6.15 respectively. Figure 6.14 shows

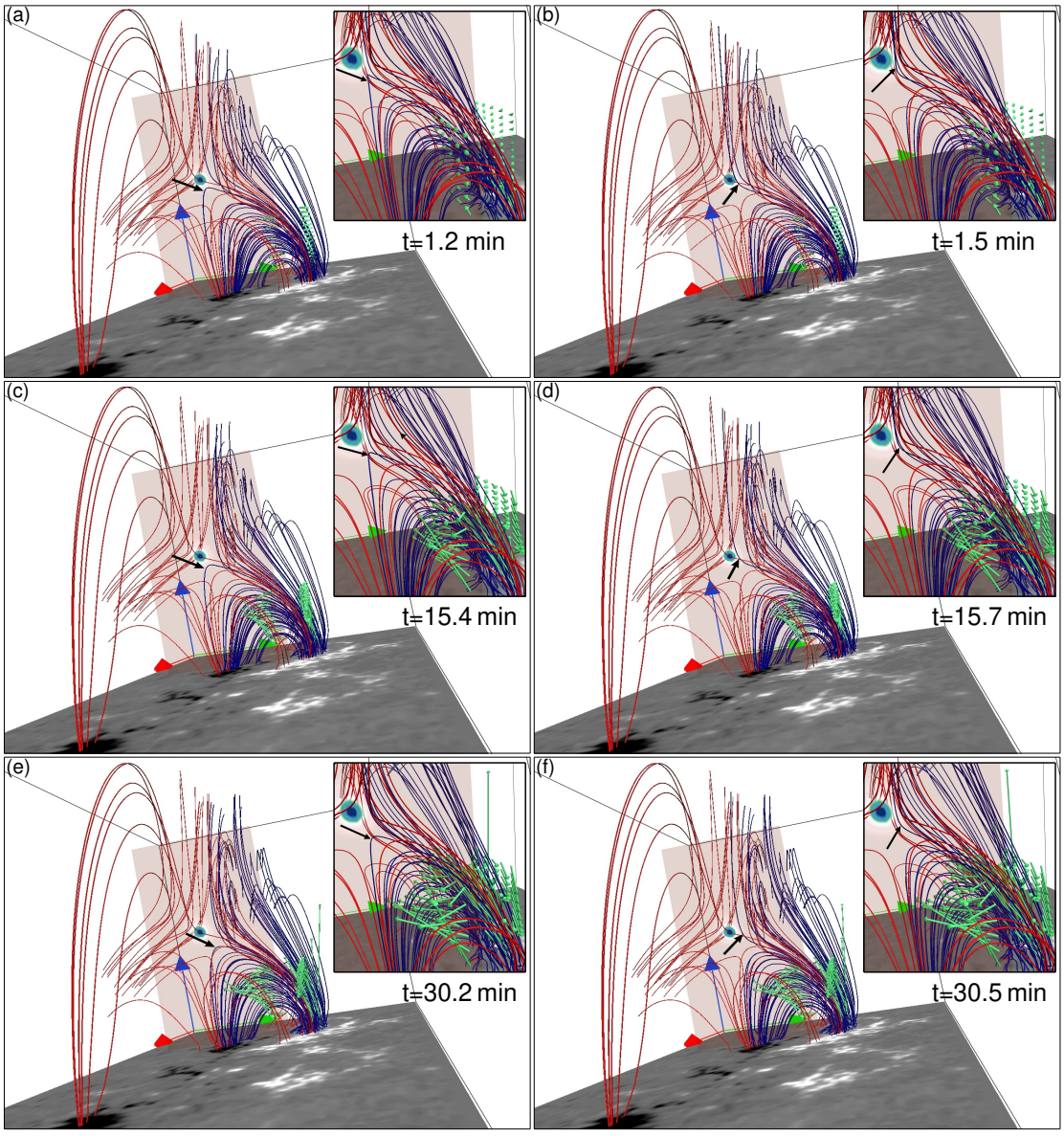

Figure 6.14: Time sequence showing the blue field line prior to and after reconnection (indicated by the black arrow) in region R3 during the Hall MHD simulation. The evolution of the flow vectors is depicted by green arrows (on the right side)—mimicking the direction of the plasma flow. The plane along the cross-section of magnetic field lines morphology in R3, showing the blue circular contours represent the value of n (also shown in Figure 6.6(d)).

the blue magnetic field lines prior to and after the reconnections (indicated by

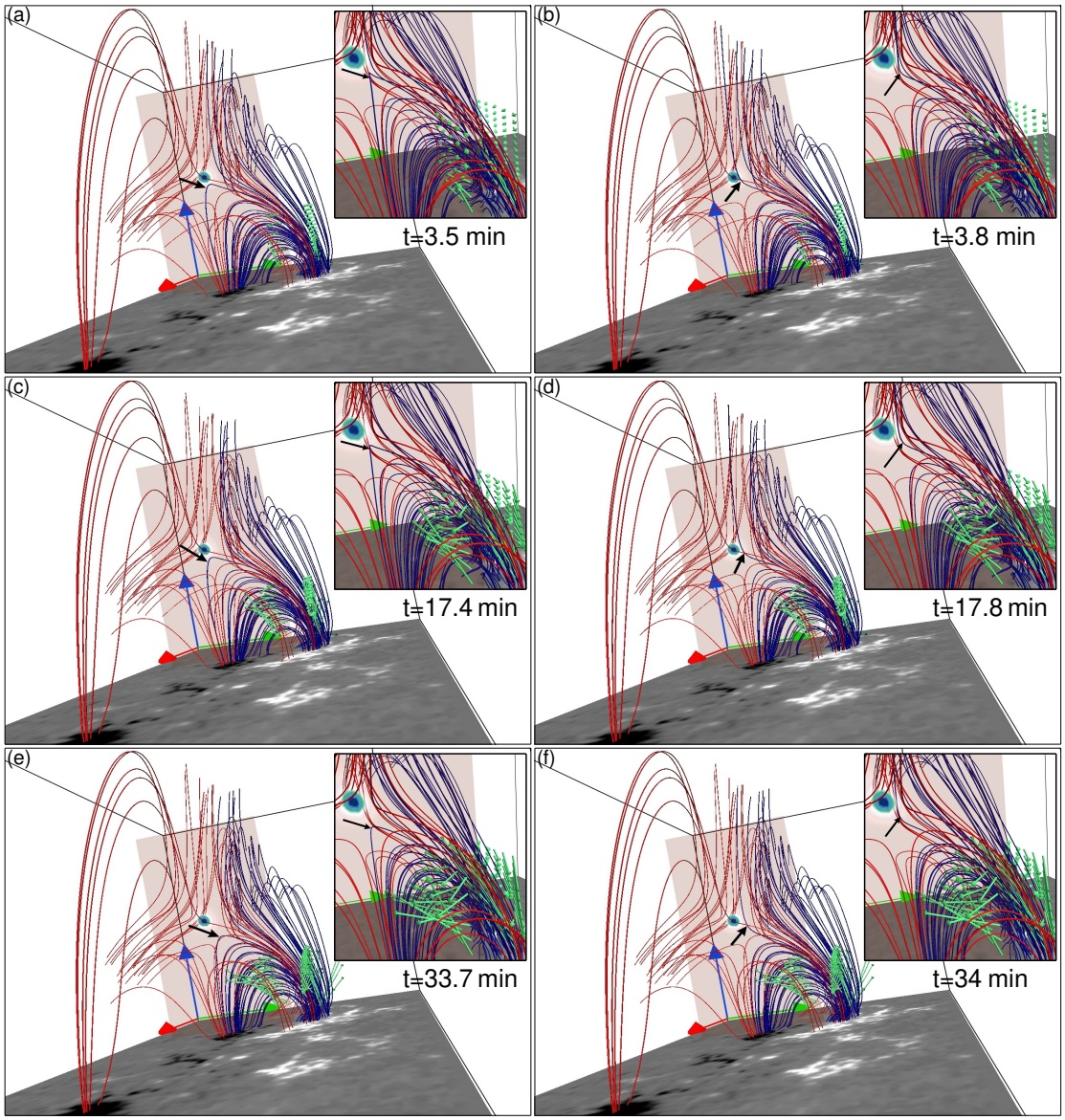

Figure 6.15: Time sequence showing the blue field line prior to and after reconnection (indicated by the black arrow) in region R3 during the MHD simulation. The evolution of the flow vectors is depicted by green arrows (on the right side)—mimicking the direction of the plasma flow. The plane along the cross-section of magnetic field lines morphology in R3, showing the blue circular contours represent the value of n (also shown in Figure 6.6(d)). Notably, reconnection of the blue magnetic field lines is slightly delayed in comparison to its Hall MHD counterpart.

black arrows) between $t = 1.2$ to 1.5 min (panels (a)-(b)), $t = 15.4$ to 15.7 min (panels (c)-(d)), and $t = 30.2$ to 30.5 min (panels (e)-(f)) during the Hall MHD simulation. Figure 6.15 shows the same blue magnetic field lines prior to and after the reconnections (indicated by black arrows) between $t = 3.5$ to 3.8 min (panels (a)-(b)), $t = 17.4$ to 17.8 min (panels (c)-(d)), and $t = 33.7$ to 34.0 min (panels (e)-(f)) during the MHD simulation. Comparison of the panels (a)-(f) of

Figure 6.14 with the same panels of Figure 6.15 reveals earlier reconnections of the blue magnetic field lines in the Hall MHD simulation. In both figures, green velocity vectors on the right represent the local plasma flow.

They get aligned downward along the foot points of the fan magnetic field lines, as reconnection progresses. Consequently, the plasma flows downward and impacts the denser and cooler chromosphere to give rise to the brightening in B3. The velocity vectors pointing upward represent a flow toward the null-line. The plasma flow pattern in R3 is the same in the Hall MHD and in the MHD simulation. The vertical yz plane passing through the cross-section of the null-line surface (also shown in Figure 6.6 (d)) in all the panels of Figure 6.14 and Figure 6.15 shows the variation of n with time. It is evident that the null is not destroyed throughout the Hall MHD and MHD evolution. Structural changes in the field lines caused by reconnection are near-identical for both the simulations, indicating the inefficacy of the Hall term. This inefficacy is justifiable as $|\mathbf{J}|/|\mathbf{B}|$ remains small ≈ 10 (not shown) in both Hall MHD and MHD evolution.

6.4.4 Region R4

The development of the circular motion of magnetic field lines in region R4 during the Hall MHD simulation is depicted in Figure 6.16. It shows the global dynamics of magnetic field lines in R4 and the inset images show the zoomed view of magnetic field lines in R4 to highlight the circular motion of magnetic field lines. The bottom boundary is B_z in the main figure while the inset images have the z component of the plasma flow at the bottom boundary (on xy plane). The red vectors represent the plasma flow direction as well as magnitude in all the panels of Figure 6.16 where the anticlockwise pattern of the plasma flow is evident. The global dynamics highlights reconnection of the loop anchored between positive and negative polarities at $t = 17.8$ min in Figure 6.16 as it gets disconnected from the bottom boundary in panels (c)-(d) of Figure 6.16. In simulation, an anticlockwise motion of the foot points is found in the same direction as the plasma flow, indicating field lines to be frozen in the fluid. The trapped plasma may cause the rotating structure B4 in the observations (c.f. Figure 6.4 (a)). However, no such motion is present during the MHD evolution of the same magnetic field lines (not

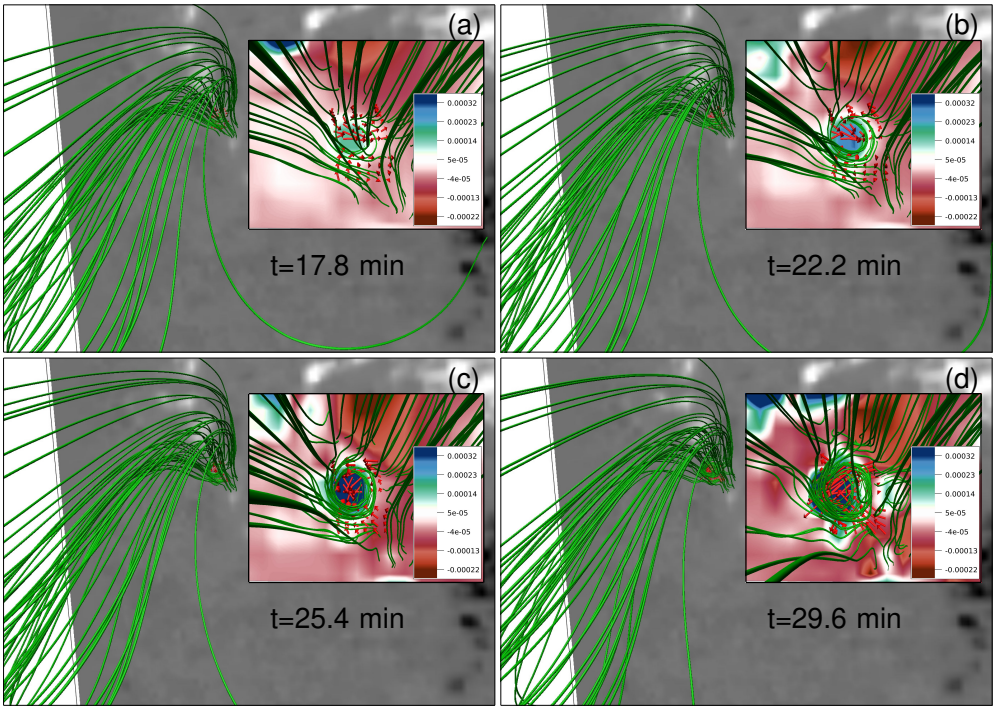

Figure 6.16: Panels (a)-(d) show the global dynamics of magnetic field lines in region R4 during the Hall MHD simulation. Inset images in each panel (on right) depict the time sequence of the zoomed top-down view of the rotational motion of magnetic field lines. The background shows the variation of the z-component of flow $\in$ [-0.00022,0.00032] in all inset images. The red vectors represent the plasma flow and change its direction in an anticlockwise manner in panels (a)-(d). The rotational motion of magnetic field lines coincides with the circular part of the flow.

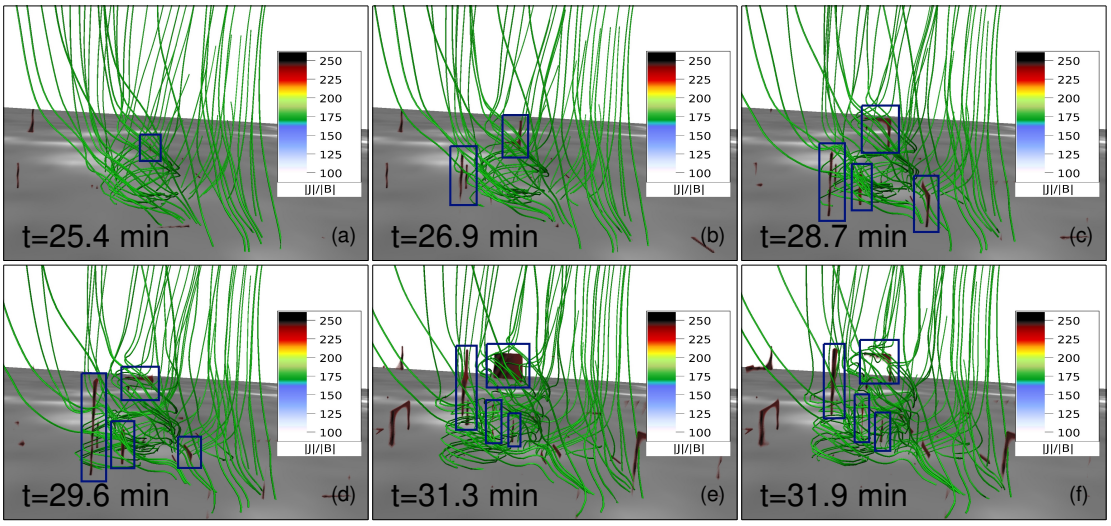

Figure 6.17: Panels (a) to (f) show the side view of the rotating magnetic field lines structure in the region R4 overlaid with $|\mathbf{J}|/|\mathbf{B}|$. The figure depicts the temporal development of strong magnetic field gradient regions of $|\mathbf{J}|/|\mathbf{B}| > 225$ (enclosed in the blue rectangular boxes) within the rotating magnetic structure.

shown). An interesting feature noted in the simulation is the clockwise slippage of field lines after the initial anticlockwise rotation. Further analysis of R4 using the direct volume rendering of $|\mathbf{J}|/|\mathbf{B}|$ is presented in Figure 6.17. The figure shows $|\mathbf{J}|/|\mathbf{B}|$ attains high values ≥ 225 (enclosed by the blue rectangles) within the rotating field lines from $t = 25.4$ min onward. This suggests the slippage of field lines is, once again, related to the high magnetic field gradients.

For completeness, we present the snapshots of an overall magnetic field lines morphology including the magnetic structures and topology of regions R1, R2, R3, and R4 together, overlaid with 304 Å and 171 Å from the Hall MHD and MHD simulations. Figure 6.18 (a) shows an instant (at $t = 22.2$ min) from the Hall MHD simulation where the topologies and magnetic structures in R1, R2, R3, and R4, plus the additionally drawn locust color magnetic field lines between R2 and R3 are shown collectively. It shows an excellent match of the magnetic field lines in R2 with the observed tip of the W-shaped flare ribbon at B2, which is pointed out by the pink arrow in panel (a). Foot points of the spine-fan geometry around the 3D null orient themselves in the same fashion as the observed tip of the W-shaped flare ribbon at B2 as seen in the 304 Å channel of SDO/AIA. The rising loops indicated by the white arrow correspond to the same evolution as shown in Figure 6.7. An overall magnetic field lines morphology mentioned in Figure 6.16 (a) is given at the same time ($t = 22.2$ min) during the MHD simulation overlaid with 304 Å image in Figure 6.16 (b). Importantly, unlike the Hall MHD simulation, the MHD simulation does not account for the anchored lower spine and fan magnetic field lines of the 3D null at the center of the B2. Also, the significant rise of overlying maroon magnetic field lines and the circular motion of the material in B4 is captured in the Hall MHD simulation only. In panel (c) magnetic field lines overlaid with 171 Å image shows the magnetic field lines (higher up in the solar atmosphere) have a resemblance with the post-flare loops during the Hall MHD. Overall, the Hall MHD evolution seems to be in better agreement with the observations in comparison to the MHD evolution.

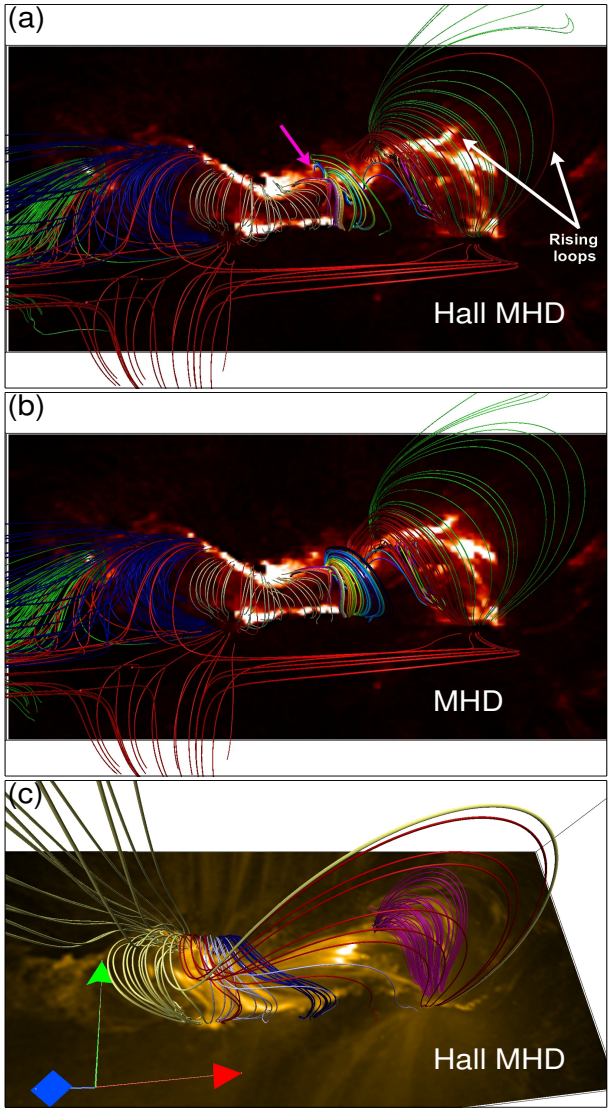

Figure 6.18: Top-down view of an overall magnetic field lines morphology overlaid on the SDO/AIA 304 Å (panels (a) and (b)) and 171 Å images (panel (c)). Anchored magnetic field lines foot points in the central part match well with the observed tip of the W-shaped flare ribbon (marked by the pink arrow in panel (a)) in the Hall MHD while magnetic field lines foot points are completely disconnected from the bottom boundary in the MHD (panel (b)). Loops rising higher up in the corona is remarkable in the Hall MHD (indicated by the white arrow in panel (a)).

6.5 Summary

In this Chapter, the data-based Hall MHD and MHD simulations are compared for the flaring Active Region NOAA 12734 as a test bed. The importance of the Hall MHD stems from the realization that the Hall term in the induction equation cannot be neglected in presence of the magnetic reconnection—the underlying cause of solar flares. The selected event is the C1.3 class flare on March 08, 2019 around 03:19 UT for the aforementioned comparison. Although the event is analyzed and

reported in the literature, it is further explored using the multiwavelength observations from SDO/AIA. The identified important features are: an elongated extreme ultraviolet (EUV) counterpart of the eruption on the western side of the AR, a W-shaped flare ribbon, and a circular motion of cool chromospheric material on the eastern part. The magnetic field line dynamics near these features are utilized to compare the simulations. Notably, the simulations idealize the corona to have an Alfvèn speed that is two orders of magnitude smaller than its typical value. Congruent to the general understanding, the Hall parameter is selected to tie the Hall dynamics to the dissipation scale $\mathcal{O}(\Delta \mathbf{x})$ in the spirit of the ILES carried out in the Chapter. The magnetic reconnection here is associated with the slippage of magnetic field lines from the plasma parcels, effective at the dissipation scale due to the local enhancement of the magnetic field gradient. The same enhancement also amplifies the Hall contribution, presumably enhancing the slippage and thereby making the reconnection faster and more effective than the MHD as put forward in Section 1.7.

The coronal magnetic field is constructed by extrapolating the photospheric vector magnetic field obtained from the SDO/HMI observations employing the non-FFF technique (Hu et al., 2010). The concentrated distribution of the Lorentz force on the bottom boundary and its decrease with the height justify the use of non-FFF extrapolation for the solar corona. The initial non-zero Lorentz force is also crucial in generating self-consistent flows that initiate the dynamics and cause magnetic reconnections. Analyses of the extrapolated magnetic field reveal several magnetic structures and topologies of interest: a flux rope on the western part at the flaring location, a 3D null point along with the fan-spine configuration at the center, a "Fish-bone-like structure" surrounding the null-line on the eastern part of the AR. All of these structures are found to be co-spatial with the observed flare ribbon brightening.

The Hall MHD simulation shows faster slipping reconnection of the flux rope foot points and overlying magnetic field lines (constituting QSLs above the flux rope) at the flaring location. Consequently, the overlying magnetic field lines rise, eventually reaching higher up in the corona and reconnecting to provide a path for plasma to eject out. The finding is in agreement with the observed elongated

EUV counterpart of the eruption on the western part of the AR. Contrarily, such a significant rise of the flux rope and overlying field lines to subsequently reconnect higher up in the corona is absent in the MHD simulation—signifying the reconnection to be slower compared to the Hall MHD. Intriguingly, the rise and expansion of the flux rope and overlying field lines owing to slipping reconnection on QSLs has also been modeled and observed in an earlier work by Dudík et al. (2014). These are typical features of the "standard solar flare model in 3D", which allows for a consistent explanation of events that are not causally connected (Dudík et al., 2014). It also advocates that null-points and true separatrices are not required for the eruptive flares to occur—concurring with the results of this work. Hall MHD evolution of the fan-spine configuration surrounding the 3D null point is in better agreement with the tip of the W-shaped flare ribbon at the center of the AR. The lower spine and fan magnetic field lines remain anchored to the bottom boundary throughout the evolution which can account for the plasma flowing downward after the reconnection and cause the brightening. Whereas in the MHD, the lower spine gets disconnected and cannot account for the brightening. The reconnection dynamics around the null-line and the corresponding plasma flow direction are same in the Hall MHD as well as the MHD simulation and agree with the observed brightening. Nevertheless, reconnection is earlier in the Hall MHD. Hall MHD evolution captures an anti-clockwise circular motion of magnetic field lines in the left part of the AR which is co-spatial with the location of the rotating chromospheric material in the eastern side of the AR. No such motion was found in the MHD simulation. Importantly, the simulations explicitly associate the generation of large magnetic field gradients to Hall MHD compared to MHD, resulting in faster and more efficient field line slippage because of the enhanced Hall term.

Overall, the results documented in the Chapter show the Hall MHD explains the flare brightening better than the MHD, prioritizing the requirement to include Hall MHD in future state-of-the-art data-based numerical simulations.

Chapter 7

Summary and Future Prospects

7.1 Summary

In this thesis, the role of the Hall effect in magnetic reconnection has been investigated by employing numerical simulations which are initiated with analytical and observed solar magnetic fields. The key problems of fast and impulsive reconnection have been addressed. For the works presented in this thesis, a comparative study of reconnections and the evolution of magnetic structures in the presence and absence of the Hall effect is carried out. For this purpose, we have developed a 3D HMHD solver by incorporating the Hall term in the well-established computational model— EULAG MHD. The development of a 3D HMHD solver benefits from the Implicit Large Eddy Simulation (ILES) nature of EULAG MHD which exhibits numerical diffusion determined by the resolution (Chapter 3). The requirement of very large spatial resolution is overcome by tying the Hall effect with the dissipation scale so that an increased current density at the dissipation scale enhances the Hall effect. Subsequently, benchmarking (Chapter 4) is done with an initially unidirectional sinusoidal magnetic field which has an initial non-zero Lorentz force. This choice of the initial condition allows us to validate the developed 3D HMHD solver without repeating the traditional simulations using the Harris current sheet equilibrium or the GEM challenge. Hall MHD and MHD numerical simulations are carried out in the presence and absence of the Hall term. MHD simulation results show a symmetric magnetic field evolution in the computation domain. Magnetic reconnections generate magnetic flux tubes made by

disjoint magnetic field lines. Whereas, during the Hall MHD simulation, the evolution becomes asymmetric and 3D due to the generation of an out-of-reconnection plane magnetic field component. The magnetic energy evolution is identical. The time derivative of the growth rate of current density shows abrupt changes during the Hall MHD—implying impulsiveness. These results are in concurrence with the earlier Hall MHD simulations in the literature and validate the developed 3D HMHD solver. Along with the flux tube, magnetic reconnections also generate a magnetic flux rope—a twisted set of field lines in the Hall MHD. When viewed favorably, the rope and the tube appear as magnetic islands. Further evolution leads to the breakage of primary islands into secondary islands and later their merging is observed. Overall, the results agree with the existing scenarios of Hall-assisted reconnection based on physical arguments and other recent simulations including those on the GEM challenge. An important finding is the formation of complex 3D magnetic structures, which cannot be apprehended from 2D models or calculations although their projections agree with the latter. Alongside, we have numerically explored the Whistler mode propagation vis-a-vis its analytical model and found the two to be matching reasonably well in the Hall MHD simulations.

Understanding the evolution of a magnetic flux rope is instructive to understand the coronal mass ejections owing to eruptive flares, prominence, or filament eruptions on the Sun. Therefore, the developed 3D HMHD solver has been further employed to simulate the Hall effect on the generation and evolution of magnetic flux rope for two cases depending upon the initial conditions (Chapter 5). The simulations in the first and second cases are initiated with an axisymmetric and the three-dimensional bipolar sheared arcade-like magnetic fields, respectively. Magnetic flux rope in the first case is levitating and unanchored one, whereas in the other case it is anchored to the bottom boundary. A comparative investigation of the Hall MHD and MHD simulations reveal that the primary reconnections through which the flux rope is generated are identical in both the simulations for both cases. However, further evolution of flux ropes is influenced by the Hall forcing as the reconnections proceed. The first case, once again shows a reasonable maintenance of symmetry in the standard MHD simulation, whereas a clear symmetry-breaking—leading to the generation of three-dimensional magnetic

structures—appears to be a signature of the Hall effect. In Hall MHD the flux rope evolves through a series of complex geometries while rotating along its axis. When viewed favorably, it appears to contain structures reminiscent of the "number eight (8)", which is the result of internal reconnection within the rope. Notably, the magnetic energies, in the presence and absence of the Hall forcing, vary almost identically for both the cases—consistent with the theoretical understanding that the Hall term directly does not change the magnetic energy dissipation rate.

In the second case, the flux rope is found to generate in consequence of repetitive reconnection at three-dimensional magnetic nulls—detected using the trilinear method of null detection techniques, in both the Hall MHD as well as MHD simulations while preserving the topological degree. Twisting of magnetic field lines in the vicinity of three-dimensional nulls—a unique feature found during the Hall MHD evolution of rope which further leads to the formation of large-scale flux rope. This result suggests that the Hall effect modifies the dynamics of magnetic structures around small-scale (reconnection site) which further generates large-scale structure, hence relating the small-scale and large-scale dynamics. Also, the faster formation of post-reconnection arcades in the Hall MHD signifies faster dynamics.

After gaining experience with the Hall effect on 3D magnetic reconnection, the numerical model has been further employed to simulate the Hall effect in magnetic reconnection for a flaring active region (AR) on the Sun as a testbed (Chapter 6). This work compares the data-based Hall MHD and MHD simulations using the flaring NOAA AR 12734 as a test bed. For this purpose, the event under consideration, is the C1.3 class flare on March 8, 2019 around 03:19 UT. Although the event is analyzed and reported in the literature, it is further explored using the multi-wavelength observations from SDO/AIA. The important features outlined in the observation include an elongated EUV counterpart of the eruption on the western side of the AR, a W-shaped flare ribbon, and the circular motion of cool chromospheric material on the eastern part. The magnetic field line dynamics related to these features are compared in the simulations. Notably, the simulations idealize the corona to have an Alfvèn speed of two orders of magnitude smaller than its typical value. Conforming with the general understanding, the Hall parameter is

selected to tie the Hall dynamics to the dissipation scale $\mathcal{O}(\Delta \mathbf{x})$ in the spirit of implicit large eddy simulations (ILES). The magnetic reconnection here is associated with the slippage of magnetic field lines from the plasma parcels, effective at the dissipation scale due to the local enhancement of magnetic field gradients. The same enhancement also amplifies the Hall contribution and enhances the slippage, thereby making the reconnection faster and more effective in Hall MHD in comparison to the MHD. The coronal magnetic field is constructed by extrapolating the photospheric vector magnetic field obtained from the SDO/HMI observations employing the non-FFF technique. The concentrated distribution of the Lorentz force on the bottom boundary and its decrease with the height justify the use of non-FFF extrapolation for the solar corona. The initial nonzero Lorentz force is also crucial in generating self-consistent flows that initiate the dynamics and cause magnetic reconnections. Analyses of the extrapolated magnetic field reveals several magnetic structures and topologies of interest: a flux rope on the western part at the flaring location, a 3D null point along with the fan-spine configuration at the center, and a "fish-bone-like structure" surrounding the null line on the eastern part of the AR. All of these structures are found to be cospatial with the observed flare ribbon brightening. The Hall MHD simulation shows faster slipping reconnection of the flux-rope footpoints and overlying magnetic field lines (constituting quasi separatrix layers (QSLs) above the flux rope) at the flaring location. Consequently, the overlying magnetic field lines rise, eventually reaching higher up in the corona and reconnecting to provide a path for plasma to eject out. This finding agrees with the observed elongated EUV counterpart of the eruption on the western part of the AR. Contrarily, such a significant rise of the flux rope and overlying field lines to subsequently reconnect higher up in the corona is absent in the MHD simulation—signifying that the reconnection is slower compared to the Hall MHD. Interestingly, the rise and expansion of the flux rope and overlying field lines due to slipping reconnection on QSLs have also been modeled and observed in the literature. Previous work in the literature, also advocates that null points and true separatrices are not required for the eruptive flares to occur—congruent with the results of our work. Hall MHD evolution of the fan-spine configuration surrounding the 3D null point is in better agreement with the tip of the W-shaped

flare ribbon at the center of the AR. The lower spine and fan magnetic field lines remain anchored to the bottom boundary throughout the evolution, which can account for the plasma flowing downward after the reconnection and cause the brightening, whereas in the MHD the lower spine gets disconnected and cannot account for the brightening. The reconnection dynamics around the null line and the corresponding plasma flow direction are the same in the Hall MHD and MHD simulations and agree with the observed brightening. Nevertheless, reconnection is earlier in the Hall MHD. Hall MHD evolution nicely captures an anticlockwise circular motion of magnetic field lines in the left part of the AR that is cospatial with the location of the rotating chromospheric material on the eastern side of the AR. No such motion was found in the MHD simulation. Importantly, the simulations explicitly associate the generation of large magnetic field gradients with Hall MHD compared to MHD, resulting in faster and more efficient field line slippage because of the enhanced Hall term.

Importantly, this thesis explores the role of the Hall effect in magnetic reconnection and addresses the fast and impulsive reconnection within the Hall MHD. A reasonable agreement between the magnetic field dynamics in a novel Hall MHD simulation of the observed flare and the spatial features of flare brightening, suggests the Hall MHD to provide a plausible explanation for the flare reconnection. The crux of the thesis work is that the Hall effect being a small-scale effect, alters the dynamics in the vicinity of the reconnection site, and in turn, affects the dynamics at large-scale (as large as the system scale size), while accommodating faster dynamics.

7.2 Future Prospects

This thesis addresses the role of the Hall effect in magnetic reconnection within the Hall MHD framework to understand fast reconnection dynamics with a particular focus on 3D. In line with the explorations carried out in this thesis work, the future scope consists of the continuation of such investigations of the Hall effect on 3D magnetic reconnection which will be beneficial in understanding the underlying physics essential for transient explosive activities occurring in astrophysical

plasmas. Additionally, further improvements in the model can account for the energy budget and thermodynamics of the transient events. Consequently, the future prospects are briefly presented as follows:

1. In this thesis, the Hall effect on the reconnections responsible for the generation and evolution of a magnetic flux rope initiated from the sheared bipolar field has been explored. However, the prominences or filaments on the Sun resemble pre-existing magnetic flux rope structure and the exploration of the Hall effect on reconnections driving the eruption of such flux ropes can be helpful in understanding the underlying physics responsible for the phenomenon like local breakage of prominences followed by the swirling motions of plasma material. In this context, we plan to do the numerical simulation of an initial analytical flux rope with an aim to explore the Hall effect on its evolution.

2. Reasonably good agreement between the dynamics obtained from the novel data-constrained Hall MHD simulation of a flare and its observations, inspires us to perform the Hall MHD data-constrained simulations for the high-resolution magnetic field data ($\sim$ few km) from the ground-based observatory DKIST.

3. We plan to perform the observational studies as well as numerical simulations to understand the small-scale transient events such as microflares and nanoflares which are important in understanding the coronal heating problems.

4. In this thesis, we have mainly carried out the incompressible Hall MHD simulations with the Cartesian geometry but in future we plan to do the compressible Hall MHD and MHD simulations.

Appendix A

Data-based Hall MHD and MHD simulations of a flaring solar active region

The dimensionless time step is obtained by employing the Hall induction equation

$$\frac{\partial \mathbf{B}}{\partial t} = -d_H \nabla \times ((\nabla \times \mathbf{B}) \times \mathbf{B}), \tag{A.1}$$

for a stationary fluid. The aforementioned equation is linearized over an equilibrium magnetic field $\mathbf{B}_0$ to obtain

$$\frac{\partial \delta \mathbf{B}}{\partial t} = -d_H [\nabla \times (\nabla \times \delta \mathbf{B}) \times \mathbf{B}_0], \tag{A.2}$$

$\delta \mathbf{B}$ being the perturbation. To obtain the wave modes, the perturbation is assumed to be periodic along x and y of a Cartesian coordinate system

$$\delta B_x = \delta B_y \propto \exp[i(k_z z - \omega t)]. \tag{A.3}$$

where the equilibrium field is selected as $\mathbf{B}_0 = B_0 \hat{e}_z$. Straightforward mathematical manipulations yield the dispersion relation for the Whistler wave as

$$\omega = d_H B_0 {k_z}^2. \tag{A.4}$$

The wave number is selected as $k_z = (2\pi)/\Delta z$, Δz is the dissipation scale in the

computational domain, making the choice harmonious with the philosophy used extensively in the paper. since the dimensionless $\rho_0 = 1$ in the numerical model, (A.4) can be written

$$\left(\frac{\Delta z}{\Delta t}\right)_{whis} = 4\pi^{\frac{3}{2}} d_H \left(\frac{\Delta z}{\Delta t}\right)_{Alf} \left(\frac{1}{\Delta z}\right)_{whis}. \tag{A.5}$$

With $\Delta z_{whis} = \Delta z_{Alfven} = 0.0078$, namely the dissipation scale in the present model along with d_H=0.004, while $\Delta t_{Alf} \approx 10^{-3}$ from previous numerical experiments; in the present model $\Delta t = \Delta t_{whis} \approx 10^{-4}$.

Bibliography

Alfvén, H. 1942, *Nature*, 150, 405

Alissandrakis, C. E. 1981, *Astron. Astrophys.*, 100, 197

Amari, T., & Aly, J. J. 2010, *Astron. Astrophys.*, 522, A52

Amari, T., Aly, J. J., Luciani, J. F., Boulmezaoud, T. Z., & Mikic, Z. 1997, *Solar Phys.*, 174, 129

Amari, T., Boulmezaoud, T. Z., & Aly, J. J. 2006, *Astron. Astrophys.*, 446, 691

Amari, T., Canou, A., & Aly, J.-J. 2014, *Nature*, 514, 465

Antiochos, S. K., DeVore, C. R., & Klimchuk, J. A. 1999, *Astrophys. J.*, 510, 485

Aschwanden, M. J. 2005, Physics of the Solar Corona. An Introduction with Problems and Solutions (2nd edition)

Aulanier, G., Pariat, E., Démoulin, P., & DeVore, C. R. 2006, *Solar Phys.*, 238, 347

Axford, W. I. 1984, Washington DC American Geophysical Union Geophysical Monograph Series, 30, 1

Beaudoin, P., Charbonneau, P., Racine, E., & Smolarkiewicz, P. K. 2013, *Solar Phys.*, 282, 335

Benz, A. O. 2008, Living Reviews in Solar Physics, 5, 1

Bhattacharjee, A. 2004, *Ann. Rev. Astron. Astrophys.*, 42, 365

Bhattacharjee, A., Ma, Z. W., & Wang, X. 2003, in Turbulence and Magnetic Fields in Astrophysics, ed. E. Falgarone & T. Passot, Vol. 614 351

Bhattacharyya, R., & Janaki, M. S. 2004, Physics of Plasmas, 11, 5615

Bhattacharyya, R., & Janaki, M. S. 2004, Physics of Plasmas, 11, 5615

Bhattacharyya, R., Janaki, M. S., Dasgupta, B., & Zank, G. P. 2007, *Solar Phys.*, 240, 63

Bhattacharyya, R., Low, B. C., & Smolarkiewicz, P. K. 2010, Physics of Plasmas, 17, 112901

Bineau, M. 1972, Communications on Pure and Applied Mathematics, 25, 77

Birn, J., et al. 2001, *J. Geophys. Res.*, 106, 3715

Birn, J., Hesse, M., & Schindler, K. 1997, Advances in Space Research, 19, 1763

Biskamp, D. 2000, Magnetic Reconnection in Plasmas, Vol. 3

Bobra, M. G., Sun, X., Hoeksema, J. T., Turmon, M., Liu, Y., Hayashi, K., Barnes, G., & Leka, K. D. 2014, *Solar Phys.*, 289, 3549

Book, D. L., Boris, J. P., & Hain, K. 1975, Journal of Computational Physics, 18, 248

Bora, K., Bhattacharyya, R., Prasad, A., Joshi, B., & Hu, Q. 2022, *Astrophys. J.*, 925, 197

Bora, K., Bhattacharyya, R., & Smolarkiewicz, P. K. 2021, *Astrophys. J.*, 906, 102

Boris, J. P., & Book, D. L. 1973, Journal of Computational Physics, 11, 38

Boris, J. P., & Book, D. L. 1976, Journal of Computational Physics, 20, 397

Carmichael, H. 1964, NASA Special Publication, 50, 451

Chandrasekhar, S., & Kendall, P. C. 1957, *Astrophys. J.*, 126, 457

Charbonneau, P., & Smolarkiewicz, P. K. 2013, Science, 340, 42

Chen, P. F. 2011, Living Reviews in Solar Physics, 8, 1

Chiu, Y. T., & Hilton, H. H. 1977, *Astrophys. J.*, 212, 873

Choudhuri, A. R. 1998, The physics of fluids and plasmas : an introduction for astrophysicists

Couvidat, S., et al. 2016, *Solar Phys.*, 291, 1887

Cowling, T. G. 1953, in The Sun, ed. G. P. Kuiper 532

Dahlburg, R. B., Antiochos, S. K., & Zang, T. A. 1991, *Astrophys. J.*, 383, 420

De Rosa, M. L., et al. 2009, *Astrophys. J.*, 696, 1780

Démoulin, P. 2006, Advances in Space Research, 37, 1269

Demoulin, P., Bagala, L. G., Mandrini, C. H., Henoux, J. C., & Rovira, M. G. 1997, *Astron. Astrophys.*, 325, 305

Demoulin, P., Henoux, J. C., Priest, E. R., & Mandrini, C. H. 1996, *Astron. Astrophys.*, 308, 643

Domaradzki, J. A., & Radhakrishnan, S. 2005, Fluid Dynamics Research, 36, 385

Domaradzki, J. A., Xiao, Z., & Smolarkiewicz, P. K. 2003, Physics of Fluids, 15, 3890

Dudík, J., Janvier, M., Aulanier, G., Del Zanna, G., Karlický, M., Mason, H. E., & Schmieder, B. 2014, *Astrophys. J.*, 784, 144

Dungey, J. 1953, The London, Edinburgh, and Dublin Philosophical Magazine and Journal of Science, 44, 725

Dungey, J. W. 1961, *J. Geophys. Res.*, 66, 1043

Eisenstat, S. C. 1983, SIAM Journal on Numerical Analysis, 20, 358

Eisenstat, S. C., Elman, H. C., & Martin, H. S. 1983, SIAM Journal on Numerical Analysis, 20, 345–357

Freidberg, J. P. 1982, Reviews of Modern Physics, 54, 801

Garcia, H. A. 1994, *Solar Phys.*, 154, 275

Gary, G. A. 1989, *Astrophys. J. Suppl.*, 69, 323

Gary, G. A. 2001, *Solar Phys.*, 203, 71

Ghizaru, M., Charbonneau, P., & Smolarkiewicz, P. K. 2010, *Astrophys. J. Lett.*, 715, L133

Giovanelli, R. G. 1946, *Nature*, 158, 81

Gonzalez, W. D., & Tsurutani, B. T. 1992, in IAU Colloq. 133: Eruptive Solar Flares, ed. Z. Svestka, B. V. Jackson, & M. E. Machado, Vol. 399 277

Gopalswamy, N., Yashiro, S., Vourlidas, A., Lara, A., Stenborg, G., Kaiser, M. L., & Howard, R. A. 2004, in Bulletin of the American Astronomical Society, Vol. 36, American Astronomical Society Meeting Abstracts #204, 738

Griebel, M., Dornseifer, T., & Neunhoeffer, T. 1998, Numerical simulation in fluid dynamics: a practical introduction (the Society for Industrial and Applied Mathematics)

Grinstein, F., Margolin, L., & Rider, W. 2007, Implicit Large Eddy Simulation: Computing Turbulent Fluid Dynamics, Cambridge University Press

Hasegawa, A. 1985, Advances in Physics, 34, 1

Haynes, A. L., & Parnell, C. E. 2007, Physics of Plasmas, 14, 082107

Hesse, M., Birn, J., & Kuznetsova, M. 2001, *J. Geophys. Res.*, 106, 3721

Hesse, M., & Schindler, K. 1988, *J. Geophys. Res.*, 93, 5559

Hirayama, T. 1974, *Solar Phys.*, 34, 323

Hoeksema, J. T., et al. 2014, *Solar Phys.*, 289, 3483

Hornig, G., & Schindler, K. 1996, Physics of Plasmas, 3, 781

Howard, T. A., & Tappin, S. J. 2009, *Space Sci. Rev.*, 147, 31

Hoyle, F. 1949, Some recent researches in solar physics.

Hu, Q., & Dasgupta, B. 2008, *Solar Phys.*, 247, 87

Hu, Q., Dasgupta, B., Choudhary, D. P., & Büchner, J. 2008, *Astrophys. J.*, 679, 848

Hu, Q., Dasgupta, B., Derosa, M. L., Büchner, J., & Gary, G. A. 2010, Journal of Atmospheric and Solar-Terrestrial Physics, 72, 219

Huba, J. D. 2003, Hall Magnetohydrodynamics - A Tutorial, ed. J. Büchner, M. Scholer, & C. T. Dum (Berlin, Heidelberg: Springer Berlin Heidelberg), 166

Illing, R. M. E., & Hundhausen, A. J. 1985, *J. Geophys. Res.*, 90, 275

Inoue, S., Hayashi, K., Magara, T., Choe, G. S., & Park, Y. D. 2014, *Astrophys. J.*, 788, 182

Jiang, C., & Feng, X. 2014, *Solar Phys.*, 289, 63

Jiang, C., Feng, X., Wu, S. T., & Hu, Q. 2013, *Astrophys. J. Lett.*, 771, L30

Jiang, C., Wu, S. T., Feng, X., & Hu, Q. 2016, Nature Communications, 7, 11522

Joshi, B., Mitra, P. K., Bhattacharyya, R., Upadhyay, K., Oberoi, D., Sasikumar Raja, K., & Monstein, C. 2021, *Solar Phys.*, 296, 85

Kliem, B., & Török, T. 2006, Phys. Rev. Lett., 96, 255002

Kopp, R. A., & Pneuman, G. W. 1976, *Solar Phys.*, 50, 85

Kumar, D., & Bhattacharyya, R. 2011, Physics of Plasmas, 18, 084506

Kumar, D., Bhattacharyya, R., & Smolarkiewicz, P. K. 2013, Physics of Plasmas, 20, 112903

Kumar, D., Bhattacharyya, R., & Smolarkiewicz, P. K. 2015a, Physics of Plasmas, 22, 012902

Kumar, S., & Bhattacharyya, R. 2016, Physics of Plasmas, 23, 044501

Kumar, S., Bhattacharyya, R., Dasgupta, B., & Janaki, M. S. 2017, Physics of Plasmas, 24, 082902

Kumar, S., Bhattacharyya, R., Joshi, B., & Smolarkiewicz, P. K. 2016, *Astrophys. J.*, (in press)

Kumar, S., Bhattacharyya, R., & Smolarkiewicz, P. K. 2015b, Physics of Plasmas, 22, 082903

Lee, C. O., Luhmann, J. G., Hoeksema, J. T., Sun, X., Arge, C. N., & de Pater, I. 2011, *Solar Phys.*, 269, 367

Lemen, J. R., et al. 2012, *Solar Phys.*, 275, 17

Liu, C., Prasad, A., Lee, J., & Wang, H. 2020, *Astrophys. J.*, 899, 34

Liu, R., et al. 2016, *Astrophys. J.*, 818, 148

Liu, Y., et al. 2012, Solar Physics, 279, 295

Liu, Y.-H., Cassak, P., Li, X., Hesse, M., Lin, S.-C., & Genestreti, K. 2022, Communications Physics, 5, 97

Low, B. C. 1996, *Solar Phys.*, 167, 217

Ma, Z. W., & Bhattacharjee, A. 2001, *J. Geophys. Res.*, 106, 3773

Mahajan, S. M., & Yoshida, Z. 1998, Phys. Rev. Lett., 81, 4863

Margolin, L. G., Rider, W. J., & Grinstein, F. F. 2006, Journal of Turbulence, 7, N15

Mininni, P. D., Gómez, D. O., & Mahajan, S. M. 2003, *Astrophys. J.*, 587, 472

Moore, R. L., Sterling, A. C., Hudson, H. S., & Lemen, J. R. 2001, *Astrophys. J.*, 552, 833

Mozer, F. S., Bale, S. D., & Phan, T. D. 2002, *Phys. Rev. Lett.*, 89, 015002

Müller, D., Marsden, R. G., St. Cyr, O. C., & Gilbert, H. R. 2013, *Solar Phys.*, 285, 25

Nakagawa, Y. 1974, *Astrophys. J.*, 190, 437

Nakagawa, Y., & Raadu, M. A. 1972, *Solar Phys.*, 25, 127

Nayak, S. S., Bhattacharyya, R., Prasad, A., Hu, Q., Kumar, S., & Joshi, B. 2019, *Astrophys. J.*, 875, 10

Nayak, S. S., Bhattacharyya, R., Smolarkiewicz, P. K., Kumar, S., & Prasad, A. 2020, *Astrophys. J.*, 892, 44

Otto, A. 2001, *J. Geophys. Res.*, 106, 3751

Pant, V., Datta, A., Banerjee, D., Chandrashekhar, K., & Ray, S. 2018, The Astrophysical Journal, 860, 80

Parker, E. N. 1957, *J. Geophys. Res.*, 62, 509

Parker, E. N. 1994, Spontaneous current sheets in magnetic fields : with applications to stellar x-rays. International Series in Astronomy and Astrophysics, 1

Parnell, C. E., Smith, J. M., Neukirch, T., & Priest, E. R. 1996, Physics of Plasmas, 3, 759

Pesnell, W. D., Thompson, B. J., & Chamberlin, P. C. 2012a, *Solar Phys.*, 275, 3

Pesnell, W. D., Thompson, B. J., & Chamberlin, P. C. 2012b, *Solar Phys.*, 275, 3

Petschek, H. E. 1964, NASA Special Publication, 50, 425

Pontin, D. I., & Priest, E. R. 2022, Living Reviews in Solar Physics, 19, 1

Prasad, A., Bhattacharyya, R., Hu, Q., Kumar, S., & Nayak, S. S. 2018, *Astrophys. J.*, 860, 96

Prasad, A., Bhattacharyya, R., & Kumar, S. 2017, *Astrophys. J.*, 840, 37

Prasad, A., Dissauer, K., Hu, Q., Bhattacharyya, R., Veronig, A. M., Kumar, S., & Joshi, B. 2020, *Astrophys. J.*, 903, 129

Priest, E. 2014, Magnetohydrodynamics of the Sun

Priest, E., & Forbes, T. 2000, Magnetic Reconnection

Priest, E. R., & Titov, V. S. 1996, Proceedings of the Royal Society of London Series A, 354, 2951

Prusa, J., Smolarkiewicz, P., & Wyszogrodzki, A. 2008, Computers & Fluids, 37, 1193

Prusa, J. M., & Smolarkiewicz, P. K. 2003, Journal of Computational Physics, 190, 601

Prusa, J. M., Smolarkiewicz, P. K., & Wyszogrodzki, A. A. 2008, Computers Fluids, 37, 1193–1207

Ramsden, E. 2006, in Hall-Effect Sensors (Second Edition) (Second Edition ed.), ed. E. Ramsden (Burlington: Newnes), 1

Rider, W. J. 2006, International Journal for Numerical Methods in Fluids, 50, 1145

Rossby, C.-G., Namias, J., & Simmers, R. G. 1938, Physical Oceanography and Meteorology, 17

Ruderman, M. S., & Roberts, B. 2002, *Astrophys. J.*, 577, 475

Sakurai, T. 1981, *Solar Phys.*, 69, 343

Sarp Yalim, M., Prasad, A., Pogorelov, N., Zank, G., & Hu, Q. 2020, arXiv e-prints, arXiv:2007.12275

Savcheva, A., Pariat, E., McKillop, S., McCauley, P., Hanson, E., Su, Y., & DeLuca, E. E. 2016, *Astrophys. J.*, 817, 43

Scherrer, P. H., et al. 2012, *Solar Phys.*, 275, 207

Schindler, K., Hesse, M., & Birn, J. 1988, *J. Geophys. Res.*, 93, 5547

Schou, J., et al. 2012, *Solar Phys.*, 275, 229

Schrijver, C. J., et al. 2006, *Solar Phys.*, 235, 161

Scudder, J. D. 1997, *Space Sci. Rev.*, 80, 235

Seehafer, N. 1978, *Solar Phys.*, 58, 215

Shi, C., Tenerani, A., Velli, M., & Lu, S. 2019, *Astrophys. J.*, 883, 172

Shibata, K., & Magara, T. 2011, Living Reviews in Solar Physics, 8

Shibata, K., & Tanuma, S. 2001, Earth, Planets, and Space, 53, 473

Smolarkiewicz, P., & Szmelter, J. 2011, Acta Geophysica, 59, 1109

Smolarkiewicz, P. K. 1983, Monthly Weather Review, 111, 479

Smolarkiewicz, P. K. 1984, Journal of Computational Physics, 54, 325

Smolarkiewicz, P. K. 1991, Monthly Weather Review, 119, 2505

Smolarkiewicz, P. K. 2006, International Journal for Numerical Methods in Fluids, 50, 1123

Smolarkiewicz, P. K., & Charbonneau, P. 2013, Journal of Computational Physics, 236, 608

Smolarkiewicz, P. K., & Clark, T. L. 1986, Journal of Computational Physics, 67, 396

Smolarkiewicz, P. K., & Grabowski, W. W. 1990, Journal of Computational Physics, 86, 355

Smolarkiewicz, P. K., Grubišić, V., & Margolin, L. G. 1997, Monthly Weather Review, 125, 647

Smolarkiewicz, P. K., & Margolin, L. G. 1993, Monthly Weather Review, 121, 1847

Smolarkiewicz, P. K., & Margolin, L. G. 1997, Atmosphere-Ocean, 35, 127

Smolarkiewicz, P. K., & Margolin, L. G. 1997, Atmosphere Ocean, 35, 127

Smolarkiewicz, P. K., & Margolin, L. G. 1998, Journal of Computational Physics, 140, 459

Smolarkiewicz, P. K., & Prusa, J. M. 2002, International Journal for Numerical Methods in Fluids, 39, 799

Smolarkiewicz, P. K., & Pudykiewicz, J. A. 1992, Journal of Atmospheric Sciences, 49, 2082

Smolarkiewicz, P. K., & Szmelter, J. 2009, Journal of Computational Physics, 228, 33

Sonnerup, B. U. Ö. 1979, Magnetic field reconnection, Vol. 3 45

Sturrock, P. A. 1966, *Nature*, 211, 695

Sweet, P. A. 1958, in IAU Symposium, Vol. 6, Electromagnetic Phenomena in Cosmical Physics, ed. B. Lehnert, 499

Terasawa, T. 1983, *Geophys. Res. Lett.*, 10, 475

Titov, V. S. 2007, *Astrophys. J.*, 660, 863

Vasyliunas, V. M. 1975, Reviews of Geophysics and Space Physics, 13, 303

Venkatakrishnan, P., & Gary, G. A. 1989, *Solar Phys.*, 120, 235

Vourlidas, A., Buzasi, D., Howard, R. A., & Esfandiari, E. 2002, in ESA Special Publication, Vol. 506, Solar Variability: From Core to Outer Frontiers, ed. A. Wilson, 91

Vourlidas, A., & Howard, R. A. 2006, *Astrophys. J.*, 642, 1216

Vourlidas, A., Lynch, B. J., Howard, R. A., & Li, Y. 2013, *Solar Phys.*, 284, 179

Wang, H., Liu, C., Deng, N., Zeng, Z., Xu, Y., Jing, J., & Cao, W. 2014, *Astrophys. J. Lett.*, 781, L23

Wang, X., Bhattacharjee, A., & Ma, Z. W. 2000, *J. Geophys. Res.*, 105, 27633

Wheatland, M. S., Sturrock, P. A., & Roumeliotis, G. 2000, The Astrophysical Journal, 540, 1150

Wiegelmann, T. 2004, *Solar Phys.*, 219, 87

Wiegelmann, T. 2008, Journal of Geophysical Research (Space Physics), 113, A03S02

Wiegelmann, T., & Inhester, B. 2010, *Astron. Astrophys.*, 516, A107

Wiegelmann, T., Inhester, B., & Sakurai, T. 2006a, *Solar Phys.*, 233, 215

Wiegelmann, T., Inhester, B., & Sakurai, T. 2006b, *Solar Phys.*, 233, 215

Wiegelmann, T., & Sakurai, T. 2012, Living Reviews in Solar Physics, 9, 5

Wiegelmann, T., & Sakurai, T. 2021, Living Reviews in Solar Physics, 18, 1

Woltjer, L. 1958, Proceedings of the National Academy of Science, 44, 489

Wyper, P. F., & Pontin, D. I. 2014, Physics of Plasmas, 21, 102102

Yoshida, Z., & Giga, Y. 1990, Mathematische Zeitschrift, 204, 235

Zhong, Z., Guo, Y., & Ding, M. D. 2021, Nature Communications, 12, 2734

Publications attached with the thesis

1. **K. Bora**, R. Bhattacharyya, Avijeet Prasad, Bhuwan Joshi, Qiang Hu (2022): *"Comparison of the Hall Magnetohydrodynamics and Magnetohydrodynamics Evolution of a Flaring Solar Active Region"*. In: *The Astrophysical Journal*, 925, 197. DOI: https://doi.org/10.3847/1538-4357/ac3bce

2. **K. Bora**, R. Bhattacharyya, P. K. Smolarkiewicz (2021): *"Evolution of Three-dimensional Coherent Structures in Hall Magnetohydrodynamics"*. In: *The Astrophysical Journal*, 906, 102. DOI: https://doi.org/10.3847/1538-4357/abc8f7

The Astrophysical Journal, 906:102 (16pp), 2021 January 10 https://doi.org/10.3847/1538-4357/abc8f7

Evolution of Three-dimensional Coherent Structures in Hall Magnetohydrodynamics

K. Bora[1,2], R. Bhattacharyya[1], and P. K. Smolarkiewicz[3]
[1] Udaipur Solar Observatory, Physical Research Laboratory, Dewali, Bari Road, Udaipur-313001, India
[2] Discipline of Physics, Indian Institute of Technology, Gandhinagar-382355, India
[3] National Center for Atmospheric Research, Boulder, CO, USA
Received 2020 August 15; revised 2020 November 6; accepted 2020 November 6; published 2021 January 13

Abstract

This work extends the computational model EULAG-MHD to include Hall magnetohydrodynamics (HMHD)—important to explore physical systems undergoing fast magnetic reconnection at the order of the ion inertial length scale. Examples include solar transients along with reconnections in magnetosphere, magnetotail, and laboratory plasmas. The paper documents the results of two distinct sets of implicit large-eddy simulations in the presence and absence of the Hall forcing term, initiated with an unidirectional sinusoidal magnetic field. The HMHD simulation while benchmarking the code also emphasizes the complexity of three-dimensional (3D) evolution over its two-dimensional counterpart. The magnetic reconnections onset significantly earlier in HMHD. Importantly, the magnetic field generated by the Hall term breaks any inherent symmetry, ultimately making the evolution 3D. The resulting 3D reconnections develop magnetic flux ropes (MFRs) and magnetic flux tubes. Projected on the reconnection plane, the ropes and tubes appear as magnetic islands, which later break into secondary islands, and finally coalesce to generate an X-type neutral point. These findings are in agreement with the theory and contemporary simulations of HMHD, and thus verify our extension of the EULAG-MHD model. The second set explores the influence of the Hall forcing on generation and ascend of an MFR from sheared magnetic arcades—a novel scenario instructive in understanding the coronal transients. The rope evolves through intermediate complex structures, ultimately breaking locally because of reconnections. Interestingly, the breakage occurs earlier in the presence of the Hall term, signifying faster dynamics leading to magnetic topology favorable for reconnections.

Unified Astronomy Thesaurus concepts: Solar magnetic reconnection (1504); Magnetohydrodynamical simulations (1966)

Supporting material: animations

1. Introduction

Magnetofluids characterized by large Lundquist numbers $S = LV_A/\eta$ ($L \equiv$ length scale of the magnetic field $\boldsymbol{B}$ variability, $V_A \equiv$ Alfvén speed, and $\eta \equiv$ magnetic diffusivity) satisfy Alfvén's flux-freezing theorem on magnetic field lines (MFLs) being tied to fluid parcels (Alfvén 1942). The astrophysical plasmas are of particular interest, because their inherently large L implies large S and the flux freezing. For example, the solar corona with global $L \approx 10^6$ m, $V_A \approx 10^6$ m s^{-1}, $B \approx 10$ G, and $\eta \approx 1$ m^2 s^{-1} (calculated using Spitzer resistivity) has a $S \approx 10^{12}$ (Aschwanden 2005). Nevertheless the coronal plasma also exhibits diffusive behavior. For example, the solar transients—such as flares, coronal mass ejections, and coronal jets—are all manifestations of magnetic reconnections (MRs) that in turn form a diffusive phenomenon, where the magnetic energy gets converted into heat and kinetic energy of plasma flow, accompanied with a rearrangement of MFLs (Choudhuri 1998). The onset of MRs is due to the generation of small scales in consequence of large-scale dynamics, eventually leading to a locally reduced characteristic length scale of the magnetic field variability and thereby resulting in intermittently diffusive plasmas. The small scales owe their origin to the presence of magnetic nulls; i.e., locations where $\boldsymbol{B} = 0$ (Priest 2014; Nayak et al. 2020). Alternatively, and more relevant to this paper, this can be due to the presence of current sheets (CSs); i.e., the ribbons of intense current, across which $\boldsymbol{B}$ has a sharp gradient (Parker 1994; Kumar & Bhattacharyya 2011). Spontaneous development of CSs is predicted by the Parker's magnetostatic theorem that implies the inevitability of CSs in an equilibrium magnetofluid with perfect electrical conductivity. This inevitability in turn is due to the general failure of a smooth magnetic field to simultaneously preserve the local force balance and the global magnetic topology (Parker 1994).

To elucidate this seminal theorem, we follow the arguments in Kumar & Bhattacharyya (2011). Let us perceive a series of contiguous fluid parcels with their frozen-in MFLs. We further assume the fluid to be incompressible. The magnetic field is everywhere continuous. If the two ends of the series are pushed toward each other, because of incompressibility the interstitial parcels will be squeezed out. Terminally, the end parcels of the series will approach each other and their MFLs being nonparallel (in general)—will create a CS. Notably, for an ideal magnetofluid having infinite electrical conductivity the creation of the CS is the terminal state, but in the presence of a small magnetic diffusivity the MFLs will ultimately reconnect. The reconnected MFLs are subsequently pushed away from the reconnection region by the outflow, and as they come out of the CS, the MFLs once again get frozen to the fluid. Afterward, these frozen MFLs can push another flux system and repeat the whole process of reconnection. This switch between large and the small scales with their inherent coupling is fundamentally interesting and has the potential to drive a myriad of MR driven phenomena observed in the solar atmosphere.

An example of this scenario is numerically demonstrated by Kumar et al. (2016) using MHD simulations. Their simulations describe the activation of a magnetic flux rope (MFR) by an interplay between the two aforementioned scales. Notably the large scale is relatively independent of the particular system under consideration but identifying the small or the diffusion

scale depends on the specific physical system involved. For instance, observations suggest the average MR time for solar flares to be 10^2–10^3 s; the impulsive rise time (Priest & Forbes 2000). Presuming the relation $L \equiv \sqrt{\tau_d \eta}$ holds well and the magnetic diffusion timescale $\tau_d \approx 10^3$ s, the L that initiates the MR turns out to be ≈32 m. The local Lundquist number then gets reduced to $S \approx 3.2 \times 10^7$. As a consequence, an ion inertial scale $\delta_i \approx 2.25$ m in the solar corona (Priest & Forbes 2000) suggests that the order of the dissipation term, $1/S \approx 10^{-7}$, is much smaller than the order of the Hall term, $\delta_i/L \approx 10^{-2}$, in an appropriate dimensionless induction equation[4] (Westerberg & Åkerstedt 2007)

$$\frac{\partial \boldsymbol{B}}{\partial t} = \nabla \times (\boldsymbol{v} \times \boldsymbol{B}) - \frac{1}{S}\nabla \times \boldsymbol{J} - \frac{\delta_i}{L}\nabla \times (\boldsymbol{J} \times \boldsymbol{B}), \quad (1)$$

where $\boldsymbol{J}(=\nabla \times \boldsymbol{B})$ and $\boldsymbol{v}$ are the volume current density and the plasma flow velocity, respectively. The disparity in the magnitude orders of the dissipation and the Hall forcing suggests that if the dissipation is important, then so is the Hall magnetohydrodynamics (HMHD). It also indicates that HMHD can be crucial for coronal transients—MRs being their underlying reason. By the same token, HMHD is also important in other systems like Earth's magnetosphere, typically at the magnetopause and the magnetotail where CSs exist (Mozer et al. 2002).

In the HMHD, the ion and electron motions decouple (Sonnerup 1979), and the MFLs are frozen in the electron fluid instead of the ion fluid. Additionally, straightforward mathematical manipulations show that the Hall term in the induction equation does not affect the dissipation rate of magnetic energy and magnetic helicity (Priest & Forbes 2000). Given the unique properties of HMHD, we expect it to reveal subtle changes in MFL evolution familiar from the standard MHD (Kumar et al. 2016; Nayak et al. 2019, 2020), and refine the dynamics leading to magnetic reconnections. To further explore HMHD specifically contextual to the solar physics, we have extended the EULAG-MHD model (Charbonneau & Smolarkiewicz 2013; Smolarkiewicz & Charbonneau 2013) by including the Hall forcing and document here the results pertaining to two distinct sets of large-eddy simulations. The first set focuses on benchmarking the numerical model by verifying the HMHD physics in three spatial dimensions. The simulations highlight the complexity in reconnection-assisted formation of coherent magnetic structures, hitherto less explored in the contemporary research. The second set, simulates, for the first time to our knowledge, the formation and evolution of an MFR under the influence of the Hall forcing—initiated from sheared bipolar magnetic loops relevant to the solar corona.

Related to our simulations, Mozer et al. (2002) using two-dimensional (2D) geometry have shown that the Hall forcing causes the electrons residing on the reconnection plane containing the MFLs to flow into and out of the reconnection region, generating the in-plane current. The in-plane current, in turn, develops a magnetic field with a component out of the reconnection plane. This out-of-plane magnetic field, or the Hall magnetic field, has quadrupole structure. The asymmetric propagation of the reconnection plane, because of a "reconnection wave" has been shown by Huba & Rudakov (2002) in a simulation of three-dimensional (3D) MR in the Hall limit, where curved out-of-plane MFLs along with the density gradient play a crucial role.

The remainder of the paper is organized as follows. Section 2 outlines the numerical model. Section 3 benchmarks the code using 3D simulations and, subsequently presents a novel numerical experiment that compares activation of a solar-like MFR under standard MHD and HMHD formulations. Section 4 summarizes the key findings of this work.

2. The Numerical Model

A numerical simulation consistent with physics of solar corona must accurately preserve the flux freezing by minimizing numerical dissipation and dispersion errors away from the reconnection regions characterized by steep gradients of the magnetic field (Bhattacharyya et al. 2010). Such minimization is a signature of a class of inherently nonlinear high-resolution transport methods that preserve field extrema along flow trajectories, while ensuring higher-order accuracy away from steep gradients in advected fields. Consequently, we incorporate the Hall forcing in the established high-resolution EULAG-MHD model (Charbonneau & Smolarkiewicz 2013; Smolarkiewicz & Charbonneau 2013), a specialized version of the general-purpose hydrodynamic model EULAG predominantly used in atmospheric and climate research (Prusa et al. 2008). Central to the EULAG is the spatio-temporally second-order-accurate nonoscillatory forward-in-time (NFT) advection scheme MPDATA, a.k.a the Multidimensional Positive Definite Advection Transport Algorithm (Smolarkiewicz 2006). A feature unique to MPDATA and important in our calculations is its widely documented dissipative property that mimics the action of explicit subgrid-scale turbulence models, wherever the concerned advective field is under-resolved—the property referred to as implicit large-eddy simulations (ILES) (Grinstein et al. 2007). The resulting MRs remove the under-resolved scales and restore the flux freezing. These MRs being intermittent and local, successfully mimic physical MRs. The ILES property of MPDATA have proven instrumental in a series of advanced numerical studies across a range of scales and physical scenarios, including studies related to the coronal heating along with data-constrained simulations of solar flares and coronal jets (Bhattacharyya et al. 2010; Kumar & Bhattacharyya 2011; Kumar et al. 2015, 2017; Prasad et al. 2017, 2018; Nayak et al. 2019, 2020). The simulations reported in this paper also benefit from the ILES property of MPDATA.

Here, the numerically integrated HMHD equations assume a perfectly conducting, incompressible magnetofluid. Using a conservative flux-form and dyadic notation, they are compactly written (assuming cgs units) as

$$\frac{\partial \boldsymbol{v}}{\partial t} + \nabla \cdot \boldsymbol{vv} = -\nabla\phi + \frac{1}{4\pi\rho_0}\nabla \cdot \boldsymbol{BB} + \mu_0 \nabla^2 \boldsymbol{v}, \quad (2)$$

$$\frac{\partial \boldsymbol{B}}{\partial t} + \nabla \cdot \boldsymbol{vB} = \nabla \cdot \boldsymbol{Bv} - \frac{d_0}{4\pi}(\nabla \times \nabla \cdot \boldsymbol{BB}) - \nabla\phi^*, \quad (3)$$

$$\nabla \cdot \boldsymbol{v} = 0, \quad (4)$$

$$\nabla \cdot \boldsymbol{B} = 0, \quad (5)$$

where ρ_0 and μ_0 denote, respectively, constant density and kinematic viscosity, $\phi = (p + \boldsymbol{B}^2/8\pi)/\rho_0$ is the density normalized total pressure, and $d_0 = \sqrt{4\pi}\,\delta_i/\rho_0$; the $-\nabla\phi^*$ term on the right-hand side (rhs) of (3) will be explained shortly.

[4] Hereafter, a constant electron number density is assumed.

To highlight the numerics of EULAG-MHD and its extension to HMHD, the prognostic PDEs (2) and (3) are further symbolized as a single equation

$$\frac{\partial \boldsymbol{\Psi}}{\partial t} + \nabla \cdot \boldsymbol{v}\Psi = \boldsymbol{R}\boldsymbol{\Psi}, \tag{6}$$

where $\boldsymbol{\Psi} = \{v_x, v_y, v_z, B_x, B_y, B_z\}^T$ is the vector of prognosed variables, and $\boldsymbol{R}(\boldsymbol{\Psi})$ is the vector of their associated rhs forcings. The principal second-order-accurate NFT Eulerian algorithm for (6) can be written compactly as

$$\begin{aligned}\boldsymbol{\Psi}_{\boldsymbol{i}}^{n} &= \mathcal{A}_{\boldsymbol{i}}(\boldsymbol{\Psi}^{n-1} + \delta_h t\, \boldsymbol{R}^{n-1}, \boldsymbol{v}^{n-1/2}) + \delta_h t\, \boldsymbol{R}(\boldsymbol{\Psi})|_{\boldsymbol{i}}^{n} \\ &\equiv \widehat{\boldsymbol{\Psi}}_{\boldsymbol{i}} + \delta_h t\, \boldsymbol{R}(\boldsymbol{\Psi})|_{\boldsymbol{i}}^{n},\end{aligned} \tag{7}$$

where $n, \boldsymbol{i}$ refer to $(t^n, \boldsymbol{x}_{\boldsymbol{i}})$ locations on a regular collocated grid, δt marks the time step with $\delta_h t = 0.5\delta t$, and $\mathcal{A}$ denotes the MPDATA advection operator, solely dependent on the preceding, $t^{n-1} = t^n - \delta t$, values of $\boldsymbol{\Psi}$ as well as a first-order estimate of the solenoidal velocity at $t^n - \delta_h t$ extrapolated from the earlier values.

The principal algorithm (7) is implicit for all prognosed variables and diagnosed potentials ϕ and ϕ^* that enter (2) and (3), respectively. While ϕ is a physical variable, ϕ^* is a numerical facilitator enabling restoration of (5)—viz. divergence cleaning—eventually polluted with truncation errors. Because of its nonlinearity, the rhs $\boldsymbol{R}$ of (7) is viewed as a combination of a linear term $\boldsymbol{L}\boldsymbol{\Psi}$ (with $\boldsymbol{L}$ denoting a known linear operator), a nonlinear term $\boldsymbol{N}(\boldsymbol{\Psi})$, and the potential term $-\nabla\boldsymbol{\Phi}$ with $\boldsymbol{\Phi} \equiv (\phi,\ \phi,\ \phi,\ \phi^*,\ \phi^*,\ \phi^*)^T$. The resulting form of (7) is realized iteratively with the nonlinear part of the rhs forcing lagged behind,

$$\boldsymbol{\Psi}_{\boldsymbol{i}}^{n,\nu} = \widehat{\boldsymbol{\Psi}}_{\boldsymbol{i}} + \delta_h t\, \boldsymbol{L}\boldsymbol{\Psi}|_{\boldsymbol{i}}^{n,\nu} + \delta_h t\, \boldsymbol{N}(\boldsymbol{\Psi})|_{\boldsymbol{i}}^{n,\nu-1} - \delta_h t\, \nabla\boldsymbol{\Phi}|_{\boldsymbol{i}}^{n,\nu}, \tag{8}$$

where $\nu = 1, .., m$ numbers the iterations. The algorithm in (8) is still implicit with respect to $\boldsymbol{\Psi}_{\boldsymbol{i}}^{n,\nu}$ and $\boldsymbol{\Phi}_{\boldsymbol{i}}^{n,\nu}$, yet straightforward algebraic manipulations lead to the closed-form expression

$$\boldsymbol{\Psi}_{\boldsymbol{i}}^{n,\nu} = [\boldsymbol{I} - \delta_h t\boldsymbol{L}]^{-1}(\widehat{\widehat{\boldsymbol{\Psi}}} - \delta_h t \nabla\boldsymbol{\Phi}^{n,\nu})|_{\boldsymbol{i}}, \tag{9}$$

where $\widehat{\widehat{\boldsymbol{\Psi}}} \equiv \widehat{\boldsymbol{\Psi}} + \delta_h t\boldsymbol{N}\boldsymbol{\Psi}|^{n,\nu-1}$ denotes the modified explicit element of the solution. Taking the divergences of the first and the second three components of (9), produces two elliptic Poisson problems, for ϕ and ϕ^*, respectively, as implied by (4) and (5).

The iterative formulation of (7) in (8) outlines the concept of the EULAG-MHD discrete integrals. The actual iterative implementation of (7), detailed in Smolarkiewicz & Charbonneau (2013), proceeds in a sequence of steps such that the most current update of a dependent variable is used in the ongoing step, wherever possible. Furthermore, to enhance the efficacy of the scheme, judicious linearization of $\boldsymbol{N}(\boldsymbol{\Psi})$ is employed, together with a blend of evolutionary and conservative forms of the induction and Lorentz forces. Each outer iteration has two distinct blocks. The focus of the first, "hydrodynamic" block is on integrating the momentum equation, where the magnetic field enters the Lorentz force and is viewed as supplementary. This block ends with the final update of the velocity via the solution of the elliptic problem for pressure. The second, "magnetic" block uses the current updates of the velocities to integrate the induction equation. It ends with the final update of the magnetic field via the solution of the elliptic problem for the divergence cleaning. Incorporating the Hall forcing into the EULAG-MHD model follows the principles of the outlined standard MHD integrator. Because the Hall term enters (3) as the curl of the Lorentz force, it can be judiciously updated and combined with the standard induction forcing, whenever the Lorentz force and/or the magnetic field are updated. In the current implementation it enters the explicit (lagged) counterpart of the induction force, and is updated after the inversion of the implicit evolutionary form of the induction equation in the "magnetic" block; see Section 3.2 in Smolarkiewicz & Charbonneau (2013) for details.

3. Results

3.1. Benchmarking the 3D HMHD Solver

To benchmark the HMHD solver, the initial field is selected as

$$B_x = 0, \tag{10}$$

$$B_y = 0, \tag{11}$$

$$B_z = 2.5\sin(x), \tag{12}$$

with $x, y, z \in [-2\pi, 2\pi]$, respectively, in each direction of a 3D Cartesian domain. This selection has two merits: first, the magnetic field reverses at $x = 0$; and second, the Lorentz force

$$(\boldsymbol{J} \times \boldsymbol{B})_x = -6.25\cos(x)\sin(x), \tag{13}$$

$$(\boldsymbol{J} \times \boldsymbol{B})_y = 0, \tag{14}$$

$$(\boldsymbol{J} \times \boldsymbol{B})_z = 0, \tag{15}$$

generates a converging flow that onsets MRs. Being different from the traditional initial conditions involving the Harris current sheet or the GEM challenge (Birn et al. 2001), this selection shows the Hall effects are independent of particular initial conditions. We have explored simulations using the traditional initial conditions (not shown) and the outcomes are similar.

The Equations (2)–(5) are integrated numerically, as described in the preceding section, for $d_0 = 0,\ 2$. The latter selection of d_0 optimizes the computation time and a tractable development of magnetic structures for the employed spatio-temporal resolution. The corresponding $\delta_i = 0.56$ is slightly higher than the spatial step size $\delta\boldsymbol{x} \approx 0.40$ set for the simulation. Consequently, the Hall forcing kicks in near the dissipation scale, thereby directly affecting the overall dynamics only in vicinities of the MR regions. With the large scale $L = 4\pi$ of the magnetic field variability, the resulting $\delta_i/L \approx 0.04$ is on the order of the solar coronal value. The simulations are then expected to capture dynamics of the HMHD and the intermittently diffusive regions of corona-like plasmas, thus shedding light on the evolution of neighboring frozen-in MFLs. Moreover, $1/S < \delta_i/L$ as discussed in Section 1. The physical domain is resolved with $32 \times 32 \times 32$ grid. A coarse resolution is selected for an earlier onset of MRs and to expedite the overall evolution. The kinematic viscosity and mass density are set to $\nu = 0.005$ and $\rho_0 = 1$, respectively. All three boundaries are kept open. The initial magnetic field is given by Equations (10)–(12) and

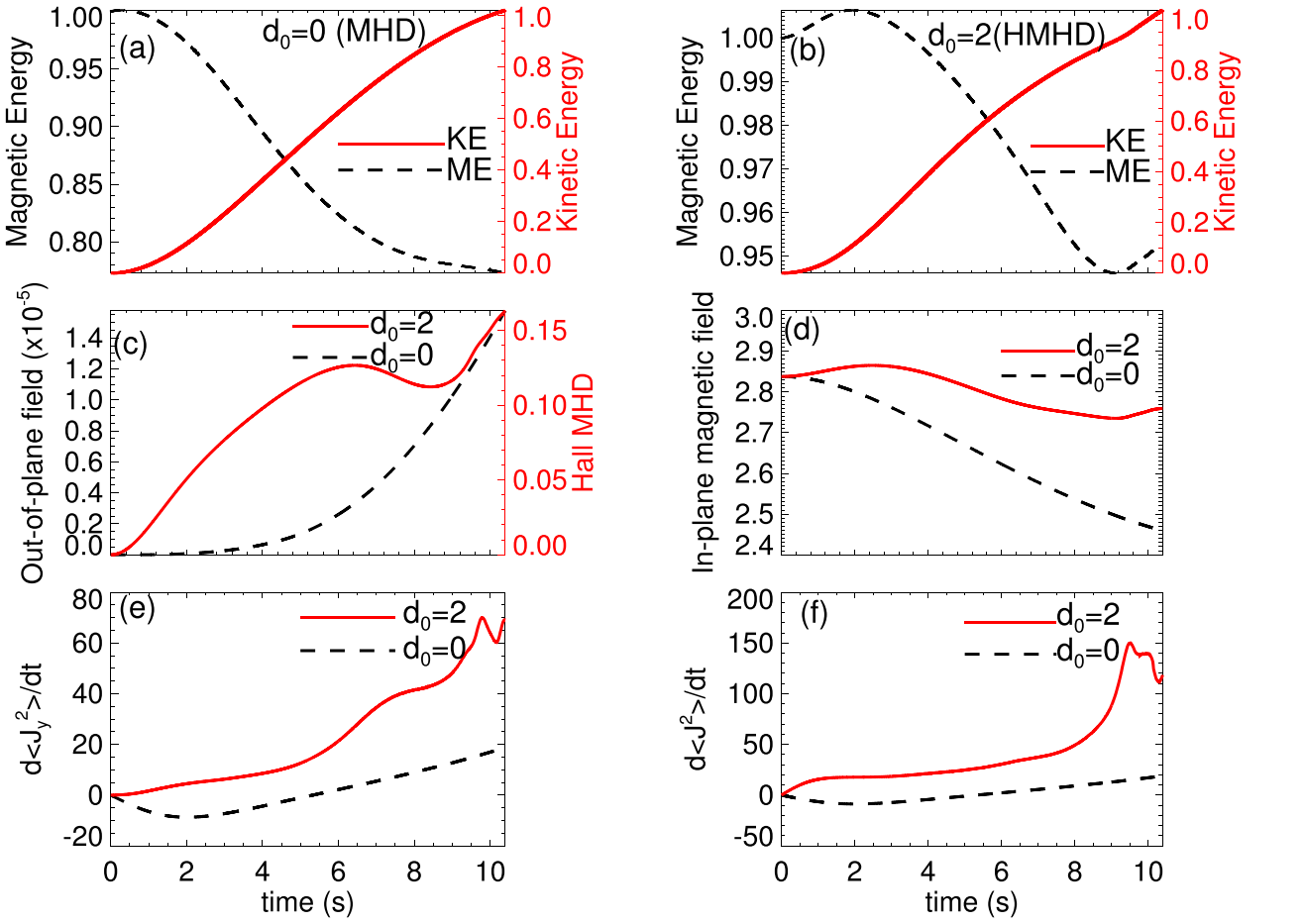

Figure 1. Panels (a) and (b) show the evolution of the magnetic energy (black dashed curve) and kinetic energy (red solid curve) for $d_0 = 0$ (MHD) and $d_0 = 2$ (HMHD) respectively. Panel (c) shows the evolution of out-of-plane magnetic field for $d_0 = 0$ (MHD) with a black dashed curve and $d_0 = 2$ (HMHD) with a red solid curve respectively. Also in panels (a) to (c), the scales for the solid and the dashed curves are spaced at right and left, respectively. Panels (d) to (f) represent in-plane magnetic field, amplitudes of the rate of change of out-of-plane and total current densities for $d_0 = 0$ (black dashed curve) and $d_0 = 2$ (red solid curve), respectively. The variables in panels (a) and (b) are normalized with the initial total energies. All the variables are averaged over the computational domain. Important are the generation of the out-of-plane magnetic field along with sharp changes in time derivatives of the out-of-plane and total volume current densities in HMHD simulations.

Table 1
List of Parameters for Simulation with Sinusoidal Initial Field

ρ_0	d_0	δ_i	L	$\frac{\delta_i}{L}$	Simulation Box Size	Resolution	ν
1.0	2.0	0.56	4π	0.04	$(4\pi)^3$	$(32)^3$	0.005

the fluid is evolved from an initially static state having pressure $p = 0$. The simulation parameters are listed in Table 1.

The overall evolution is depicted in different panels of Figure 1. The initial Lorentz force, given by Equations (13)–(15), pushes segments of the fluid on either side of the field reversal layer toward each other. Consequently, magnetic energy gets converted into kinetic energy of the plasma flow: panels (a) and (b). Panels (c) and (d) show the history of grid-averaged magnitude of the out-of-plane (along y) and in-plane (xz plane) magnetic fields. Notably, for $d_0 = 0$ (MHD) the out-of-plane field is negligibly small compared to its value for $d_0 = 2$ (HMHD). Such generation of the out-of-plane magnetic field is inherent to HMHD and is in conformity with the result of another simulation (Ma & Bhattacharjee 2001). Panels (e) and (f) illustrate the variation of the rate of change of out-of-plane current density and total volume current density. Importantly, in contrast to the $d_0 = 0$ curve, the rate of change of volume current density shows an early bump at ($\approx$7.5 s) and a well defined peak ($t \approx 9.75$ s) for $d_0 = 2$. Such peaks in the current density are expected in the impulsive phase of solar flares, and they manifest MRs in the presence of the Hall term (Bhattacharjee 2004).

Figure 2 plots MFLs tangential to preselected planes during different instances of the evolution for $d_0 = 0$. Panel (a) plots the initial MFLs for reference. The initial Lorentz force pushes antiparallel MFLs (depicted in the inset) toward each other. Subsequently, X-type neutral points develop near $z = \pm 2\pi$. The consequent MRs generate a complete magnetic island, which maintains its identity for a long time. Such islands, stacked on each other along the y, generate an extended magnetic flux tube (MFT) at the center, which in its generality is a magnetic flux surface. Further evolution breaks the MFT such that the cross section of the broken tube yields two magnetic islands. The point of contact between the two tear-drop shaped MFLs generates an X-type neutral point. Notably, within the computational time, no field is generated along the y-direction and the corresponding symmetry is exactly preserved. In Figure 3 we provide the 2D projection of the MFLs on the

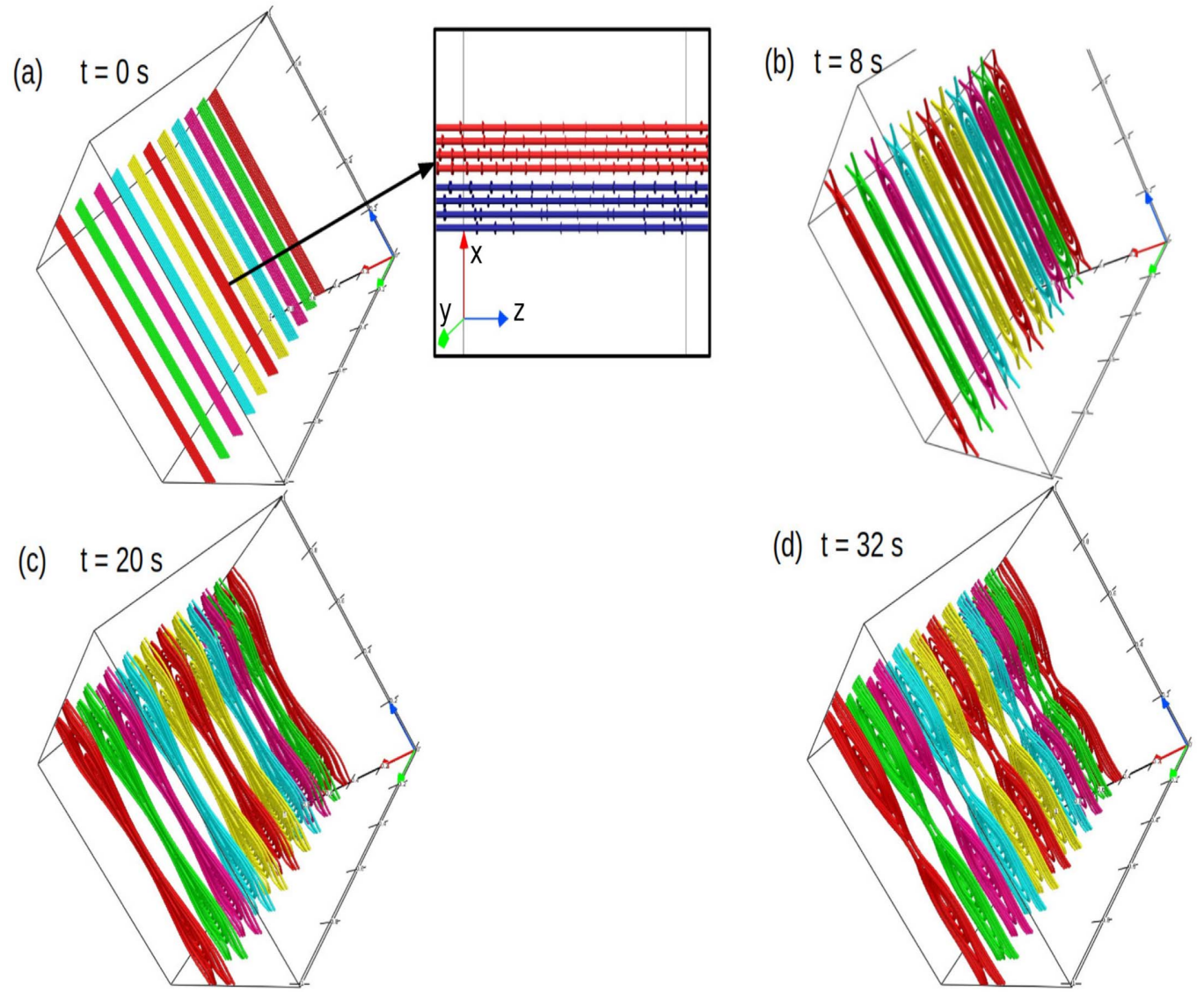

Figure 2. Snapshots of preselected MFLs for the $d_0 = 0$ (MHD) simulation, plotted on equidistant y-constant planes. In all figures (this and hereafter), the red, green, and blue arrows represent the x-, y-, and z-axes, respectively. The inset in panel (a) highlights the polarity reversal of the initial magnetic field lines. The plots illustrate the formation of a primary flux tube (panel (b)) made by stacking of the depicted MFLs. Notably symmetry is preserved throughout evolution.

(An animation of this figure is available.)

$y = 0.5$ plane, for later comparison with similar projection for the $d_0 = 2$ case.

Panels (a) to (b) and (c) to (d) of Figure 4 show MFL evolution for $d_0 = 2$ from two different vantage points. The MFLs are plotted on different y-constant planes centered at $x = 0.5$ and $x = 0.74435$. The planes are not connected by any field lines at $t = 0$. Importantly out-of-plane magnetic field is generated with time in both sets of MFLs (at $x = 0.5$ and $x = 0.74435$), which connects two adjacent planes (see panel (b) of Figures 2 and 4) and breaks the y-symmetry that was preserved in the $d_0 = 0$ case—asymmetry in reconnection planes. Consequently the evolved $\boldsymbol{B}$ is 3D. Also, the out-of-plane component (B_y) has a quadrupole structure, shown in Figure 5, which is in congruence with observations and models (Mozer et al. 2002).

For better clarity the MFL evolution is further detailed in Figures 6 and 7. In Figure 6 important is the development of two MFTs constituted by disjointly stacked magnetic islands. The islands are undulated and appear much earlier compared to the $d_0 = 0$ case, indicating the faster reconnection. Notable is also the creation of flux ropes where a single helical MFL makes a large number of turns as the out-of-plane field B_y develops (Figure 7). In principle, the MFL may ergodically span the MFS, if the "safety factor" $q = rB_y/\mathcal{L}B_T$ is not a rational number (Freidberg 1982); here r and $\mathcal{L}$ are the radius and length of the rope, respectively, and $B_T = \sqrt{B_x^2 + B_y^2}$. Further evolution breaks the flux rope into secondary ropes by internal MRs—i.e., reconnections between MFLs constituting the rope—shown in panels (a) to (d) of Figure 7, where two oppositely directed sections of the given MFLs reconnect (location marked by arrows in the Figure 7). Since most of the contemporary Hall simulations are in 2D, in Figure 8 we plot the projection of MFLs depicted in Figure 4 on the $y = 0.5$ plane. The corresponding evolution is visibly similar to the

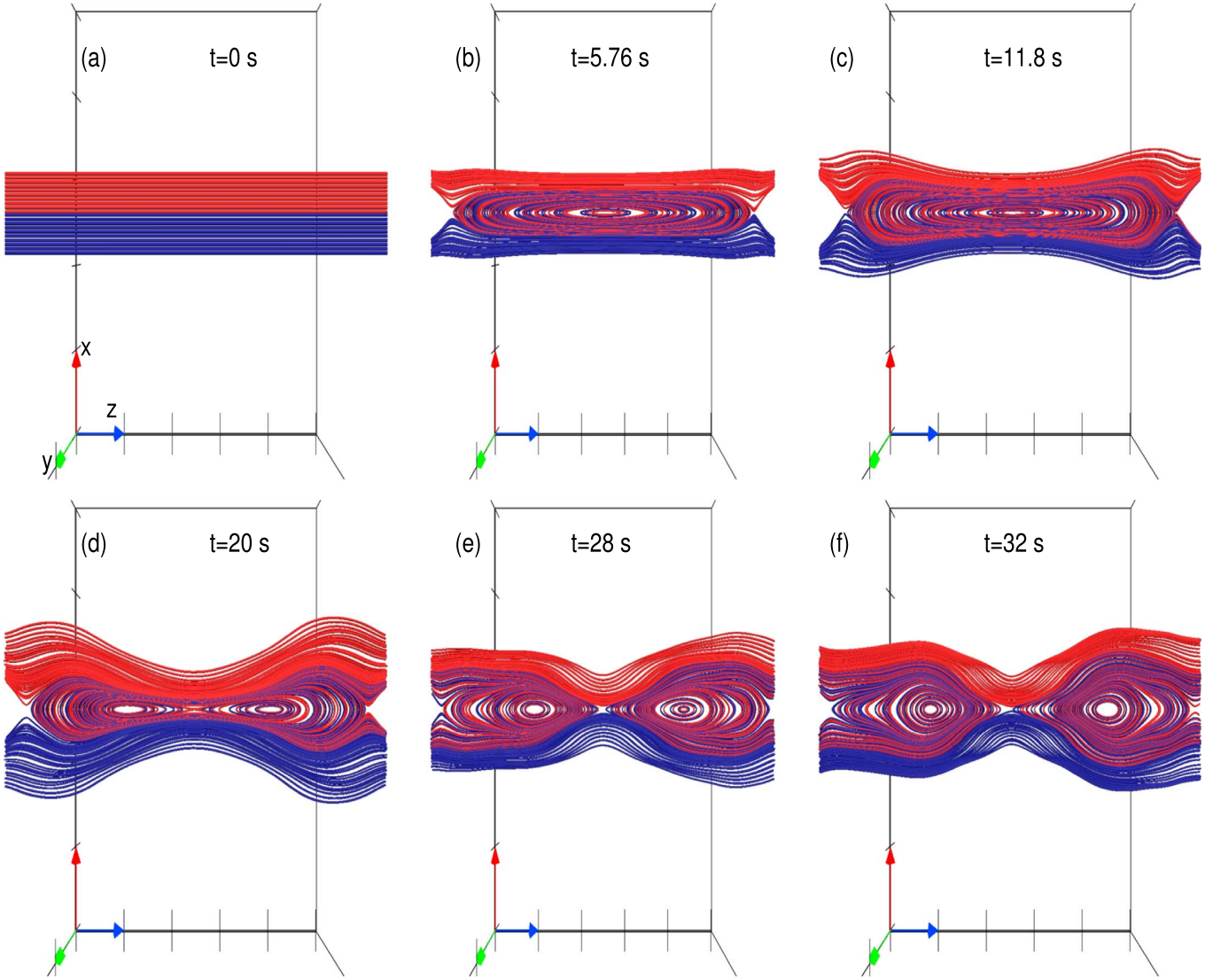

Figure 3. Projection of MFLs depicted in Figure 2 on a y-constant plane during their evolution. Notable is the formation of a primary magnetic island having a single O-type neutral point. Subsequently, the primary island breaks into two secondary islands, which are separated by an X-type neutral point.

generation of secondary islands (Shi et al. 2019), and their later coalescence as envisioned by Shibata & Tanuma (2001).

To complete the benchmarking, we repeated the numerical experiment described in Huba (2003), where wave propagation in the presence of the Hall forcing is explored. Notably, the EULAG-MHD being incompressible, we only concentrate on the whistler wave. The experimental setup is identical to that in the Huba (2003); the ambient field is given by

$$\boldsymbol{B} = B_0 \cdot \hat{e_z}, \tag{16}$$

whereas the perturbations are

$$\delta B_x = \delta B_0 \sin\left(\frac{2\pi m z}{L_0}\right), \tag{17}$$

$$\delta B_y = \delta B_0 \cos\left(\frac{2\pi m z}{L_0}\right), \tag{18}$$

where $B_0 = 1000$, $\delta B_0 = 10$, and $L_0 = 7\pi$. The mode number is represented by m. The simulations are carried out on a computational domain of size $128 \times 128 \times 128$, and the dimensionless HMHD equations (discussed shortly) are employed. The analytical and the numerical frequencies obtained for various modes are listed in Table 2, confirming the simulations to replicate the analytical calculations fairly well.

3.2. Activation of MFR from Bipolar Magnetic Field

Sheared bipolar magnetic field is ubiquitous in solar plasma and plays an important role in the onset of solar transients. In brief, the coronal mass ejection models require MFRs to confine plasma. Destabilized from its equilibrium, as the MFR ascends with height, it stretches the overlaying MFLs. The ascend of the rope decreases the magnetic pressure below it, which in turn sucks in more MFLs. These nonparallel MFLs reconnect and the generated outflow further pushes the MFR up. Details about the coronal mass ejection can be found in the review article by Chen (2011). Recently, Kumar et al. (2016) numerically simulated the above scenario to explain generation and dynamics of an MFR beginning from initial sets of sheared and twisted MFLs. In the following, we conduct simulations to numerically explore such activations of MFRs in the presence

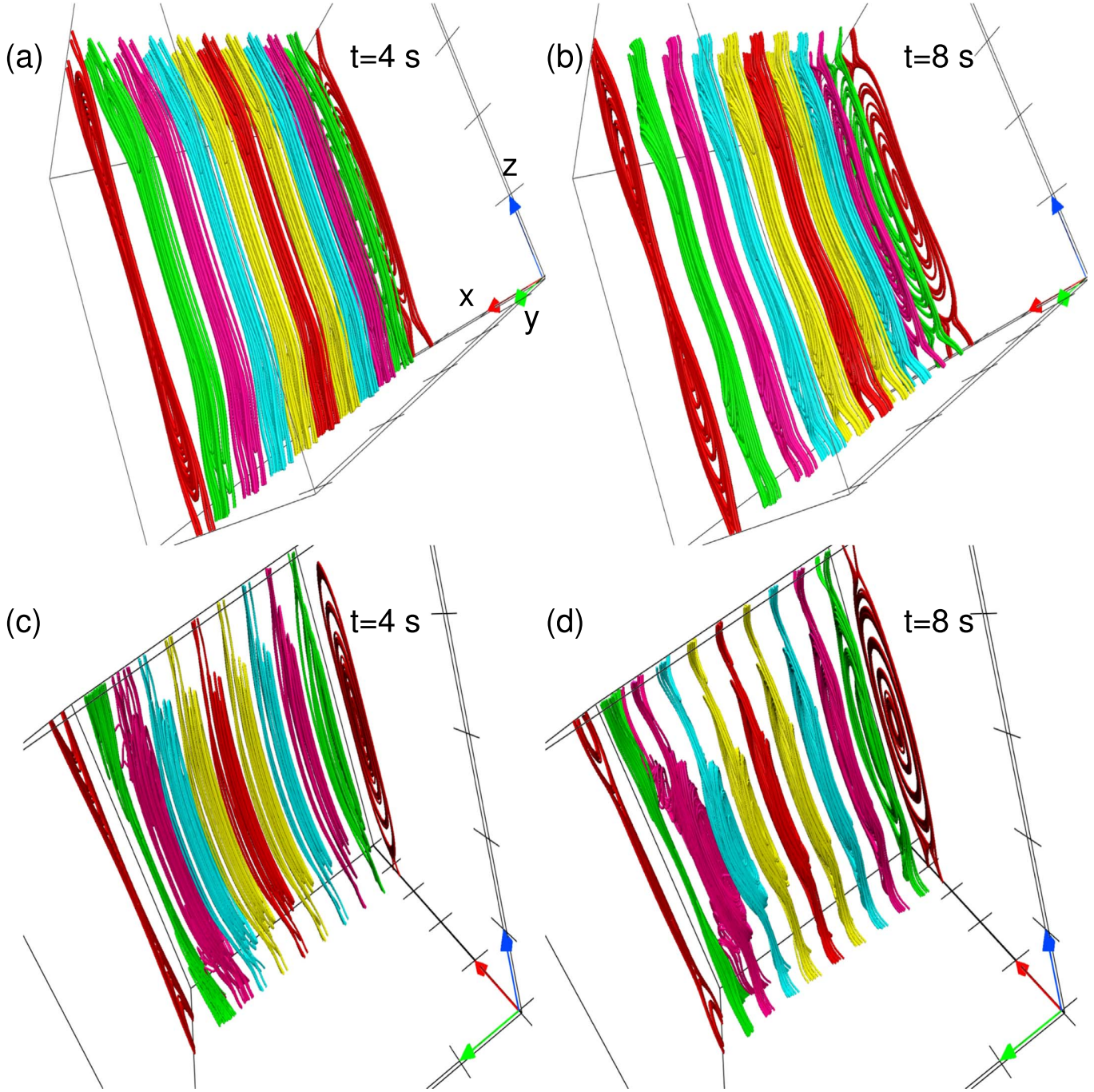

Figure 4. MFL evolution for $d_0 = 2$ (HMHD) case, from two vantage points. The field lines are plotted on planes centered at $x = 0.5$ and $x = 0.74435$ and equidistant along y. Important is the symmetry breaking, see MFLs at $y = -2\pi$ and $y = 2\pi$ of panels (b) and (d). The out-of-plane magnetic field is generated throughout the domain. (A combined animation showing MFL evolution for the top and the bottom panels is available.)

(An animation of this figure is available.)

of the Hall term. For this purpose, we employ the dimensionless form of the HMHD equations achieved through the following normalizations (Kumar et al. 2016)

$$\boldsymbol{B} \longrightarrow \frac{\boldsymbol{B}}{B_0}, \quad \boldsymbol{v} \longrightarrow \frac{\boldsymbol{v}}{v_{\rm A}}, \quad L \longrightarrow \frac{L}{L_0},$$
$$t \longrightarrow \frac{t}{\tau_a}, \quad p \longrightarrow \frac{p}{\rho {v_a}^2}. \tag{19}$$

The constant B_0 is kept arbitrary, whereas L_0 is fixed to the system size. Further, $v_{\rm A} \equiv B_0/\sqrt{4\pi\rho_0}$ is the Alfvén speed, where ρ_0 is a constant mass density. The $\tau_{\rm A}$ and τ_ν are, respectively, the Alfvén transit time ($\tau_{\rm A} = L_0/v_{\rm A}$) and viscous diffusion timescale ($\tau_\nu = L_0^2/\nu$). The kinematic viscosity is denoted by ν. The normalized equations can be readily visualized by setting $1/(4\pi\rho_0) = 1$ and $\mu_0 = \tau_{\rm A}/\tau_\nu$ in (2), $d_0/(4\pi) = \delta_i/L$ in (3), while keeping (4) and (5) unchanged.

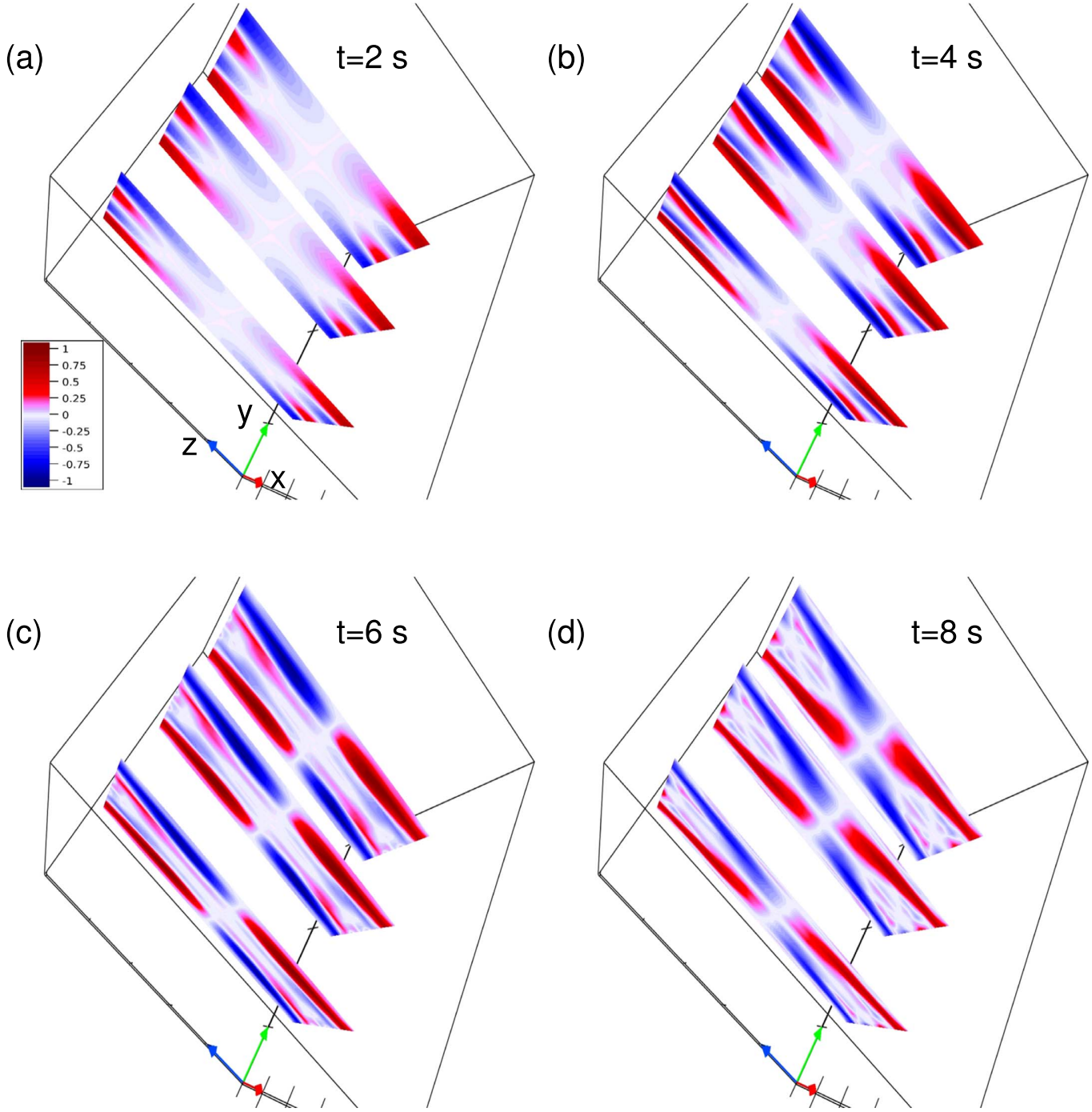

Figure 5. Contour plots of $B_y(x, z)$ (out-of-plane component) on y-constant planes for $d_0 = 2$ (HMHD), with time. The plots confirm the quadrupolar nature of the out-of-plane component of the magnetic field.

The ratio τ_A/τ_ν is an effective viscosity of the system that, along with the other forces, influences the magnetofluid evolution.

The simulation is initiated with the magnetic field given in Kumar et al. (2016)

$$B_x = k_z \sin(k_x x)\exp\left(\frac{-k_z z}{s_0}\right), \tag{20}$$

$$B_y = \sqrt{k_x^2 - k_z^2}\,\sin(k_x x)\exp\left(\frac{-k_z z}{s_0}\right), \tag{21}$$

$$B_z = s_0 k_x \cos(k_x x)\exp\left(\frac{-k_z z}{s_0}\right), \tag{22}$$

with $k_x = 1.0$, $k_z = 0.9$, and $s_0 = 6$. The effective viscosity and mass density are set to $\tau_A/\tau_\nu = 2 \times 10^{-5}$ and $\rho_0 = 1$,

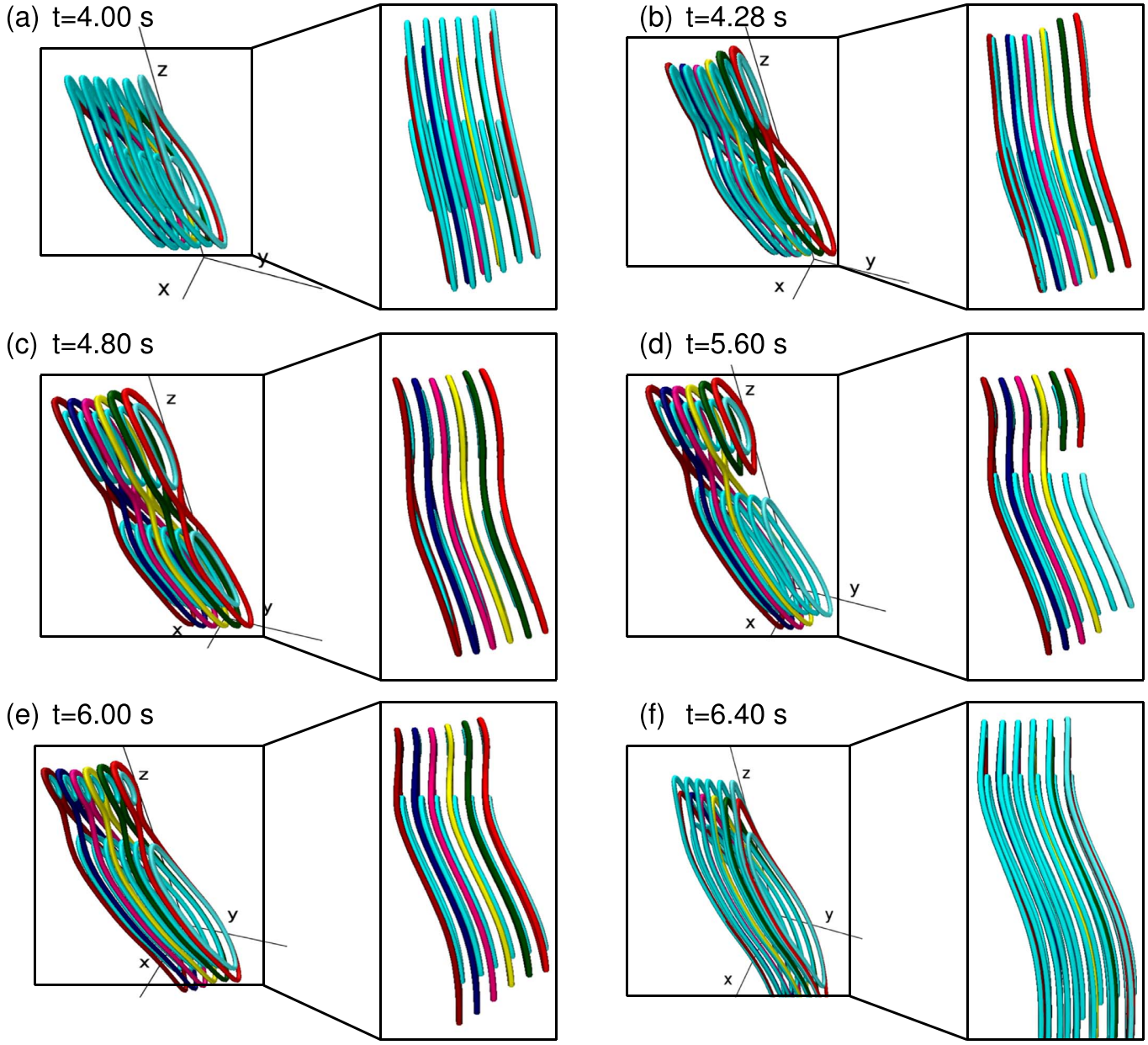

Figure 6. Panels (a) to (f) show the MFL evolution for $d_0 = 2$ (HMHD) case, from two different angles to highlight the generation of two MFTs constituted by disjoint MFLs. The islands look like "Figure 8" structure; panels (b) to (d). The side view of the MFLs are shown in the insets, highlighting their undulated geometry. The three black lines in the background represent the three axes.

respectively. The MFLs are depicted in panel (a) of Figure 9, which are sheared bipolar loops having a straight polarity inversion line and no field-line twist. For simulations, a physical domain of the extent $[\{0, 2\pi\}, \{0, 2\pi\}, \{0, 8\pi\}]$ is resolved on the computational domain of size $64 \times 64 \times 128$, making the spatial step sizes $\delta x = \delta y = 0.0997$, $\delta z = 0.1979$. The temporal step size is $\delta t = 16 \times 10^{-4}$. The initial state is assumed to be motionless and open boundary conditions are employed. The simulations are carried out for $\delta_i/L_0 = 0$ and $\delta_i/L_0 = 0.04$, having a simulated physical time of $7000\tau_A \delta t$. The arbitrary B_0 can be selected such that the Alfvén transit time, $\tau_A \in \{1, 10\}$ s, makes the simulated time, 11.2–112 s, consistent with the beginning of the impulsive phase of a flare 100–1000 s. The simulation parameters for MFR are listed in Table 3.

The evolution onsets as the Lorentz force

$$(\boldsymbol{J} \times \boldsymbol{B})_x = \left[-k_x(k_x^2 - k_z^2) + k_x s_0 \left(s_0 k_x^2 - \frac{k_z^2}{s_0}\right)\right] \times \sin^2(k_x x) \exp\left(-\frac{2k_z z}{s_0}\right), \quad (23)$$

$$(\boldsymbol{J} \times \boldsymbol{B})_z = \left[\frac{k_z}{s_0}(k_x^2 - k_z^2) - k_z \left(s_0 k_x^2 - \frac{k_z^2}{s_0}\right)\right] \times \frac{\sin(2k_x x)}{2} \exp\left(-\frac{2k_z z}{s_0}\right), \quad (24)$$

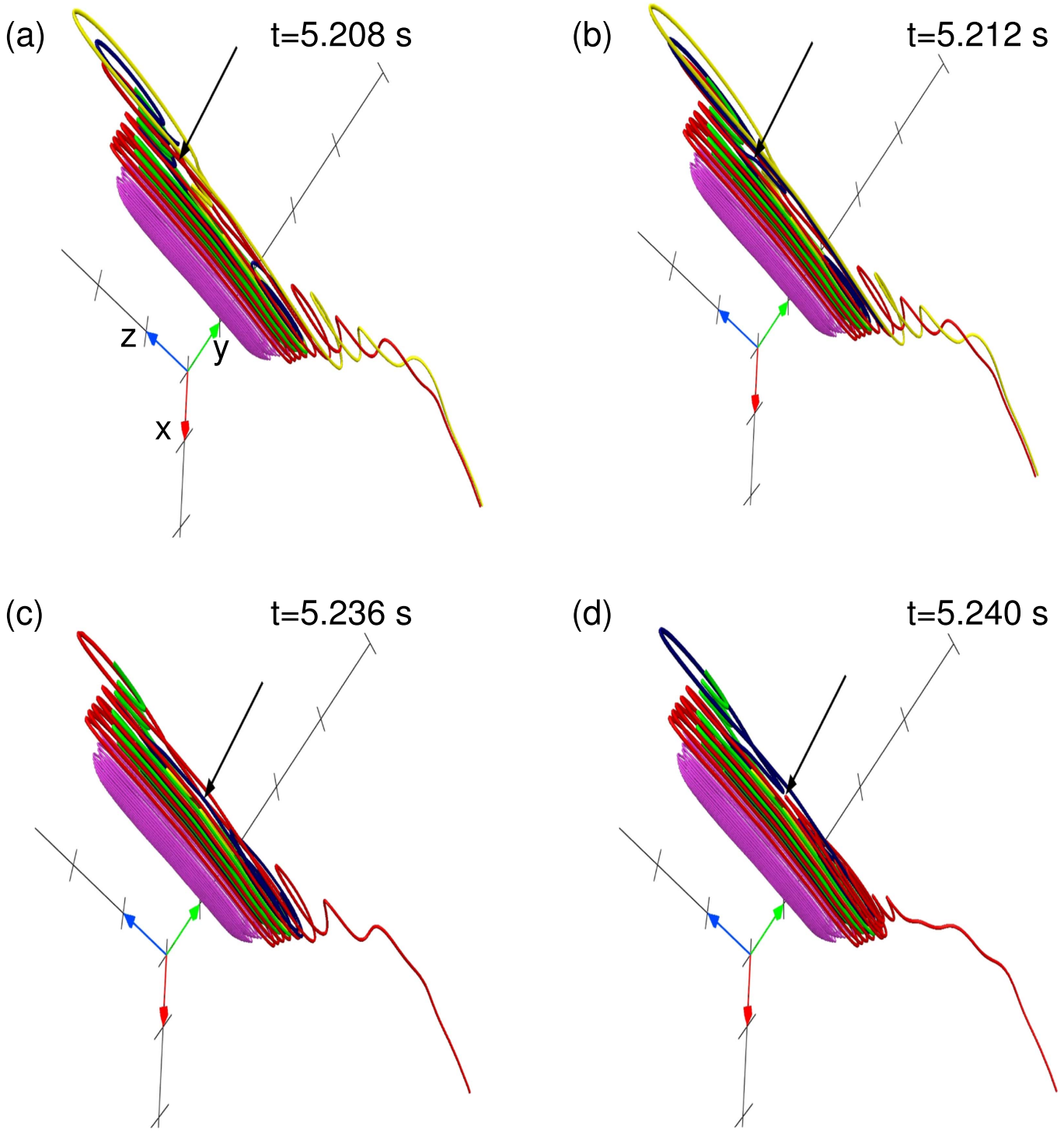

Figure 7. Panels (a) and (b) show the topology of the MFLs for the $d_0 = 2$ (HMHD) evolution, prior to and after the internal reconnection of the dark blue colored MFL (marked by the arrow). Panels (c) and (d) depict the topology of MFLs prior to and after the internal reconnection of blue and red color MFLs within the rope, marked by an arrow.

(An animation of this figure is available.)

pushes oppositely directed segments of MFLs toward each other, generating the neck at $t = 3.264$, panel (b) of the Figure 9—demonstrating the MFL dynamics for $d_0 = 0$. The MRs at the neck generate the MFR—which we refer to as the primary MFR (panel (c) of Figure 9). Further evolution preserves the primary MFR by not allowing it to go through any internal MRs. Notably, the rope loses its initial symmetry along the y-direction by a marginal amount, which we attribute to the open boundary conditions. Nevertheless, the rope rises uniformly about a slightly inclined axis.

The MFL evolution for $\delta_i/L = 0.04$ is exhibited in Figure 10. The selected value is on the order of the coronal

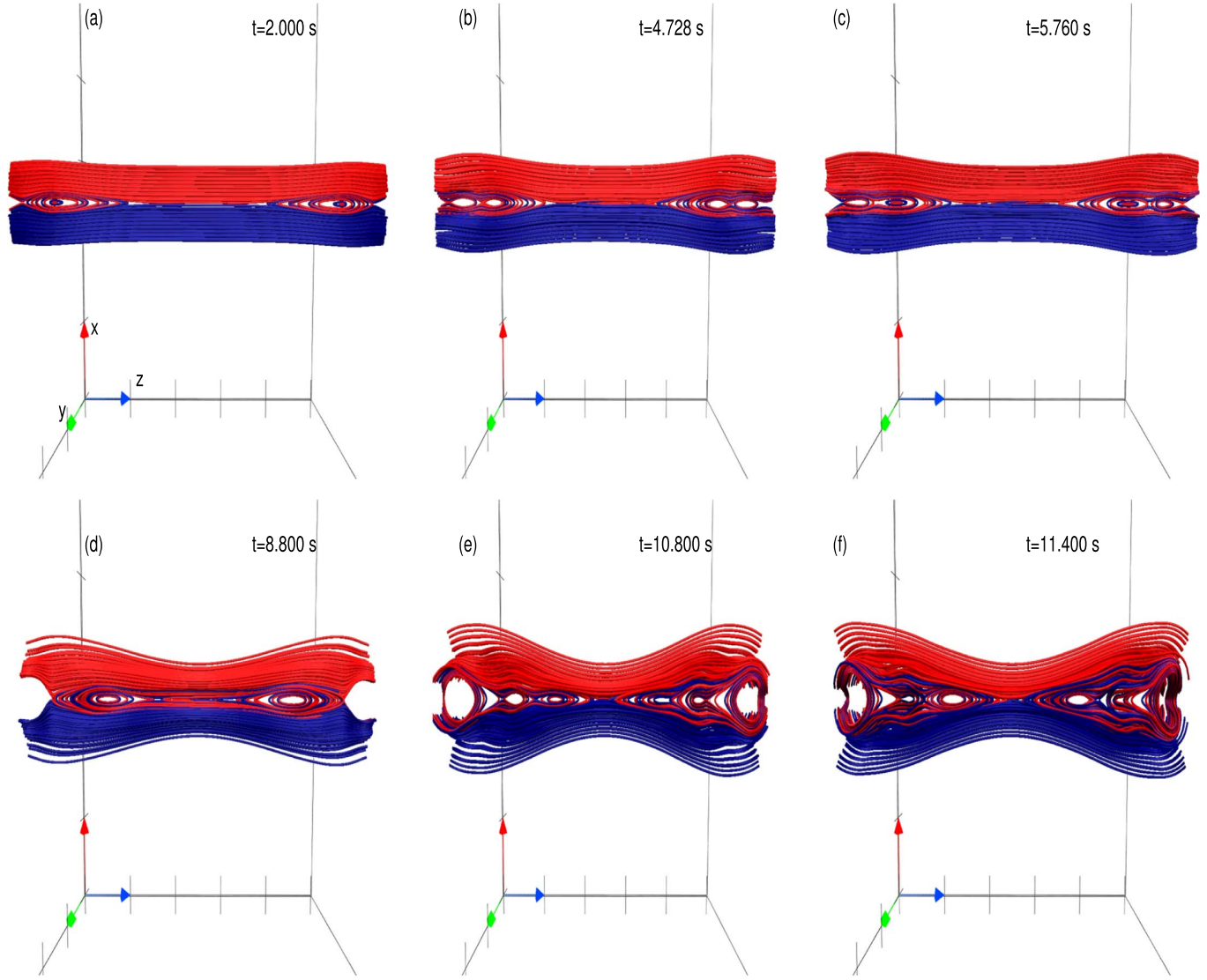

Figure 8. MFL evolution for $d_0 = 2$ (HMHD), projected on the y-constant plane. Panel (a) depicts the development of two primary magnetic islands. Panels (b) and (c) show their further breakage into secondary islands. Panels (d) to (f) show the generation of an X-type neutral point by subsequent merging of the two islands. (An animation of this figure is available.)

Table 2
List of Parameters for the Wave Simulation

m	Analytical Frequency (ω_A)	Numerical Frequency (ω_N)
2	26.12	27.50
3	132.237	141.88
4	417.92	430.04

value quoted in Section 1 and optimizes the computation. The primary MFR develops at $t = 4$, which is similar to the instant at which the primary MFR was generated for the $\delta_i/L = 0$ case. The overall dynamics leading to the primary MFR also remains similar to the one without the Hall forcing. The similar dynamics and the near-simultaneity in the onset of the primary MFR in both cases indicate the large-scale dynamics—i.e., the dynamics before or away from MRs—to be insensitive to the particular Hall forcing. However, there are conspicuous differences between the MHD and HMHD realizations of the MFR morphology. In the HMHD case the primary MFR undergoes multiple internal MRs highlighted in Figure 11, leading to MFL morphologies which when projected favorably look like magnetic islands similar to those found in the sinusoidal simulation. A swirling motion is also observed; see panels (a) to (f) of Figure 11 (better visualized in the animation). Noteworthy, swirling motion during evolution of a prominence eruption has been observed (Pant et al. 2018).

To complete the analyses, we plot the overall evolution of magnetic and kinetic energies, amplitude of the out-of-plane field, and the rate of change of the total volume current density in panels (c) and (d) of Figure 12. The similarity of the energy curves in the presence and absence of the Hall forcing is reminiscent of the fact that the Hall term does not affect the system energetics directly. Importantly, the out-of-plane magnetic field (approximated by the axial magnetic field B_y) is larger than that in the absence of the Hall forcing, in accordance with the expectation. Further, contrary to its smooth variation in the MHD case, the rate of change of total volume

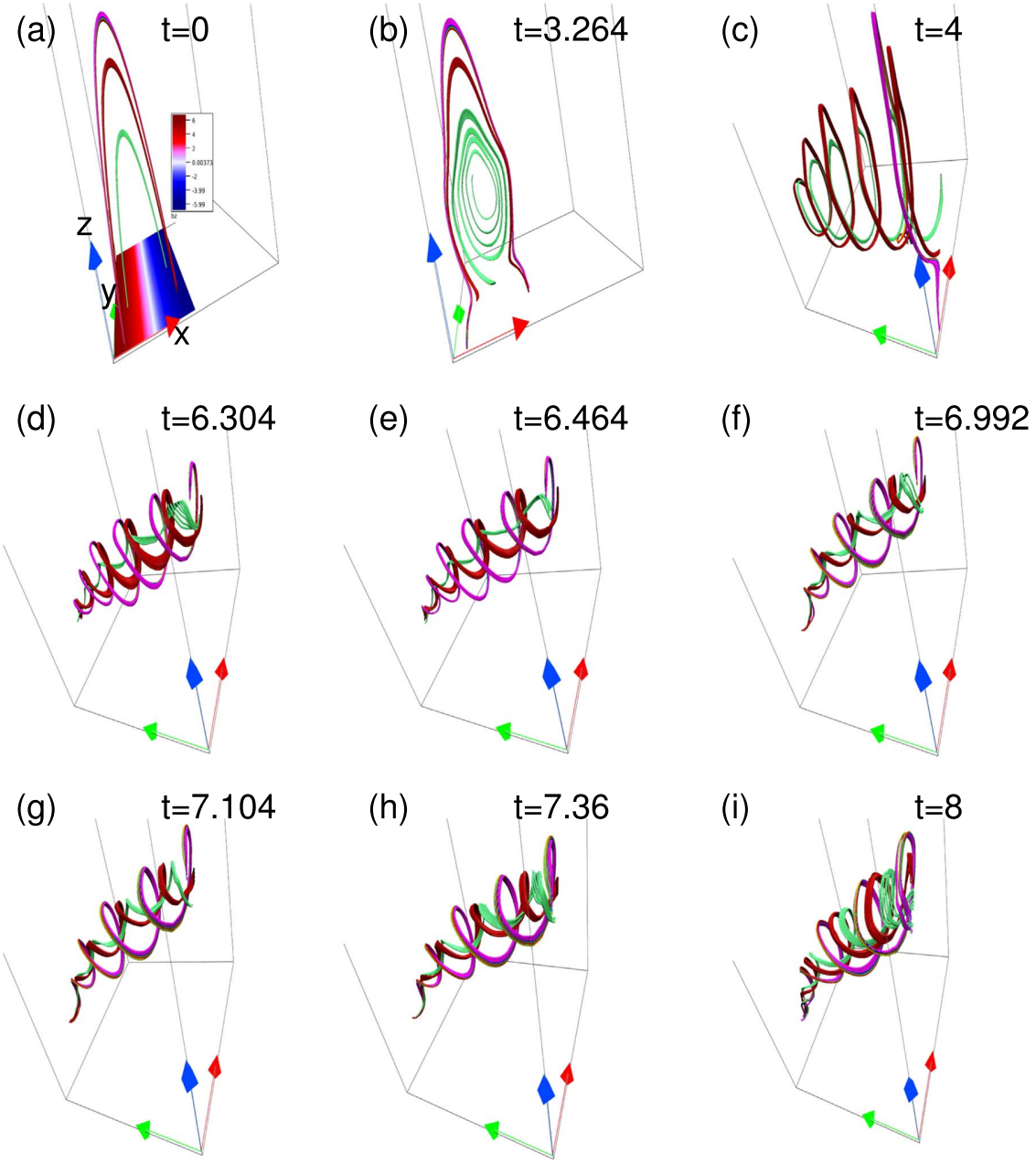

Figure 9. Panel (a) shows the initial bipolar sheared arcade configuration along with polarity inversion line. Panels (b) and (c) show the formation of magnetic flux rope. Panels (d) to (i) represent the further evolution of the magnetic flux rope with a tilted axis (along y) of it for the $\delta_i/L = 0$ (MHD) case.

Table 3
List of Parameters for Simulation with Bipolar Sheared Magnetic Arcade Initial Field

ρ_0	δ_i	L	$\frac{\delta_i}{L}$	Simulation Box Size	Resolution	Effective Viscosity $\frac{\tau_A}{\tau_\nu}$
1.0	1.005	8π	0.04	$2\pi \times 2\pi \times 8\pi$	$64 \times 64 \times 128$	2×10^{-5}

current density in HMHD goes through small but abrupt changes. Such abrupt changes may correspond to a greater degree of impulsiveness (Bhattacharjee 2004).

To check the dependence of the above findings on the grid resolution, we have carried out auxiliary simulations with $32 \times 32 \times 64$ grid resolution, spanning the same physical domain with all the other parameters kept identical (not shown). The findings are similar to those at the higher resolution. In particular, they evince the nearly simultaneous formation of the primary MFR, with and without the Hall forcing, through the similar dynamical evolution. Also, breakage of the primary MFR through internal MRs is found in the presence of Hall forcing whereas no such breakage is seen in the absence of the Hall forcing. The identical dynamics in two separate resolutions indicate the findings to be independent of the particular resolution used.

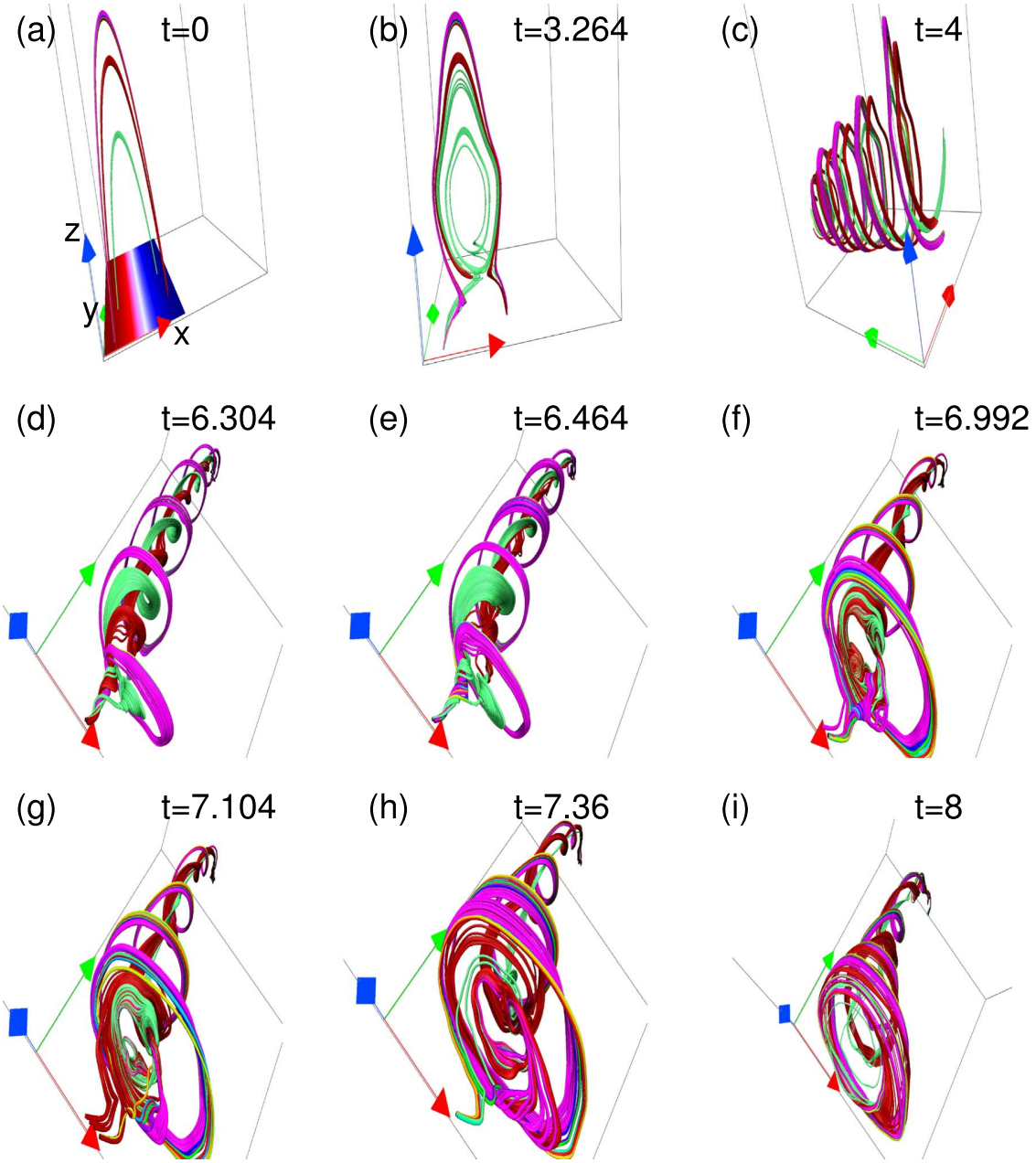

Figure 10. Panels (a) to (i) show the topology of MFLs in their evolution for $\delta_i/L = 0.04$ under the Hall forcing. Important is the similarity of the dynamics leading to the formation of primary MFR which generates at a similar instant as the primary MFR in the absence of the Hall forcing. (A combined animation of Figures 9 and 10 is available.)

(An animation of this figure is available.)

4. Summary

The Eulerian–Lagrangian model EULAG-MHD has been extended to the HMHD regime, by modifying the induction equation to include the Hall term. Subsequently, benchmarking is done with an initially sinusoidal magnetic field, symmetric in the y-direction of the employed Cartesian coordinate system. The choice of the field is based on its simplicity and non-force-free property to exert Lorentz force on the magnetofluid at $t = 0$. Moreover, the selected field provides an opportunity to independently verify the physics of HMHD without repeating the more traditional computations related to the Harris equilibrium or the GEM challenge. Simulations are carried out in the absence and presence of the Hall term. In the absence of the Hall term the magnetic field maintains its symmetry as MRs generate MFTs made by disjoint MFLs. With the Hall term, the evolution becomes asymmetric and 3D due to the development of magnetic field, which is directed out of the reconnection plane. This is in concurrence with earlier simulations. Along with the flux tube, MRs also generate MFR in the HMHD. When viewed along the negative y-direction, the rope and the tube appear as magnetic islands. Further evolution leads to breakage of the primary islands into secondary islands and later their coalescence. The results,

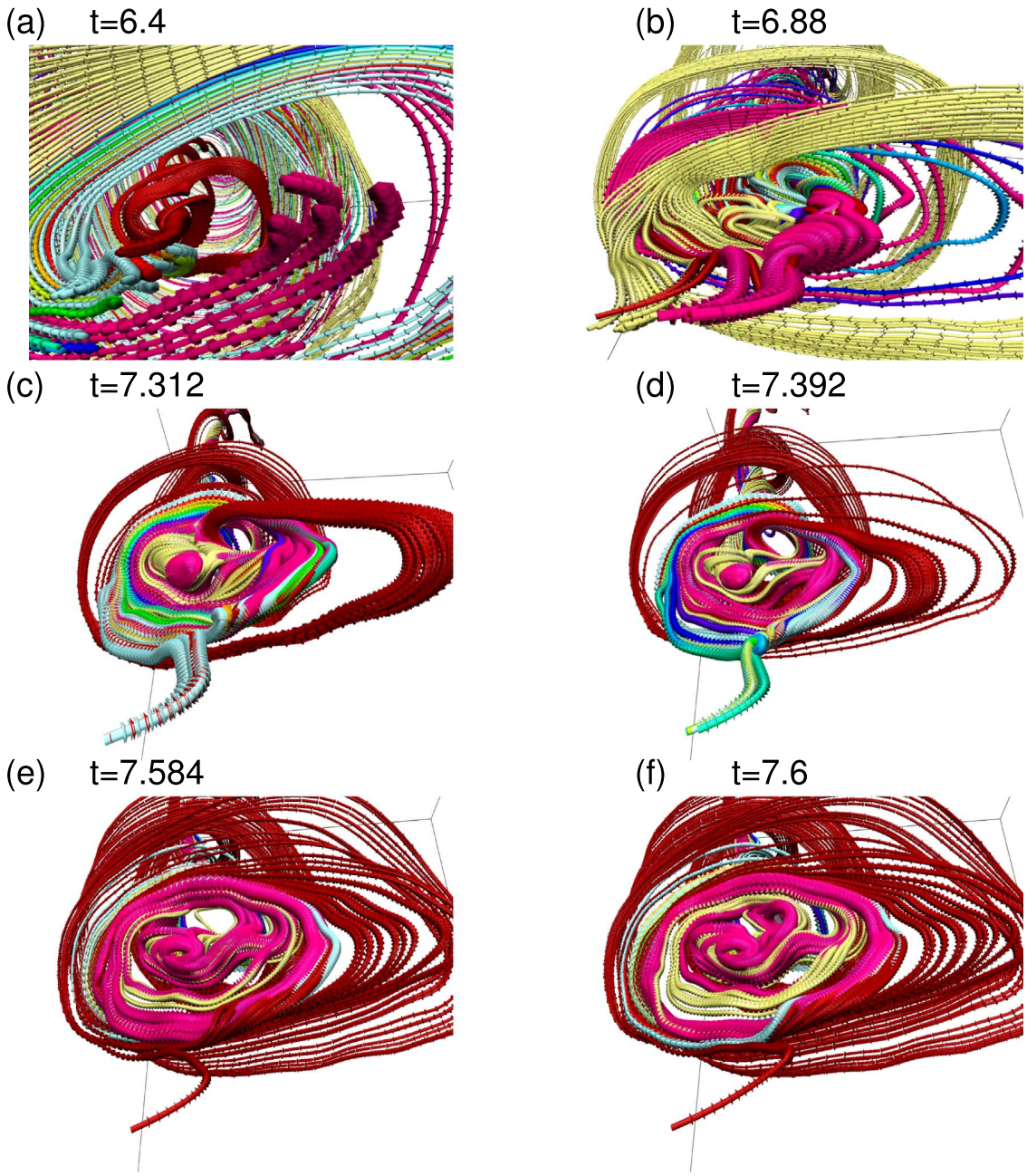

Figure 11. Sequence of MFL evolution under the Hall forcing ($\delta_i/L = 0.04$ case), zoomed to reveal intricate magnetic topologies generated by the MRs. Formation of a number eight like magnetic structures (panels (a) to (f))—the magnetic islands—can be seen clearly. Importantly, such intricate topologies are absent in the MFR evolution without the Hall forcing. (An animation of the evolution from $t = 7.312$ onward is available.)

(An animation of this figure is available.)

overall, agree with the existing scenarios of Hall-reconnection based on physical arguments and other recent simulations including those on the GEM challenge. An important finding is the formation of complex 3D magnetic structures, which cannot be apprehended from 2D models or calculations although their projections agree with the latter. Alongside, we have numerically explored the Whistler mode propagation vis-à-vis its analytical model and found the two to be matching reasonably well.

We have further carried out simulations where the EULAG-MHD is used to simulate the onset and dynamics of an MFR initiating from a sheared magnetic arcade. Such computations are relevant in understanding the solar eruptions. Simulations conducted with and without the Hall term are compared once more. Once again a reasonable maintenance of symmetry is observed in the standard MHD simulation, whereas a clear symmetry-breaking—leading to generation of 3D magnetic structures—appears to be a signature of the Hall effect. In HMHD the MFR evolves through a series of complex geometries while rotating along its axis. When viewed favorably, it appears to contain structures reminiscent of the number eight, which is the result of internal reconnection within MFR. Notably, the magnetic and kinetic energies, in the presence and absence of the Hall forcing, behave almost

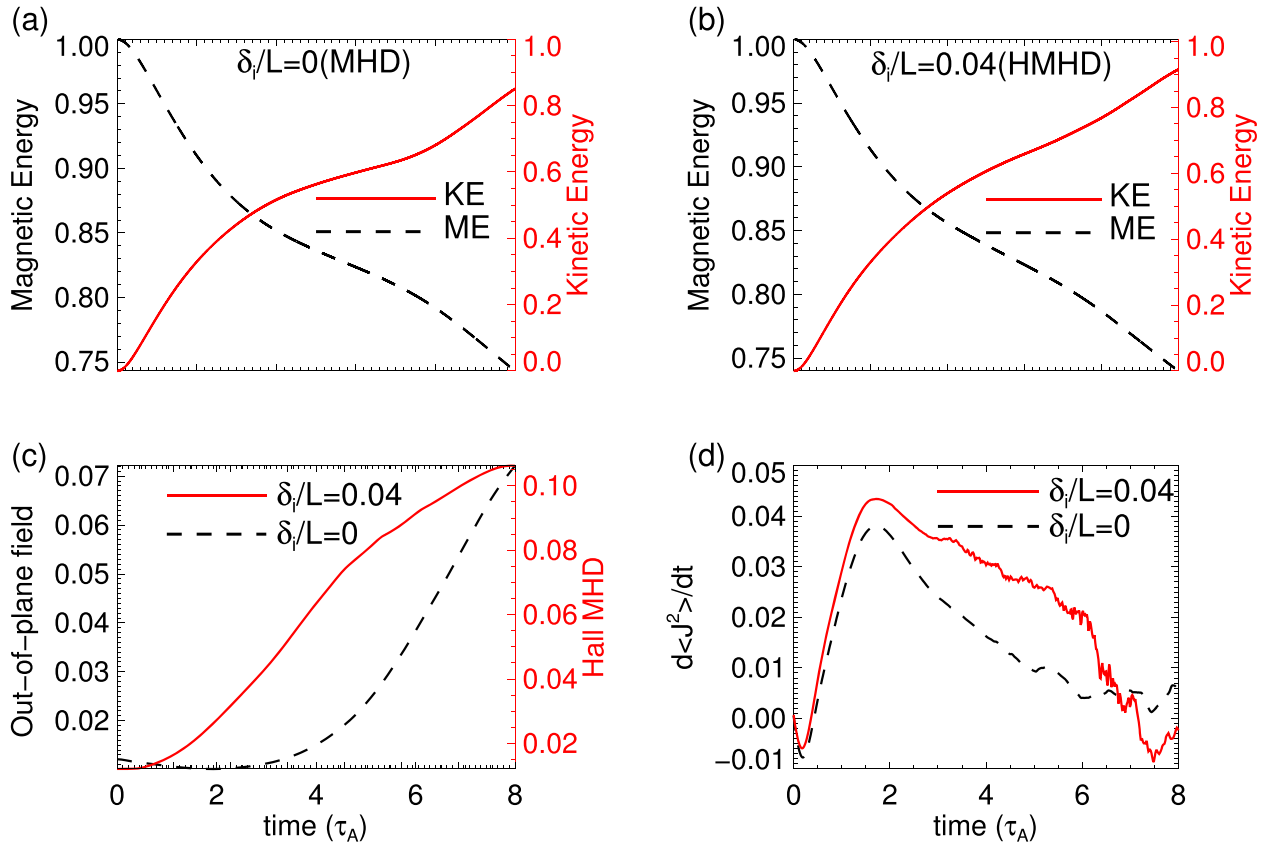

Figure 12. Panels (a) and (b) show the evolution of normalized (with the initial total energy) grid-averaged magnetic energy (black dashed curve) and kinetic energy (red solid curve) for $\delta_i/L = 0$ (MHD) and $\delta_i/L = 0.04$ (HMHD), respectively. Panel (c) shows the evolution of grid-averaged out-of-plane magnetic field for $\delta_i/L = 0$ (MHD) with the black dashed curve and for $\delta_i/L = 0.04$ (HMHD) with the red solid curve, respectively. Also in Panels (a) to (c), the scales for the solid and the dashed curves are spaced at right and left respectively. Panel (d) represents the grid-averaged rate of change of total current density for $\delta_i/L = 0$ (black dashed curve) and $\delta_i/L = 0.04$ (red solid curve) respectively. Important are the generation of the out-of-plane magnetic field along with small but abrupt changes in time derivative of the total volume current density in HMHD simulation.

identically—consistent with the theoretical understanding that the Hall term does not directly change the magnetic energy. Moreover, we have performed and analyzed the simulations with half the resolution and found their results to be similar to the reference results. The same process of the primary MFR formation and its further breakage through multiple internal magnetic reconnections does confirm the independency of the results on the grid resolution.

Overall, the extended EULAG-MHD is giving results in accordance with the theoretical expectations and other contemporary simulations. The Hall simulation documenting activation of an MFR from initial sheared arcade field lines is of particular importance and is a new entry to the ongoing research. It shows that Hall magnetohydrodynamics can account for a richer complexity during evolution of the rope by breaking any preexisting 2D symmetry, thus opening another degree of freedom for the MFL evolution. The resulting local breakage of the rope is intriguing by itself and calls for further research.

The authors thank the anonymous referee for providing insightful comments and suggestions that increased the scientific content and readability of the paper. The simulations are performed using the 100TF cluster Vikram-100 at Physical Research Laboratory, India. We wish to acknowledge the visualization software VAPOR (www.vapor.ucar.edu), for generating relevant graphics. NCAR is sponsored by the National Science Foundation.

ORCID iDs

K. Bora https://orcid.org/0000-0002-3402-273X
R. Bhattacharyya https://orcid.org/0000-0003-4522-5070
P. K. Smolarkiewicz https://orcid.org/0000-0001-7077-3285

References

Alfvén, H. 1942, Natur, 150, 405
Aschwanden, M. J. 2005, Physics of the Solar Corona. An Introduction with Problems and Solutions (2nd ed.; Chichester: Praxis)
Bhattacharjee, A. 2004, ARA&A, 42, 365
Bhattacharyya, R., Low, B. C., & Smolarkiewicz, P. K. 2010, PhPl, 17, 112901
Birn, J., Drake, J. F., Shay, M. A., et al. 2001, JGR, 106, 3715
Charbonneau, P., & Smolarkiewicz, P. K. 2013, Sci, 340, 42
Chen, P. F. 2011, LRSP, 8, 1
Choudhuri, A. R. 1998, The Physics of Fluids and Plasmas: An Introduction for Astrophysicists (New York: Cambridge Univ. Press)
Freidberg, J. P. 1982, RvMP, 54, 801
Grinstein, F., Margolin, L., & Rider, W. 2007, Implicit Large Eddy Simulation: Computing Turbulent Fluid Dynamics (Cambridge: Cambridge Univ. Press),
Huba, J. D. 2003, in Hall Magnetohydrodynamics—A Tutorial, ed. J. Büchner, M. Scholer, & C. T. Dum (Berlin: Springer), 166
Huba, J. D., & Rudakov, L. I. 2002, PhPl, 9, 4435

Kumar, D., & Bhattacharyya, R. 2011, PhPl, 18, 084506
Kumar, S., Bhattacharyya, R., Dasgupta, B., & Janaki, M. S. 2017, PhPl, 24, 082902
Kumar, S., Bhattacharyya, R., Joshi, B., & Smolarkiewicz, P. K. 2016, ApJ, 830, 80
Kumar, S., Bhattacharyya, R., & Smolarkiewicz, P. K. 2015, PhPl, 22, 082903
Ma, Z. W., & Bhattacharjee, A. 2001, JGR, 106, 3773
Mozer, F. S., Bale, S. D., & Phan, T. D. 2002, PhRvL, 89, 015002
Nayak, S. S., Bhattacharyya, R., Prasad, A., et al. 2019, ApJ, 875, 10
Nayak, S. S., Bhattacharyya, R., Smolarkiewicz, P. K., Kumar, S., & Prasad, A. 2020, ApJ, 892, 44
Pant, V., Datta, A., Banerjee, D., Chandrashekhar, K., & Ray, S. 2018, ApJ, 860, 80
Parker, E. N. 1994, Spontaneous Current Sheets in Magnetic Fields: With Applications to Stellar X-rays, Vol. 1 (New York: Oxford Univ. Press)
Prasad, A., Bhattacharyya, R., Hu, Q., Kumar, S., & Nayak, S. S. 2018, ApJ, 860, 96
Prasad, A., Bhattacharyya, R., & Kumar, S. 2017, ApJ, 840, 37
Priest, E. 2014, Magnetohydrodynamics of the Sun (Cambridge: Cambridge Univ. Press)
Priest, E., & Forbes, T. 2000, Magnetic Reconnection (New York: Cambridge Univ. Press)
Prusa, J., Smolarkiewicz, P., & Wyszogrodzki, A. 2008, CF, 37, 1193
Shi, C., Tenerani, A., Velli, M., & Lu, S. 2019, ApJ, 883, 172
Shibata, K., & Tanuma, S. 2001, EP&S, 53, 473
Smolarkiewicz, P. K. 2006, IJNMF, 50, 1123
Smolarkiewicz, P. K., & Charbonneau, P. 2013, JCoPh, 236, 608
Sonnerup, B. U. Ö. 1979, Magnetic Field Reconnection, Vol. 3 (Amsterdam: North-Holland), 45
Westerberg, L. G., & Åkerstedt, H. O. 2007, PhPl, 14, 102905

The Astrophysical Journal, 925:197 (19pp), 2022 February 1 https://doi.org/10.3847/1538-4357/ac3bce

Comparison of the Hall Magnetohydrodynamics and Magnetohydrodynamics Evolution of a Flaring Solar Active Region

K. Bora[1,2], R. Bhattacharyya[1], Avijeet Prasad[3,4,5], Bhuwan Joshi[1], and Qiang Hu[3,6]
[1] Udaipur Solar Observatory, Physical Research Laboratory, Dewali, Bari Road, Udaipur 313001, India
[2] Discipline of Physics, Indian Institute of Technology, Gandhinagar 382355, India
[3] Center for Space Plasma & Aeronomic Research, The University of Alabama in Huntsville, Huntsville, AL 35899, USA
[4] Institute of Theoretical Astrophysics, University of Oslo, Postboks 1029, Blindern NO-0315 Oslo, Norway
[5] Rosseland Centre for Solar Physics, University of Oslo, Postboks 1029, Blindern NO-0315, Oslo, Norway
[6] Department of Space Science, The University of Alabama in Huntsville, Huntsville, AL 35899, USA
Received 2021 September 13; revised 2021 November 13; accepted 2021 November 20; published 2022 February 4

Abstract

This work analyzes the Hall magnetohydrodynamics (HMHD) and magnetohydrodynamics (MHD) numerical simulations of a flaring solar active region as a test bed while idealizing the coronal Alfvén speed to be less by two orders of magnitude. HMHD supports faster magnetic reconnection and shows richer complexity in magnetic field line evolution compared to the MHD. The magnetic reconnections triggering the flare are explored by numerical simulations augmented with relevant multiwavelength observations. The initial coronal magnetic field is constructed by non-force-free extrapolation of photospheric vector magnetic field. Magnetic structure involved in the flare is identified to be a flux rope, with its overlying magnetic field lines constituting the quasi-separatrix layers (QSLs) along with a three-dimensional null point and a null line. Compared to the MHD simulation, the HMHD simulation shows a higher and faster ascent of the rope together with the overlying field lines, which further reconnect at the QSL located higher up in the corona. The footpoints of the field lines match better with the observations for the HMHD case, with the central part of the flare ribbon located at the chromosphere. Additionally, field lines are found to rotate in a circular pattern in the HMHD, whereas no such rotation is seen in the MHD results. Interestingly, plasma is also observed to be rotating in a cospatial chromospheric region, which makes the HMHD simulation more credible. Based on the aforementioned agreements, HMHD simulation is found to agree better with observations and thus opens up a novel avenue to explore.

Unified Astronomy Thesaurus concepts: Solar magnetic reconnection (1504); Magnetohydrodynamical simulations (1966)

Supporting material: animations

1. Introduction

The astrophysical plasmas characterized by high Lundquist number $S \equiv Lv_A/\eta$ ($L \equiv$ length scale of the magnetic field $\boldsymbol{B}$ variability, $v_A \equiv$ Alfvén speed, and $\eta \equiv$ magnetic diffusivity) satisfy Alfvén's flux-freezing theorem in the presence of laminar plasma flow, ensuring that magnetic field lines are tied to fluid parcels (Alfvén 1942). The scenario is different in a turbulent magnetofluid; see Lazarian & Vishniac (1999, 2000) and Eyink & Aluie (2006) for details. An inherent large L implies large S and ensures flux freezing in the astrophysical plasmas. Particularly, the solar corona with global $L \approx 100$ Mm, $v_A \approx 10^6$ ms^{-1}, $B \approx 10$ G, and $\eta \approx 1$ m^2 s^{-1} (calculated using Spitzer resistivity) has $S \approx 10^{14}$ (Aschwanden 2005). However, the coronal plasma also exhibits diffusive behavior in the form of solar transients—such as solar flares, coronal mass ejections, and jets. All of these are manifestations of magnetic reconnections that in turn lead to dissipation of magnetic energy into heat and kinetic energy of plasma flow, accompanied by a rearrangement of magnetic field lines (Choudhuri 1998). The magnetic reconnections being dissipative processes, their onset is due to the generation of small scales as a consequence of large-scale dynamics, ultimately increasing the magnetic field gradient and thereby resulting in intermittently diffusive plasma. The small scales may naturally occur as current sheets (CSs; Parker 1994), magnetic nulls (Parnell et al. 1996; Nayak et al. 2020), and quasi-separatrix layers (QSLs; Démoulin 2006; Prasad et al. 2020), or can develop spontaneously during the evolution of the magnetofluid. Such spontaneous developments (owing to discontinuities in the magnetic field) are expected from Parker's magnetostatic theorem (Parker 1994) and have also been established numerically by magnetohydrodynamics (MHD) simulations (Kumar & Bhattacharyya 2011; Kumar et al. 2015, 2016, 2017, 2021; Prasad et al. 2017, 2018; Nayak et al. 2019, 2020). Identification of the small (viz., the dissipation) scale depends on the specific physical system under consideration. For example, the length scale at which the reconnection occurs is found to be $L_\eta \equiv \sqrt{\tau_d \eta} \approx 32$ m, based on $\eta \approx 1$ m^2 s^{-1} and the magnetic diffusion timescale τ_d approximated by the impulsive rise time of hard X-ray flux $\approx 10^3$ s (Priest & Forbes 2000) during a flare. Consequently, the estimated ion inertial length scale $\delta_i \approx 2.25$ m in the solar corona (Priest & Forbes 2000) suggests that the order of the dissipation term, $1/S \approx 10^{-5}$ (approximated with L_η), is smaller than the order of the Hall term, $\delta_i/L_\eta \approx 10^{-2}$, in the standard dimensionless induction equation (Westerberg & Åkerstedt 2007; Bora et al. 2021)

$$\frac{\partial \boldsymbol{B}}{\partial t} = \nabla \times (\boldsymbol{v} \times \boldsymbol{B}) - \frac{1}{S}\nabla \times \boldsymbol{J} - \frac{\delta_i}{L_\eta}\nabla \times (\boldsymbol{J} \times \boldsymbol{B}), \quad (1)$$

where $\boldsymbol{J}(=\nabla\times\boldsymbol{B})$ and $\boldsymbol{v}$ are the volume current density and the plasma flow velocity, respectively. This difference in the order of magnitude irrefutably indicates the importance of the Hall term in the diffusive limit (Birn et al. 2001; Bhattacharjee 2004) of the solar coronal plasma, which further signifies that the Hall magnetohydrodynamics (HMHD) can play a crucial role for coronal transients, as the magnetic reconnections are their underlying mechanism. Importantly, the aforesaid activation of the Hall term only in the diffusive limit is crucial in setting up an HMHD-based numerical simulation, invoked later in the paper.

Important insight into magnetic reconnection can be gained by casting Equation (1) in the absence of dissipation as

$$\frac{\partial \boldsymbol{B}}{\partial t}=\nabla\times(\boldsymbol{w}\times\boldsymbol{B}), \tag{2}$$

following Hornig & Schindler (1996). The velocity $\boldsymbol{w}=\boldsymbol{v}-\delta_i/L_\eta\boldsymbol{J}$, which is also the electron fluid velocity, conserves magnetic flux (Schindler et al. 1988) and topology (Hornig & Schindler 1996) since field lines are tied to it. Consequently, field lines slip out from the fluid parcels advecting with velocity $\boldsymbol{v}$ to which the lines are frozen in ideal MHD. Importantly, the resulting breakdown of the flux freezing is localized to the region where current density is large and the Hall term is effective. Because of the slippage, two fluid parcels do not remain connected with the same field lines over time—a change in field line connectivity. Quoting Schindler et al. (1988), such localized breakdown of flux freezing, along with the resulting change in connectivity, can be considered as the basis of reconnection (Axford 1984). Additional slippage of field lines occurs in the presence of the dissipation term, but with a change in magnetic topology. The present paper extensively relies on this interpretation of reconnection as the slippage of magnetic field lines and the resulting change in magnetic connectivity.

The importance of HMHD is by no means limited to coronal transients. For example, HMHD is important in Earth's magnetosphere, particularly at the magnetopause and the magnetotail, where CSs are present (Mozer et al. 2002). Generally, the HMHD is expected to support faster magnetic reconnections, yet without directly affecting the dissipation rate of magnetic energy and helicity by the Hall term in the induction equation (Priest & Forbes 2000; Shi et al. 2019). The faster reconnection may be associated with a more effective slippage of field lines in HMHD compared to the resistive MHD, compatible with the arguments presented earlier. Nevertheless, these unique properties of the HMHD are expected to bring subtle changes in the dynamical evolution of plasma, particularly in the small scales dominated by magnetic reconnections, presumably bringing a change in the large scales as a consequence. Such subtle changes were found in the recent HMHD simulation (Bora et al. 2021), performed by extending the computational model EULAG-MHD (Smolarkiewicz & Charbonneau 2013) to include the Hall effects. Notably, the faster reconnection compared to MHD led to a breakage of a magnetic flux rope, generated from analytically constructed initial bipolar magnetic field lines (Kumar et al. 2016). In turn, the flux-rope breakage resulted in the generation of magnetic islands as theorized by Shibata & Tanuma (2001). Clearly, it is compelling to study the HMHD evolution in a more realistic scenario with the initial magnetic field obtained from a solar magnetogram. To attain such an objective, we select the recently reported active region (AR) NOAA AR 12734 by Joshi et al. (2021) that produced a C1.3 class flare.

In the absence of reliable direct measurement of the coronal magnetic field, several extrapolation models such as nonlinear force-free field (NLFFF) (Wiegelmann 2008; Wiegelmann & Sakurai 2012) and non-force-free field (non-FFF) (Hu & Dasgupta 2008; Hu et al. 2010) have been developed to construct the coronal magnetic field using photospheric magnetograms. The standard is the NLFFF, and the recent data-based MHD simulations initialized with it have been reasonably successful in simulating the dynamics of various coronal transients (Jiang et al. 2013; Amari et al. 2014; Inoue et al. 2014; Savcheva et al. 2016). However, the NLFFF extrapolations require that we treat the photosphere as force-free, while it is actually not so (Gary 2001). Hence, a "preprocessing technique" is usually employed to minimize the Lorentz force on the photosphere in order to provide a boundary condition suitable for NLFFF extrapolations (Wiegelmann et al. 2006; Jiang & Feng 2014) and thereby compromising the reality. Recently, the non-FFF model, based on the principle of minimum energy dissipation rate (Bhattacharyya & Janaki 2004; Bhattacharyya et al. 2007), has emerged as a plausible alternative to the force-free models (Hu & Dasgupta 2008; Hu et al. 2008, 2010). In the non-FFF model, the magnetic field $\boldsymbol{B}$ satisfies the double-curl Beltrami equation (Mahajan & Yoshida 1998), and the corresponding Lorentz force on the photosphere is nonzero, while it decreases to small values at the coronal heights (Prasad et al. 2018, 2020; Nayak et al. 2019)—concurring with the observations. In this paper, we use non-FFF extrapolation (Hu et al. 2010) to obtain the magnetic field in the corona using the photospheric vector magnetogram obtained from the Helioseismic Magnetic Imager (HMI; Schou et al. 2012) on board the Solar Dynamics Observatory (SDO; Pesnell et al. 2012).

The paper is organized as follows. Section 2 describes the flaring event in NOAA AR 12734, Section 3 presents the magnetic field line morphology of NOAA AR 12734, along with the preferable sites for magnetic reconnections such as QSLs, 3D null point, and null line found from the non-FFF extrapolation. Section 4 focuses on the numerical model, numerical setup, and evolution of magnetic field lines obtained from the extrapolation, along with their realizations in observations. Section 5 highlights the key findings.

2. Salient Features of the C1.3 Class Flare in NOAA AR 12734

NOAA AR 12734 produced an extended C1.3 class flare on 2019 March 8 (Joshi et al. 2021). The impulsive phase of the flare started at 03:07 UT as reported in Figure 3 of Joshi et al. (2021), which shows the X-ray flux in 1–8 Å and 0.5–4 Å detected by the Geostationary Operational Environmental Satellite (GOES; Garcia 1994). The flux evinces two subsequent peaks after the onset of the flare, one around 03:19 UT and another roughly around 03:38 UT. Joshi et al. (2021) suggested that the eruptive event takes place in a coronal sigmoid with two distinct stages of energy release. Additional observations using the multiwavelength channels of the Atmospheric Imaging Assembly (AIA; Lemen et al. 2012) on board SDO are listed below to highlight important features pertaining to simulations reported in this paper. Figure 1

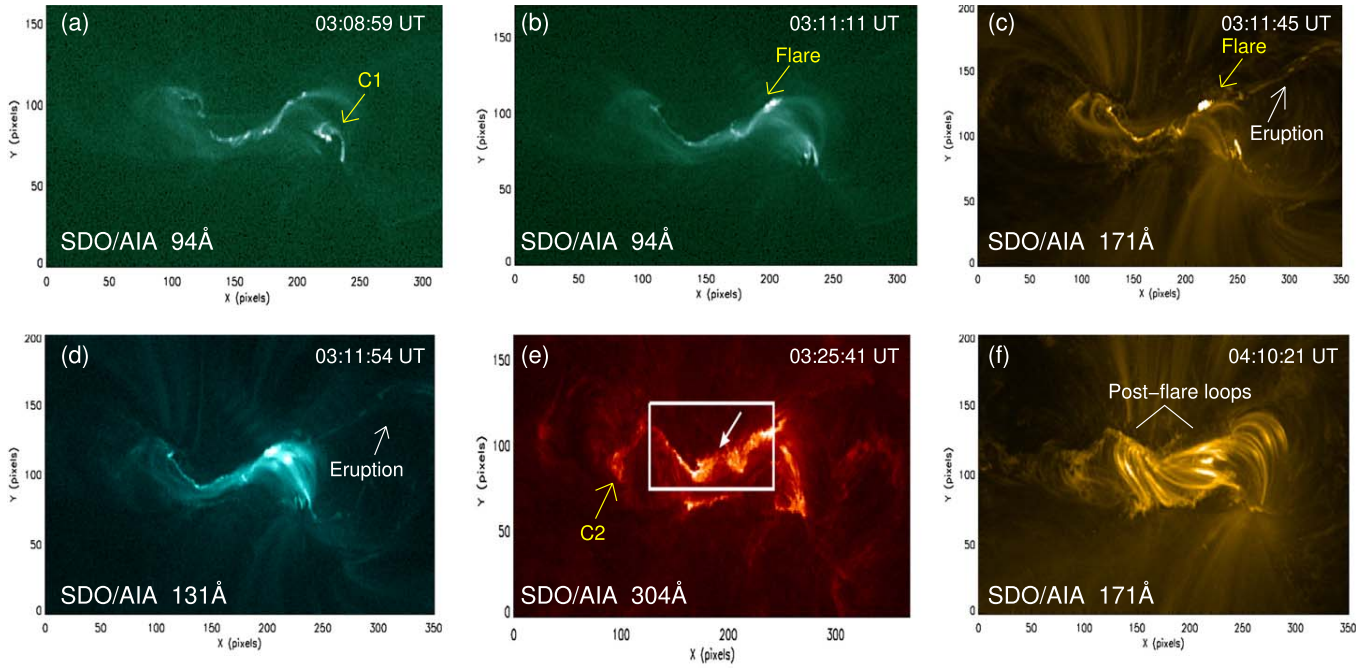

Figure 1. Panels (a)–(f) are SDO/AIA images showing the multiwavelength observations of the flaring NOAA AR 12734. Panel (a) shows the quasi-circular brightening at the western part of the AR prior to the flare (marked by C1). Panels (b)–(d) show the initiation of the flare followed by eruption (indicated by the yellow arrow). Panel (e) shows the circular structure after eruption at the eastern part of the AR (marked by C2) and the W-shaped flare ribbon (enclosed by the white box). Panel (f) shows the post-flare loops.

illustrates a spatio-temporal observational overview of the event. Panel (a) shows the remote semicircular brightening (C1) prior to the impulsive phase of the flare (indicated by the yellow arrow). Panels (b)–(d) indicate the flare by the yellow arrow and the eruption by the white arrow in the 94 Å, 171 Å, and 131 Å channels, respectively. Notably, the W-shaped brightening appears in panels (b)–(d), along with the flare in different wavelength channels of SDO/AIA. Panel (e) shows the circular structure of the chromospheric material (C2) during the impulsive phase of the flare. It also highlights the developed W-shaped flare ribbon (enclosed by the white box), which has a tip at the center (marked by the white arrow). Panel (f) depicts the post-flare loops in the 171 Å channel, indicating the post-flare magnetic field line connectivity between various negative and positive polarities on the photosphere.

3. Non-FFF Extrapolation of NOAA AR 12734

As stated up front, the non-FFF extrapolation technique proposed by Hu & Dasgupta (2008) and based on the minimum dissipation rate theory (Bhattacharyya & Janaki 2004; Bhattacharyya et al. 2007) is used to obtain the coronal magnetic field for NOAA AR 12734. The extrapolation essentially solves the equation

$$\nabla \times \nabla \times \nabla \times \boldsymbol{B} + a_1 \nabla \times \nabla \times \boldsymbol{B} + b_1 \nabla \times \boldsymbol{B} = 0, \quad (3)$$

where parameters a_1 and b_1 are constants. Following Hu et al. (2010), the field is constructed as

$$\boldsymbol{B} = \sum_{i=1,2,3} \boldsymbol{B}_i, \quad \nabla \times \boldsymbol{B}_i = \alpha_i \boldsymbol{B}_i, \quad (4)$$

where α_i is constant for a given $\boldsymbol{B}_i$. The subfields $\boldsymbol{B}_1$ and $\boldsymbol{B}_3$ are linear force-free, having $\alpha_1 \neq \alpha_3$, whereas $\boldsymbol{B}_2$ is a potential field with $\alpha_2 = 0$. An optimal pair of $\alpha = \{\alpha_1, \alpha_3\}$ is iteratively found by minimizing the average deviation between the observed transverse field ($\boldsymbol{B}_t$) and the computed ($\boldsymbol{b}_t$) transverse field, quantified by

$$E_n = \left(\sum_{i=1}^{M} |\boldsymbol{B}_{t,i} - \boldsymbol{b}_{t,i}| \times |\boldsymbol{B}_{t,i}| \right) \Big/ \left(\sum_{i=1}^{M} |\boldsymbol{B}_{t,i}|^2 \right), \quad (5)$$

on the photosphere. Here $M = N^2$ represents the total number of grid points on the transverse plane. The grid points are weighted with respect to the strength of the observed transverse field to minimize the contribution from weaker fields, see Hu & Dasgupta (2008) and Hu et al. (2010) for further details.

Since Equation (3) involves the evaluation of the second-order derivative, $(\nabla \times \nabla \times \boldsymbol{B})_z = -(\nabla^2 \boldsymbol{B})_z$ at $z = 0$, evaluation of $\boldsymbol{B}$ requires magnetograms at two different values of z. In order to work with the generally available single-layer vector magnetograms, an algorithm was introduced by Hu et al. (2010) that involves additional iterations to successively fine-tune the potential subfield $\boldsymbol{B}_2$. The system is reduced to second order by taking initial guess $\boldsymbol{B}_2 = 0$, which makes it easier to determine the boundary condition for $\boldsymbol{B}_1$ and $\boldsymbol{B}_3$. If the calculated value of E_n turns out to be unsatisfactory—i.e., overly large—then a potential field corrector to $\boldsymbol{B}_2$ is calculated from the difference in the observed and computed transverse fields and subsequently summed with the previous $\boldsymbol{B}_2$ to further reduce E_n. Notably, recent simulations initiated with the non-FFF model have successfully explained the circular ribbon flares in NOAA AR 12192 (Prasad et al. 2018) and NOAA AR 11283 (Prasad et al. 2020), as well as a blowout jet in NOAA AR 12615 (Nayak et al. 2019), thus validating the non-FFF model's credibility.

The vector magnetogram is selected for 2019 March 8, at 03:00 UT (≈7 minutes prior to the start of flare). The original

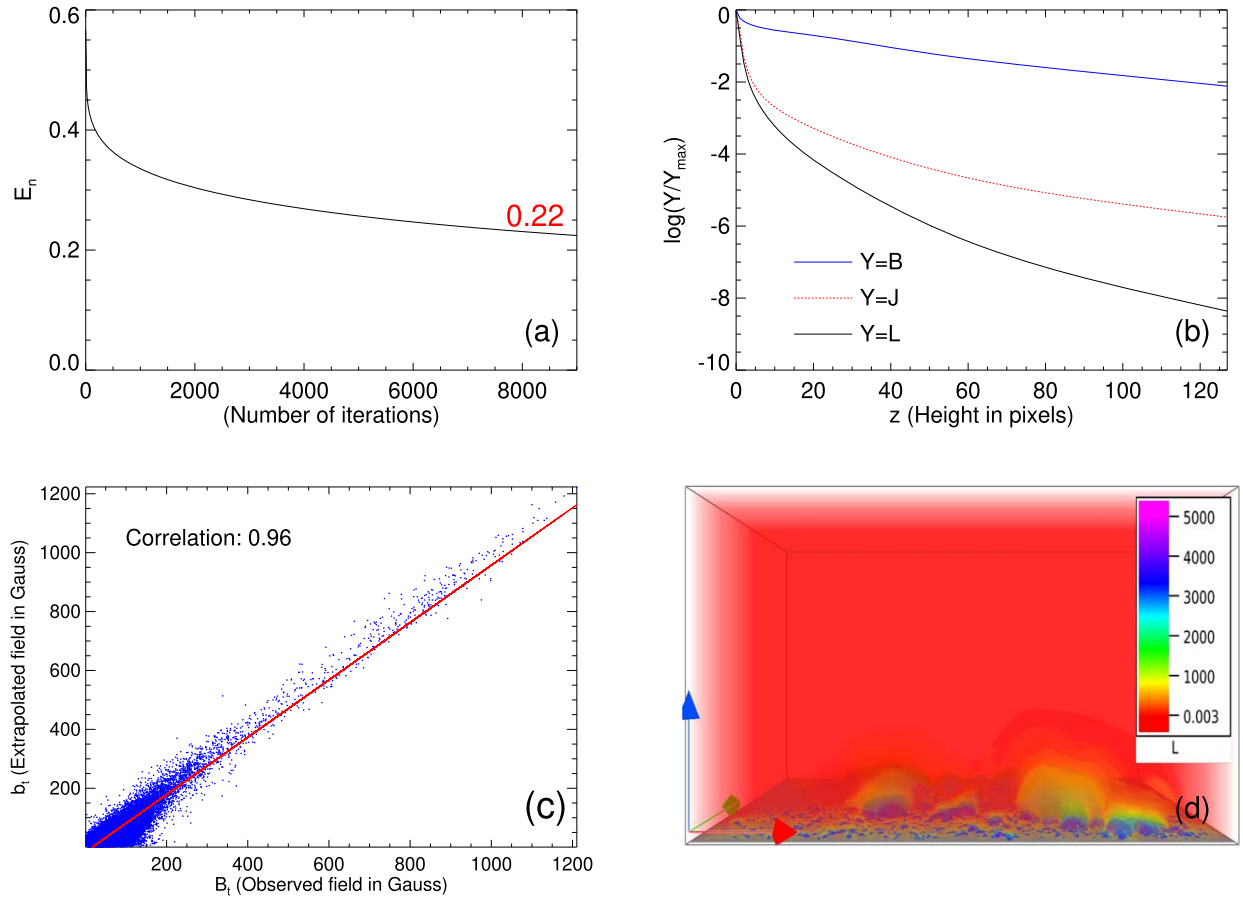

Figure 2. Panel (a) shows the variation of the deviation E_n with number of iterations in the non-FFF extrapolation. Panel (b) shows the logarithmic variation of horizontally averaged magnetic field ($Y = B$), the current density ($Y = J$), and the Lorentz force ($Y = L$) with height z in pixels. All the quantities plotted in panel (b) are normalized with their respective maximum values. Panel (c) shows the scatter plot of the correlation between the observed and extrapolated magnetic field. The red line is the expected profile for perfect correlation. Distribution of the magnitude of the Lorentz force for initial extrapolated field is shown in panel (d) using direct volume rendering. The distribution clearly shows that the Lorentz force is maximum at the bottom boundary and decreasing with the height in computational volume. The red, green, and blue arrows in the lower left corner represent x-, y-, and z-directions, respectively, here and hereafter. The color bars on the right side of the panel represent the magnitude of the strength of Lorentz force.

magnetogram cut out of dimensions 342×195 pixels with pixel resolution $0\farcs5$ pixel^{-1} having an extent of $124\,\mathrm{Mm} \times 71\,\mathrm{Mm}$[7] from the "hmi.sharp_cea_720s" series is considered, which ensures an approximate magnetic flux balance at the bottom boundary. To optimize the computational cost with the available resources, the original field is rescaled and non-FFF-extrapolated over a volume of $256 \times 128 \times 128$ pixels while keeping the physical extent the same and preserving all magnetic structures throughout the region. The reduction, in effect, changes the conversion factor of 1 pixel to $\approx$0.484 Mm along x and $\approx$0.554 Mm along the y- and z-directions of the employed Cartesian coordinate system.

Panel (a) of Figure 2 shows E_n in the transverse field, defined in Equation (5), as a function of the number of iterations. It shows that E_n tends to saturate at the value of $\approx$0.22. Panel (b) of Figure 2 shows the logarithmic decay of the normalized horizontally averaged magnetic field, current density, and Lorentz force with height. It is clear that the Lorentz force is appreciable on the photosphere but decays off rapidly with height, agreeing with the general perception that the corona is force-free while the photosphere is not (Liu et al. 2020; Sarp Yalim et al. 2020). Panel (c) shows that the Pearson-r correlation between the extrapolated and observed transverse fields is $\approx$0.96, implying strong correlation. The direct volume rendering of the Lorentz force in panel (d) also reveals a sharp decay of the Lorentz force with height, expanding on the result of panel (b).

To facilitate description, Figure 3(a) shows the SDO/AIA 304 Å image at 03:25 UT, where the flare ribbon brightening has been divided into four segments marked as B1–B4. Figure 3(b) shows the initial global magnetic field line morphology of NOAA AR 12734, partitioned into four regions R1–R4, corresponding to the flare ribbon brightening segments B1–B4. The bottom boundary of panel (b) is composed of B_z maps in gray scale, where the lighter shade indicates positive-polarity regions and the darker shade marks negative-polarity regions. The magnetic field line topologies and structures belonging to a specific region and contributing to the flare are documented below.

Region R1: The top-down view of the global magnetic field line morphology is shown in panel (a) of Figure 4. To help locate QSLs, the bottom boundary is overlaid with the $\log Q$ map of the squashing factor Q (Liu et al. 2016) in all panels of the figure. Distribution of high Q values along with B_z on the bottom boundary helps in identifying differently connected

[7] At a distance of 1 au, an angular diameter of $1''$ represents 0.725 Mm on the Sun.

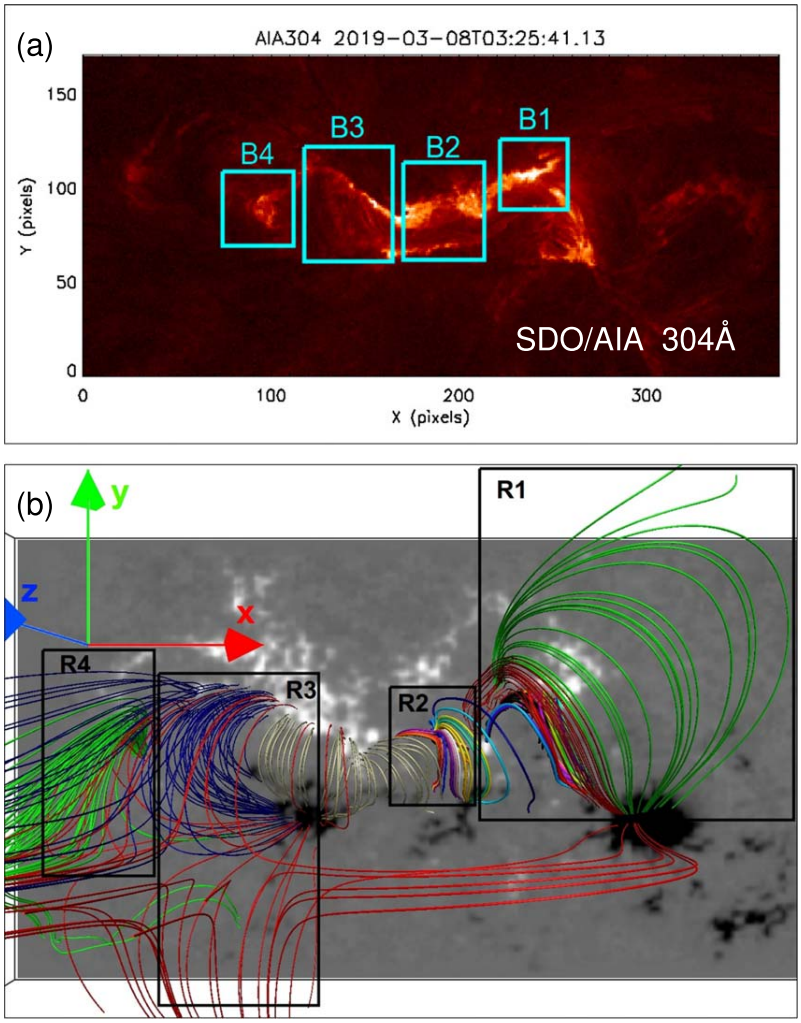

Figure 3. Panel (a) shows the SDO/AIA 304 Å image, where the flare ribbon brightening has been divided into four parts B1, B2, B3, and B4 (enclosed by boxes). Panel (b) shows an overall extrapolated magnetic field lines morphology of NOAA AR 12734 with the B_z-component of the magnetogram at the bottom boundary. Footpoints of the magnetic structures contained in regions R1, R2, R3, and R4 correspond to brightening B1, B2, B3, and B4, respectively.

regions. The region with a large Q is prone to the onset of slipping magnetic reconnections (Démoulin 2006). Footpoints of magnetic field lines constituting QSL1 and QSL2 trace along the high Q values near the bottom boundary. QSL1, involving the magnetic field lines in Set I (green) and Set II (maroon), is shown in panel (b). Particularly, Set I (green) extends higher in the corona, forming the largest loops in R1. Panel (c) illustrates a closer view of QSL2 (multicolored) and the flux rope (black) beneath, situated between the positive and negative polarities P1, P2, and N1, respectively. In panel (d), the flux rope (constituted by the twisted black magnetic field lines) is depicted using the side view. The twist value T_w (Liu et al. 2016) in the three vertical planes along the cross section of the flux rope is also overlaid. Notably, the twist value is 2 at the center of the rope and decreases outward (see vertical plane in the middle of the flux rope in panel (d)).

Region R2: Figure 5(a) shows the side view of a 3D null-point geometry of magnetic field lines and the bottom boundary B_z overlaid with log Q ranging between 5 and 10. Panel (b) depicts an enlarged view of the 3D null location, marked black. The height of the null is found to be $\approx$3 Mm from the photosphere. The null is detected using the bespoke procedure (Kumar & Bhattacharyya 2011; Nayak et al. 2020) that approximates the Dirac delta on the grid as

$$n(B_i) = \exp\left[-\sum_{i=x,y,z}(B_i - B_o)^2/d_o^2\right], \quad (6)$$

where small constants B_o and d_o correspond to the isovalue of B_i and the Gaussian spread. The function $n(B_i)$ takes significant values only if $B_i \approx 0\ \forall i$, whereupon a 3D null is the point where the three isosurfaces having isovalues $B_i = B_o$ intersect.

Region R3: The side view of the magnetic field line morphology in region R3 is shown in Figure 5(c), where the yellow surface corresponds to $n = 0.9$. Panel (d) highlights a "fish-bone-like" structure, similar to the schematic in Figure 5 of Wang et al. (2014). To show that in the limiting case $n = 0.9$ reduced to a null line, we plot corresponding contours in the range $0.6 \leqslant n \leqslant 0.9$ on three preselected planes highlighted in panel (e). The size reduction of the contours with increasing n indicates the surface converging to a line. Such null lines are also conceptualized as favorable reconnection sites (Wang et al. 2014).

Region 4: Figure 5(f) shows magnetic field lines relevant to plasma rotation in B4. Notably, the null line from R3 intrudes

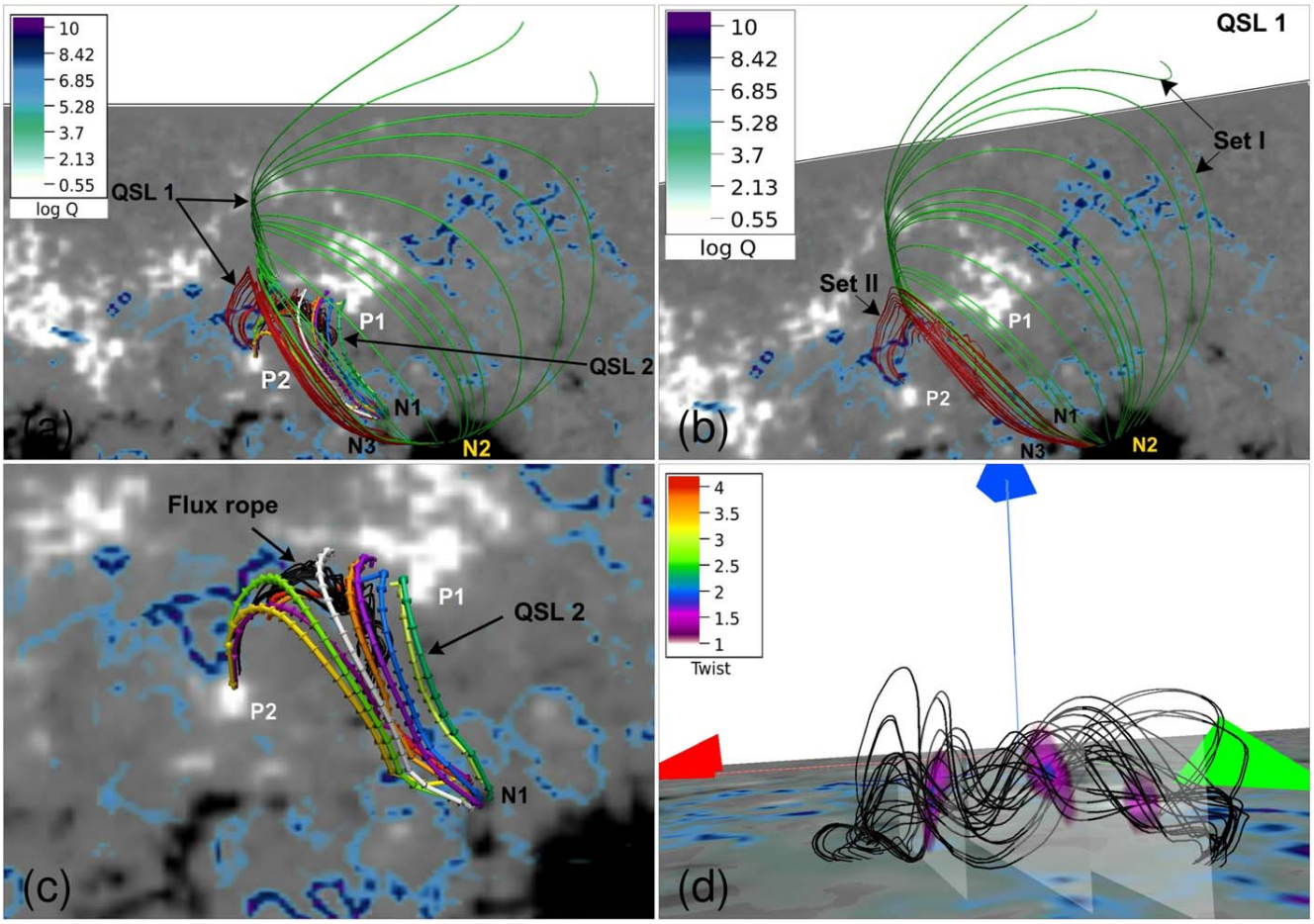

Figure 4. Panel (a) shows magnetic field line morphology of region R1 between positive and negative polarities P1, P2, N1, N2, and N3, respectively. Panel (b) highlights the structure of QSL1 composed of magnetic field lines in Set I (green) and Set II (maroon). Panel (c) shows the zoomed-in top view of the flux-rope structure (black) and an overlying QSL2 (multicolor arrowed magnetic field lines), between the positive and negative polarities P1, P2, and N1, respectively. Panel (d) shows the side view of the flux rope, where three vertical planes along the cross section of the flux rope show the twist value T_w at different locations along the flux rope. In all the panels the log Q between 5 and 10 is overlaid on the B_z-component of the magnetogram at the bottom boundary.

into R4, and the extreme left plane in R3 (Figure 5(e)) is also shared by R4.

4. HMHD and MHD Simulations of NOAA AR 12734

4.1. Governing Equations and Numerical Model

In the spirit of our earlier related works (Prasad et al. 2018, 2020; Nayak et al. 2019), the plasma is idealized to be incompressible and thermodynamically inactive, as well as explicitly nonresistive. While this relatively simple idealization is naturally limited, it exposes the basic dynamics of magnetic reconnections unobscured by the effects due to compressibility and heat transfer. Although the latter are important for coronal loops (Ruderman & Roberts 2002), they do not directly affect the magnetic topology—the focus of this paper. Historically rooted in classical hydrodynamics, such idealizations have a proven record in theoretical studies of geo/astrophysical phenomena (Rossby 1938; Dahlburg et al. 1991; Bhattacharyya et al. 2010; Bora et al. 2021). Inasmuch as their cognitive value depends on an a posteriori validation against the observations, the present study offers yet another opportunity to do so.

The Hall forcing has been incorporated (Bora et al. 2021) in the computational model EULAG-MHD (Smolarkiewicz & Charbonneau 2013) to solve the dimensionless HMHD equations,

$$\frac{\partial \boldsymbol{v}}{\partial t} + (\boldsymbol{v}\cdot\nabla)\boldsymbol{v} = -\nabla p + (\nabla\times\boldsymbol{B})\times\boldsymbol{B} + \frac{1}{R_F^A}\nabla^2\boldsymbol{v}, \quad (7)$$

$$\frac{\partial \boldsymbol{B}}{\partial t} = \nabla\times(\boldsymbol{v}\times\boldsymbol{B}) - d_{\rm H}\nabla\times((\nabla\times\boldsymbol{B})\times\boldsymbol{B}), \quad (8)$$

$$\nabla\cdot\boldsymbol{v} = 0, \quad (9)$$

$$\nabla\cdot\boldsymbol{B} = 0, \quad (10)$$

where $R_F^A = (v_{\rm A}L/\nu)$ (ν being the kinematic viscosity) is an effective fluid Reynolds number, having the plasma speed replaced by the Alfvén speed $v_{\rm A}$. Hereafter R_F^A is denoted as fluid Reynolds number for convenience. The transformation of the dimensional quantities (expressed in cgs units) into the corresponding nondimensional quantities,

$$\boldsymbol{B}\longrightarrow\frac{\boldsymbol{B}}{B_0}, \boldsymbol{x}\longrightarrow\frac{\boldsymbol{x}}{L_0}, \boldsymbol{v}\longrightarrow\frac{\boldsymbol{v}}{v_{\rm A}},$$
$$t\longrightarrow\frac{t}{\tau_{\rm A}}, p\longrightarrow\frac{p}{\rho_0 {v_{\rm A}}^2}, \quad (11)$$

assumes arbitrary B_0 and L_0, while the Alfvén speed $v_{\rm A}\equiv B_0/\sqrt{4\pi\rho_0}$. Here ρ_0 is a constant mass density, and $d_{\rm H}$ is the

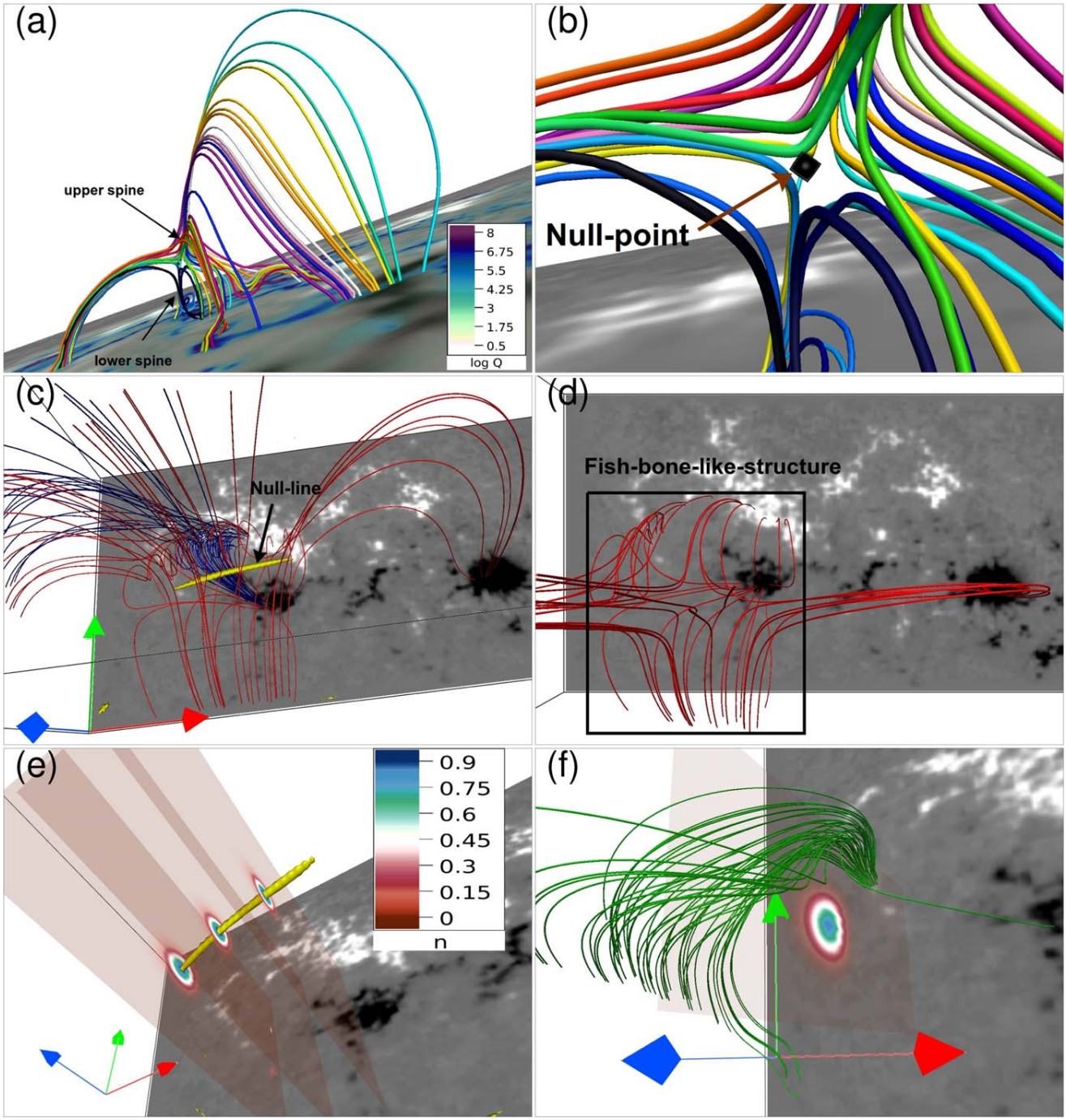

Figure 5. Panel (a) shows a 3D null spine-fan configuration in region R2, with B_z as the bottom boundary overlaid with log Q between 5 and 10. Panel (b) is the zoomed-in view of panel (a), highlighting the 3D null point (in black)—with an isosurface of $n = 0.6$ indicated by an arrow. Panel (c) shows the side view of magnetic field line structure in region R3, along with the yellow surface representing the null line corresponding to $n = 0.9$. Panel (d) shows the top-down view of red magnetic field lines of panel (c) forming a fish-bone-like structure. In panel (e) we show the value of n on three different vertical planes passing through the cross sections of the null-line surface. Notably, the planes show circles in the cross section at different locations, which indicates that the yellow surface is a null line. Panel (f) depicts magnetic field line morphology in region R4, along with the value of n on a vertical plane, where the green circular contour corresponds to $n = 0.6$, suggesting that the right part of magnetic field line morphology may be a part of the null-line geometry (shown in panel (c)).

Hall parameter. In the limit of $d_H = 0$, Equations (7)–(9) reduce to the MHD equations (Prasad et al. 2018).

The governing Equations (7)–(9) are numerically integrated using EULAG-MHD—an MHD extension (Smolarkiewicz & Charbonneau 2013) of the established Eulerian/Lagrangian comprehensive fluid solver EULAG (Prusa et al. 2008) predominantly used in atmospheric research. The EULAG solvers are based on the spatio-temporally second-order-accurate nonoscillatory forward-in-time advection scheme MPDATA (for *multidimensional positive-definite advection transport algorithm*; Smolarkiewicz 2006). Importantly, unique to MPDATA is its widely documented dissipative property mimicking the action of explicit subgrid-scale turbulence models wherever the concerned advective field is underresolved, the property known

Table 1
Salient Features of Magnetic Field Line Dynamics in R1

Magnetic Field Line Structure	HMHD	MHD
QSL1	Fast reconnection followed by a significant rise of loops, eventually reconnecting higher in the corona.	Slow reconnection followed by a limited rise of loops.
QSL2	Fast reconnection causing the magnetic field lines to entirely disconnect from the polarity P2.	Due to slow reconnection, magnetic field lines remain connected to P2.
Flux rope	Fast slipping reconnection of the flux-rope footpoints, followed by the expansion and rise of the rope envelope.	Slow slipping reconnection and rise of the flux-rope envelope; the envelope does not reach the QSL1.

as implicit large-eddy simulations (ILES; Margolin et al. 2006). In effect, magnetic reconnections resulting in our simulations dissipate the under-resolved magnetic field along with other advective field variables and restore the flux freezing. These reconnections, being intermittent and local, successfully mimic physical reconnections.

4.2. Numerical Setup

The simulations are carried out by mapping the physical domain of $256 \times 128 \times 128$ pixels on the computational domain of $x \in \{-1, 1\}$, $y \in \{-0.5, 0.5\}$, $z \in \{-0.5, 0.5\}$ in a Cartesian coordinate system. The dimensionless spatial step sizes are $\Delta x = \Delta y = \Delta z \approx 0.0078$. The dimensionless time step is $\Delta t = 5 \times 10^{-4}$, set to resolve whistler speed—the fastest speed in incompressible HMHD. The rationale is briefly presented in the Appendix. The corresponding initial state is motionless ($\boldsymbol{v} = 0$), and the initial magnetic field is provided from the non-FFF extrapolation. The nonzero Lorentz force associated with the extrapolated field pushes the magnetofluid to initiate the dynamics. Since the maximal variation of magnetic flux through the photosphere is only 2.28% of its initial value during the flare (not shown), the B_z at the bottom boundary (at $z = 0$) is kept fixed throughout the simulation, while all other boundaries are kept open. For velocity, all boundaries are set open. The mass density is set to $\rho_0 = 1$.

The fluid Reynolds number is set to 500, which is roughly two orders of magnitude smaller than its coronal value ≈25,000 (calculated using kinematic viscosity $\nu = 4 \times 10^9\ \mathrm{m^2\ s^{-1}}$ (Aschwanden 2005) in solar corona). Without any loss in generality, the reduction in R_F^A can be envisaged to cause a reduction in computed Alfvén speed, $v_\mathrm{A}|_\mathrm{computed} \approx 0.02 \times v_\mathrm{A}|_\mathrm{corona}$, where the L for the computational and coronal length scales are set to 71 and 100 Mm, respectively. This diminished Alfvén speed reduces the requirement of computational resources and also relates it to the observation time. The results presented herein pertain to a run for $1200\Delta t$ that, along with the normalizing $\tau_\mathrm{A} \approx 3.55 \times 10^3$ s, roughly corresponds to an observation time of ≈35 minutes. For the ease of reference in comparison with observations, we present the time in units of $0.005\tau_a$ (which is 17.75 s) in the discussions of the figures in subsequent sections.

Although the coronal plasma idealized to have reduced Reynolds number is inconsequential here, in a comparison of MHD and HMHD evolution, we believe that the above rationale merits further contemplation. Undeniably such a coronal plasma is not a reality. Nevertheless, the reduced R_F^A does not affect the reconnection or its consequence but slows down the dynamics between two such events and, importantly, reduces the computational cost, making data-based simulations realizable even with reasonable computing resources. A recent work by Jiang et al. (2016) used a homologous approach toward simulating a realistic and self-consistent flaring region.

In the present simulations, all parameters are identical for the MHD and the HMHD except for the d_H, respectively set to 0 and 0.004. The value 0.004 is motivated by recognizing ILES dissipation models intermittent magnetic reconnections at the $\mathcal{O}(\|\Delta \boldsymbol{x}\|)$ length scales, consistent with the thesis put forward in Introduction, we specify an appreciable Hall coefficient as $d_\mathrm{H} = 0.5\Delta z/L \approx 0.004$, where $L = 1 \equiv$ smallest extent of the computational volume, having $\Delta y = \Delta z \approx 0.0078$ as the dissipation scales because of the ILES property of the model. Correspondingly, the value is also at the lower bound of the pixel or scale order approximation and, in particular, an order of magnitude smaller than its coronal value valid at the actual dissipation scale. An important practical benefit of this selection is the optimization of the computational cost while keeping magnetic field line dynamics tractable. Importantly, with dissipation and Hall scales being tied, an increased current density at the dissipation scale introduces additional slippage of field lines in HMHD over MHD (due to the Hall term) and may be responsible for more effective and faster reconnections found in the Hall simulation reported below.

4.3. Comparison of the HMHD and MHD Simulations

The simulated HMHD and MHD dynamics leading to the flare show unambiguous differences. This section documents these differences by comparing methodically simulated evolution of the magnetic structures and topologies in NOAA AR 12734—namely, the flux rope, QSLs, and null points—identified in the extrapolated initial data in regions R1–R4.

4.3.1. Region R1

The dynamics of region R1 are by far the most complex among the four selected regions. To facilitate future reference, as well as to outline the organization of the discussion that follows, Table 1 provides a brief summary of our findings—in a spirit of theses to be proven by the simulation results.

The global dynamics of magnetic field lines in region R1 is illustrated in Figure 6; consult Figure 4 for the initial condition and terminology. The snapshots from the HMHD and MHD simulations are shown in panels (a)–(d) and (e)–(f), respectively. In panels (a) and (b), corresponding to $t = 19$ and $t = 46$, the footpoints of magnetic field lines in Set II (near P2, marked maroon) exhibit slipping reconnection along high values of the squashing factor Q indicated by black arrows. Subsequently, between $t = 80$ and 81 in panels (c) and (d), the magnetic field lines in Set II rise in the corona and reconnect with magnetic field lines in Set I to change connectivity. The MHD

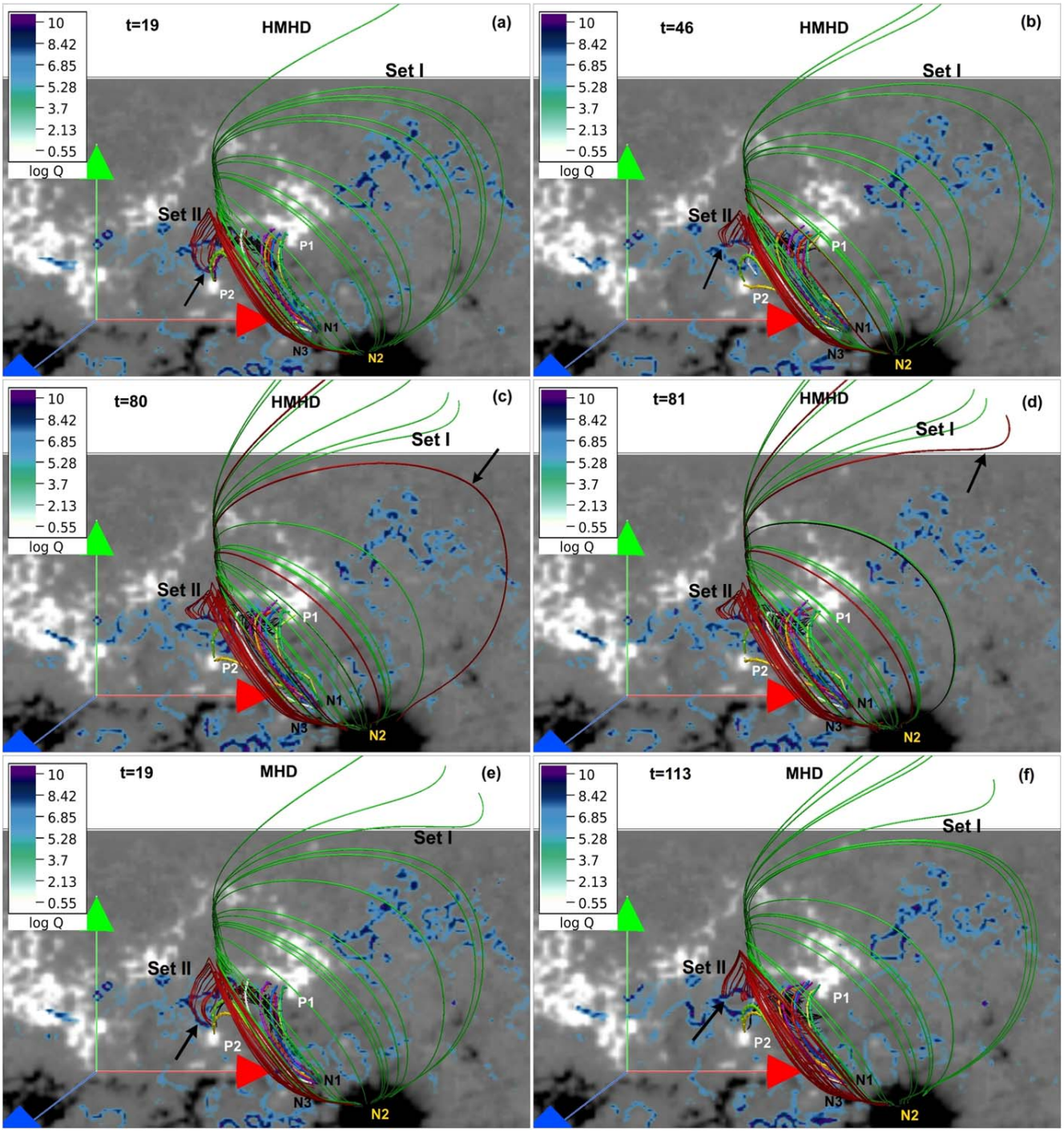

Figure 6. Snapshots of the global dynamics of magnetic field lines in region R1 during the HMHD and MHD simulations are shown in panels (a)–(d) and (e)–(f), respectively. Panels (a) and (b) show the departure of footpoints of magnetic field lines in Set II (maroon) away from polarity P2 between $t = 19$ and 46 on the bottom boundary (marked by black arrow). Panel (c) depicts the rising magnetic field lines in Set II (maroon) higher up in the solar corona at $t = 80$ (marked by black arrow), and panel (d) shows subsequent connectivity change of rising magnetic field lines at $t = 81$, due to reconnection with the Set I (green) magnetic field lines. Panels (e) and (f) depict the departure of footpoints of magnetic field lines in Set II (maroon) away from P2 between $t = 19$ and 113, which is similar to the HMHD but delayed in time—indicating the slower dynamics in the MHD. Notably, significant rise of magnetic field lines in Set II and consequent reconnection of it with magnetic field lines in Set I higher up in the solar corona are absent in the MHD simulation. An animation of this figure is available. The video shows the evolution of magnetic field lines in region R1 from $t = 0$ to 109 for the HMHD and from $t = 0$ to 120 for the MHD simulations, respectively. The real-time duration of the video is 12 s.

(An animation of this figure is available.)

counterpart of the slipping reconnection in panels (e) and (f) corresponds to magnetic field lines in Set II between $t = 19$ and 113. It lags behind the HMHD displays, thus implying slower dynamics. Furthermore, the magnetic field lines in Set II, unlike for the HMHD, do not reach up to the magnetic field lines in Set I constituting QSL1 and hence do not reconnect. A

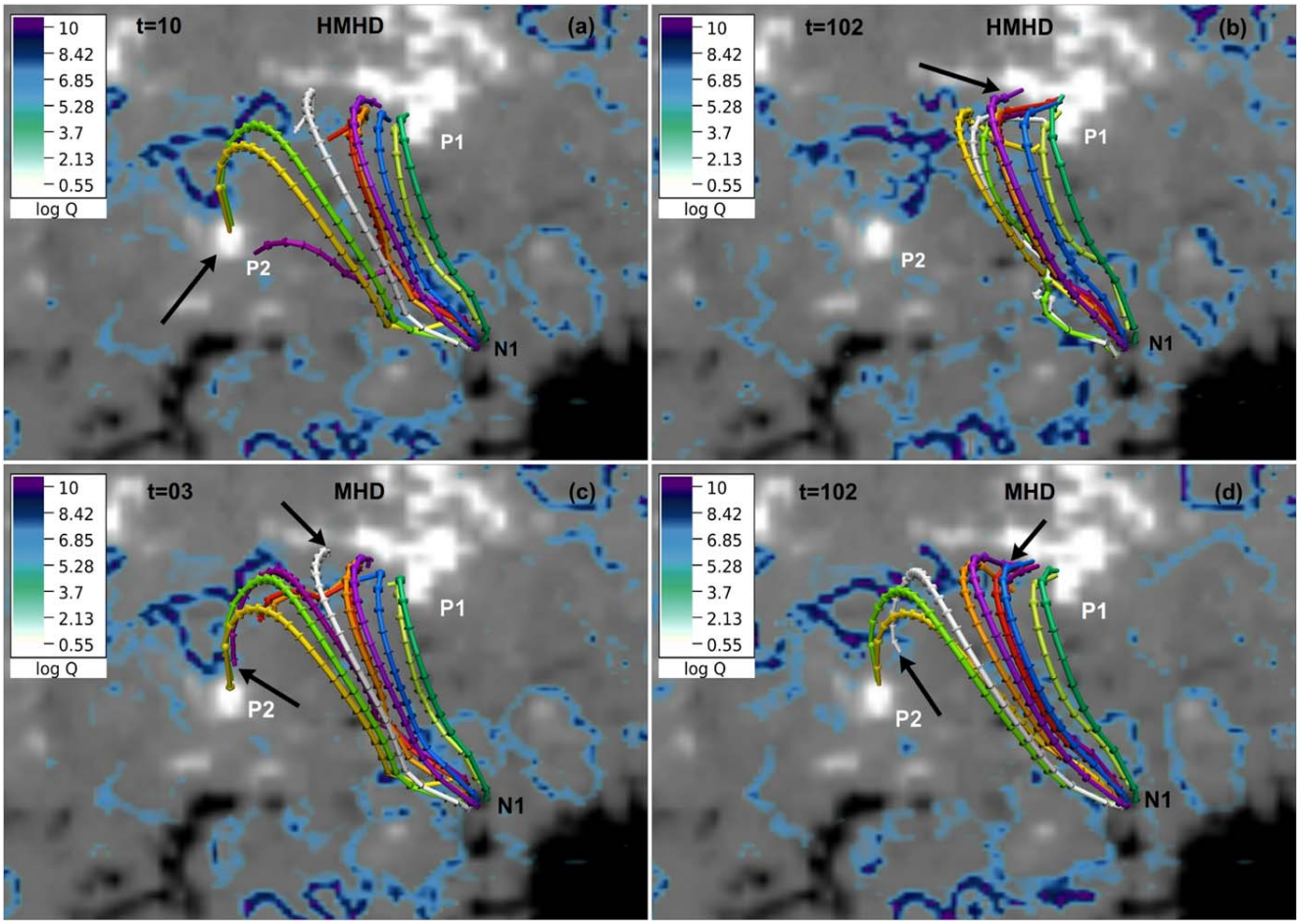

Figure 7. Snapshots of the HMHD and MHD evolution of QSL2 (Figure 4(c)) are shown in panels (a)–(b) and (c)–(d), respectively. Panels (a)–(b) show that magnetic field lines anchored in the positive polarity P2 at $t = 10$ have moved to the polarity P1 by $t = 102$ and changed their connectivity (marked by black arrow) owing to reconnection along QSL during the HMHD. Panels (c)–(d) show the connectivity changes of the violet and white color magnetic field lines during the MHD evolution. The white field line was initially connecting the polarities P1 and N1, whereas the violet field line was connecting P2 and N1. As a result of reconnection along QSL, the white field line changes its connectivity from P1 to P2, and the violet field line changes the connectivity from P2 to P1 (marked by black arrows). Notably, unlike the HMHD simulation, not all magnetic field lines move to P1 from P2 owing to reconnection along QSL during the MHD, which indicates the slower dynamics. An animation of this figure is available. The video shows the evolution of QSL2 (shown in Figure 4) in region R1 from $t = 0$ to 120 for the HMHD and MHD simulations, respectively. The real-time duration of the video is 12 s.

(An animation of this figure is available.)

more informative visualization of the highlighted dynamics is supplemented in an online animation. The decay index is calculated for each time instant for both the simulations and is found to be less than 1.5 above the flux rope, indicating an absence of the torus instability (Kliem & Török 2006). For more detail, Figures 7 and 8 illustrate the evolution of QSL2 and flux rope separately.

Panels (a)–(b) and (c)–(d) of Figure 7 show, respectively, the instants from the HMHD and MHD simulations of QSL2 between P1, P2, and N1. The HMHD instants show that magnetic field lines that were anchored between P2 and N1 at $t = 10$ have moved to P1 around $t = 102$, marked by black arrows in both panels. The magnetic field lines anchored at P2 moved to P1 along the high Q values—signifying the slipping reconnection. The MHD instants in panels (c)–(d) show the connectivity changes of the violet and white colored magnetic field lines. The white field line was initially connecting P1 and N1, whereas the violet field line was connecting P2 and N1. As a result of reconnection along QSL, the white field line changed its connectivity from P1 to P2, and the violet field line changes the connectivity from P2 to P1 (marked by black arrows). Notably, in contrast to the HMHD evolution, all magnetic field lines initially anchored in P2 do not change their connectivity from P2 to P1 during the MHD evolution, indicating the slower dynamics.

The flux rope has been introduced in panels (c) and (d) of Figure 4, respectively, below the QSL2 and in enlargement. Its HMHD and MHD evolutions, along with the twists on three different vertical cross sections, are shown in panels (a)–(f) and (g)–(i) of Figure 8, respectively. Magnetic field lines constituting the rope rise substantially higher during the HMHD evolution as a result of slipping reconnection along the high Q in panels (c)–(f). In panel (c) at $t = 32$, the footpoints of the rope that are anchored on the right side (marked by the black arrow) change their connectivity from one high Q regime to another in panel (d) at $t = 33$, i.e., the footpoints on the right have moved to the left side (marked by the black arrow). Afterward, the magnetic field lines rise because of the continuous slipping reconnection, as evidenced in panels (e)–(f) and the supplemented animation. Comparing panel (a) with

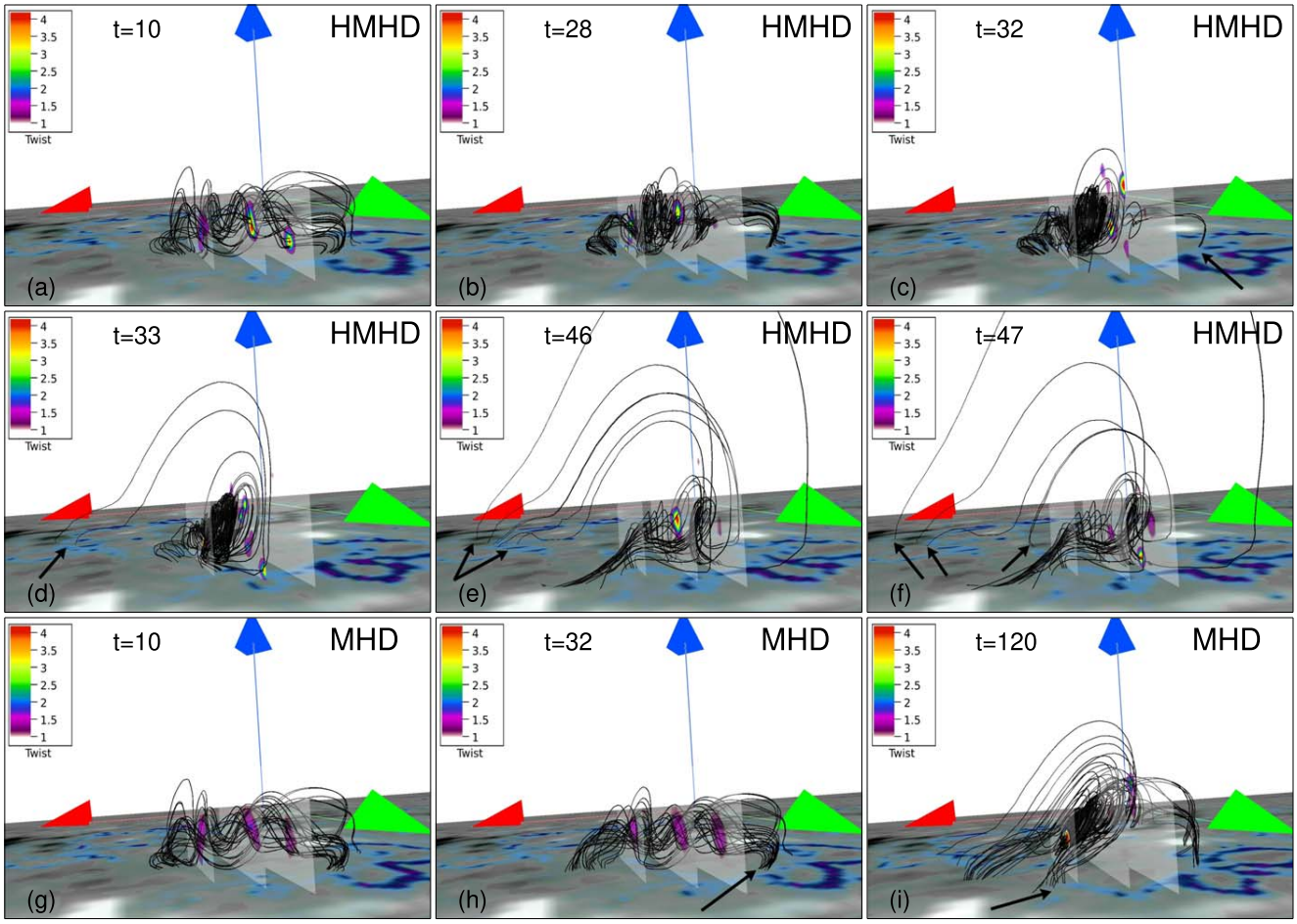

Figure 8. Time sequence showing the HMHD (panels (a)–(f)) and MHD (panels (g)–(i)) evolution of the flux rope (shown in Figure 4(c)), along with the twist T_w. Panel (a) shows that the twist on the middle and the right plane on flux rope is higher than initial values (see Figure 4(d)) and reduced with time in panel (b). Panels (c)–(d) depict the connectivity change of the footpoint of the rope from right to left (indicated by the black arrow) due to reconnection along QSL. Panels (e)–(f) show the connectivity change of magnetic field lines on left-hand side (indicated by the black arrow). Panels (g)–(i) depict the dynamic rise of the flux rope between $t = 10$ and 120 during the MHD simulation. Notably, the footpoints of the rope on the right side (marked by the black arrow) at $t = 32$ in panel (h) have moved toward left by $t = 120$ in panel (i) as a result of reconnection along QSL. An animation of this figure is available. The video shows the evolution of magnetic flux rope in region R1 from $t = 0$ to 92 for the HMHD simulations and from $t = 0$ to 120 for the MHD simulations. The real-time duration of the video is 12 s.

(An animation of this figure is available.)

panel (g) at $t = 10$ and panel (c) with panel (h) at $t = 32$, we note that the twist value T_w is higher in the HMHD simulation. Panels (h)–(i) highlight the displaced footpoints of the flux rope due to slipping reconnection at $t = 32$ and 120 (see the black arrow). The rope is preserved throughout the HMHD and MHD simulations.

The rise and expansion of the flux-rope envelope owing to slipping reconnection are remarkable in the HMHD simulation. Dudík et al. (2014) have already shown such a flux-rope reconnection along QSL in a J-shaped current region, with slipping reconnection causing the flux rope to form a sigmoid (S-shaped hot channel observed in EUV images of SDO/AIA) followed by its rise and expansion. Further insight is gained by overlaying the flux-rope evolution shown in Figure 8 with direct volume rendering of $|\boldsymbol{J}|/|\boldsymbol{B}|$ (Figures 9 and 10) as a measure of magnetic field gradient for the HMHD and MHD simulations. In the HMHD case, the appearance of large values of $|\boldsymbol{J}|/|\boldsymbol{B}| > 475$ inside the rope (panels (a)–(c)) and footpoints on the left of the rope (panels (d)–(e)) are apparent. The development of the large $|\boldsymbol{J}|/|\boldsymbol{B}|$ is indicative of reconnection within the rope. Contrarily, MHD simulation lacks such high values of $|\boldsymbol{J}|/|\boldsymbol{B}|$ in the same time span (panels (a)–(b)), and the field lines show no slippage—agreeing with the proposal that large currents magnify the Hall term, resulting in more effective slippage of field lines.

4.3.2. Region R2

To compare the simulated magnetic field lines dynamics in region R2 with the observed tip of the W-shaped flare ribbon B2 (Figure 3(a)) during the HMHD and MHD evolution, we present the instants from both simulations at $t = 70$ in panels (a) and (b) of Figure 11, respectively. Importantly, the lower spine remains anchored to the bottom boundary during the HMHD simulation (evident from the supplemented animation along with Figure 11). Further, Figure 12 shows the evolution of the lower spine along with the $|\boldsymbol{J}|/|\boldsymbol{B}|$ on the bottom boundary for the HMHD (panels (a)–(d)) and MHD (panels (e)–(h)) cases. In the HMHD case, noteworthy is the slipping motion of the lower spine (marked by the black arrows) tracing the $|\boldsymbol{J}|/|\boldsymbol{B}| > 350$ regions on the

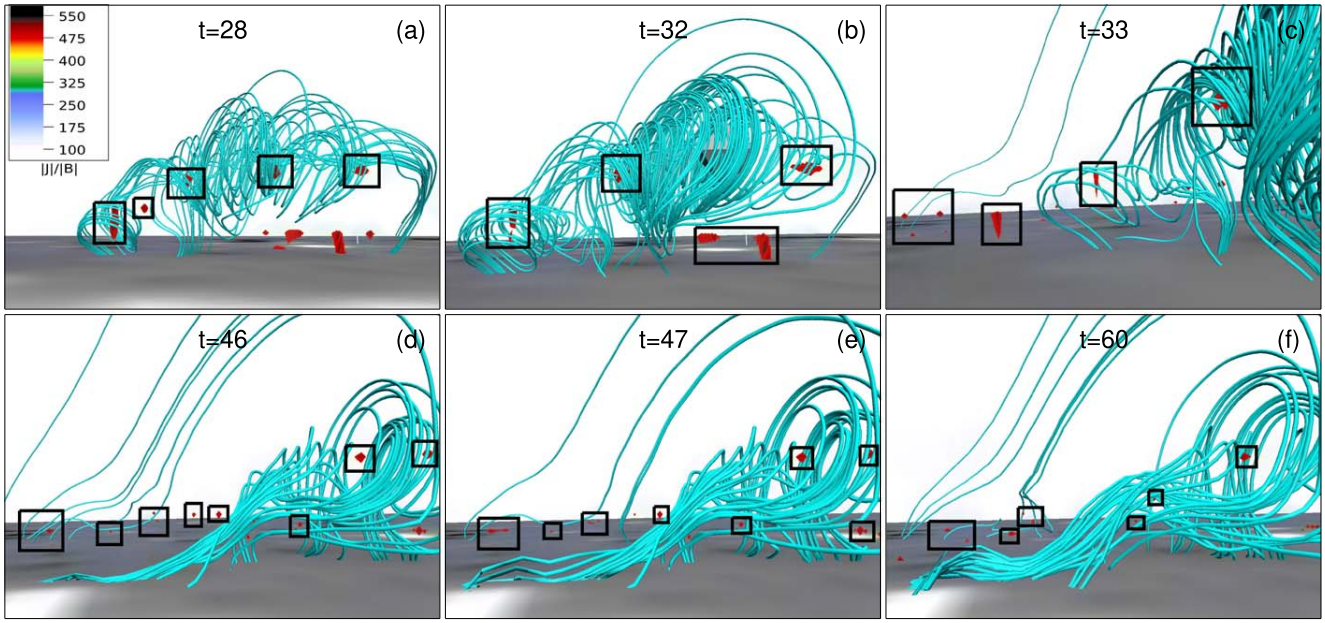

Figure 9. Temporal variation of the direct volume rendering of ($|\boldsymbol{J}|/|\boldsymbol{B}|$) along with the flux rope is shown during the HMHD simulation. Noticeably, the high magnetic field gradient regions with ($|\boldsymbol{J}|/|\boldsymbol{B}|$) $\geqslant 475$ develop within (panels (a)–(c)) and on the left side of the flux rope (panels (d)–(f)). The values ($|\boldsymbol{J}|/|\boldsymbol{B}|$) $\geqslant 475$ in each panel are enclosed within the black rectangular boxes. The color of flux rope has been changed to cyan to show ($|\boldsymbol{J}|/|\boldsymbol{B}|$) values in region R1.

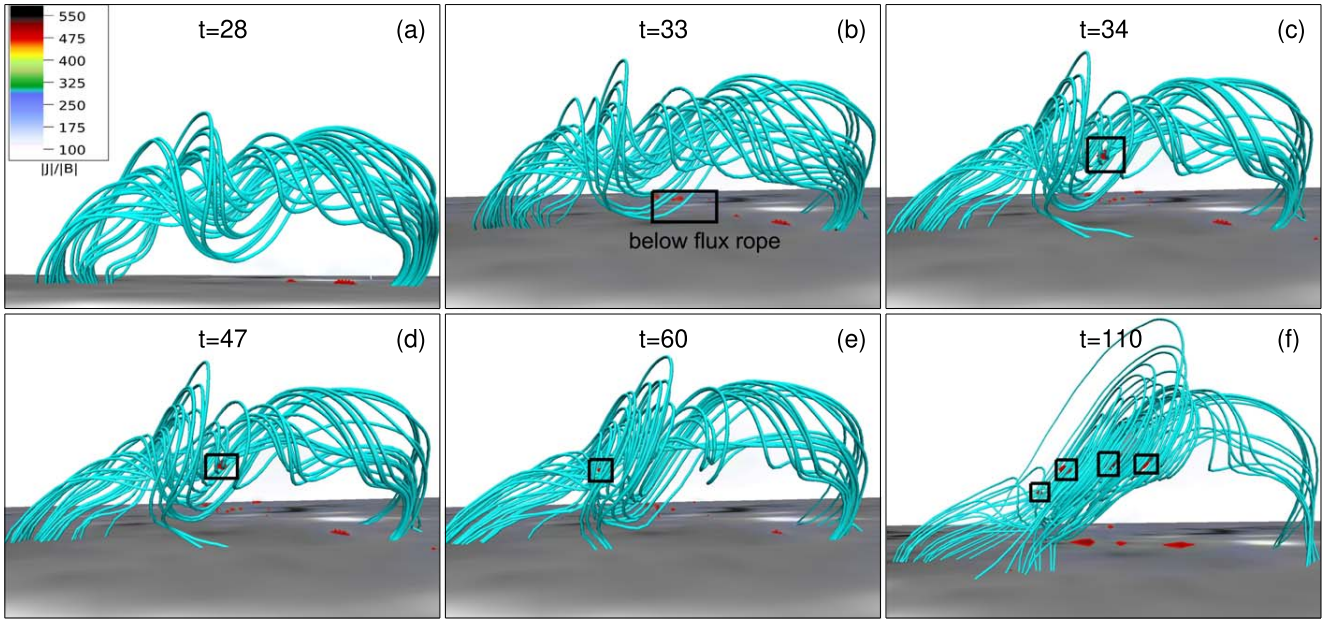

Figure 10. Temporal variation of the direct volume rendering of ($|\boldsymbol{J}|/|\boldsymbol{B}|$) along with the flux rope is shown during the MHD simulation. Panels (a) and (b) show the absence of high values of ($|\boldsymbol{J}|/|\boldsymbol{B}|$) within the rope at $t = 28$ and 32, but in later panels (c)–(f) ($|\boldsymbol{J}|/|\boldsymbol{B}|$) $\geqslant 475$ appears (enclosed by the black rectangular boxes). Notably, as compared to the HMHD case (Figure 9), the development of ($|\boldsymbol{J}|/|\boldsymbol{B}|$) is not significant in region R1 during the MHD. The color of flux rope has been changed to cyan to show ($|\boldsymbol{J}|/|\boldsymbol{B}|$) values in region R1.

bottom boundary (panels (a)–(b)), whereas in the MHD such high values of $|\boldsymbol{J}|/|\boldsymbol{B}|$ are absent on the bottom boundary—suggesting that the slippage of the field lines on the bottom boundary is less effective compared to the HMHD. The finding is in agreement with the idea of enhanced slippage of field lines due to high current densities as conceptualized in the introduction. The anchored lower spine provides a path for the plasma to flow downward to the brightening segment B2. In the actual corona, such flows result in flare brightening (Benz 2017). In contrast, the lower spine gets completely disconnected from the bottom boundary (Figure 11(b)) in the MHD simulation, hence failing to explain the tip of the W-shaped flare ribbon in B2. The anchored lower spine in the HMHD simulation is caused by a complex series of magnetic field line reconnections at the 3D null and along the QSLs in R2, as depicted in the animation.

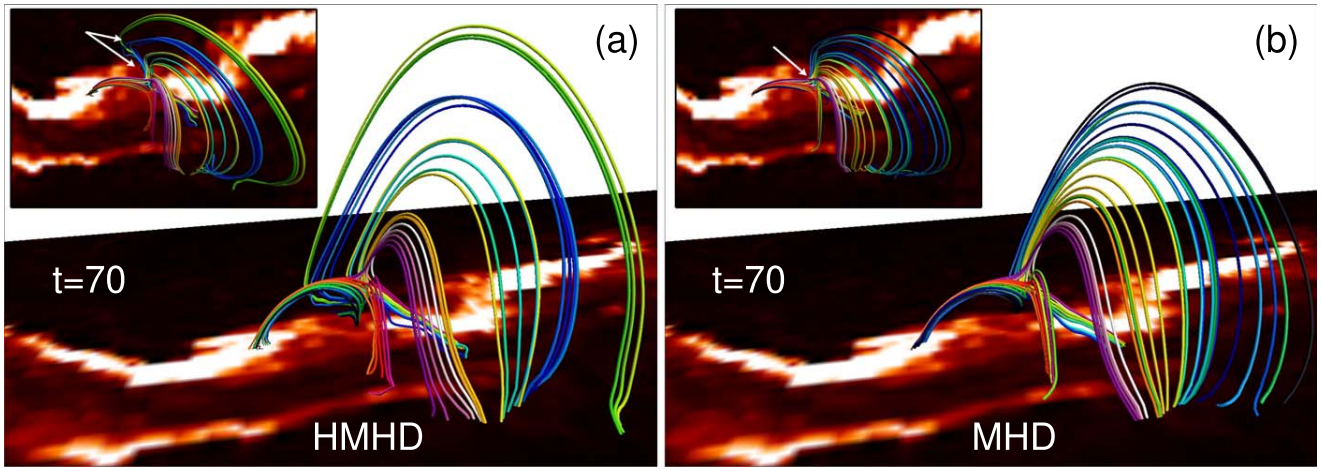

Figure 11. Panels (a) and (b) show the comparison of magnetic field line topology in region R2 at $t = 70$ with the flare ribbons observed in the SDO/AIA 304 Å channel (side views) during the HMHD and MHD simulations, respectively. The inset images in the upper left corner in each panel show the top view of the same magnetic field line topology. Notably, the spine is anchored in the HMHD, while it is not connected to the bottom boundary in the MHD at $t = 70$ (marked by the white arrow in inset images). An animation of this figure is available. The video shows the evolution of magnetic field lines in region R2 with the AIA 304 Å image at the bottom boundary from $t = 0$ to 117 for the HMHD simuations and from $t = 0$ to 120 for the MHD simulations. The real-time duration of the video is 12 s.

(An animation of this figure is available.)

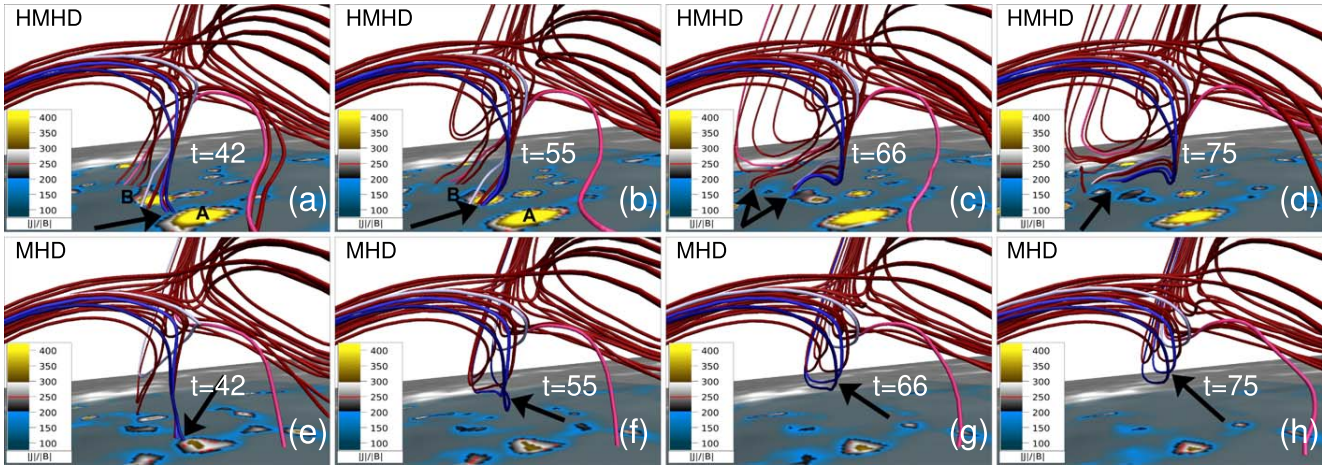

Figure 12. Panels (a)–(d) depict the slipping motion of the lower spine field lines (also shown in the Figure 5 but the color of field lines has been changed) overlaid with the $|\boldsymbol{J}|/|\boldsymbol{B}|$ on the bottom boundary during the HMHD evolution. The motion is marked by the black arrows in all the panels, indicating the successive change in the location of field lines on the bottom boundary. A and B (in panels (a) and (b)) are the two regions with $|\boldsymbol{J}|/|\boldsymbol{B}| > 350$ on the bottom boundary (just below the lower spine). Notably, the field lines follow the high values of $|\boldsymbol{J}|/|\boldsymbol{B}|$ on the bottom boundary and remain anchored. Panels (e)–(h) show the evolution of the same lower spine field lines during the MHD simulation. The large values of $|\boldsymbol{J}|/|\boldsymbol{B}|$ do not appear below the lower spine (on the bottom boundary), and it does not remain anchored from $t \approx 55$ onward (panels (f)–(h)).

4.3.3. Region R3

HMHD and MHD simulations of magnetic field lines dynamics around the null line are shown in Figures 13 and 14, respectively. Figure 13 shows the blue magnetic field lines prior to and after the reconnections (indicated by black arrows) between $t = 4$ and 5 (panels (a)–(b)), between $t = 52$ and 53 (panels (c)–(d)), and between $t = 102$ and 103 (panels (e)–(f)) during the HMHD simulation. Figure 14 shows the same blue magnetic field lines prior to and after the reconnections (indicated by black arrows) between $t = 12$ and 13 (panels (a)–(b)), between $t = 59$ and 60 (panels (c)–(d)), and between $t = 114$ and 115 (panels (e)–(f)) during the MHD simulation. Comparison of panels (a)–(f) of Figure 13 with the same panels of Figure 14 reveals earlier reconnections of the blue magnetic field lines in the HMHD simulation. In both figures, green velocity vectors on the right represent the local plasma flow. They get aligned downward along the footpoints of the fan magnetic field lines, as reconnection progresses. Consequently, the plasma flows downward and impacts the denser and cooler chromosphere to give rise to the brightening in B3. The velocity vectors pointing upward represent a flow toward the null line. The plasma flow pattern in R3 is the same in the HMHD and MHD simulations. The vertical y-z plane passing through the cross section of the null-line surface (also shown in Figure 5(d)) in all the panels of Figures 13 and 14 shows the variation of n with time. It is evident that the null is not destroyed throughout the HMHD and MHD evolution. Structural changes in the field lines caused by reconnection are nearly identical for both the simulations, indicating inefficacy of the Hall term. This inefficacy is justifiable, as $|\boldsymbol{J}|/|\boldsymbol{B}|$ remains small $\approx$10 (not shown) in both HMHD and MHD evolution.

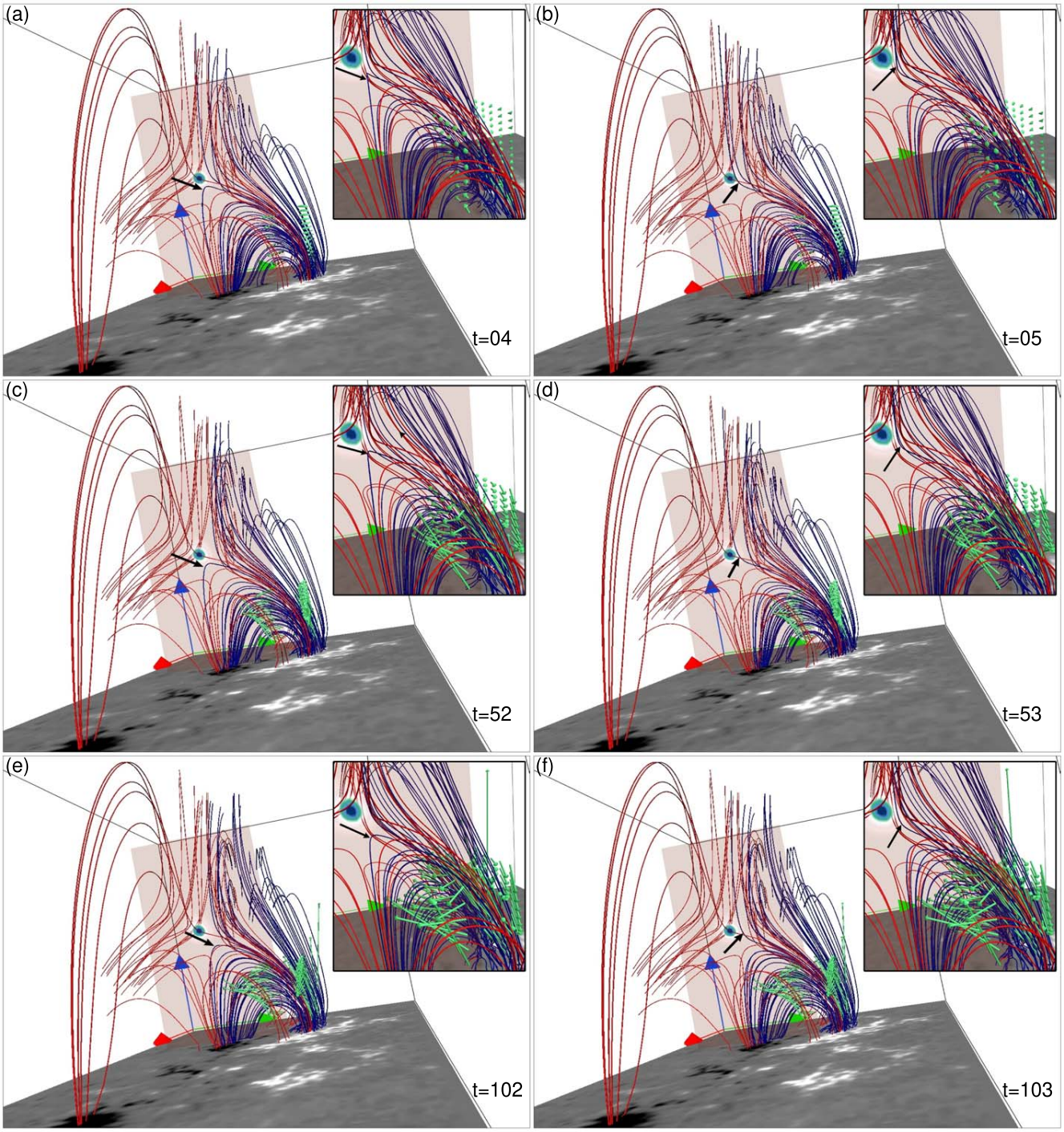

Figure 13. Time sequence showing the blue field line prior to and after reconnection (indicated by the black arrow) in region R3 during the HMHD simulation. Evolution of the flow vectors is depicted by green arrows (on the right side)—mimicking the direction of the plasma flow. The plane along the cross section of magnetic field line morphology in R3, showing the blue circular contours, represents the value of n (also shown in Figure 5(d)).

4.3.4. Region R4

The development of the circular motion of magnetic field lines in region R4 during the HMHD simulation is depicted in Figure 15. It shows the global dynamics of magnetic field lines in R4, and the inset images show the zoomed-in view of magnetic field lines in R4 to highlight the circular motion of magnetic field lines. The bottom boundary is B_z in the main figure, while the inset images have the z-component of the plasma flow at the bottom boundary (on the x-y plane). The red vectors represent the plasma flow direction and magnitude in all the panels of Figure 15, where the counterclockwise pattern of the plasma flow is evident. The global dynamics highlight reconnection of the loop anchored between positive and negative polarities at $t = 60$ in Figure 15 as it gets disconnected from the bottom boundary in panels (c)–(d) of Figure 15. The animation accompanying

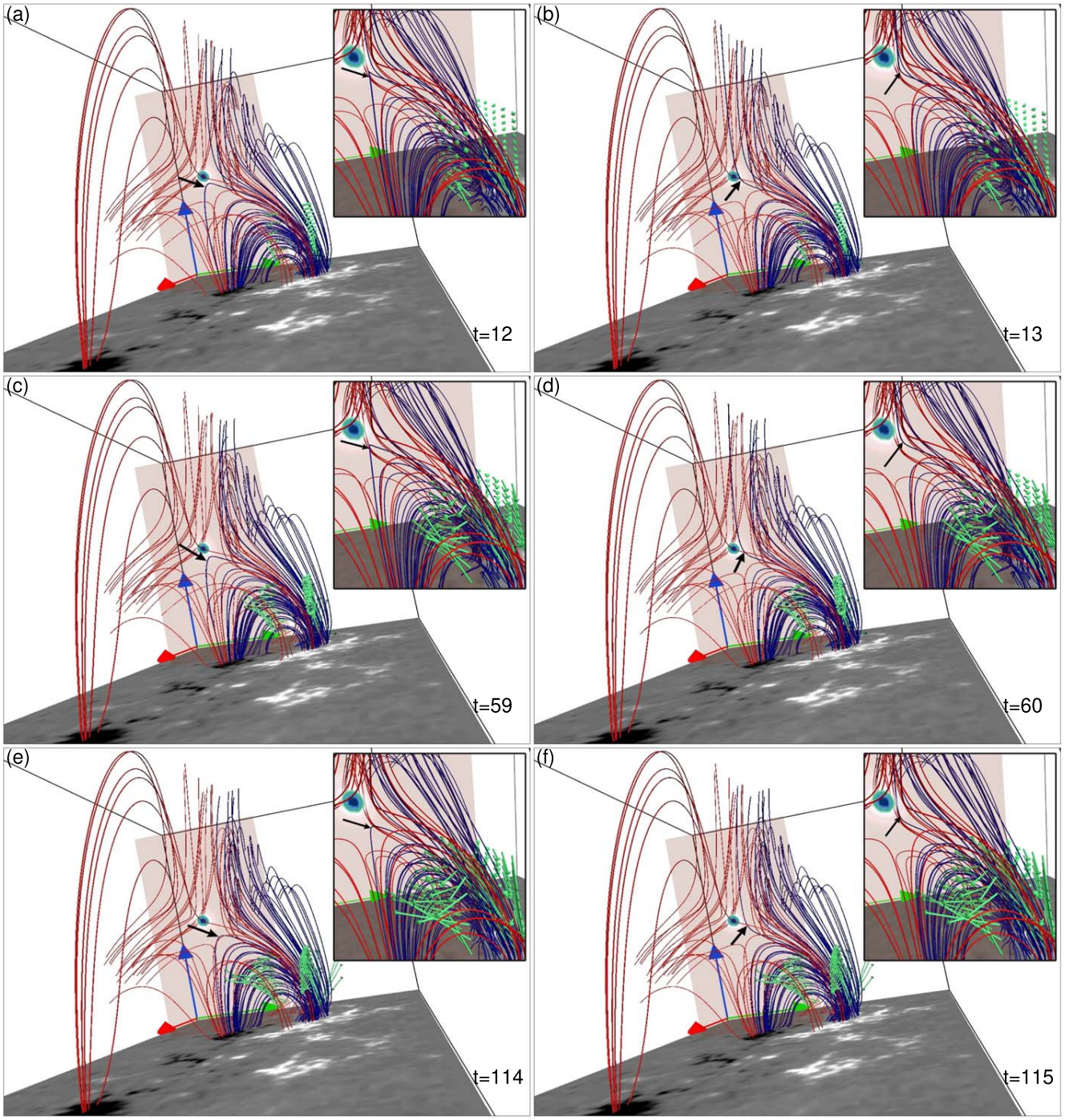

Figure 14. Time sequence showing the blue field line prior to and after reconnection (indicated by the black arrow) in region R3 during the MHD simulation. Evolution of the flow vectors is depicted by green arrows (on the right side)—mimicking the direction of the plasma flow. The plane along the cross section of magnetic field line morphology in R3, showing the blue circular contours, represents the value of n (also shown in Figure 5(d)). Notably, reconnection of the blue magnetic field lines is slightly delayed in comparison to its HMHD counterpart. A combined animation of Figure 13 and this figure is available. The video shows the evolution of magnetic field lines of region R3 along with the flow vectors (green) from $t = 0$ to 120 for the HMHD and MHD simulations, respectively. The real-time duration of the video is 12 s.

(An animation of this figure is available.)

Figure 15 highlights a counterclockwise motion of footpoints in the same direction as the plasma flow, indicating that field lines are frozen in the fluid. The trapped plasma may cause the rotating structure B4 in the observations (see Figure 3(a)). However, no such motion is present during the MHD evolution of the same magnetic field lines (not shown). An interesting feature noted in the animation is the clockwise slippage of field lines after the initial counterclockwise rotation. Further analysis of R4 using the direct volume rendering of $|\boldsymbol{J}|/|\boldsymbol{B}|$ is presented in Figure 16. The figure shows that $|\boldsymbol{J}|/|\boldsymbol{B}|$ attains high values $\geqslant$225 (enclosed by

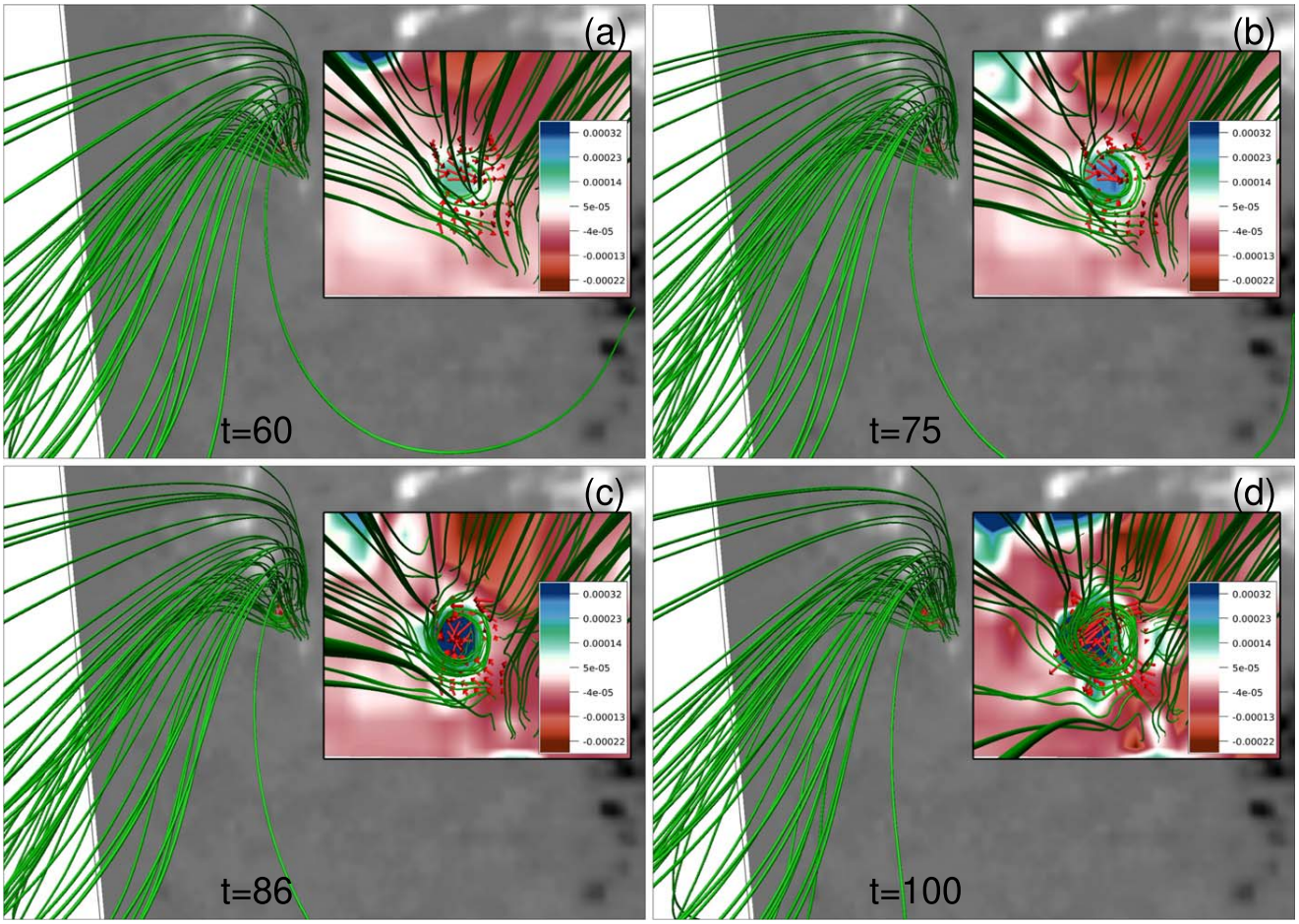

Figure 15. Panels (a)–(d) show the global dynamics of magnetic field lines in region R4 during the HMHD simulation. Inset images in each panel (on the right) depict the time sequence of the zoomed top-down view of the rotational motion of magnetic field lines. The background shows the variation of the z-component of flow $\in [-0.00022, 0.00032]$ in all inset images. The red vectors represent the plasma flow and change its direction in a counterclockwise manner in panels (a)–(d). The rotational motion of magnetic field lines coincides with the circular part of the flow. An animation of this figure is available. The video shows the evolution of magnetic field lines in region R4 from $t = 0$ to 100 for the HMHD simulation. The development of a counterclockwise rotational motion of the footpoints from $t \approx 33$ onward and the clockwise slippage of the field line from $t \approx 76$ onward are evident in the video. The real-time duration of the video is 10 s.

(An animation of this figure is available.)

the blue rectangles) within the rotating field lines from $t \approx 86$ onward. This suggests that the slippage of field lines is, once again, related to the high magnetic field gradients.

For completeness, we present the snapshots of an overall magnetic field line morphology including the magnetic structures and topology of regions R1, R2, R3, and R4 together, overlaid with 304 and 171 Å from the HMHD and MHD simulations. Figure 17(a) shows an instant (at $t = 75$) from the HMHD simulation where the topologies and magnetic structures in R1, R2, R3, and R4, plus the additionally drawn locust color magnetic field lines between R2 and R3, are shown collectively. It shows an excellent match of the magnetic field lines in R2 with the observed tip of the W-shaped flare ribbon at B2, which is pointed out by the pink arrow in panel (a). Footpoints of the spine-fan geometry around the 3D null orient themselves in the same fashion as the observed tip of the W-shaped flare ribbon at B2 as seen in the 304 Å channel of SDO/AIA. The rising loops indicated by the white arrow correspond to the same evolution as shown in Figure 6. The overall magnetic field line morphology mentioned in Figure 15(a) is given at the same time ($t = 75$) during the MHD simulation overlaid with the 304 Å image in Figure 15(b). Importantly, unlike the HMHD simulation, the MHD simulation does not account for the anchored lower spine and fan magnetic field lines of the 3D null at the center of the B2. Also, the significant rise of the overlying maroon magnetic field lines and the circular motion of the material in B4 are captured in the HMHD simulation only. In panel (c) magnetic field lines overlaid with the 171 Å image show that the magnetic field lines (higher up in the solar atmosphere) have resemblance with the post-flare loops during the HMHD. Overall, the HMHD evolution seems to be in better agreement with the observations in comparison to the MHD evolution.

5. Summary and Discussion

This paper compares data-based HMHD and MHD simulations using the flaring NOAA AR 12734 as a test bed. The importance of the HMHD stems from the realization that the Hall term in the induction equation cannot be neglected in the presence of the magnetic reconnection—the underlying cause of solar flares. The selected event is the C1.3 class flare on 2019 March 8 around 03:19 UT for the aforementioned comparison. Although the event is analyzed and reported in the

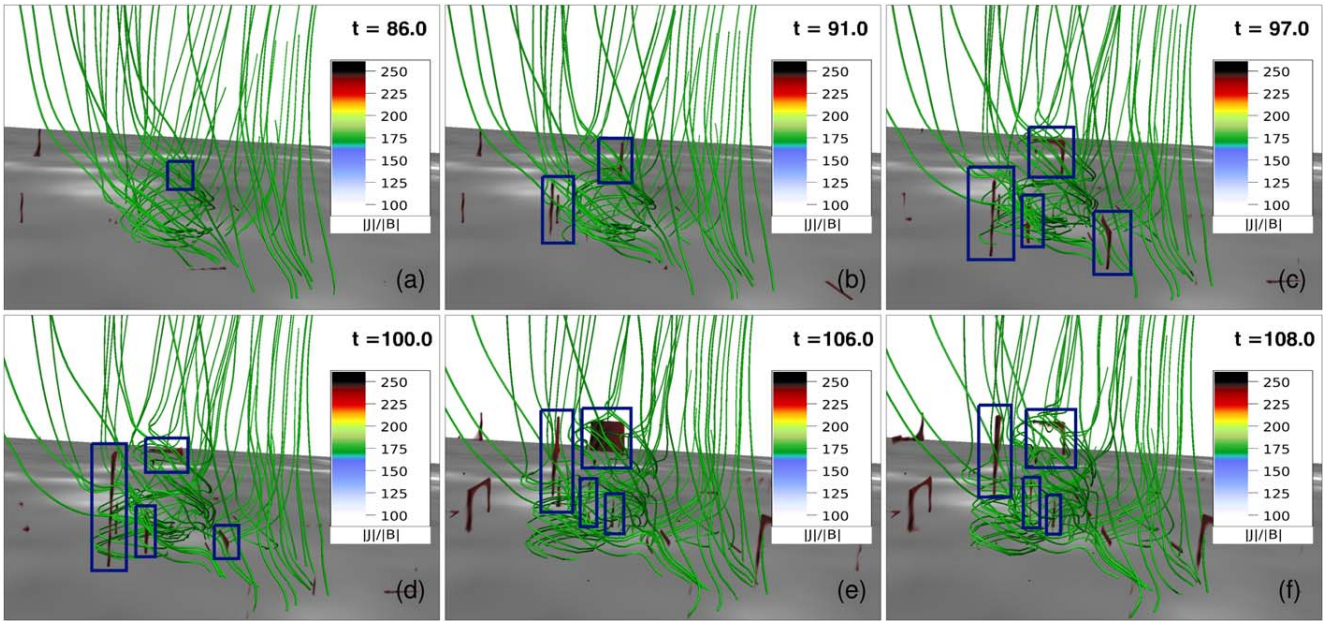

Figure 16. Panels (a)–(f) show the side view of the rotating magnetic field line structure in region R4 overlaid with $|\boldsymbol{J}|/|\boldsymbol{B}|$. The figure depicts the temporal development of strong magnetic field gradient regions of $|\boldsymbol{J}|/|\boldsymbol{B}| > 225$ (enclosed in the blue rectangular boxes) within the rotating magnetic structure.

literature, it is further explored using the multiwavelength observations from SDO/AIA. The identified important features are an elongated EUV counterpart of the eruption on the western side of the AR and a W-shaped flare ribbon and circular motion of cool chromospheric material on the eastern part. The magnetic field line dynamics near these features are utilized to compare the simulations. Notably, the simulations idealize the corona to have an Alfvén speed that is two orders of magnitude smaller than its typical value. Congruent to the general understanding, the Hall parameter is selected to tie the Hall dynamics to the dissipation scale $\mathcal{O}(\Delta \boldsymbol{x})$ in the spirit of the ILES carried out in the paper. The magnetic reconnection here is associated with the slippage of magnetic field lines from the plasma parcels, effective at the dissipation scale due to local enhancement of magnetic field gradient. The same enhancement also amplifies the Hall contribution, presumably enhancing the slippage and thereby making the reconnection faster and more effective than the MHD.

The coronal magnetic field is constructed by extrapolating the photospheric vector magnetic field obtained from the SDO/HMI observations employing the non-FFF technique (Hu et al. 2010). The concentrated distribution of the Lorentz force on the bottom boundary and its decrease with the height justify the use of non-FFF extrapolation for the solar corona. The initial nonzero Lorentz force is also crucial in generating self-consistent flows that initiate the dynamics and cause the magnetic reconnections. Analyses of the extrapolated magnetic field reveal several magnetic structures and topologies of interest: a flux rope on the western part at the flaring location, a 3D null point along with the fan-spine configuration at the center, and a "fish-bone-like structure" surrounding the null line on the eastern part of the AR. All of these structures are found to be cospatial with the observed flare ribbon brightening.

The HMHD simulation shows faster slipping reconnection of the flux-rope footpoints and overlying magnetic field lines (constituting QSLs above the flux rope) at the flaring location. Consequently, the overlying magnetic field lines rise, eventually reaching higher up in the corona and reconnecting to provide a path for plasma to eject out. The finding is in agreement with the observed elongated EUV counterpart of the eruption on the western part of the AR. Contrarily, such a significant rise of the flux rope and overlying field lines to subsequently reconnect higher up in the corona is absent in the MHD simulation—signifying that the reconnection is slower compared to the HMHD. Intriguingly, rise and expansion of the flux rope and overlying field lines due to slipping reconnection on QSLs have also been modeled and observed in an earlier work by Dudík et al. (2014). These are typical features of the "standard solar flare model in 3D," which allows for a consistent explanation of events that are not causally connected (Dudík et al. 2014). It also advocates that null points and true separatrices are not required for the eruptive flares to occur—concurring with the results of this work. HMHD evolution of the fan-spine configuration surrounding the 3D null point is in better agreement with the tip of the W-shaped flare ribbon at the center of the AR. The lower spine and fan magnetic field lines remain anchored to the bottom boundary throughout the evolution, which can account for the plasma flowing downward after the reconnection and cause the brightening, whereas in the MHD the lower spine gets disconnected and cannot account for the brightening. The reconnection dynamics around the null line and the corresponding plasma flow direction are the same in the HMHD and MHD simulations and agree with the observed brightening. Nevertheless, reconnection is earlier in the HMHD. HMHD evolution captures an anticlockwise circular motion of magnetic field lines in the left part of the AR that is cospatial with the location of the rotating chromospheric material on the eastern side of the AR. No such motion was found in the MHD simulation. Importantly, the simulations explicitly associate generation of large magnetic field gradients with HMHD compared to MHD, resulting in faster and more efficient field line slippage because of the enhanced Hall term.

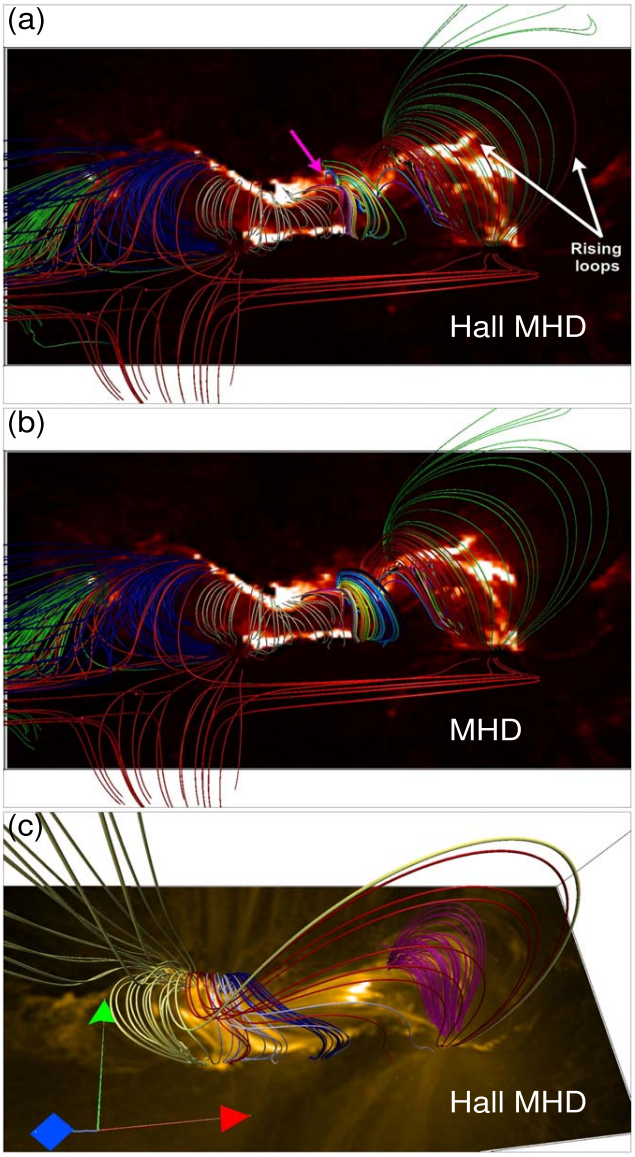

Figure 17. Top-down view of an overall magnetic field line morphology overlaid on the SDO/AIA 304 Å (panels (a) and (b)) and 171 Å images (panel (c)). Anchored magnetic field line footpoints in the central part match well with the observed tip of the W-shaped flare ribbon (marked by the pink arrow in panel (a)) in the HMHD, while magnetic field line footpoints are completely disconnected from the bottom boundary in the MHD (panel (b)). Loops rising higher up in the corona are remarkable in the HMHD (indicated by the white arrow in panel (a)). An animation of panels (a) and (b) is available. The video shows the evolution of magnetic field lines in AR along with the AIA 304 Å image at the bottom from $t = 0$ to 120 for the HMHD and MHD simulations, respectively. The real-time duration of the video is 12 s.

(An animation of this figure is available.)

Overall, the results documented in the paper show that the HMHD explains the flare brightening better than the MHD, prioritizing the requirement to include HMHD in future state-of-the-art data-based numerical simulations.

The authors thank the anonymous referee for providing insightful comments and suggestions that increased the scientific content of the paper. The simulations are performed using the 100TF cluster Vikram-100 at Physical Research Laboratory, India. We wish to acknowledge the visualization software VAPOR (www.vapor.ucar.edu), for generating relevant graphics. Q.H. and A.P. acknowledge partial support of NASA grants 80NSSC17K0016, 80NSSC21K1671, L.W.S. 80NSSC21K0003 and NSF awards AGS-1650854 and AGS-1954503. This research was also supported by the Research Council of Norway through its Centres of Excellence scheme, project No. 262622, as well as through the Synergy grant No. 810218 (ERC-2018-SyG) of the European Research Council.

Appendix

The dimensionless time step is obtained by employing the Hall induction equation

$$\frac{\partial \boldsymbol{B}}{\partial t} = -d_{\rm H}\nabla \times ((\nabla \times \boldsymbol{B}) \times \boldsymbol{B}), \tag{A1}$$

for a stationary fluid. The aforementioned equation is linearized over an equilibrium magnetic field $\boldsymbol{B}_0$ to obtain

$$\frac{\partial \delta \boldsymbol{B}}{\partial t} = -d_{\rm H}[\nabla \times (\nabla \times \delta \boldsymbol{B}) \times \boldsymbol{B}_0], \tag{A2}$$

$\delta \boldsymbol{B}$ being the perturbation. To obtain the wave modes, the perturbation is assumed to be periodic along x and y of a Cartesian coordinate system

$$\delta B_x = \delta B_y \propto \exp[i(k_z z - \omega t)], \tag{A3}$$

where the equilibrium field is selected as $\boldsymbol{B}_0 = B_0 \hat{e}_z$. Straightforward mathematical manipulations yield the dispersion relation for the Whistler wave as

$$\omega = d_{\rm H} B_0 {k_z}^2. \tag{A4}$$

The wavenumber is selected as $k_z = (2\pi)/\Delta z$, where Δz is the dissipation scale in the computational domain, making the choice harmonious with the philosophy used extensively in the paper. Since the dimensionless $\rho_0 = 1$ in the numerical model, Equation (A4) can be written as

$$\left(\frac{\Delta z}{\Delta t}\right)_{\rm whis} = 4\pi^{\frac{3}{2}} d_{\rm H} \left(\frac{\Delta z}{\Delta t}\right)_{\rm Alf} \left(\frac{1}{\Delta z}\right)_{\rm whis}. \tag{A5}$$

Where $\Delta z_{\rm whis} = \Delta z_{\rm Alfvén} = 0.0078$, the dissipation scale in the present model along with $d_{\rm H} = 0.004$, while $\Delta t_{\rm Alf} \approx 10^{-3}$ from previous numerical experiments; suggest $\Delta t = \Delta t_{\rm whis} \approx 10^{-4}$ in the present model.

ORCID iDs

K. Bora https://orcid.org/0000-0002-3402-273X
R. Bhattacharyya https://orcid.org/0000-0003-4522-5070
Avijeet Prasad https://orcid.org/0000-0003-0819-464X
Bhuwan Joshi https://orcid.org/0000-0001-5042-2170
Qiang Hu https://orcid.org/0000-0002-7570-2301

References

Alfvén, H. 1942, Natur, 150, 405
Amari, T., Canou, A., & Aly, J.-J. 2014, Natur, 514, 465
Aschwanden, M. J. 2005, Physics of the Solar Corona. An Introduction with Problems and Solutions (2nd ed.; Chichester: Praxis)
Axford, W. I. 1984, Geophysical Monograph Series, Vol. 30 (Washington DC: American Geophysical Union), 1
Benz, A. O. 2017, LRSP, 14, 2
Bhattacharjee, A. 2004, ARA&A, 42, 365
Bhattacharyya, R., & Janaki, M. S. 2004, PhPl, 11, 5615

Bhattacharyya, R., Janaki, M. S., Dasgupta, B., & Zank, G. P. 2007, SoPh, 240, 63
Bhattacharyya, R., Low, B. C., & Smolarkiewicz, P. K. 2010, PhPl, 17, 112901
Birn, J., Drake, J. F., Shay, M. A., et al. 2001, JGR, 106, 3715
Bora, K., Bhattacharyya, R., & Smolarkiewicz, P. K. 2021, ApJ, 906, 102
Choudhuri, A. R. 1998, The Physics of Fluids and Plasmas: An Introduction for Astrophysicists (New York: Cambridge Univ. Press)
Dahlburg, R. B., Antiochos, S. K., & Zang, T. A. 1991, ApJ, 383, 420
Démoulin, P. 2006, AdSpR, 37, 1269
Dudík, J., Janvier, M., Aulanier, G., et al. 2014, ApJ, 784, 144
Eyink, G. L., & Aluie, H. 2006, PhyD, 223, 82
Garcia, H. A. 1994, SoPh, 154, 275
Gary, G. A. 2001, SoPh, 203, 71
Hornig, G., & Schindler, K. 1996, PhPl, 3, 781
Hu, Q., & Dasgupta, B. 2008, SoPh, 247, 87
Hu, Q., Dasgupta, B., Choudhary, D. P., & Büchner, J. 2008, ApJ, 679, 848
Hu, Q., Dasgupta, B., Derosa, M. L., Büchner, J., & Gary, G. A. 2010, JASTP, 72, 219
Inoue, S., Hayashi, K., Magara, T., Choe, G. S., & Park, Y. D. 2014, ApJ, 788, 182
Jiang, C., & Feng, X. 2014, SoPh, 289, 63
Jiang, C., Feng, X., Wu, S. T., & Hu, Q. 2013, ApJL, 771, L30
Jiang, C., Wu, S. T., Feng, X., & Hu, Q. 2016, NatCo, 7, 11522
Joshi, B., Mitra, P. K., Bhattacharyya, R., et al. 2021, SoPh, 296, 85
Kliem, B., & Török, T. 2006, PhRvL, 96, 255002
Kumar, D., & Bhattacharyya, R. 2011, PhPl, 18, 084506
Kumar, S., Bhattacharyya, R., Dasgupta, B., & Janaki, M. S. 2017, PhPl, 24, 082902
Kumar, S., Bhattacharyya, R., Joshi, B., & Smolarkiewicz, P. K. 2016, ApJ, 830, 80
Kumar, S., Bhattacharyya, R., & Smolarkiewicz, P. K. 2015, PhPl, 22, 082903
Kumar, S., Nayak, S. S., Prasad, A., & Bhattacharyya, R. 2021, SoPh, 296, 26
Lazarian, A., & Vishniac, E. 2000, arXiv:astro-ph/0002067
Lazarian, A., & Vishniac, E. T. 1999, ApJ, 517, 700
Lemen, J. R., Title, A. M., Akin, D. J., et al. 2012, SoPh, 275, 17
Liu, C., Prasad, A., Lee, J., & Wang, H. 2020, ApJ, 899, 34
Liu, R., Kliem, B., Titov, V., et al. 2016, ApJ, 818, 148
Mahajan, S. M., & Yoshida, Z. 1998, PhRvL, 81, 4863
Margolin, L. G., Rider, W. J., & Grinstein, F. F. 2006, JTurb, 7, 15
Mozer, F. S., Bale, S. D., & Phan, T. D. 2002, PhRvL, 89, 015002
Nayak, S. S., Bhattacharyya, R., Prasad, A., et al. 2019, ApJ, 875, 10
Nayak, S. S., Bhattacharyya, R., Smolarkiewicz, P. K., Kumar, S., & Prasad, A. 2020, ApJ, 892, 44
Parker, E. N. 1994, Spontaneous Current Sheets in Magnetic Fields: With Applications to Stellar X-rays, Vol.1 (New York: Oxford Univ. Press), 1
Parnell, C. E., Smith, J. M., Neukirch, T., & Priest, E. R. 1996, PhPl, 3, 759
Pesnell, W. D., Thompson, B. J., & Chamberlin, P. C. 2012, SoPh, 275, 3
Prasad, A., Bhattacharyya, R., Hu, Q., Kumar, S., & Nayak, S. S. 2018, ApJ, 860, 96
Prasad, A., Bhattacharyya, R., & Kumar, S. 2017, ApJ, 840, 37
Prasad, A., Dissauer, K., Hu, Q., et al. 2020, ApJ, 903, 129
Priest, E., & Forbes, T. 2000, Magnetic Reconnection (New York: Cambridge Univ. Press)
Prusa, J. M., Smolarkiewicz, P. K., & Wyszogrodzki, A. A. 2008, Comput. Fluids, 37, 1193
Rossby, C. G. 1938, Preface & Acknowledgments, Fluid Mechanics Applied to the Study of Atmospheric Circulations, Pt. I. Papers in Physical Oceanogr. & Met., Vol. VII (Massachusets: Cambridge and Woods Hole)
Ruderman, M. S., & Roberts, B. 2002, ApJ, 577, 475
Sarp Yalim, M., Prasad, A., Pogorelov, N., Zank, G., & Hu, Q. 2020, arXiv:2007.12275
Savcheva, A., Pariat, E., McKillop, S., et al. 2016, ApJ, 817, 43
Schindler, K., Hesse, M., & Birn, J. 1988, JGR, 93, 5547
Schou, J., Scherrer, P. H., Bush, R. I., et al. 2012, SoPh, 275, 229
Shi, C., Tenerani, A., Velli, M., & Lu, S. 2019, ApJ, 883, 172
Shibata, K., & Tanuma, S. 2001, EP&S, 53, 473
Smolarkiewicz, P. K. 2006, IJNMF, 50, 1123
Smolarkiewicz, P. K., & Charbonneau, P. 2013, JCoPh, 236, 608
Wang, H., Liu, C., Deng, N., et al. 2014, ApJL, 781, L23
Westerberg, L. G., & Åkerstedt, H. O. 2007, PhPl, 14, 102905
Wiegelmann, T. 2008, JGRA, 113, A03S02
Wiegelmann, T., Inhester, B., & Sakurai, T. 2006, SoPh, 233, 215
Wiegelmann, T., & Sakurai, T. 2012, LRSP, 9, 5